PhD THESIS PROJECT PROPOSAL
School of Arts and Sciences
University of Virginia

An Indirect Search for Weakly Interacting Massive Particles in the Sun Using Upward-going Muons in NOvA

Submitted by

Cristiana Principato

Physics

High Energy Physics

April 26, 2021

Approved ______________________________ Date __________
Advisor - Prof. Robert Group

Approved ______________________________ Date __________
Prof. Peter Arnold

Approved ______________________________ Date __________
Prof. Christopher Neu

Approved ______________________________ Date __________
Prof. Francesca Calamita

Contents

Abstract

I present the first Dark Matter search results using the full data set collected with the upward-going muon trigger in NOvA. Weakly Interactive Massive Particles (WIMPs) are a theoretical non-baryonic form of Dark Matter. The nature of Dark Matter is one of the most exciting open questions in modern physics. Though its existence can be inferred by astrophysical evidence, its properties are not yet understood. If we assume that Dark Matter particles can produce Standard Model particles through their interactions, an indirect search can help shed light on this mystery. The NOvA collaboration has built a 14 kton, fine-grained, low-Z, total absorption tracking calorimeter at an off-axis angle to the NuMI neutrino beam. Even though the detector is optimized to observe electron neutrino appearance from a muon neutrino beam, it has a unique potential for more exotic searches given its excellent granularity and energy resolution and relatively low-energy neutrino thresholds. In fact, with an efficient upward-going muon trigger and sufficient background suppression offline, NOvA is capable of a competitive indirect Dark Matter search for low-mass WIMPs. The idea of the upward-going muon trigger is first to select high-quality muon tracks, then use the timing information of all of the hits of each track to estimate directionality. In this way, the background flux is suppressed by more than a factor of 10^5 at trigger level to a rate of approximately 1 Hz. To further optimize this search, we use only upward-going muons that point to the Sun, so our search occurs at night when the Sun is on the other side of the Earth. This strategy also allows us to use the time when the Sun is above the horizon as a control region to estimate the background. Ultimately, implementation of a cut based and maximum likelihood analysis provides a powerful tool for rejecting background and selecting a sample of neutrino-induced upward-going muons. The overall background rejection power achieved by the analysis is substantial and impressive. Starting with approximately 150,000 events per second, we reduced it to 40 events per year. Since no statistically significant excess was found, a 90% C.L. upper limit on the expected muon flux of upward-going muons has been set using the upper limit on the number of events given the number of observed events in the signal region. Lastly, by assuming the theory behind the upward-going muon flux, a limit on the WIMP-nucleon spin-dependent cross-section in the Sun was estimated. Although the limits on the spin-dependent cross-section do not appear to be competitive with previous indirect Dark Matter searches, the upward-going muon flux limits are promising. The upward-going muon flux limits could extend these results to a broader class of models that are not specific to the dark matter theory but produce upward-going muons, leading to competitive results.

Acknowledgements

Pursuing a Ph.D. is a complicated and sometimes lonely path.

It would not have been possible without the support and guidance that I received from many people. I hope to convey here some of all the devotion and gratitude I feel for each of you.

First and foremost, I would first like to thank my amazing supervisor, Professor Craig Group. I deeply appreciate how you have been continuously encouraging and guiding me in the last years. You have always been so friendly and supportive of my efforts and struggles. I would have never succeeded in my Ph.D. program if it wasn't for you. Thank you.

I would like to express my most profound appreciation to my committee, Prof. Chris Neu, Prof. Peter Arnold, and Prof. Francesca Calamita, for all of their guidance through this process. You have raised many precious points in our discussion.

I'm incredibly grateful to Ralf Ehrlich and Yuri Oksuzian for their valuable guidance throughout my research. You provided me with the tools that I needed to successfully complete my dissertation.

A special thanks to Serdar Kurbanov. You have always been ready to help with a patience that cannot be underestimated and have been a great friend through the years.

I would also like to acknowledge Andrew Suttman, Enhao Song, Michael Baird, and Rob Mina for their extraordinary collaboration.

I would like to extend my sincere thanks to Andrew Norman and his group, Aristeidis Tsaris, Leo Aliaga, Pengfei Ding, for their invaluable contribution to this research and the insightful discussions.

I'd like to recognize the guidance and help that I received through the years from NOvA scientists, in particular, Alex Himmel, Brian Rebel, Chris Backhouse, Evan Niner, Gavin Davis, Jeremy Wolcott, and Mayly Sanchez. I have learned a lot from your constructive advice and your extensive knowledge. Thank you for the time and patience you had while I was learning.

Furthermore, I would like to thank the rest of my NOvA colleagues. I have enjoyed working and spending time with, during collaboration meetings, Bruce Howard, Erica Smith, Erika Catano-Mur, Linda Cremonesi, Karl Warburton, and Justin Vasel. I'm incredibly grateful for Diana and Kanika, with whom I shared so much during the "NOvA years," and I am glad to still keep close in my life.

Getting through my dissertation required more than academic support, and I have many, many people to thank for listening to and, at times, having to tolerate me over the past years.

I cannot express my gratitude and appreciation for all the good friends I have met at Fermilab: Martina and Mattia, Raquel, Rizki, Rob, Mateus, Paolo, Omar, and

Giuseppe. Moving to a new place so far from home can be challenging. You made it much more manageable.

I am also grateful to my friends at UVA: Rajveer, Sanjay, Cina, Zack, Eddie, and Charlie. I would have never passed the qualifier if I had to study all by myself. You made it much more fun.

Physics can be hard sometimes, especially when you are a woman. Luckily I had many great girlfriends that I look for inspiration. Thank you, Federica, Giada, Rosina, and Valeria for the help and support during my college years.

I also want to thank my undergraduate teacher, Prof. Marco Casolino. I would not be a physicist had it not been for your encouragement.

I could not have completed this dissertation without my closest friends, Chiara, Giulia, Greta, Natasha, and my sister Flavia. Thank you for the unconditional love and support you gave me from across the ocean. Every time I thought I couldn't do it, you were there to remind me why I could. You are always there for me, and I am incredibly grateful to have you in my life.

Most importantly, none of this could have happened without my family. To my new family for being so welcoming. To my cousin, since the day we were born. To my brother, that always brings me back to Earth. To my parents that grew up with me and gave me everything they had. I am forever grateful.

Finally, I want to thank my husband, Ben, for doing the dishes so I could work on my thesis. Maybe that's why I took so long to graduate (Just kidding :)).

You are the most amazing person I met, and I am so glad you chose me.

To my parents

Contents

List of Tables

List of Figures

List of Abbreviations

DOE	US Department Of Energy
Fermilab	Fermi National Accelerator Laboratory
NOvA	NuMI Off-axis ν_e Appearance experiment
NuMI	Neutrinos at the Main Injector
DM	Dark Matter
WIMPs	Weakly Interacting Massive Particle
WMAP	Wilkinson Microwave Anisotropy Probe
MOND	Modified Newtonian Gravity theories
LSP	Lightest Supersymmetric Particle
MSSM	Minimal Supersymmetric Standard Model
SLAC	Stanford Linear Accelerator
CC	Charge Current interaction
NC	Neutral Current interaction
CCQE	Charge Current Quasi Elastic
RES	Resonance
DIS	Deep Inelastic Scattering
SNO	Sudbury Neutrino Observatory
PMNS matrix	PontecorvoMakiNakagawaSakata matrix
APD	Avalanche Photo-Diode
PE	Photo-Electron
FEB	Front-End Board
DDT	Data-Driven Trigger system of NOvA
DAQ	Data Acquisition system of NOvA
DCM	Data Concentrator Module
FD	NOvA Far Detector
ND	NOvA Near Detector
ASIC	Application Specific Integrated Circuit
DCS	Dual Correlated Sampling
PDG	Particle Data Group
MSV	Michaev–Smirnov–Wolfenstein matter effect
NH, RH	Normal Hierarchy of neutrino masses and Reversed Hierarchy respectively
ADC	Amplitude to Digital Converter
TDC	Time to Digital Converter, also used as general unit of time
HV	High Voltage
AU	Astronomic Unit
CoM	Center of Mass

Chapter 1

Introduction

"Don't assume that what we currently think is out there is the full story. Go after the dark matter, in whatever field you choose to explore."

Nathan Wolfe

This thesis presents the first Dark Matter search results for Weakly Interactive Massive Particles (WIMPs) using upward-going muons in NOvA. Still today, Dark Matter has not been found, but it remains an important question that needs to be answered. Independent cosmological and astrophysical phenomena could be explained by a theoretical framework which includes Dark Matter. Weakly Interactive Massive Particles, in particular, are a potential candidate for DM, being independently predicted by theories that were introduced to explain a different phenomenon. The NOvA collaboration has built a 14 kiloton, fine-grained, low-Z, total absorption tracking calorimeter at an off-axis angle to the NuMI neutrino beam.

Even if the detector is optimized to observe electron neutrinos appearing from a muon neutrino beam, it has a unique potential for more exotic searches given its excellent granularity and energy resolution and relatively low-energy neutrino thresholds. In fact, with an efficient upward-going muon trigger and sufficient background suppression offline, NOνA is capable of a competitive indirect dark matter search for low-mass WIMPs. A particular advantage that NOνA has, compared to past experiments that have performed similar dark matter annihilation searches, is the experiment's low energy threshold for muon reconstruction. A 1 GeV muon travels approximately 5 meters in the NOνA detector and can leave visible energy over 120 detection cells. The NOνA detector is located on the surface of the earth with only a 3 m earth equivalent overburden. For this reason, the cosmic ray muon rate at the NOνA far detector is about 150 kHz and provides the primary challenge for triggering and optimizing such a search analysis. For the upward-going muon trigger, the idea is first to select high-quality muon tracks, then use the timing information of all of the hits of each track to estimate directionality. In this way, the background flux is suppressed by more than a factor of 10^5 at trigger level to a rate of less than 10 Hz.

In the case of long tracks, the timing information is aggregated across all the hits in the track, and the physical size length of the track provides a long lever arm for determination of the track's directionality. For shorter tracks, the timing information is not as powerful for rejecting downward-going backgrounds. Ultimately, implementation of a cut based and maximum likelihood analysis provides a powerful tool for rejecting background and selecting a sample of neutrino-induced upward-going muons, leading to a competitive dark matter search.

Figure 1.1: Fermi National Accelerator Laboratory

The work was developed under the supervision of Prof. R. C. Group. The central part of this analysis was done during my stay at Fermi National Accelerator Laboratory (Fermilab, IL, USA) from May 2015 to December 2019.

Chapter 2

Dark Matter and WIMPs

" Dark Matter was headline news. There was only one small problem no-one had actually found any Dark Matter."

Most of our Universe is Missing

2.1 Overview

During the last decade, physicists have drawn a picture of the Universe in which roughly a quarter of the energy density of the Universe consists of Dark Matter (DM). However, still today, the existence of DM in the Universe is a "hot topic" in physics. Even if there is compelling evidence for its existence and an extensive search has been done using several detection techniques, no experimental confirmation of DM particles has been found at the time of writing this thesis, and its elusive nature remains unknown. Nevertheless, the existence of dark matter is a theoretical framework that could explain those independent cosmological and astrophysical phenomena, keeping researchers and funding agencies interested in investing in it. In this chapter, we outline the observational evidence for DM, then review some of the hypothetical candidates and ultimately discuss the different detection techniques used in DM

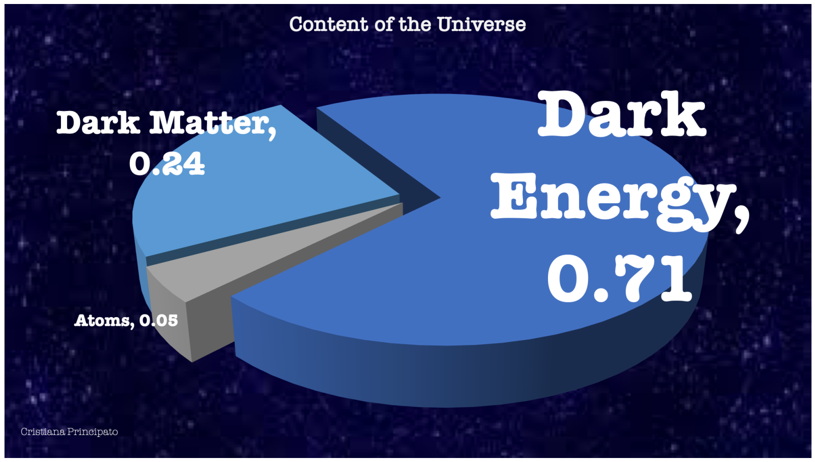

Figure 2.1: WMAP measures the composition of the universe.

searches.

2.2 Observational Evidence

Nowadays the accepted and also most common model for the origin of the Universe is the Lambda Cold Dark Matter model, upon which the currently used measurement of astrophysical quantities and constants depend. According to this model, the Universe is 13.7 billion years old and is made up of approximately 4% baryonic matter, 23% DM and 73% Dark Energy with a Hubble constant of 71 km/s/Mpc (See Fig 2.1 from Ref. [1].). While the baryonic content of the Universe is well-known, the evidence for the existence of DM is supported by cosmological and astrophysical phenomena that originate at very different scales and seems to be independent of one another.

2.2.1 Galaxy Clusters

Swiss astronomer Fritz Zwicky is known as the first astronomer to suggest the existence of a kind of nonvisible matter that he, therefore, called dark matter [2]. In 1933, Zwicky calculated the range of the galaxies' radial velocity in the Coma cluster and estimated the galaxy cluster's gravitational mass. To do this, he used the virial theorem, which relates the time-averaged total kinetic energy to the averaged overall potential in a stable n-body system:

$$< K.E. >= -\frac{1}{2}P.E.. \tag{2.1}$$

While the bodies' potential energy in a gravitationally bound system depends on the entire system's mass and can be challenging to estimate, the kinetic energy can be inferred easily from the body's motion.

A few assumptions have to be made: it is assumed that the system's equilibrium is on average in a stable state, all bodies are the same mass, and the velocity distribution is isotropic.

Therefore, the virial mass of a system can be calculated by observing the system's true overall extent and mean square velocities of each of the objects that makes up the system. The virial theorem applies, in a slightly different form, even if the motion is random or not isotropic.

Combining all this information, the total mass of the cluster can be calculated:

$$< K.E. >= -\frac{1}{2}P.E. \tag{2.2}$$

$$\frac{1}{2} \cdot mv^2 = \frac{1}{2}\frac{GMm}{r} \tag{2.3}$$

where m is the mass of the star, v^2 is the velocity squared, r is the typical distance between the center of mass and the star that can be replaced by $\frac{1}{2}R$, with R being the radius of the cluster, and M representing the total mass of the cluster.

Zwicky first determined the clusters' total mass to be the observed galaxies' product, using an average mass for a galaxy to be 10^9 solar masses. Using an estimated number for the radius of the system, he then calculated the total potential energy. From there, he was able to estimate the velocity dispersion. The vast discrepancies between the estimated velocity dispersion and the observed average velocity dispersion could be explained by a discrepancy between the observable, luminous mass and the total mass of the cluster. Zwicky made the hypothesis that there must have been an enormous amount of other non-luminous matter contributing to his results, “dark matter”. Part of the discrepancy was due to the Hubble constant value, H_0 [3] being larger at that time due to calibration errors, but the discrepancy was confirmed in 1936 by Sinclair Smith using observations of the Virgo cluster [4].

2.2.2 Galaxy Rotation Curves

Another piece of evidence that supports the existence of DM came in the 1970s when Vera C. Rubin and W. Kent Ford Jr. published a study showing that the rotation curve of galaxies is flat [5]. Under the assumption that Newtonian mechanics and Kepler’s third law are correct and that the galactic bulge contains most of the mass of the galaxy, the rotational velocity is expected to decrease as the distance from the bulge of the galaxy increases. In their studies, Rubin and Ford analyzed the rotational velocity of the galaxy M31 in the Andromeda Nebula. The result, shown in Fig. 2.2 showed that most of the stars in the spiral galaxy were orbiting at the same speed, meaning that the galaxy masses were growing linearly with the radius well beyond the galactic bulge. That observation was in disagreement with the theoretical prediction based only on visible matter. A similar finding has been discovered in the most recent years for all galaxies studied, including the Milky Way. A possible explanation is that galaxies contain far more mass, extending far beyond the visible edge of the galaxies, than what can be accounted for by the bright stellar objects residing in galactic disks. In this scenario, the galaxies would have an enormous dark halo made of non visible matter that provides the force to speed up the stars’ orbits to give a better fit to the data. Numerous other alternatives have been proposed to explain these observed properties of galaxies. In particular, is worth mentioning

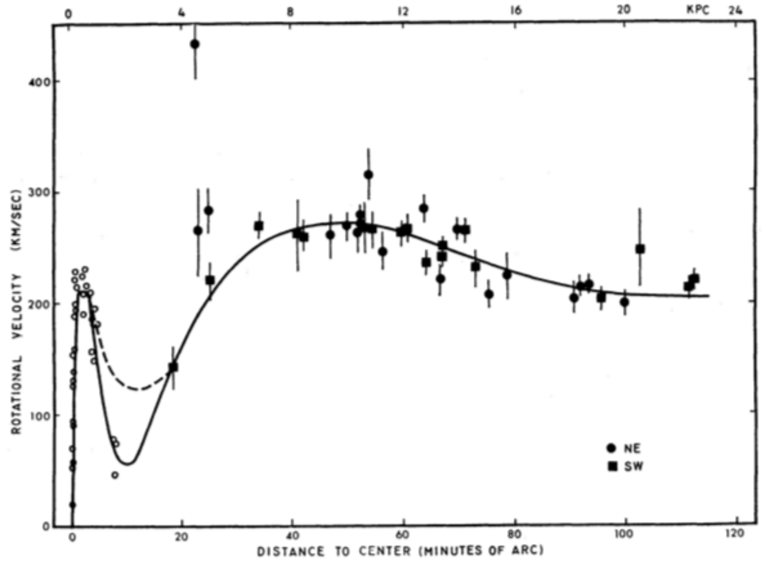

FIG. 9.—Rotational velocities for OB associations in M31, as a function of distance from the center. *Solid curve*, adopted rotation curve based on the velocities shown in Fig. 4. For $R \leq 12'$, curve is fifth-order polynomial; for $R > 12'$, curve is fourth-order polynomial required to remain approximately flat near $R = 120'$. Dashed curve near $R = 10'$ is a second rotation curve with higher inner minimum.

Figure 2.2: Measures of the rotational velocity in the Vera Rubin paper, Image Credit: [5]

the theories that proposed a modification to Newton's law of gravity, also called the Modified Newtonian Gravity (MOND) theories.

Even if many versions of those theories have been successful in explaining the data, it seems unlikely that the MOND theories could solve the whole DM existence problem. In fact, they are still unable to explain some phenomena such as gravitation lensing, which is discussed in the next subsection.

2.2.3 Gravitational Lensing

Gravitational lensing is one of the most astonishing proofs of Einstein's theory of General Relativity, and one more piece of evidence for the existence of DM. Einstein's theory of General Relativity effectively predicts the amount of bending that light experiences due to a mass, a factor of two bigger than what was predicted by Newton.

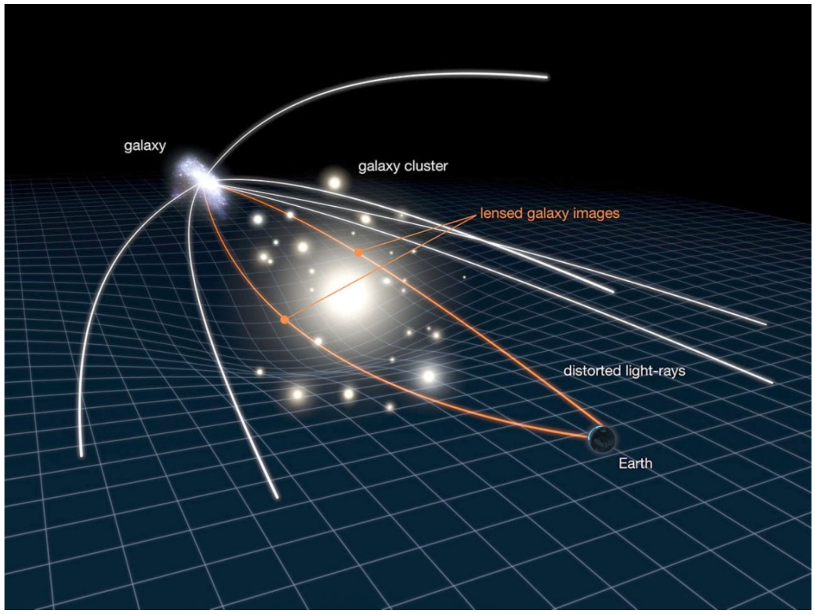

Figure 2.3: Gravitational lensing cartoon showing the bending of the light as travelling near a massive object. Image Credit: NASA/ESA.

In particular, the deflection is equal to

$$\delta = \frac{4 \cdot G \cdot M}{R \cdot c^2}. \tag{2.4}$$

The first observation was conducted by studying the position of the stars near the Sun during the solar eclipse on May 29, 1919, by Arthur Eddington and Frank Watson Dyson, concluding that the stars were slightly out of position when the Sun was closest to the stars [6]. In empty space, the light would travel at the speed of light, in a straight line, while a mass would create a curvature in the space-time due to the gravitational field proportional to the mass itself. So by examining the curvature of the light, one could infer the mass of the object that creates that curvature. However, the notion that halo of DM surround galaxies did not become widespread until the late 1980s with the launch of the Hubble Space Telescope and the spectroscopic data from the Sloan Digital Sky Survey. The team at SLAC isolated 98 elliptical galaxies, which are a compact and dense object and thus the perfect gravitational lens [7].

Because the redshifts of both the lens and the background source are known, the lensing formulation revealed by Hubble Space Telescope images can be used to determine the total mass density in the lens as a function of the distance from the galactic center. The study proved that the total mass distribution is uniform and spatially more extended than that of the visible baryons. Since then, many other studies have been conducted, including of the Milky Way, using weak gravitational lensing, which is an intrinsically statistical measurement used when the distortion of the background sources are much smaller, requiring a large number of sources in order to show a statistically coherent effect. The results seems to confirm that galaxy clusters are the largest gravitationally bound structures in the Universe with approximately 80% of cluster content in the form of DM. One of the most outstanding outcomes of these results is that DM can be seen at a much larger scale than it could have been with the rotation curve studies alone [8]. Gravitational lensing is now one of the most commonly used tools in the astronomer's toolbox and can be used to explain the behavior of the Bullet Cluster, explained in the next subsection.

2.2.4 Hot Gas in Clusters

Another form of gravitational evidence for DM comes from the hot gas in clusters. One of the most outstanding piece, which MOND theories can't explain, was given by images of two galaxies colliding. When combining two different images, one of the x-ray emission of the galaxy and the other one of the visible light, one can see the existence of a hot gas in the cluster, created by the electromagnetic interaction between the baryonic matter. This could be explained by a significant DM component that provides the potential well to hold on to the gas. Without that, the hot gas would evaporate. On the other hand, using gravitational lensing, one can infer that the majority of the mass composition of those two galaxies, instead, passes through each other without interacting. The most famous example of this phenomena is the Bullet Cluster, measured in August 2006 [9].

Figure 2.4: The Bullet clusters. In blue an estimate of the total mass of the two galaxies undergoing collision while in red the the x-ray detected by the Chandra X-ray Observatory showing the location of the x-ray emission of the hot gas. Most of the matter in the clusters (blue) is separate from the ordinary matter (pink), giving direct evidence that nearly all of the matter in the clusters is dark.
Image Composite Credit:X-ray: NASA/CXC/CfA/M.Markevitchet al.; Lensing Map: NASA/STScI; ESO WFI; Magellan/U.Arizona/D.Clowe et al.
Optical: NASA/STScI; Magellan/U.Arizona/D.Clowe et al.

In Fig 2.4, one can see the image of the Bullet Cluster, a cluster formed by the collision of two smaller galaxies, in the visible light range as observed by the Magellan Telescope and the image from the Chandra X-ray Observatory showing the location of the x-ray emission of the hot gas. The blue shade estimates the total mass of the two galaxies undergoing a collision determined by astronomers from gravitational lensing, while in red is showing the location of the x-ray emission of the hot gas. The collisions did not slow down the dark matter in blues as it can be seen proceeding first, while the hot gas undergoing collision is slowed down and stays behind.

2.2.5 Cosmic Microwave Background

The measurement of the cosmic abundance, in particular of the Cosmic Microwave Background (CMB), provides another independent evidence of DM existence. The CMB is the oldest electromagnetic radiation in the Universe, the remnant radiation from the recombination epoch. This radiation is almost uniform and isotropic, with a black body spectrum at a temperature of 2.7 K. It is the oldest information that we can obtain about the early universe's state and composition, and a "limit for our knowledge". After the Big Bang, which is also supported by the CMB, the Universe was in a much hotter and much denser, fully ionized, state. During this time, electrons and protons could not bind to form atoms because the mean photon energy exceeded the hydrogen bonding energy of 13.6 eV causing any forming hydrogen atoms to immediately re-ionize. As the Universe expanded and cooled down, the energy of the photons, which is directly proportional to the photon wavelength, started to diminish until they weren't energetic enough for the scatter to happen. The time of the formation of the first atoms is called the recombination epoch, and the following time, when photons started to travel freely in space is referred to as photon decoupling. Those photons that couldn't be coupled anymore and kept traveling isotropically, now redshifted, are the radiation that we observed and call the CMB. For a long time,

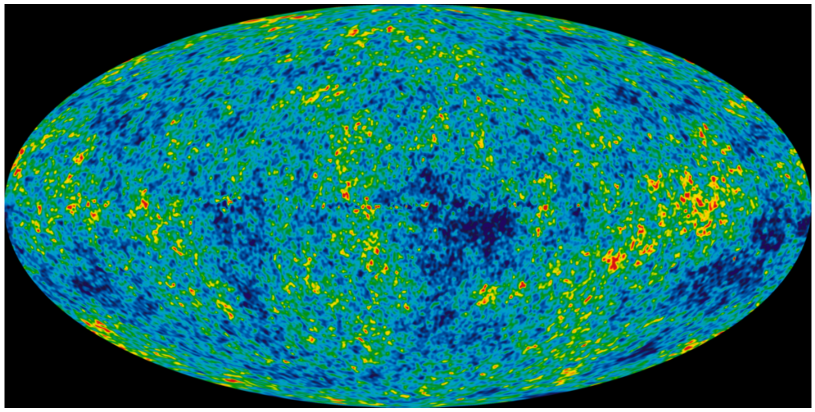

Figure 2.5: The full-sky image of the temperature fluctuations (shown as color differences) in the cosmic microwave background, made from nine years of WMAP observations. Image Credit: NASA

we didn't have the right instrument to detect such a small signal; in fact, the space between stars and galaxies appears to be completely dark with an optical telescope. The first discovery of the CMB radiation as faint isotropic background noise happened by accident by the radio astronomers Penzias and Wilson in 1964, who later won the Nobel prize for the discovery. Later on, other experiments were built to study the CMB, with the Wilkinson Microwave Anisotropy Probe (WMAP) being the first experiment to develop a full-sky map of temperature fluctuations in the CMB, and the latest results obtained by the Planck mission team [10].

The CMB features that we can observe from those experiments are its frequency spectrum, its temperature, and its polarization states, and each of these contains information about the creation and evolution of the Universe and cosmological information. If the CMB was exactly isotropic, as it was thought to be and measured at the beginning, the formation of large structure couldn't be possible. The vast majority of information that we can infer from studying the CMB actually comes from the small temperature anisotropy. The small fluctuation in the temperature provided, in fact, overdense and underdense regions, with the cold spots representing regions where there is a greater gravitational pull due to a higher density of matter, and the hot spots being hotter because the radiation in that region lives in a shallower gravitational well. The evidence for the existence of DM comes from the studies of that anisotropy. The peaks and the valleys in the CMB anisotropies spectrum, in fact, depend on the amount of baryonic matter and DM in the Universe. With the presence of DM, the same happens, but because there is no interaction cross-section between baryonic and DM or between radiation and DM, the spectrum of the anisotropies would be different [11]. CMB also provides insight on the composition of the Universe as a whole, with the ordinary matter, including stars, galaxies and all the visible world around us, being only 4% of the total composition. Primordial nucleosynthesis also makes those predictions.

2.2.6 Primordial Nucleosynthesis

The standard model of Big Bang nucleosynthesis (BNN), was developed from the original idea of element formation due to nucleosynthesis in the expanding Universe at a very high temperature. Primordial nucleosynthesis anticipates the amount of Hydrogen, Helium, and Lithium contained in the Universe and their abundance by mass. The BBN, hence, provides a limit on the abundance of nucleons in any form. A discrepancy in a detailed comparison of element abundances with the theoretically predicted one, introduced the idea that New Physics can modify the synthesis of light element abundances. Many possibilities might account for departure from the standard model, yet the hypothesis of the existence of a non-baryonic kind of matter seems to be a very compelling one. These predictions seem to match exactly the data as long as only 4% of the total constituent of the Universe are atoms, which agree with the CMB finding [12], [13], [14].

2.3 Dark Matter Candidates

A long list of DM candidates has been suggested throughout the years, and despite all the evidence for its existence, its nature remains unknown. There is a hypothesis about "hot" versus "cold" DM, where hot and cold refer to the speed at which DM was moving at the time when galaxies started to form. There is also a hypothesis about baryonic versus non-baryonic DM, with masses that range over 75 orders of magnitude. For this thesis, only a few, most successful examples are described in this zoo of theories and particles:

1. **WIMPS:** Among the non-baryonic DM candidates, the most popular are the Weakly Interacting Massive Particles or WIMPS, which is the main focus of this thesis and described in more detail later.

2. **Axions:** Axions are another important non-baryonic DM candidates. As for the WIMPs, their popularity arises from the fact that they were independently predicted to explain other unsolved physics problems. Axions, naturally appear in the Peccei-Quinn solution to the strong-CP problem in the theory of strong interactions [15]. Unfortunately, the experiments looking for the existence of these light DM particles have already explored most of their parameter space and so far have shown negative results [16].

3. **Baryonic DM:** MACHOs, or Massive Compact Halo Objects, that are the only DM candidate made up of baryonic matter and were a prevalent theory until a few years ago. According to the theory that hypothesizes their existence, they might be brown dwarf stars, primordial black holes or neutron stars. However, even if these could be DM candidates, there are not enough of them to explain the entire observed DM abundance [17]. In addition, all the experiments that have searched for them have not found any evidence of their existence, such as

projects in [18], [19], [20].

4. **Light Scalar DM:** Lately, new theories for light scalar DM have been proposed. Ultra Light Scalar DM has mass on the scale of 10^{-22} eV, so light that it would behave according to string theory and quantum mechanics laws [21].

5. **Sterile Neutrinos:** The Sterile Neutrino is another popular DM candidate because the ordinary neutrino appears to be too light to be cosmologically significant. This particle, the heavier cousin of the Standard Model neutrino, is thought to interact only via a weaker interaction and gravitation [22].

6. **Self-interacting DM:** According to this theory, DM is many different particles only observable indirectly because they only undergo gravitational interactions [23].

2.3.1 Dark Matter Properties

Cosmological observation puts some constraints on the nature of the DM candidate. In order to survive until today DM particles need to be stable. Because they are not visible they do not interact electromagnetically. They must be massive in order to explain the composition of the Universe, and non-relativistic to explain the structure formation of the Universe compatible with Universe as we observe it today. In addition to DM being cold, there are constraints on the annihilation cross-section. Of the two possible creation mechanism that have been hypothesized, thermal in the early Universe and non-thermal during phase transition, only the first one is considered in this thesis.

In the early Universe, particles were supposed to be in thermal equilibrium. Statistical and chemical equilibrium need to occur to achieve thermal equilibrium. The first one occurs when elastic scattering reactions occur faster than the expansion, while chemical equilibrium occurs when the reaction that creates and destroys parti-

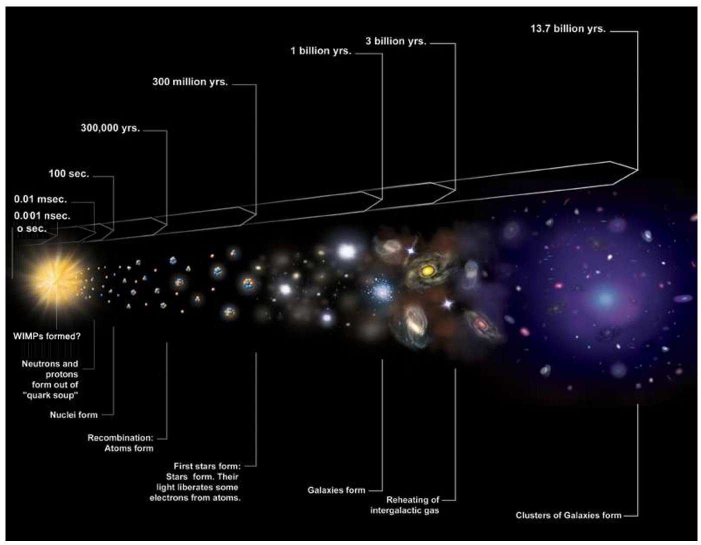

Figure 2.6: The nature of dark matter is unknown. A substantial body of evidence indicates that it cannot be baryonic matter, i.e., protons and neutrons. The favored model is that dark matter is mostly composed of exotic particles formed when the universe was a fraction of a second old. Such particles, which would require an extension of the so-called Standard Model of elementary particle physics, could be WIMPs (weakly interacting massive particles), or axions, or sterile neutrinos. - Caption and Image Credit: NASA

cles occurs faster than the expansion, such that the interaction rate is greater than the expansion rate

$$\Gamma = n \cdot \sigma \cdot v > H \sim \frac{T^2}{m_{PL}}. \tag{2.5}$$

where H is the Hubble constant. The equilibrium abundance, and the thermal equilibrium , is maintained if the same rate of creation and destruction between DM and Standard Model particles is achieved, such that

$$\chi\bar{\chi} \leftrightarrow l\bar{l}. \tag{2.6}$$

where χ is a DM particle and l is a lighter SM particles. The rate of annihilation of DM particles in lighter particle is then:

$$\Gamma_{\chi\bar{\chi}\to l\bar{l}} = \langle \sigma_{\chi\bar{\chi}\to l\bar{l}} \cdot |v| \rangle n_\chi. \tag{2.7}$$

As the Universe expanded and cooled down, $T > m_\chi$ doesn't hold anymore. The equilibrium abundance dropped so the annihilation partners got separated, and a relic abundance of χ particles was created. Using the Boltzmann equation, one can study the evolution of the total DM density, [24]:

$$\frac{dn_\chi}{dt} = -3 \cdot H \cdot n_\chi - < \sigma_A \cdot v > [(n_\chi)^2 - ({n_\chi}^{eq})^2] \tag{2.8}$$

the equation can be rewritten as

$$\frac{dn_\chi}{dt} + 3 \cdot H \cdot n_\chi = - < \sigma_A \cdot v > [(n_\chi)^2 - ({n_\chi}^{eq})^2] \tag{2.9}$$

where the left side gives information related to the expansion rate, while the right side is the effect of the annihilation on the density. Because $(n_\chi)^2 = ({n_\chi}^{eq})^2$ the right side is equal to zero at equilibrium. Once the temperature drops and the system goes out of thermal equilibrium, the term ${n_\chi}^{eq}$ can be approximated by

$$ {n_\chi}^{eq} \sim (\frac{m_\chi T}{2\pi})^{3/2} \cdot \exp\left\{-\frac{m_\chi c^2}{k_B T}\right\}. \tag{2.10} $$

where h is the reduced Hubble constant, defined as: $h = H_0/100\mathrm{km\,s^{-1}\,Mpc^{-1}}$.

Relating this result with the approximate solution of the density parameter Ω, one can find that the approximate solution for the cold DM composition of the universe is [25],

$$ \Omega_c \cdot h^2 = \frac{m_\chi \cdot n_\chi}{\rho} \sim \frac{3 \cdot 10^{-27} cm^3/s}{< \sigma_A \cdot v >}. \tag{2.11} $$

Using the results obtained by studies of the CMB, in particular PLANK 2015 [10],

$$ \Omega_c \cdot h^2 = 0.1199 \pm 0.0027 \tag{2.12} $$

the order of scale of the annihilation cross section can be obtained. The cross-section obtained as such is in the region of the electroweak interaction. So, if this particle exists, it should have a weak interaction and mass, hence the name Weakly Interactive Massive Particles or WIMPs.

2.3.2 WIMPs

At the time of writing this thesis, WIMPs are still considered the best DM candidate. WIMP particles were independently hypothesized by three different theories: supersymmetry (SUSY), universal extra dimension (UED) and little Higgs theories. Each of those theories hypothesize the existence of a lightest particle with the WIMPs' main theoretical characteristics described above. This thesis presents a search for WIMPs hypothesized by supersymmetry theories.

The fact that WIMPs were independently hypothesized and supported by supersymmetry theories and that their relic abundance gives the annihilation cross-section

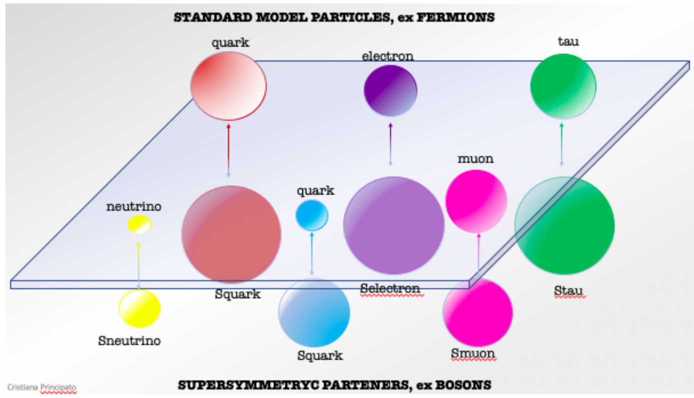

Figure 2.7: Cartoon showing Standard Model particles and their Supersymmetric partner.

on the weak scale is the reason why they have been taken so seriously as DM candidate. This is known as the "WIMP miracle."

The Standard Model (SM) does a fantastic job at describing the behavior and the interaction of the elementary particles that compose our world. Most of the SM's predictions have been confirmed with very high precision. Nevertheless, there are still some gaps in the SM that need to be filled, such as the hierarchy problem, gauge coupling unification, and radiative electroweak symmetry breaking. The supersymmetry principle was introduced to address some of the shortcoming of the SM with an elegant solution.

The supersymmetry principle is a conjectured symmetry of the space-time under which each particle in the SM has a supersymmetric partner particle. Particles and fields of integer spin (bosons) are mapped into particles and fields of half-integer spin (fermions), and vice-versa. This simple property gives the Lagrangian a new symmetry under the swap of force and matter. Besides being very elegant, it also allows explanations of several of the gaps in the SM. An easy example to understand this symmetry can be shown using colors. The SM Lagrangian is not symmetric under the swap of force and matter, in fact

$$\mathcal{L} = \color{red}{Force} + \color{blue}{Matter} \tag{2.13}$$

is different from

$$\mathcal{L} = Force + Matter. \tag{2.14}$$

With the introduction of the new SUSY term instead

$$\mathcal{L} = Force + Matter + Force + Matter \tag{2.15}$$

one can see that the Lagrangian simply acquires a new overall symmetry. The SUSY generators Q behaves as

$$Q|Boson > = \ |Fermion > \tag{2.16}$$

$$Q|Fermion > = \ |Boson > . \tag{2.17}$$

The first essential property of Q is that it changes the spin a particle

$$Q|j > = \ |j \pm 1/2| \tag{2.18}$$

and hence its space-time properties. For this reason, SUSY is a space-time symmetry and not only an internal one [26]. More than 10,000 papers have been written on many SUSY theories, some of which have already been excluded by experiment. In this analysis, only a Minimal Supersymmetric theory is considered. In more detail, a new symmetry is introduced in the SUSY theory that we are considering, called the R-parity. The R-parity is defined as

$$R = (-1)^{(3B+L+2j)} \tag{2.19}$$

where B is the baryon number, L is the lepton number, and j is particle spin. The R parity would then be R = + 1 for SM particles and R = -1 for the supersymmetric partners. So in the SUSY theories where R-parity is conserved, supersymmetric particles have constraints on their creation, annihilation and decay. They can only be created or annihilated in pairs and they can only decay into final states containing an odd number of supersymmetric particles. For this reason, the lightest supersymmetric particle, also known as LSP, cannot decay in any state with negative R-parity, and hence, it is stable. This particle, the lightest supersymmetric particle (LSP), is the most popular WIMP candidate [27].

Neutralino as a Dark Matter Candidate

In some SUSY theories, in particular the Minimal Supersymmetric Standard Model (MSSM), there are four neutralinos, (χ_{01},χ_{02},χ_{03},χ_{04}), where the LSP is one eigenstate, χ_{01}. The LSP is a natural candidate for WIMP. It is stable over cosmological time scales, electrically neutral, weakly interacting, has a mass predicted to be in the mass range of a few GeV to TeV, and it is expected to have a substantial relic density. In the analysis done in this thesis, the reference to WIMP search implies a search for the MSSM LPS neutralino.

Chapter 3

Neutrino Physics

> *"Want to hear a joke about neutrinos? It'd probably go straight through you."*
>
> Shane Greenstein

3.1 Introduction

The neutrino is now a central particle in elementary particle physics, astrophysics, and cosmology. Discoveries involving neutrinos are reshaping the foundations of the understanding of nature, and the discovery that neutrinos have mass provided the first tangible evidence for physics beyond the very successful Standard Model of elementary particles. Enrico Fermi invented the name "neutrino" as a wordplay on "neutrone," which means neutron in Italian. Its existence was first hypothesized by W. Pauli in 1930, desperate to preserve the principle of energy conservation in order to explain the energy spectrum of the beta decay, the decay of a neutron into a proton and an electron. The neutrino was supposed to be responsible for carrying away the difference in energy and angular momentum of the initial and final particles observed in one experiment. The particle that Pauli theorized was expected to be undetectable and massless, but luckily, turned out to be neither of those.

Neutrinos were detected 25 years later, in 1956, by C. Cowan and F. Reines, who observed neutrino induced events in a scintillation detector. The results were published in Science with the article *Detection of the Free Neutrino: a Confirmation* [28], for which Reines was awarded the Nobel Prize in 1995. Scientists started to then wonder if neutrinos were all the same or if there was more than one kind of neutrino. In 1962 an experiment lead by Leon M. Lederman, M. Schwartz, and J. Steinberger detected interactions of the muon neutrino and revealed that more than one type of neutrino exists, an idea called "the two-neutrino hypothesis" [29]. After the tau particle was discovered at SLAC, the third type of neutrino associated with the new lepton was hypothesized to exist, and afterward observed in a tau decay experiment. An important measurement was also made at LEP that observed Z production in e^+e^- collisions and determined the number of light neutrino types to be $N_\nu = 2.984 \pm 0.008$. The tau neutrino's first detection, the last SM particle to be detected before the recent discovery of the Higgs boson, finally happened in 2000 by the DONUT collaboration at Fermilab [30].

3.2 Neutrinos in the Standard Model

The Standard Model of elementary particles describes the elementary particles and forces acting among them as understood today.

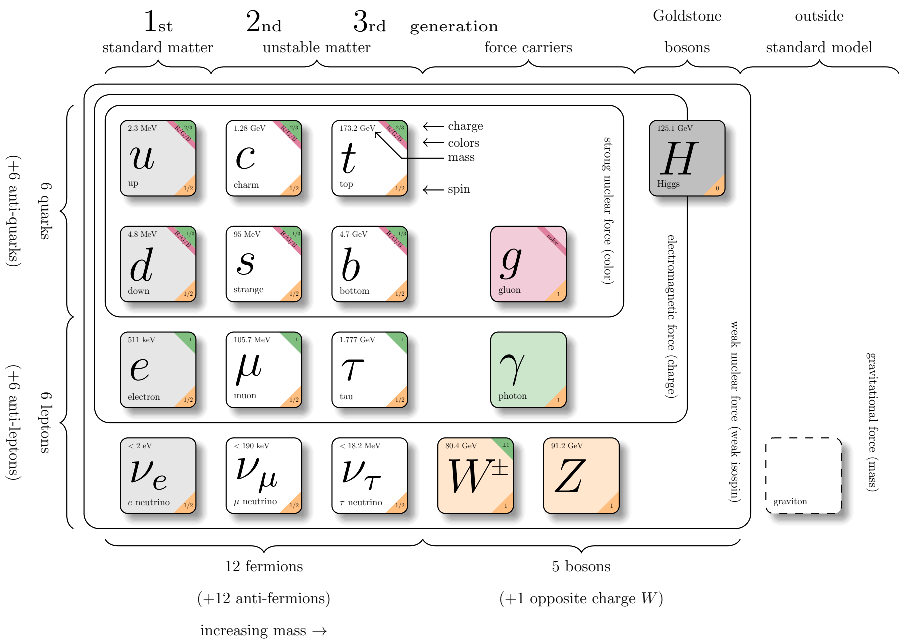

In this model, there are six leptons, among which there are three types of neutrinos, six quarks, and six bosons which constitute the basic building block of the universe and the rules governing their interactions. Neutrinos differ from all the other particles because they are incredibly light, and they only interact weakly. Although trillions of neutrinos go through each of us every second, neutrinos are very elusive particles.

When neutrinos were discovered, because the energy of neutrinos could not be determined even in the most sensitive beta decay measurements, the interaction of this particle with matter was soon thought to be extremely small. As consequence of their elusiveness they were thought to have no electric charge, and subsequently, no mass or magnetic moment. Further experimental observations of the angular momentum balance during beta decay also showed that neutrinos have spin 1/2.

The interaction between neutrinos and other forms of matter is extremely rare because they interact only via the weak force, an interaction known today but not well understood at the time of their discovery. The weak interaction is mediated by three heavy mediators, the $W^{\pm}$ and the Z^0 bosons. The $W^{\pm}$ are the ones responsible for the Charged Current (CC) interactions, while the Z^0 is responsible for the Neutral Current (NC), flavor independent interactions. Given the difficulty in knowing the flavor of the neutrino involved in the NC interaction, the vast majority of neutrino detection techniques involves only CC interactions. Depending on the energy of the incoming neutrinos there are different kinds of processes that they can undergo. These are Charged Current Quasi Elastic (CCQE), Resonance (RES) and Deep Inelastic Scattering (DIS).

The SM was built under the assumption that neutrino was a massless particle, that there are exactly three neutrinos, lepton number is conserved separately for each of the three lepton families, neutrinos and antineutrinos are distinct particles, and all neutrinos are left-handed while all antineutrinos are right-handed.

3.3 Extending the Standard Model

The SM is an elegant scheme, with well-defined calculation rules, agreeing well with experiments. It does contain some shortcomings though, and many questions still need an answer. Neutrinos are one of the troublesome parts of this model and the first evidence of physics beyond it. In the SM, fermions differ from bosons due to their their fractional spin, equal to 1/2. Trying to describe the interaction of those particles, generalizing Schrodinger's equation for relativistic particles, Dirac found an elegant solution for the problem. For massless fermions the Dirac equation is:

$$i\frac{\partial\psi}{\partial t} = \vec{\sigma}\cdot\vec{\mathbf{p}}\,\psi. \tag{3.1}$$

For a free particle with zero mass the solution of the equation has two different states. Since $\vec{\sigma}\cdot\vec{\mathbf{p}}$ measures the component of the spin along the direction of motion, there is a ψ_R solution for $\vec{\sigma}\cdot\vec{\mathbf{p}} > 0$ and $p_0 > 0$ and a ψ_L solution for the rotated component. The quantity $\frac{\vec{\sigma}\cdot\vec{\mathbf{p}}}{p_0}$ is called helicity. Chirality is an intrinsic, fundamental property of the particle, but helicity is not. In the case, of a free particle with zero mass the chirality is the same as the helicity. For a massive particle, the sign of its helicity depends on the frame of reference while for free massless particles have a fixed helicity.

In a famous experiment performed by Goldhaber et al. in 1957 [31] the helicity of the neutrino was shown to be -1.0 ± 0.2, which was considered as the conclusive evidence that the neutrino were left handed.

However, observations of neutrino oscillations imply that neutrinos have mass like the other fermions, and the helicity assumption had to be reviewed. It is now understood that the spin parallel to their momentum for neutrinos is a consequence of the $V - A$ structure of the weak interaction, which contains a vector and axial part, $\gamma^{\mu}(1 - \gamma^{5})$.

In this theory, particles are produced in weak interaction vertices with a well-defined chirality. The inclusion of the left-handed chiral projection operator in the current implies that the charged weak interaction only couples left-handed chiral particles or right-handed chiral antiparticles. This result can be achieved by absorbing the matrix $\frac{1}{2}(1 - \gamma^{5})$ in the particle spinor itself to create a left-handed particle and $\frac{1}{2}(1 + \gamma^{5})$ for the corresponding right-handed particles.

Scientists have never seen right-handed neutrinos, so if they do exist, they must be very different from left-handed neutrinos. This mystery of left-handedness is particularly fascinating if neutrinos are Majorana particles, a fermion that is its own antiparticle. If this is the case, then chirality would be the only difference between neutrinos and antineutrinos. Neutrinos would be left-chiral neutrinos, while antineutrinos would be right-chiral neutrinos.

In summary, because the neutrino is not massless, the Standard Model is known to need to be extended in the neutrino sector, and constraints on the theoretical mechanism could be achieved by future experiments.

3.4 Neutrino Oscillation

The first hint of neutrino oscillation was discovered in the "solar neutrino problem". In the late 1960s, R. Davis and J. Bahcall, using a chlorine based detector to reveal v_e neutrinos found a deficit of solar neutrino events compared to the one predicted from the standard solar model [32]. The Italian physicist B. Pontecorvo was the first one, in 1957, to propose that if neutrinos had mass, then they could oscillate, in analogy to the quark sector mixing matrix, changing from one flavor state to another [33]. Thus, the "missing" solar neutrinos were not really missing, but rather they oscillated, changing to a different flavor that could not be detected by the experiment. The very contradictory results were, in fact, confirmed later by other radiochemical and water Cherenkov detectors at Kamioka Observatory and Sudbury Neutrino Observatory (SNO) [34], [35], and awarded in 2015 the Nobel Prize for Physics.

The quantum mechanical phenomenon of oscillation can only happen if the state in which a particle is produced in is not a mass eigenstate. Neutrino oscillation are thought to be due to mixing between the weak flavor eigenstates under which they are produced and the mass eigenstates under which which they propagate. The weak flavor eigenstates ν_e, ν_μ and ν_τ that interact are a superposition of the mass eigenstates ν_1, ν_2 and ν_3 that propagate. The Pontecorvo Maki Nakagawa Sakata matrix (PMNS matrix) is a unitary matrix that parameterizes the transformation between the weak flavor and mass bases and has the form:

$$\begin{bmatrix} U_{e,1} & U_{e,2} & U_{e,3} \\ U_{\mu,1} & U_{\mu,2} & U_{\mu,3} \\ U_{\tau,1} & U_{\tau,2} & U_{\tau,3} \end{bmatrix}. \tag{3.2}$$

For simplicity we will assume only two neutrinos types in the following description.

At t = 0 the two states can be written as

$$|\nu_e(0)\rangle = \sum_{m=1}^{2} U_{e,m} |\nu_m(0)\rangle \tag{3.3}$$

$$|\nu_\mu(0)\rangle = \sum_{m=1}^{2} U_{\mu,m} |\nu_m(0)\rangle . \tag{3.4}$$

As you let the system evolve freely, it oscillates and after a time t, the mass state, being an eigenstate of the free neutrino Hamiltonian, evolves as:

$$U_j = e^{iE_j t} |\nu_j(0)\rangle \tag{3.5}$$

$$|\nu_e(t)\rangle = \sum_{m=1}^{2} U_{e,m} |\nu_m(t)\rangle = \sum_{m=1}^{2} U_{e,m} \exp\{-iE_m t\} \ |\nu_m(0)\rangle \tag{3.6}$$

$$|\nu_\mu(t)\rangle = \sum_{m=1}^{2} U_{\mu,m} |\nu_m(t)\rangle = \sum_{m=1}^{2} U_{\mu,m} \exp\{-iE_m t\} |\nu_m(0)\rangle . \tag{3.7}$$

Because the energy of the neutrino is much higher than its mass value, one can rewrite the exponent using the relations

$$E_m = \sqrt{p^2 + m^2} \approx E_m(1 + \frac{m^2}{2E^2}) \tag{3.8}$$

and because the neutrino is ultra relativistic $t \approx L$, where L is the travelled distance. To calculate the probability of transition of the ν_e with energy E, for example, in the ν_μ after travelling a distance L in t,

$$Prob_{e\to\mu}(E, L) = \Big|\langle\nu_\mu| \, |\nu_e(t)\rangle\Big|^2 = \Big|\sum_m \exp\Big\{-i\frac{m^2 L}{2E}\Big\} U^*{}_{\mu,m} U_{e,m}\Big| \tag{3.9}$$

which can be rewritten as

$$Prob_{e\to\mu}(E,L) = \sin^2 2\theta \cdot \sin\frac{\Delta m^2 L}{2E}. \tag{3.10}$$

The PMNS matrix is usually parameterized using three angles: $\theta_{1,2}, \theta_{2,3}$ and $\theta_{1,3}$ and a phase δ_{CP} and the value of each parameter has been measured by different experiments. It is also important to notice that for this reason the oscillation experiment cannot probe the exact mass of each mass eingenstate but only the mass square difference, so oscillation experiments can only measured those values.

3.4.1 Contribution of the NOvA experiment

NOvA will be setting a limit on the $\theta_{1,3}$ angle by looking at $\nu_\mu \to \nu_e$ transitions coming from the NuMI beam at Fermilab. If a non-zero value of $\theta_{1,3}$ is found, it will then be possible to obtain measurements of δ_{CP} and the mass ordering by also seeing $\bar{\nu}_\mu \to \bar{\nu}_e$ transitions. δ_{CP} can be measured because it modifies oscillation probabilities uniquely for neutrinos and anti-neutrinos. Measuring the neutrino masses and mixing angles is an essential requirement for understanding how the universe works. To discover the value of the CP-violating parameter, will help shed light on why the universe has a matter-antimatter asymmetry, and the neutrino offers a direct probe to study them. There is no motive why the neutrino mixing angles should have any particular values in our modern physics theory. Nevertheless, only $\theta_{1,2}$ has been resolved as being neither maximal or minimal of the three neutrino mixing angles. NOvA measurements, together with other experiments, could give more information on the $\theta_{1,3}$ angle and δ_{CP}, discovering some still unknown symmetry of the universe.

Chapter 4

Dark Matter Detection

"Yours be the dark matter.

Mine be the white.

And together when they collide

We would have our Universe"

Dinil

4.1 Detection Methods for Neutralino Dark Matter

The existence of particle Dark Matter (DM) has been searched for in several ways from many experiments. There are different types of experiments that are looking or have looked for DM, and they can be generalized into three categories: direct detection search, indirect detection search, and production at collider experiments [36]. DM direct-detection searches look for a signal of DM particle collisions with atomic nuclei in ultra-low background detectors deep underground. Indirect detection searches assume that DM particles annihilate or decay into SM particles leaving behind a distinct signature, such as gamma rays, neutrinos, positrons, antiprotons, or even anti-nuclei, and aim to detect those. Lastly, collider experiments, at LEP first followed by the Tevatron and lastly the LHC, expect DM particles to be created in high energy

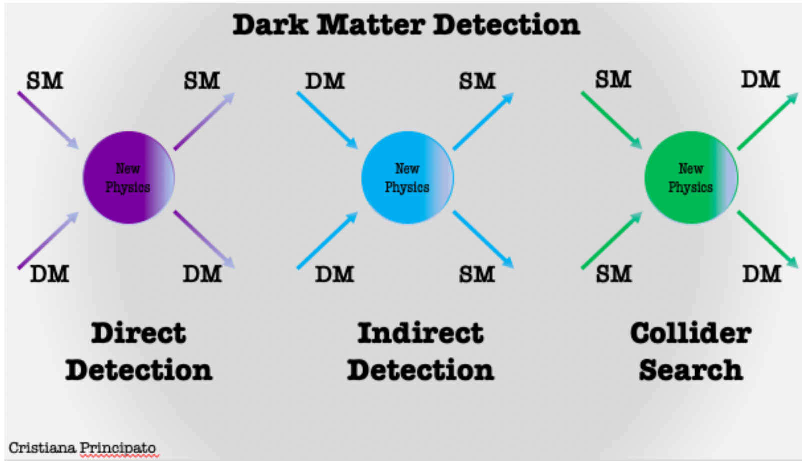

Figure 4.1: The three DM detection process.

collisions and look for missing energy in an event. It would be ideal if DM particle could be found in collider experiments because this would allow scientists to directly measure some of the properties of this particle.

Not only have none of these methods produced a DM discovery, but in addition, the WIMP miracle, that DM particles interact through the weak force at the electroweak scale, has started to become disfavored by both collider and direct detection.

However, experiments are rapidly gaining in sensitivity, and further light may be shed on the DM mystery in the coming years.

4.2 Direct Detection Experiments

If the neutralino is the particle needed to explain the DM abundance in the Universe, there should be plenty of it in the Milky Way halo [36]. With this premise, there is a non-negligible chance that those particles will be detected in a low background counting experiment. The most important process for direct detection experiments is elastic scattering of a DM particle (χ) on detector nuclei (N):

$$\chi + N \rightarrow \chi + N. \tag{4.1}$$

Two main interactions could then occur between a WIMP and the nucleus: spin-

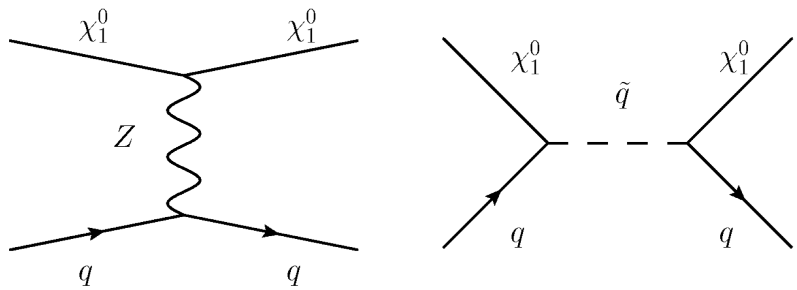

Figure 4.2: Neutralino-quark spin-dependent elastic scattering processes. Image Credit: [21]

independent (or scalar-scalar coupling) and spin-dependent (axial-axial current). The first one occurs between the DM particle and the mass of the nuclei, while the second one occurs between the DM particle's spin and the total angular momentum of the nuclei.

The differential recoil spectrum, from dark matter interactions is, from [37],

$$\frac{dR}{dE}(E,t) = \frac{\rho_{DM}}{m_W m_N}\int_{v_{MIN}}^{v_{MAX}} v f(\vec{v},t)\,\frac{d\sigma}{dE} d^3v \tag{4.2}$$

where N_T is the number of target nuclei, ρ_{DM} is the local DM density in the galactic halo, m_W the WIMP mass, $vf(\vec{v},t)$ are the WIMP velocity and velocity distribution function in the Earth frame and $\frac{d\sigma}{dE}$ is the WIMP-nucleus differential cross-section

Different expected signals are considered by different experiments. Some experiments look for the signals after WIMP-nucleus interaction in the form of nuclear recoil. The DM particle bumping into a nucleus causes energy transfer, which can be detected by various signal channels, such as scintillation light, phonon signals, ionization signals, and bubble generation. Another category of DM search experiments instead looks for the directionality of nuclear recoils. This signal is looking for an excess of nuclear recoils in forward angles, which would differ from what is expected if we assume isotropic scattering in the center of mass frame. To be detected, these

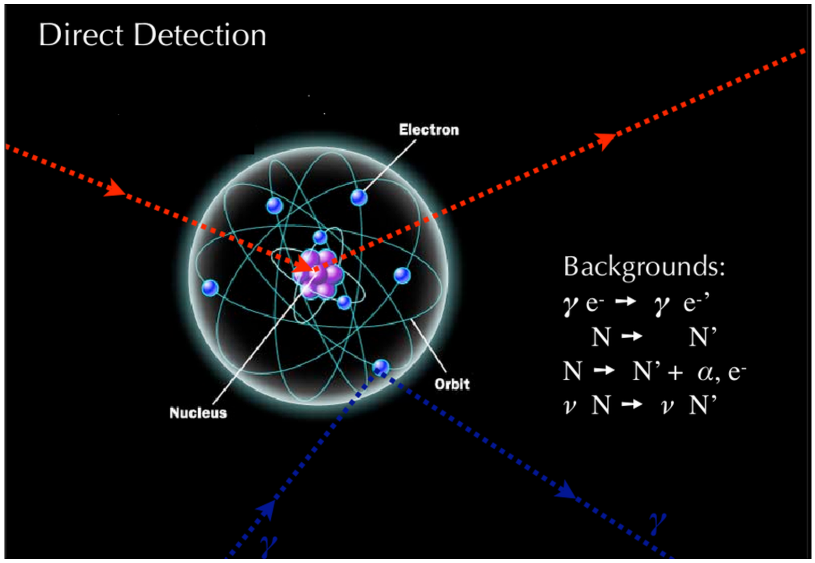

Figure 4.3: Nuclear recoil of DM in direct detection experiment. Image Credit: [38]

.

signals need a very fine track readout, on the order of 0.1 m, which can be very challenging to achieve.

The last possible signal is the annual modulation. The targets in laboratories are moving in the galaxy with the Sun, at 230 km/s, and the Earth, moving at 30 km/s around the Sun, while the WIMP velocity follows a Maxwell distribution. This effect would make the event rate, as well as the nuclear-recoil spectrum, change as a function of time over a sidereal year. Such an effect would not be substantial but would be considered an important finding in support of the interpretation of positive signals. There are several sources of uncertainties that need to be taken into account for the direct detection experiments and can be divided into two categories: the particle physics and the astrophysical uncertainties. In the first category, there are the uncertainties due to the nuclear form factor and the $\chi - N$ vertices and the numerical values of the nucleon matrix element, which are approximated, and on the values of the parameters of the underlying model which can vary over many orders of magnitude. The astrophysical uncertainties, instead, are due to the parameters that model the DM distribution in the Milky Way halo: the local DM density, the local DM

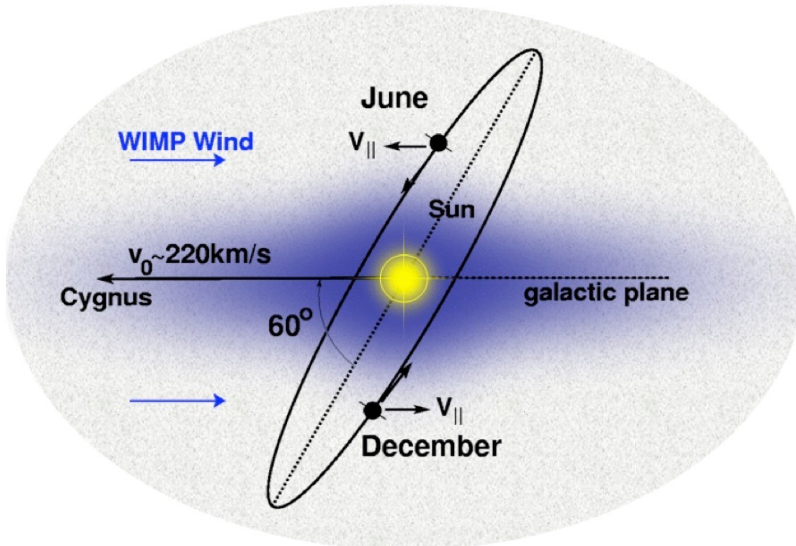

Figure 4.4: Annual modulation of DM signal. Image Credit: [39]

escape velocity and the circular velocity of the Sun around the center of the galaxy. There are different challenges that those experiments have to overcome. A minimal event rate and recoil energy, on the order of the keV range, is counted with a massive detector with low energy threshold. The electron recoil background due to the decay of α particles and γ particles and nuclear recoils due to neutrons from cosmic rays or local radioactivity is fought by using multiple energy deposition channels (ionization, scintillation, phonons) to distinguish electron and nuclear recoils, using shielding and radiopure detector components and by going many meters underground, in a region of so-called cosmic silence. The total predicted rate can be compared with the upper limits from direct detection experiments for spin-dependent and spin-independent interactions. The results are shown in Fig. 4.6. DAMA is the only experiment that claims a 9σ observation of an annual modulation that could be attributed to WIMP-nuclei recoils. So far none of the other experiments have been able to exclude or prove those observations except for two new experiments built with the same DAMA's technology [40].

The most stringent modern constraints come from LUX and XENON 1T [41], [42]. These results show that the interaction cross-section for protons and neutrons is ex-

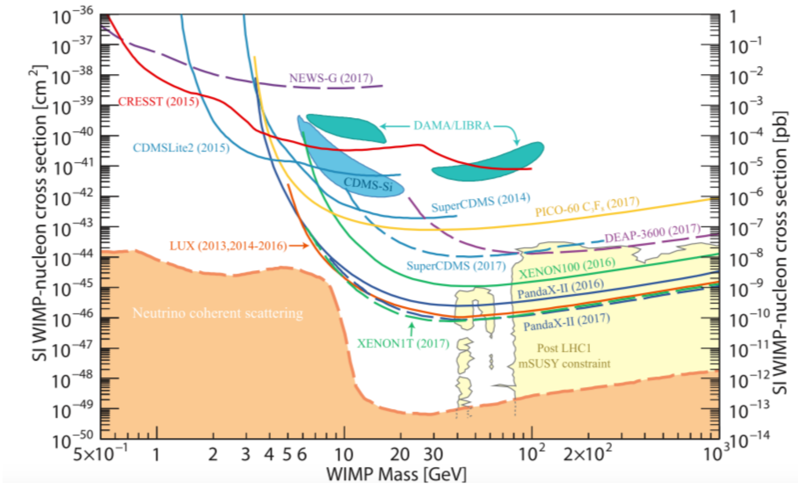

Figure 4.5: Limits on WIMPs-nucleon Spin Independent cross sections from different experiment. Image Credit: [42]

traordinarily tiny, and are different for both spin-dependent and spin-independent scenarios. LUX put the spin-dependent cross-section limits below $1.0-1.6\times10^{-41}$ cm^2 for protons and neutrons and spin-independent ones below 1.0×10^{-46} cm^2. These limits ruled out all the models of SUSY DM proposed before 2001. A more sensitive con-

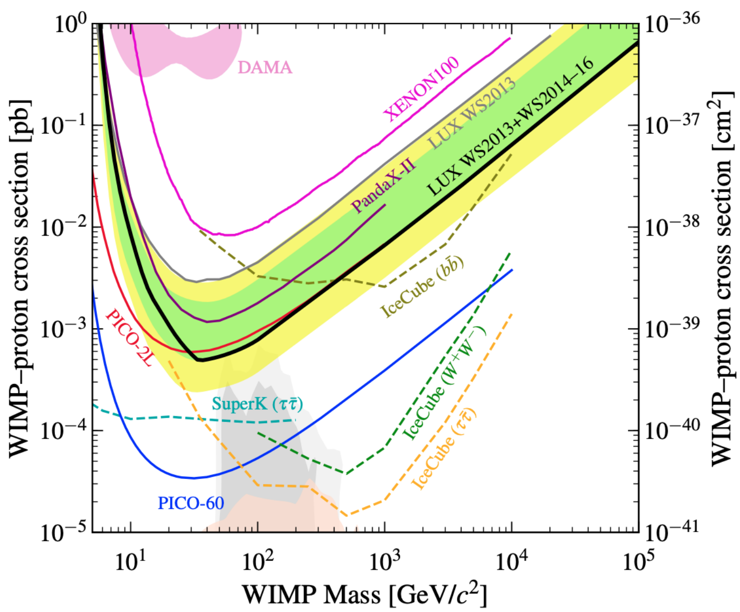

Figure 4.6: Limits on spin-dependent WIMP-proton cross section obtained from the complete LUX exposure compared with several experiment. Image Credit: [41]

straint comes from XENON: the spin-dependent neutron constraint is $6 \times 10^{-42}\ cm^2$ at 30 GeV/c^2 and 90% confidence level , while the spin-independent cross-sections are below $4.1 \times 10^{-47}\ cm^2$.

4.3 Indirect Detection Experiments

Indirect detection experiments look for neutralino annihilation in the galactic halo by investigating the cosmic ray background. This category of experiments assume that the DM particles annihilate into SM particles that can be detected [43]. The an-

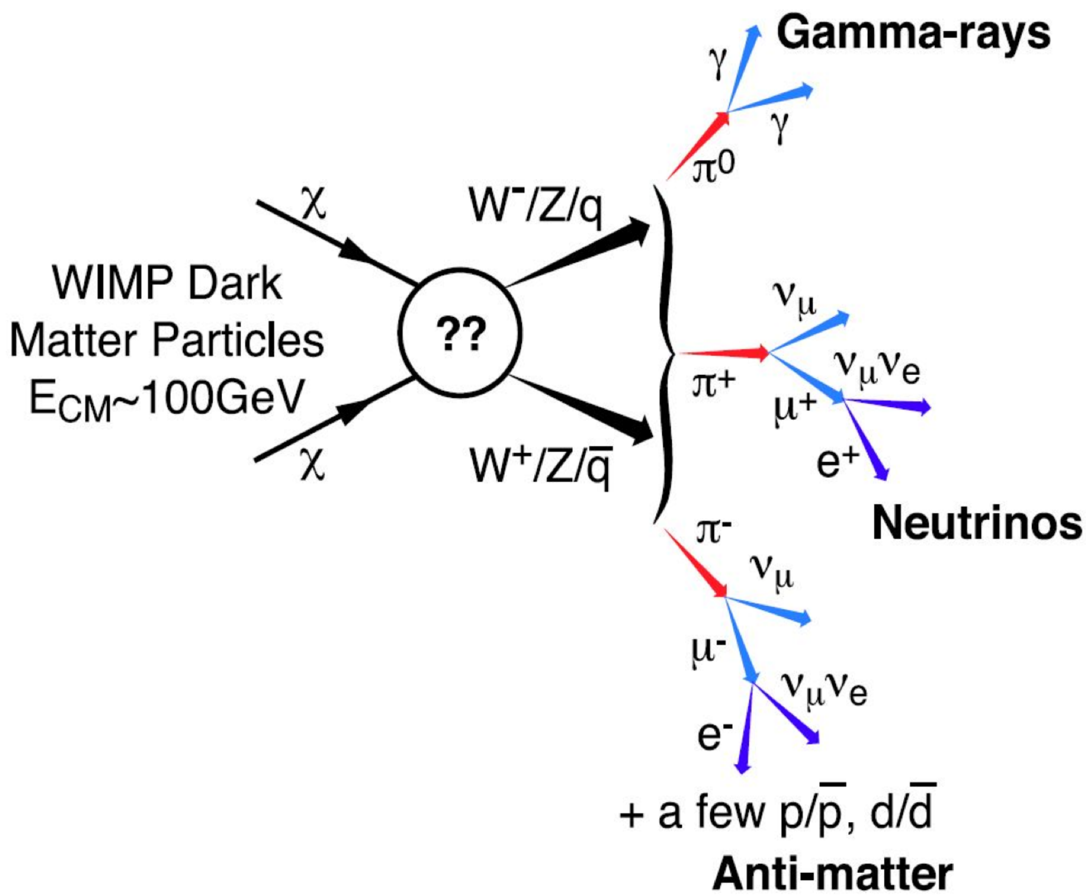

Figure 4.7: A diagrammatic flowchart of Standard Model particles produced by annihilation of dark matter. Image Credit: [44]

nihilation products are different e.g. gamma-rays, positrons, anti-protons, neutrinos.

The annihilation rate is proportional to the velocity-averaged DM self-annihilation cross-section $\sigma_A\, v$ and density squared:

$$\Gamma_A \propto < \sigma_A\, v > {n_\chi}^2 = < \sigma_A\, v > \frac{{\rho_\chi}^2}{{M_\chi}^2} \tag{4.3}$$

where ρ_χ corresponds to DM particles density in the local halo.

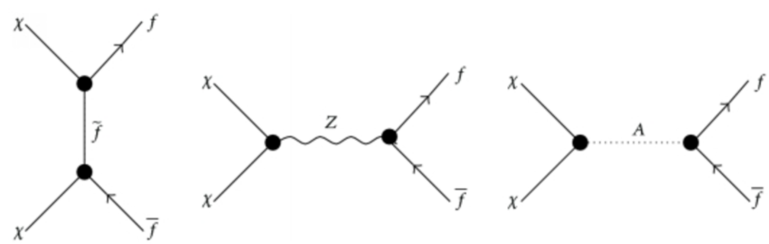

Figure 4.8: annihilation feynman diagram

4.3.1 Indirect Detection through Neutrinos

Model-independent predictions suggest that particle DM may have been gravitationally trapped in the center of the Earth or the Sun and therefore their density enhanced. If their density is enhanced, so is the annihilation probability. The DM particle may then annihilate into many SM final states. These initial Standard Model annihilation products will also decay and in the process produce neutrinos of all flavors. The annihilation channel defines the energy spectrum, hard or soft, of the neutrinos. A generic hard channel (typically $\tau^+\tau^-$) and a generic soft channel (typically $b\bar{b}$) are selected to evaluate the full possible sensitivity range, and sensitivity to these two scenarios is calculated separately. While neutrinos are weakly interacting particles and they need a large detector to be found, the main advantage of choosing neutrino particles is that being electrically neutral they will not be affected by magnetic fields and will travel in a straight line in outer space, allowing directionality reconstruction. The muon neutrinos, in particular, can be used for indirect detection of neutralino annihilation processes, since muons have a quite a long-range in a suitable detector medium. Therefore they can be easily detected through their Cherenkov radiation or ionization processes after having been produced at or near the detector, through the action of a charged current weak interaction $\nu_\mu \ + \ A \rightarrow \mu + X$. Given the enormous amount of cosmic rays background coming downward, neutrinos that are going upward are selected, given that neutrinos the only particle that could travel through the Earth without interacting.

4.3.2 Indirect Detection through Gamma Rays

Various experimental signatures of dark particle matter may leave imprints in the visible energy spectra and spatial distribution of gamma-ray photons or charged cosmic rays, and many detectors, like FERMI-LAT, are looking for those signals [45].

A principal challenge for indirect detection methods is the issue of source confusion and poorly determined backgrounds. The gamma-ray and the charged cosmic ray channel pulsars provide spectral signatures that seems to be, in most practical cases, indistinguishable from dark matter. Signatures of dark matter annihilation in the Milky Way halo and extra galactic dark matter may be hidden in the extra galactic gamma-ray background (E.G.B.). The E.G.B. is an anisotropic component of the gamma-ray sky, which is thought to be composed of many unresolved point sources. However, analysis of the E.G.B. has found a significant excess of gamma-ray emission even after subtracting the expected contribution from known point-source populations, such as active galactic nuclei (A.G.N.) star-forming galaxies. This excess could be a signature of dark matter annihilation in galactic dark matter substructures or dark matter halos beyond our Galaxy.

4.4 Search at Colliders

One possible manner in which WIMPs can be produced at colliders is via pair production. This search could give a direct measurement of the mass and some of the properties. It could, in fact,be able to create light DM particles which the direct detection experiment is not able to detect due to the small momentum transfer and it is more sensitive since it does not have to deal with uncertainties in the knowledge of the distribution of DM in the Universe. On the other hand, there is a limitation that requires the DM particle and its mediator to be within the energetic reach of the collider itself.

One strategy for WIMP searches in hadron colliders is to use mono-jet, mono-photon and mono-lepton signatures with energy or momentum imbalance in the final state. The missing reconstructed energy or momentum could be an indication of the production of heavy neutral stable particles in a collision. The WIMP-nucleon scattering cross section can be deduced by these searches. However, it is a model dependent approach relying on effective field theories and assumptions on masses of mediating particles.

The processes are topologically similar to the scattering processes in direct detection experiment, thus complementary to traditional DM detection. At hadron colliders, the presence of the WIMP pair is inferred from the Missing Transverse Energy (MET), which is the momentum of undetected collision products in the plane transverse to the beam. So far no evidence of DM existence has been shown, but only a limited portion of the DM model phase space has been explored, and much more has yet to be investigated [46].

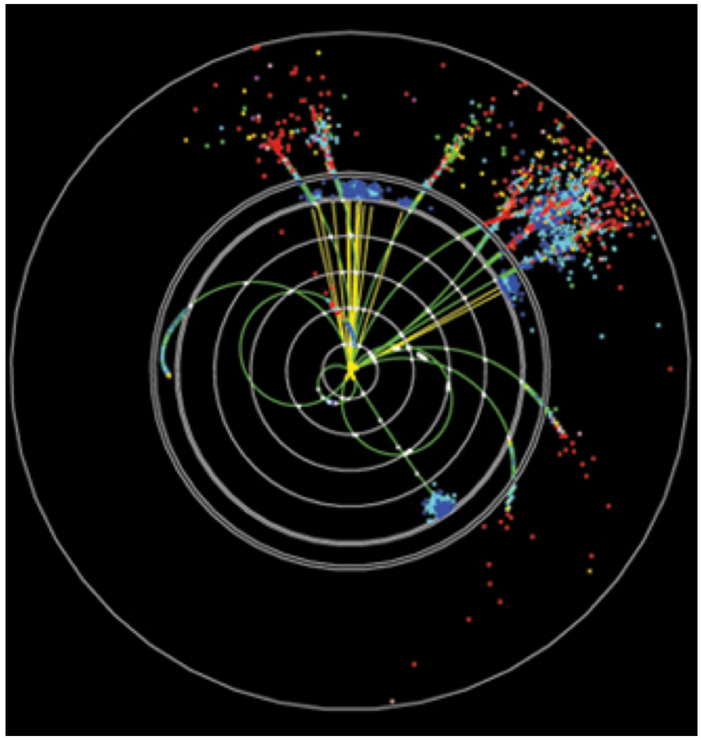

Figure 4.9: Event topology at LHC. The DM particle will leave no trace in the detector, resulting in an imbalance of momentum in the transverse plane. Image Credit: [46].

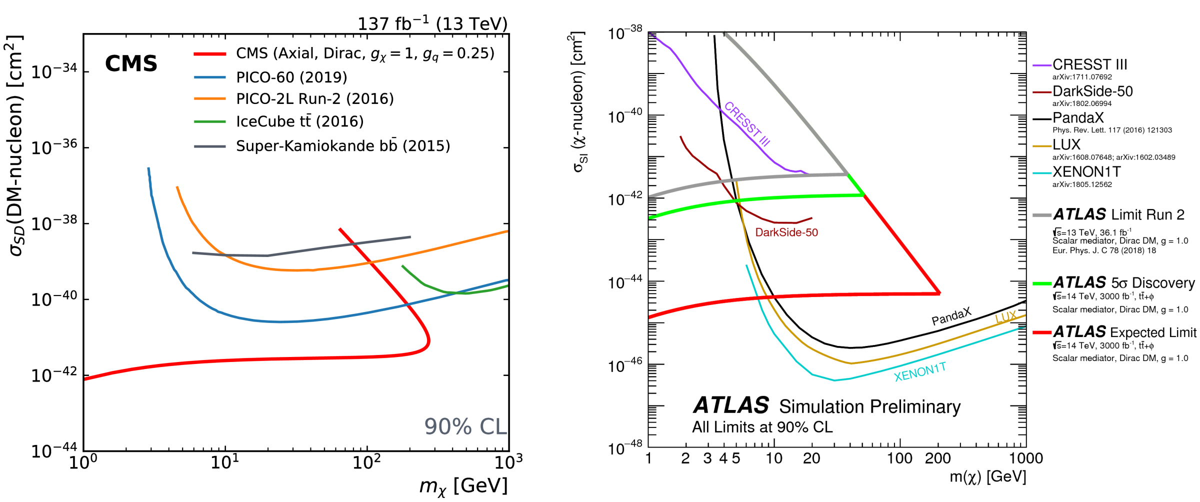

Figure 4.10: LHC exclusion limits on chargino and neutralino masses for different simplified models for the CMS and ATLAS experiments. Image Credit: [47, 48].

Chapter 5

The NOvA Experiment

Equipped with his five senses, man
explores the universe around him
and calls the adventure science.

Edwin P. Hubble

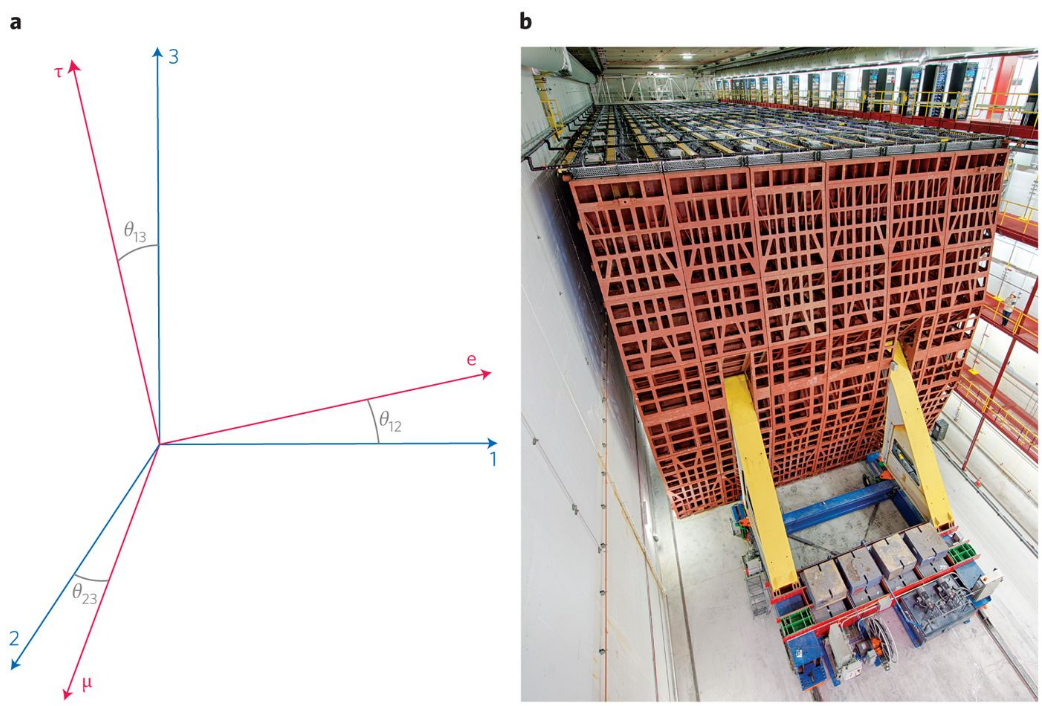

Figure 5.1: The NOvA Experiment, Image Credit: [49].

5.1 Overview

The NOvA experiment consists of two functionally identical detectors, see Fig. 5.2.

Figure 5.2: The NOvA Far and Near detectors, compared to an airplane, Airbus A380, for size inference. The Far detector being the size of the airplane ones, while the two smaller ones next to it are the Near Detector and NDOS (Near Detector on Surface). Image Credit: Fermi National Accelerator Laboratory.

The first one, the Near Detector, is located at Fermilab, while the second one, the Far Detector, is located in Ash River, Minnesota, 500 miles away form the Near Detector, see Fig. 5.3.

The Near Detector is made up of 0.3 kT of active detector mass and is situated underground, 100 m below the surface in a position which provides shielding from cosmic rays. The Near detector dimensions are approximately, 4 meters wide and deep and 15.5 meters long. The Far Detector, on the other hand, is a huge construction that weighs 14 kT and is located on the surface with only 3 m of equivalent shielding. The Far detector dimensions are approximately, 15.5 meters wide, 15.5 meters deep and 60 meters long. Being on the surface, the Far Detector is exposed to a high flux of cosmic rays. This flux is the main background for our analysis, but at the same time provides a good source of cosmic data, which allows for calibration and other

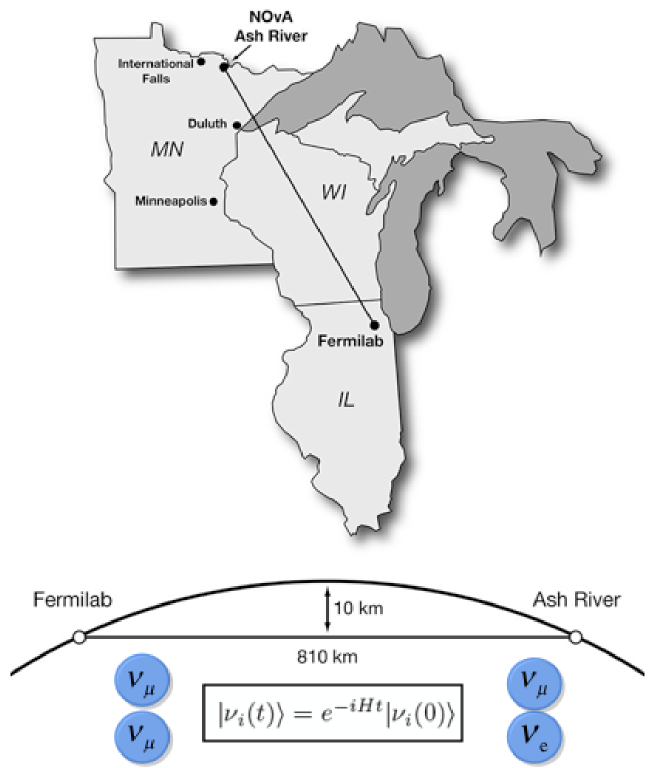

Figure 5.3: NOvA Far and Near detector baseline

exotic studies.

This chapter draws heavily from the NOvA Technical Design Report [50], and the Timing Calibration Technical Note [51], which may be consulted for greater detail.

5.2 The NOvA Detector Design

The Far Detector and Near Detector technologies are the same. The detectors are made of cells, each made of plastic extrusions (PVC) of 4×6 cm^2 cross section, filled with liquid scintillator and wavelength shifting fibers (WLS), each ending with an Avalanche Photodiode (APD).

A charged particle that passes through the detector will excite atoms in the liquid scintillator, that will subsequently return to a stable state by emitting photons, or light, which then propagates in fibers and is transformed into electric signals in the photodiodes. The configuration of the detector, composed of layers of orthogonal extrusions in two Z views and YZ views, where Z is the axis aligned with direction of the beam, the Y axis points vertically up, and the X axis is orthogonal to these two. This configuration allows for a 3D reconstruction of particle tracks, see Fig. 5.4.

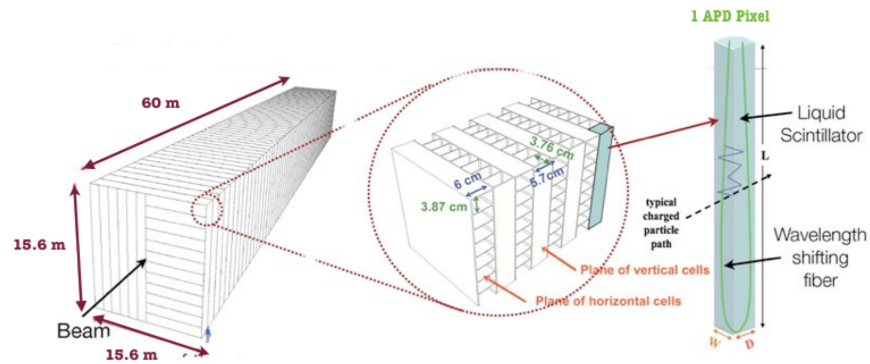

Figure 5.4: NOvA Far and Near detectors technology is the same. The detectors are made of unit cells, organized in two plane, for a 3D reconstruction of the particle's tracks. The Far detector measures are approximately, 15.5 meters wide, 15.5 meters deep and 60 meters long.

Cell signals (hits) are collected by the NOvA data acquisition system (DAQ) with the use of software data-driven triggers (DDT), which send messages telling the DAQ to collect specific chunks of data [52]. This occurs when the data have some preselected features. The collected data is then analyzed using offline analysis software.

5.2.1 The Unit Cell

The NOvA detectors are composed of cells. Each of these cells is made up of plastic extrusions (PVC). The cells are 3.6 cm wide, 5.6 cm deep, and 15.5 m long in the Far Detector and 4 m in the Near Detector. Cells are organized in two planes, respectively the XZ view and the YZ view to allow 3D reconstruction of the particle's track, for a total of 384 cells per plane in the Far Detector and 48 in Near Detector. Each cell is filled with liquid scintillator and a loop of wavelength shifting fibers to capture the scintillation light. Every cell is read out by a pixel of an APD.

5.2.2 The Liquid Scintillator Technology

Sixty-five percent of the total mass of the NOvA detectors is made up of liquid scintillator.

The liquid scintillator technology used in NOvA consists of three components. The first one is the scintillator. A scintillator emits light when charged particles pass through it. In particular, NOvA uses pseudocumene as active scintillator, which is approximately 5% of the total liquid component and emits photons in the range 270 - 320 nm (UV range).

The second component is the wavelength shifters (WLS) that absorb the light emitted by the scintillator and emit longer wavelength radiation. The wavelength shifter used in NOvA is PPO (2,5-Diphenyloxazole), which de-excites by emitting photons in the wavelength range of 340 - 380 nm. These photons excite the second wavelength shifter in the NOvA blend, bis-MSB (1,4-bis-(o-methyl-styryl-)-benzene), which de-excites through emission in the range 390 - 440 nm, which can be picked up by the wavelength-shifting fibers and transported to the APD.

Finally a mineral oil is added as a solvent. The solvent is used to blend these components together into a stable solution and makes up 95% of the NOvA scintillator. An anti-static agent (Stadis-425) at 3 ppm is added to reduce the risk of fire hazard by making it semi-conducting. Vitamin E is also added as an anti-oxidant to prevent yellowing of the scintillator.

5.2.3 Wavelength Shifting Fiber

The NOvA wavelength shifting fiber collects the violet light emitted by the NOvA scintillator and shifts it to a blue-green light with a wavelength range 450-650 nm. The core of the fiber is made of polystyrene with a refractive index of 1.59 followed by an inner acrylic cladding, which improves the acceptance angle for total internal reflection of light in the core with a refractive index of 1.49. The fibers have an outer fluorinated-polymer cladding with a refractive index of 1.42, see Fig. 5.5.

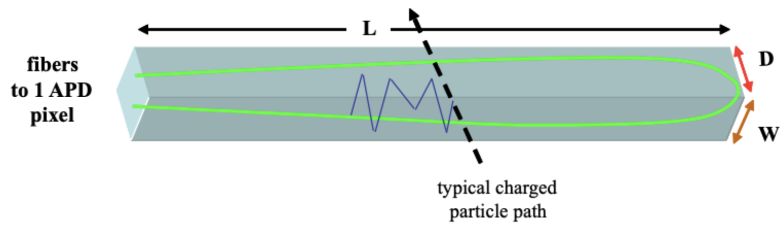

Figure 5.5: Schematic illustration of a PVC cell of dimensions $W \times D \times L$ containing liquid scintillator and a wavelength shifting fiber. Image Credit: [52].

The average length of the fiber in each tube is approximately 32 m in the NOvA Far Detector and 8 m in the NOvA Near Detector. The fibers are folded into a loop so that the far-end is 15.5 m (4 m) from the avalanche photo diode in the Far (Near) detector, as it can be seen in Fig. 5.5. Both ends of a fiber arrive at one pixel of a 32 pixel APD array. Due to attenuation in the fiber, the minimum yield is obtained for light generated near the end of the fiber loop, though the minimum is rather flat near the end of the tube. The yield for a MIP is approximately 25 Photo Electrons (PE) at the Far Detector end.

5.2.4 Avalanche Photodiode

The APDs are photo-sensitive avalanche diodes manufactured by Hamamatsu. As mentioned above, each NOvA APD array consists of 32 pixels, where each pixel reads out both wavelength shifting fiber's from a single cell, see Fig. 5.6.

An APD generates a readable signal by a process called impact-ionization. When a photon coming from the fiber strikes the surface of the APDs, an electron is emitted and accelerated in the strong internal electric field of the diode. These electron are called Photo Electron (PE). As these highly energetic electrons move, they strike other electrons. These secondary electrons are themselves accelerated and strike more electrons and so on. At the end, an avalanche of charge carriers in the diode leads to a significant amplification of the photocurrent.

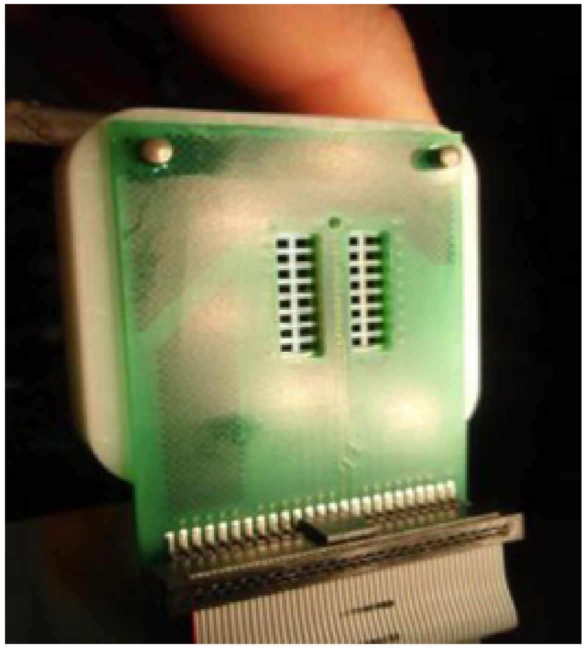

Figure 5.6: APD in NOvA. Image Credit: [52].

The APDs for the NOvA detectors have a high quantum efficiency, at almost 85%, which is necessary for the NOvA experiment because it allows the detection of signals originated at the far end of the Far Detector. Another important detail is that to minimize the current created by electron-hole pairs in the absence of light, also known as dark current, the APDs must operate at a low temperature of -15 degrees Celsius.

Due to the statistical nature of the avalanche process, there are current fluctuations. The APD performance might be further degraded by what is known as an excess noise factor. This is a known effect, included in simulation, and it is a function of the gain and the carrier ionization ratio, named k, defined as the ratio of ionization probabilities of holes to electrons. In the NOvA APDs, this ratio is about 1:50. The APDs were initially operated at a voltage close to 425V which is known to produce a gain of about 100. This was increased for a nominal gain of 150.

The operational conditions have been designed and demonstrated to produce a signal to noise ratio of 10:1 or better for the majority of APDs.

Lastly, The APDs are operated continuously without dead time and do not require any external triggering.

5.2.5 PVC Modules

The last part of the NOvA detectors are the PVC modules, which make up of almost 30% of the total NOvA detector mass. The PVC modules are the structural elements of the NOvA detector and serve as the containment for the liquid scintillator, see Fig. 5.7.

(a) NOvA cell extruder PVC.

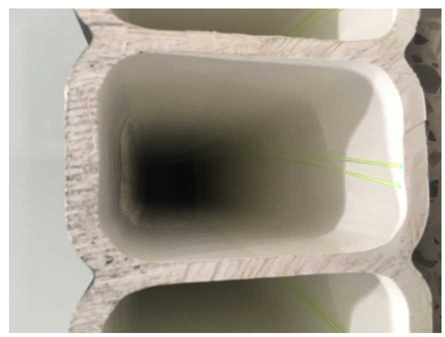

(b) NOvA cell extruder PVC details

Figure 5.7: From left to right: PVC, fibers and avalanche photodiodes which form cells of NOvA detectors

The reflectivity attained in this manner is about 90% at the peak wavelength of scintillator emission of 430 nm. The shape of the PVC extrusions has been chosen in such a way as to optimize this light reflectivity, and to reduce PVC stress concentration on corners. The corners are rounded or scalloped.

For the assembly of the modules, adhesive epoxies that are inert to the liquid scintillator were used.

5.3 The Data Acquisition and Timing System

A great timing system performance is a critical component of this analysis. The track directionality, upward and downward, that enables us to distinguish signal from background, is estimated from the track hit timing, and a background flux reduction of more than a factor of 10^4 at trigger level is an essential requirement to be able to collect an upward-going muons signal. Consequently, to achieve this level of performance in background reduction, there is the need for the timing system performance to be exceptional. This allows to confidently identify a particle direction. The rest this chapter is based on the references [51], [53], [54], [55].

5.3.1 Overview of NOvA DAQ System

The Data Acquisition System (DAQ) is responsible for collecting the physical signal in the detector and transmitting it to the DAQ network. For non beam physics, specific signals coming from each cell are collected by the DAQ if they have the features that have been selected by the Data-Driven Triggers (DDT).

In the DAQ coordinates, the detector is composed and based on the following building structure: Pixel, APD, Front-End Board (FEB), Data Concentrator Module (DCM), and Diblock. The 32 channels of an APD, the pixels, are read by a FEB. Each FEB services one APD. The FEB is instrumented with an Application Specific Integrated Circuit (ASIC) to shape the signal and an Analog to Digital Converter (ADC) to digitize it.

For each 64 FEBs, there is a DCM, which is a custom built computer that collects the signal from the FEB and transmits packets of data onto the DAQ network. Each DCM only communicates with FEBs in the same diblock and in the same view. A Diblock is physical unit of a certain number of planes. For the Far Detector, each diblock consists of two blocks, which are alternating planes glued together. Each block is composed of 32 planes, 16 in each view, for a total of 64 planes per diblock. Finally, the NOvA Far Detector is constituted of a total of 14 diblocks.

5.3.2 Timing System Design

For redundancy purposes, the NOvA Timing Distribution System consist of two identical independent clock distribution systems at the Far Detector, see Fig. 5.13.

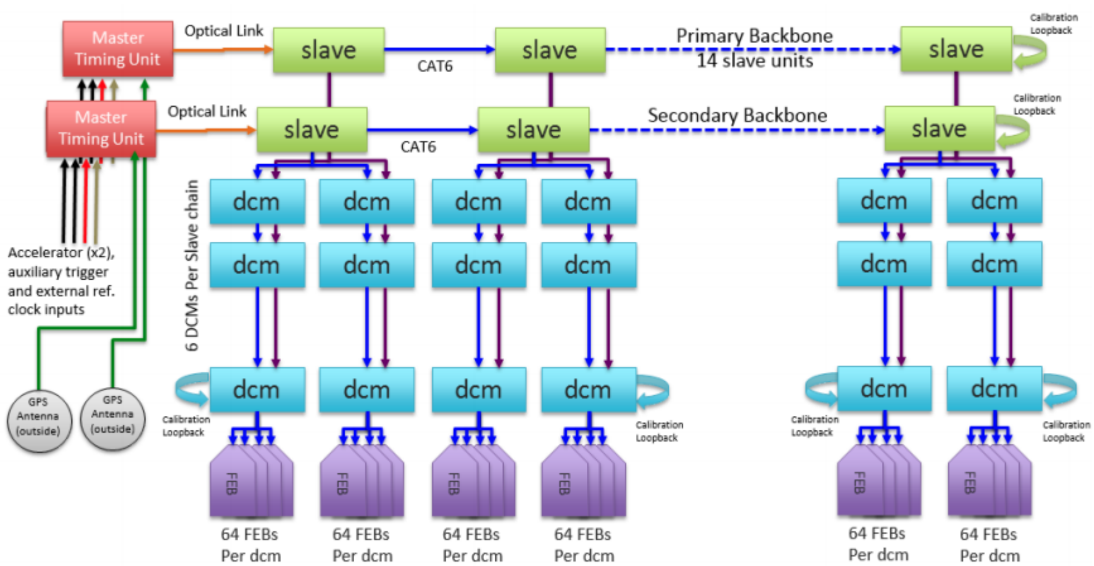

Figure 5.8: Far Detector timing system design. Image Credit: [54]

Each system consist of a Master Timing Distribution Unit (MTDU) connected to a GPS receiver. A Slave Timing Distribution Units (STDU) outfits each diblocks, plus cabling. The GPS receiver used in the MTDU allows for synchronizing the timing systems to a known time standard.

Each STDU slits the commands in two branches, one for the six DCMs on top of the diblock and the other for the six DCMs on the side. For calibration purposes each DCM chain is terminated at the end with a loop-back connector.

Single point and multipoint readout

The FEBs use a Dual Correlated Sampling (DCS) algorithm to determine if a pulse is signal or not. Two different implementations of this algorithm have been used. In the first one, so called single-point mode, the FEB only process the difference between the ADC counts of the s_i sample and the ADC counts from the samples s_{i-3}, corresponding to three clocks before. A predetermined value defines the threshold

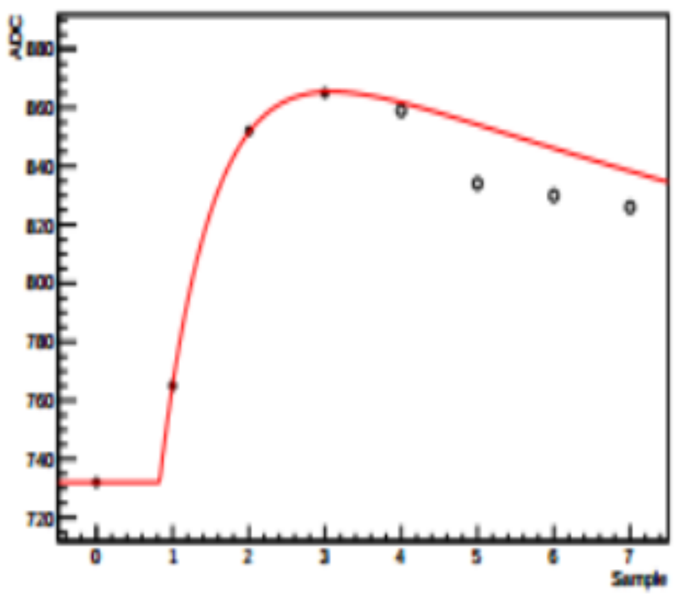

Figure 5.9: An example of fitting the electronics response curve to multiple readouts from a single cell hit. The time coordinate of the inflection point where the curve begins to rise is the fitted parameter t_0.

value for discriminating signal versus noise. If the ADC value of the s_i sample is higher than the threshold value, the ADC and Time to Digital Converter (TDC) values of the s_i point are recorded as a hit. Using this approach the best case achievable timing resolution for the Far Detector, is given by:

$$\sigma_{tsingle} = \frac{t_{sample}}{\sqrt{12}} = 144\, ns \tag{5.1}$$

with t_{sample} being the time between samples, 500 ns in the Far Detector. To achieve a better timing resolution a multi-point readout was implemented. In the multi-point readout, multiple samples s_{i-3}, s_{i-2}, s_{i-1}, s_i are stored, and compared to pre-calculated values stored in a lookup table. The lookup table contains values from different fits calculated offline and allows to estimate more precisely the hit time from the rising edge of the pulse.

The electronic response to an incident particle depositing energy in a cell can be parameterized in terms of two intrinsic timing values, (T_R and T_F), the number of photoelectrons (pe), and a timing "offset" (t_0), or the elapsed time between a read-out and the time of incidence of the particle:

$$f(t) = \alpha p e^{-(t-t_0)/T_F}(1 - e^{-(t-t_0)/T_R}) \tag{5.2}$$

Here, α is a proportionality factor that does not affect the timing fit. The parameters T_F and T_R correspond to the intrinsic falling and rising time of the response curve, respectively. The Far Detector ASIC shapes the pulse with a 460 ns rise-time and a 7000 ns fall-time. These shaping parameters have been determined empirically. For the purpose of determining hit timing, the parameter of note is t_0. By performing a simple χ^2 minimization, the data-preferred value of t_0 can be extracted from multiple readouts on a single channel. For the purposes of the trigger, where hit processing time must be minimized, fit results were pre-calculated and tabulated such that the computationally expensive minimization need not be repeated for each individual hit.

An example of fitting the electronics response curve to multiple readouts from a single cell hit is shown in Fig. 5.9.

Further work to improve the timing resolution has been done. First by using a new pulse shape function with a more realistic pre-amplifier response. See [56] and

[57] for more information.

$$f(t) = HFI(\frac{e^{\frac{t-t_0}{F}}}{(I-F)(F-R)} - \frac{e^{\frac{t-t_0}{I}}}{(I-F)(I-R)} + \frac{e^{\frac{t-t_0}{R}}}{(I-R)(R-F)}) + C \qquad (5.3)$$

where H, F, I, R, C are respectively the pulse height, fall time, pre-amplification time, rise time and baseline. After that, a scan of rise and fall time parameters with a new pulse shape was performed [58].

Following the scan of the rise and fall parameters, new values were used in the timing resolution. More detail is given in Section 5.3.4. Lastly, a change in the APD gain, which allowed a higher number of photo electrons further improved the timing resolutions by few percentages, as can be seen in Fig. 5.10.

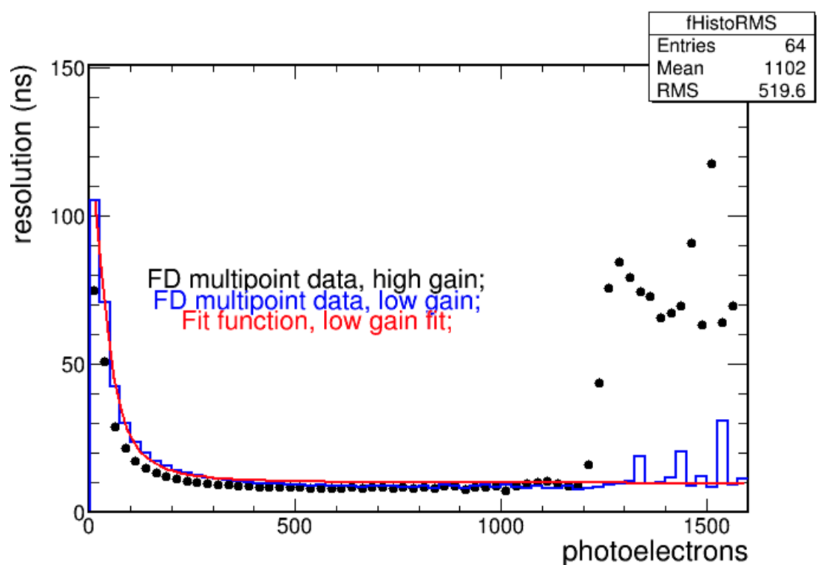

Figure 5.10: Timing resolution after changing the gain in the APD. In the plot the high gain resolution curve is scaled by PE/1.5 to take into account the different gain

5.3.3 Timing Calibration Online and Offline

Two different methods are used in NOvA for calibrating the timing system, as described in detail in [51], [55]. The complex timing system requires precise calibration of the delay from the MTDU to each component in the chain.

The first method is the online TDU delay. In this case, the MTDU sends a sync pulse. When each TDU and DCM gets the sync pulse, a counter clock is cleared and starts its count. The sync travels along the whole chain until at the end of the branch the loop back connector sends it back. When the sync returns, the units stops counting, measuring the delay. In this way the delay can be regularly calculated to monitor the system and track seasonal variations. At the moment of writing this thesis, this method is not currently being used, because there is an observed drift starting from the 7th diblock. Therefore the time offset between DCM is solely based on the length of the cable.

The second method uses offline cosmic rays to calculate the absolute timing offset between DCMs. Starting with a cosmic sample, quality track selection cuts are applied. For the tracks that pass those cuts, the difference in the expected and recorded time for each hit in the track is calculated. With this relative difference, a matrix is constructed. To find the absolute time offset between DCMs, DCMs 6 and 7 are fixed to a zero value and the other offsets are calculated. Then a matrix of these relative differences is inverted to solve for the absolute timing offsets between each DCM in the detector and a fixed reference DCM. If the synchronization described previously is performed properly, all the absolute offsets should come out to zero. However, as of the time of writing this document the synchronization only accounts for the cable delay between STDUs and not for the delays between DCMs on a given STDU branch.

5.3.4 Timing Resolution

Each time measurement has an uncertainty associated with it, which varies with the amount of energy deposited. The time uncertainty on a given hit from a reconstructed muon track affects the determination of track directionality, so a parametrization of uncertainty in terms of energy deposition is necessary for the timing-based trigger. To determine the time resolution, cosmic tracks were used. The selected tracks are through-going muons, with a minimum of thirty hits and with start/end planes agreement between views. The cell hit time is corrected for time-of-flight of the track, assuming that muons travel at the the speed of light, and distance to readout, assuming the speed 15.3 cm/ns in fiber.

Lastly, the time difference between all pairs of hits is computed for each and plotted in a 2D plot as a function of PE value. Each PE bin gives information about the spread of the time for the tracks at that PE value. By taking the distribution of the hit time difference for each PE and fitting it with a truncated Gaussian, we can convert the median value in the time resolution value corresponding to that that PE.

Single-hit time resolution is measured by comparing hit times on a cosmic ray muon track as a function of hit ADC. This is shown in Fig. 5.11. For high-energy hits the Δt is measured to be better than 15 ns in the data using the four-point readout scheme.

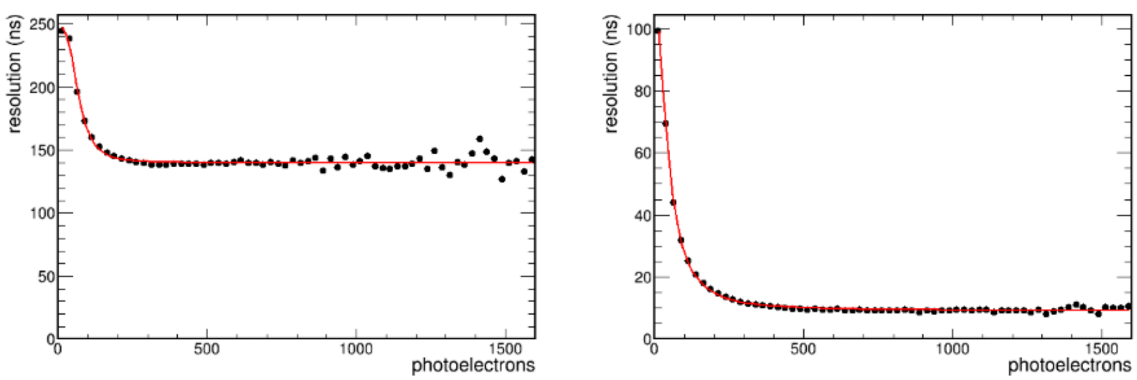

(a) single-point (b) multi-point

Figure 5.11: Single-hit timing resolution as observed in NOνA far detector data with four-point readout, before (left) and after (right) fine timing implementation. See [51] for more details.

Details of the timing resolution scan

To select the parameters that give the best time resolution, a scan of the rise and fall time values for the new pulse-shape function, Eq. 5.3.2, was performed. First the pulse-shape function was modified in the *Calibrator* package, and then the rise and fall time were varied to scan a broad range of parameters, as can be seen in Fig. 5.12.

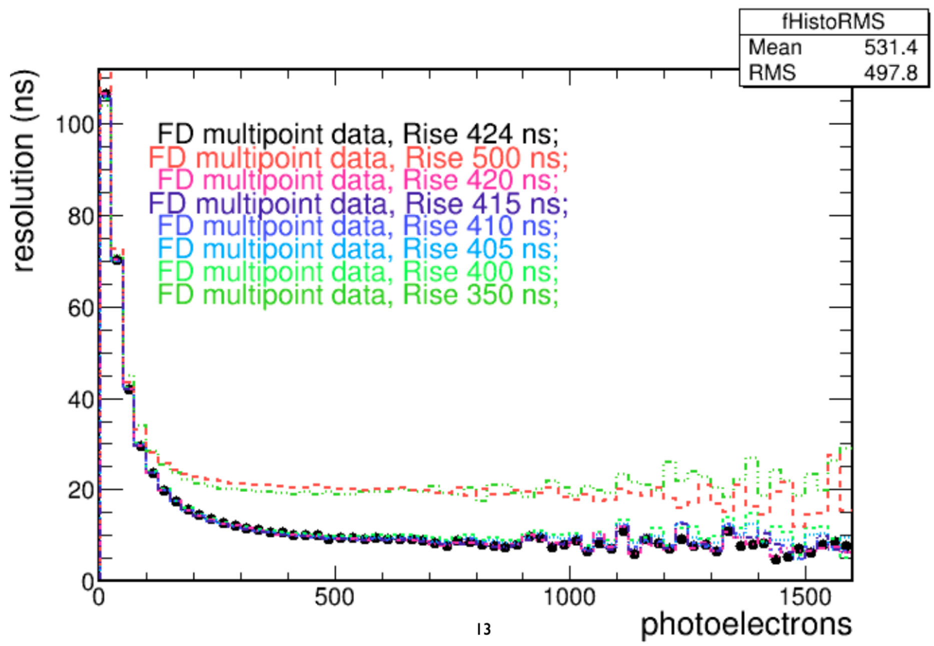

Figure 5.12: Example of a scan for different rise values in Eq. 5.3.2. Different rise values give different resolution functions.

No modification from the values chosen in [51] were made for the data, while a significant improvement was obtained in the MC simulation by changing the value of the rise time from 380 ns to 460 ns, as can be seen in Fig 5.13.

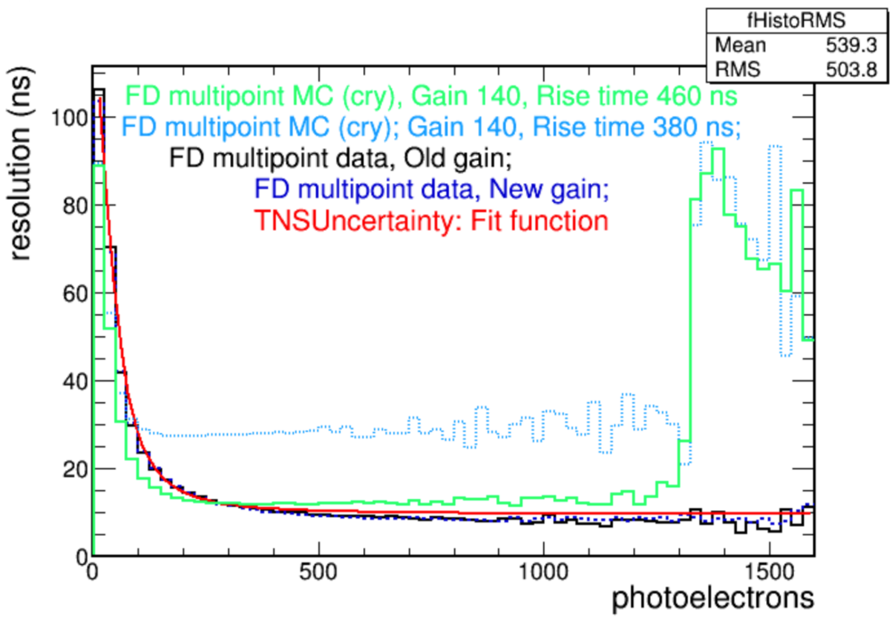

Figure 5.13: Improvement in the timing resolution after changing the rise time value in the MC function from 380 ns to 460 ns.

Chapter 6

Upward-Going Muon Trigger

If computing power, data storage capacity and rates were infinite and available at no cost, triggers would not be needed. Real-world limitations do not allow us to record and store all the data accumulated in a high energy physics experiment. Different experiments have different trigger requirements depending on the operating environments. Beam events in NOvA require a trigger constructed around the beam's timing structure, while cosmic ray triggers that have no periodic time structure require the triggers to be constructed around the signal's characteristics. This chapter first presents an overview of the current upward-going muon trigger implemented in the NOvA experiment and collected data for this analysis. Then several studies related to understanding the efficiency of the trigger are presented. The strategy is to prove that the trigger is working using beam neutrinos, then using cosmic rays muons prove that the simulation models imported trigger variables, and then show that the trigger is close to fully efficient after offline cuts are applied.

6.1 Data-Driven Trigger

In December of 2014, two triggers were implemented at NOvA to select upward-going muons. In these triggers, first muons are identified as long straight tracks using the Hough transform algorithm. Then, the timing information from each hit on a track is used to estimate the directionality of the track. The probability that a track is upward-going is estimated by calculating the χ^2 comparing the hit times to the hypothesis for an upward-going track. A Log-Likelihood Ratio (LLR) is constructed from the ratio of the upward-going probability to the downward-going probability. The LLR is a powerful tool for determining the directionality of a track. For long tracks (e.g., >5 m, corresponding to muon energy >1 GeV), it reduces the trigger rate to a reasonable value by merely cutting on only the LLR. The *DDUpMu* trigger requires that tracks are at least 5 m long and cuts on the LLR to reduce the rate to about 1 Hz (a factor of 100,000 below the rate of cosmic ray downward-going muons). This trigger is referred to as the "through-going" trigger. The complete list of the "through-going" trigger cuts is shown in Table 6.1. In a second version of the trigger, (*ddcontained*), the starting point is a "contained slice." It requires that tracks are at least 2m long. This trigger is referred to as the "contained" trigger. The upward-going muon trigger was first implemented and tested in August 2014 but did not run in a stable configuration until December 12, 2014, corresponding to the run number 18398.

Variable	**Cut Value**	**Description**
TrackLen	500.0 cm	3 dimensional reconstructed track length
TrackHitsXY	60	total number of hits associated with 3D track
TrackHitsX	15	number of hits associated with XZ projection of track
TrackHitsY	15	number of hits associated with YZ projection of track
dX	15	Track cell length in XZ view
dY	3 m	Track cell length in yz view
dZ	3 m	Track plane length
R2X	0.99	Coefficient of determination for fit in XZ view
R2Y	0.99	Coefficient of determination for fit in YZ view
Chi2	2.0	Fit χ^2/NDF of time distribution
LLR	3.0	LLR of time distribution

Table 6.1: Selection criteria used by the upward-going through-going muon trigger. These cuts are designed to select muon tracks with lengths and numbers of hits sufficient to compute reliable likelihood values for track direction.

This search requires understanding the efficiencies of these triggers. Early work first demonstrated that the trigger was feasible and should be able to reject background sufficiently while efficiently selecting upward-going muons [59], and then studied a sample of through-going events better to understand the composition of selected events [60]. This chapter will summarize work done to understand the trigger efficiencies of the upward-going muon triggers. In one effort, muons from the ν_μ analysis were used to prove that the trigger is successfully working on neutrino events. Statistics are limited there, so it is difficult to constrain the efficiency. A follow-up study inverted the timing requirements and studied the trigger's efficiency on selecting downward-going cosmic-ray muons. Using the cosmic sample, trigger performance in Monte Carlo simulated samples and with data performance can be compared. Once the simulation's performance is understood, Monte Carlo simulated samples of upward-going muon data were used to measure trigger efficiencies for specific search signal samples.

6.2 Track Directionality

When an electrically charged particle goes through the NOvA detector, it leaves a record of its passage by interacting with the detector's material and components. The process of reconstructing the particle trajectory is called *tracking*. A track is defined as the trajectory of a particle inside the detector. More details about track reconstruction are given in Chapter 7. The trigger is based on simple track ID, track quality cuts, and the hits' timing information on a track. The Hough transform algorithm [61], is used for reconstruction, and the tracks are required to match in both XZ and YZ views. For the YZ view, one can start from the hit with the lowest y cell value, y_0, at time T_0. Then, the observed time and the expected time for each hit can be calculated as:

$$T_{obs} = TDC_{y_i} \cdot 15.625ns - T_0; \quad T_{exp} = TOF_\mu \frac{y_i - y_0}{y_1 - y_0} \tag{6.1}$$

Similarly, for the XZ view:

$$T_{obs} = TDC_{x_i} \cdot 15.625ns - T_0; \quad T_{exp} = TOF_\mu \frac{x_i - x_0}{x_1 - x_0}, \tag{6.2}$$

with x_i and y_i being the cell numbers in XZ and YZ view, and the time measurement (in TDC units) being $TDC_{x(y)_i}$. The time is then converted to ns with the equation:

$$T = \frac{15.625\,ns}{TDC} \tag{6.3}$$

The other quantity that needs to be defined is the time-of-flight of the muon track, TOF_μ, which can be defined from the equation of dynamics as length over velocity:

$$TOF_\mu = \frac{L}{29.98cm/ns}, \tag{6.4}$$

where L, the track length (in cm), and the expected speed, assuming that the muon is relativistic, 29.98 cm/ns.

Since it is required that each track is reconstructed and matched in both views, (x_0; y_0) and (x_1; y_1) must correspond to the lowest and highest points of the track, respectively. Furthermore, an estimate of the missing coordinate for a particular hit in either view using the 3-D requirement can be achieved. The estimated (x; y; z) coordinates for each hit in each view can be used to calculate the distance from the point where the particle hit the detector in a cell to the APD readout end. A hit that is further away from the readout will take longer to propagate and be detected by the APD. The variable of interest is the muon's hit time passing through the extrusion, so a correction for the fiber's light propagation time needs to be applied. In the wavelength shifting fiber, the speed of light is measured to be 15.3 cm/ns.

The distribution of the expected time versus observed time can be made for each track using Eqns. 6.1 and 6.2. An example is shown in Fig. 6.1. The distribution is produced using a reconstructed upward-going muon track simulated with Wimp-

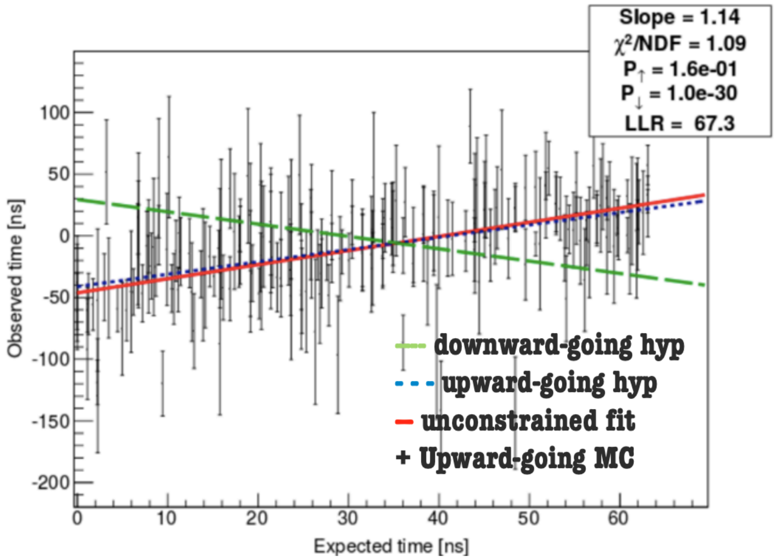

Figure 6.1: The expected versus observed time distribution for an upward-going muon track reconstructed in the NOvA far detector, using fine timing. The linear unconstrained fit (solid red line) has approximately a slope equal to one. The fit with the upward-going track hypothesis (slope = 1) is shown as the blue dashed line. The fit with the downward-going hypothesis is shown in the green dashed line and has a very low probability [59].

Sim [79,80]. It can be seen in the plot; the hits have a rising trend, which is consistent with the upward-going track hypothesis. From the figure, one can notice clearly, that the fitted slope value can estimate the muon direction (up or down). As shown in Fig. 6.2, the slope values for cosmics and WimpSim MC samples are consistent with the downward- and upward-going hypothesis, respectively. The assumption made going forward is that there are only two options for the relativistic limit's slope values. Therefore, a fit can be done on the time distribution on Fig. 6.1 with fixed values of slopes. For the upward-going track the fit with the slope constrained to "1" results in a good χ^2 probability value of the fit, $P_{\uparrow}$. However the fit with slope of "-1" yields a low probability value, $P_{\downarrow}$. Using the probability values from the fits with the fixed slope value, a log-likelihood ratio (LLR) is formed as:

$$LLR = Log(\frac{P_{\uparrow}}{P_{\downarrow}}). \tag{6.5}$$

The LLR distributions for the cosmic and WimpSim MC samples are shown in Fig. 6.3. From this distribution, it is clear that a cut on LLR slightly above zero will reduce the cosmic background by the desired amount while preserving a high signal acceptance. Note that the WimpSim sample used is for dark matter with a 20 GeV mass annihilating through the $b\bar{b}$ channel. As such, the neutrinos from the b-meson decay produce muons, which, on average, have much lower energy compared to the cosmic ray muons. The signal shown here has shorter tracks with fewer hits than the events in the cosmic ray muon sample. This explains why the LLR for the signal has a larger component close to zero than the cosmic sample.

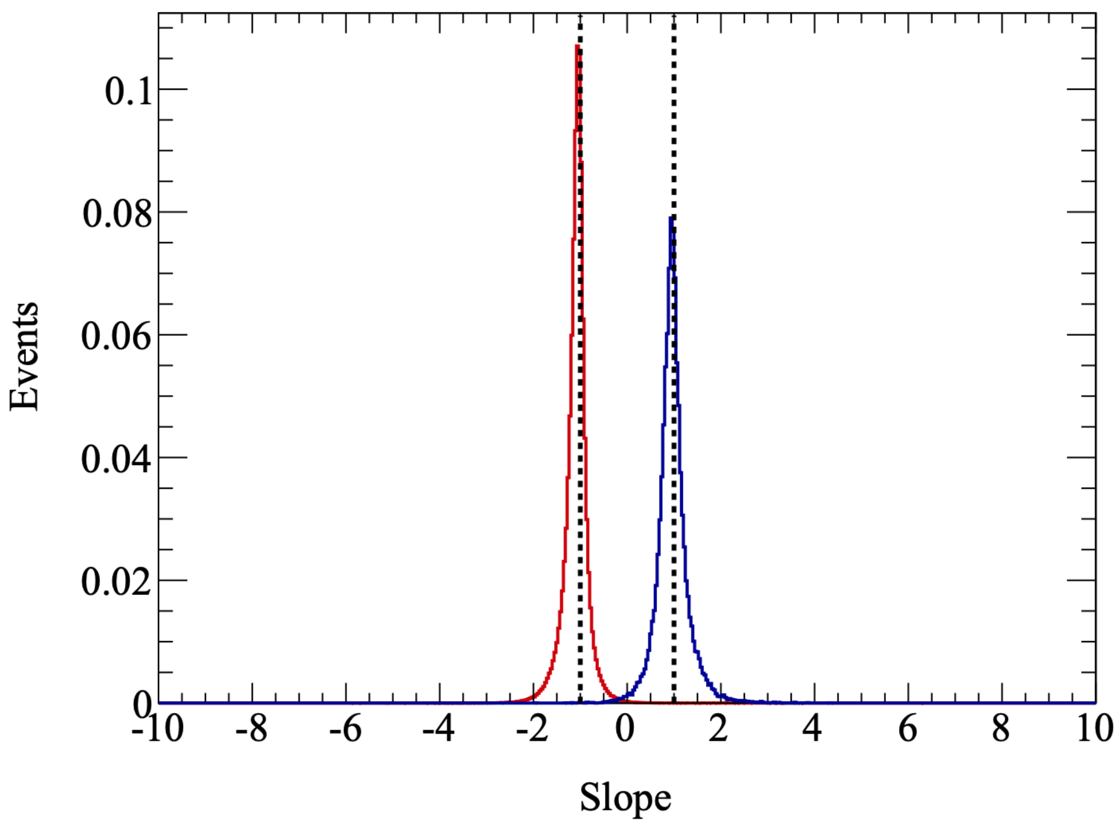

Figure 6.2: The slope distributions for cosmics (red) and WimpSim (blue) MC samples [59].

The LLR yields better performance for cosmic background rejection for the same signal acceptance in the regime where the cosmic rejection is sufficient (at least four

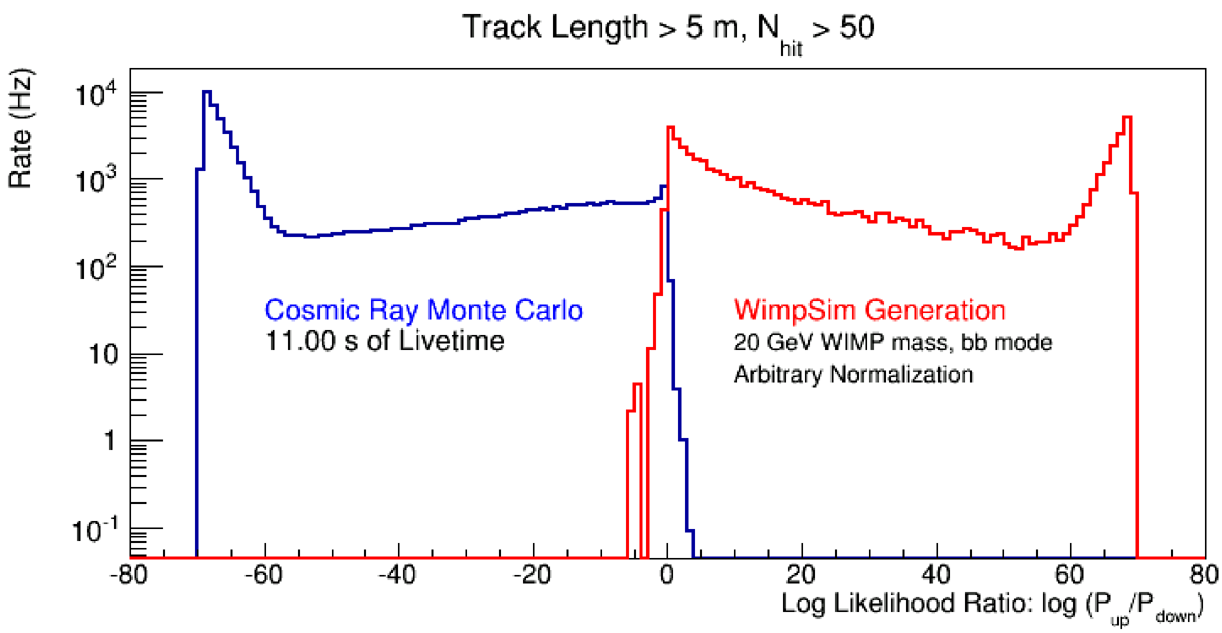

Figure 6.3: The LLR distributions for cosmics (blue) and WIMPSIM (red) MC samples. Note that only tracks longer then 5 m and with more than 50 hits are included [59].

orders of magnitude), compared to a cut on the best-fit slope. For example, for a signal acceptance of 0.7, the background rejection is about a factor of three better for the LLR. At this point, the MC predicts background rejection of close to five orders of magnitude.

In addition to being a more powerful discriminator observed in the MC studies, the LLR estimator is more robust to mis-reconstructed tracks, an essential feature in real data. Since mis-reconstructions will result in time distributions that follow neither the upward-going nor the downward-going hypothesis, the result of mis-reconstruction will yield LLR values close to "0" and not values consistent with a high-probability for being upward-going.

6.2.1 Trigger Cuts Update

In July 2017, after different studies were conducted on the upward-going muon trigger, two of the nominal cut values, the x-view and the y-view track linearity cuts

(R2X and R2Y), were changed from 0.99 to 0.95. The reason behind this choice was to increase the rate of acceptance of upward-going muons while maintaining a high rate of quality tracks, as shown in Table 6.2. Following the change, the rate went from one Hz to four Hz and stabilized around 4 Hz, as it can be seen from the Figs. 6.4 and 6.5. Besides the increasing rate, the variables exhibit the same overall shape distribution, especially important for the timing variables. The following variables are shown in Fig. 6.6 .

Variable	Cut Value	Events before cut	Events after cut	Rate (Hz)
R2X, R2Y	0.99	4827	12	1.38
R2X, R2Y	0.95	4827	29	3.32

Table 6.2: Different rate for the two values of the track linearity requirement in the x and y view. The rate with the newer value, 0.95, is approximately three times higher.

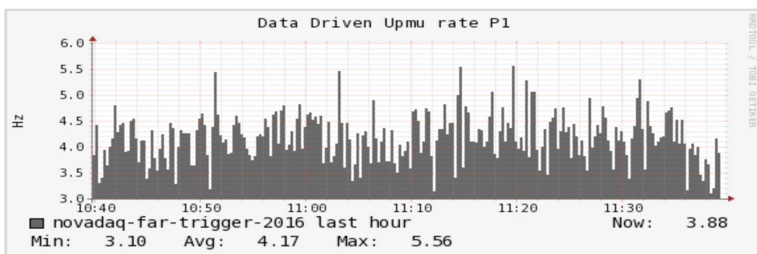

Figure 6.4: Trigger rate after change, stable around 4 Hz.

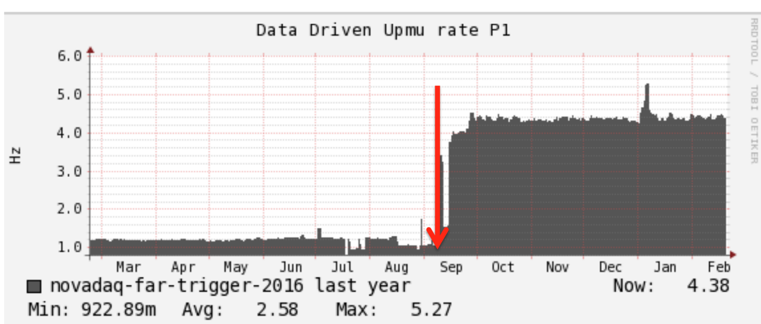

Figure 6.5: Trigger rate in Hz from February 2017 to February 2018. After changing the cut values for R2X and R2Y, the trigger rate increased by approximately 3 Hz.

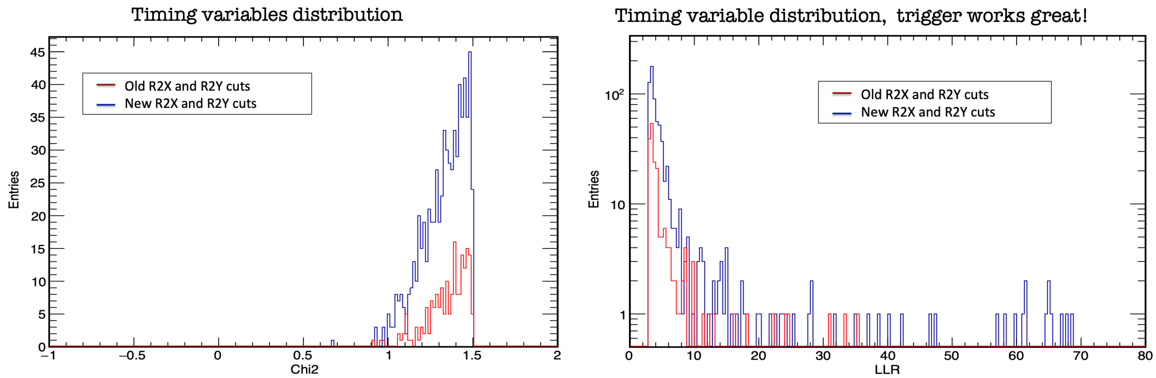

Figure 6.6: χ^2 and LLR distributions for the tracks in the trigger with the two different value of R2X and R2Y cuts.

6.3 Data-Driven Trigger Efficiency

The result presented in this section, have been presented in detail in [63].

By checking to see if offline reconstructed tracks would have been identified by the trigger one can measure the efficiency for the trigger reconstruction algorithm. For these studies, the efficiency of the Data-Driven Trigger (DDT) in NOvA has been defined as follow:

$$E = \frac{N_{both}}{N_{off}}, \tag{6.6}$$

where N_{off} is the number of tracks seen by the offline tracker, and N_{both} stands for the number of coincidences between offline and trigger tracks (two tracks are defined to be matched if their start and endpoints are separated by no more than 1.5m).

As shown in Fig. 6.7, the online trigger reconstructs about 85% of the offline reconstructed tracks, and that this is stable in time.

The results show that online trigger reconstructs about 0.85 of the offline reconstructed tracks and is stable in time.

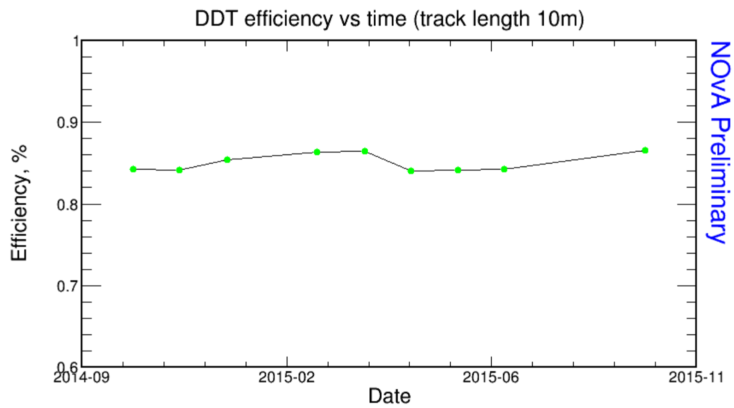

Figure 6.7: Track finding efficiency of the data-driven trigger (DDT) as a function of time for tracks longer than 10 m [63].

6.4 The ν_μ Sample Test

In the most recent ν_μ disappearance analysis, there were 78 fully-contained candidate events [64]. One can expect that approximately half of these events, that came from the beam, should be upward-going, and our triggers should have selected them.

The analysis strategy is straightforward and consists of the following steps:

1) Start with the 78 fully-contained candidate events from the ν_μ disappearance analysis.

2) Apply offline the same good quality track cuts that would have been applied at the trigger level (track length, N hits, dX, dY, dZ, R2X, and R2Y), as shown in Table 6.3.

3) Check how many and which one of the 78 events pass the cuts. Of these 78 events only 7 events survive.

4) Scan the events to select 4 upward-going muon events (assuming the beam direction).

5) Look for matches between those events and the events selected by the *DDUpMu* trigger.

Using this strategy 4 out of 78 ν_μ beam events were found, events that would be a candidate for our upward-going muon trigger, and out of those four candidates, three out of four were recorded, as summarized in Table 6.4 and shown in Fig. 6.8 and Fig. 6.9. This results have limited statistics but shows that the *DDUpMu trigger* is capturing upward-going tracks that pass the quality cuts.

Variable	**Cut**	**Num of Events**
ν_μ sample		78
Track Length	> 5 m	51
Track hits X	> 15	50
Track hits Y	> 15	24
R2X	> 0.99	7
R2Y	> 0.99	7
dX	> 5 cells	7
dY	> 10 cells	7
dZ	> 5 cells	7

Table 6.3: Selection criteria used by the upward-going through-going muon trigger applied on the 78 numu events to see which would have passed our through going selection criteria.

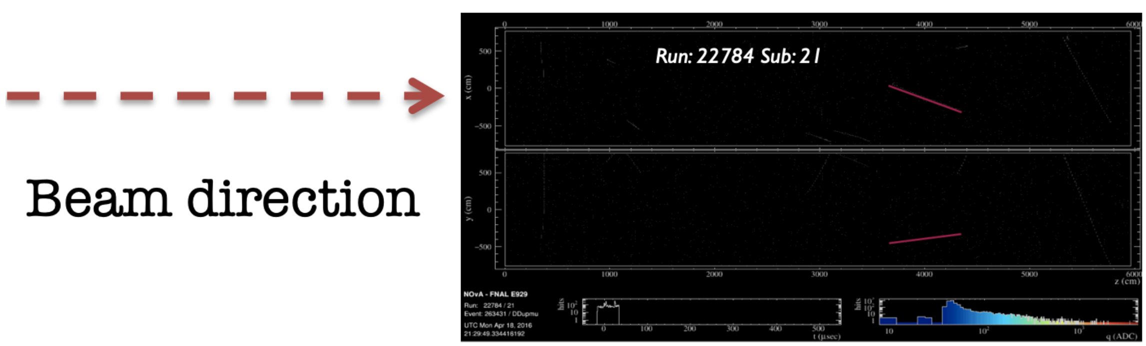

Figure 6.8: The event display of the first ν_μ event captured by the *DDUpMu* trigger. In this test the direction of the particle was assumed to be the direction of the beam, which allowed identification of the upward-going particles.

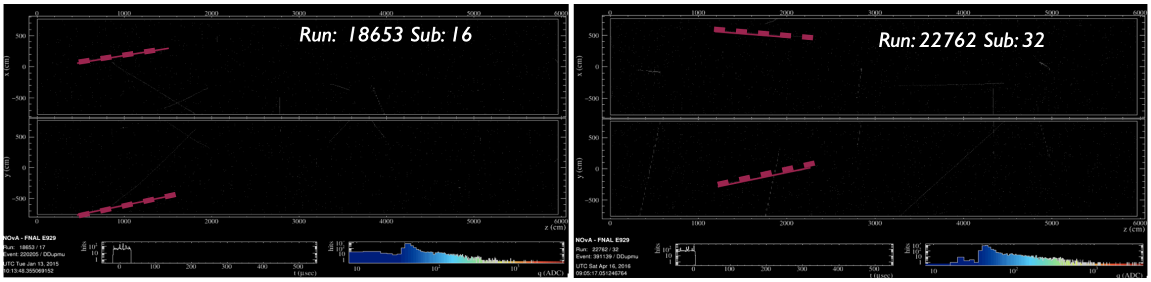

Figure 6.9: The event display showing the second and third ν_μ events captured by the *DDUpMu* trigger.

Step	Number of events
Sample from analysis	78
Apply quality track cuts	7
Upward-going selection	4
Events saved by the trigger	3

Table 6.4: Summary of the steps applied to test the trigger's ability to capture upward-going muons.

6.5 Trigger Studies with Downward-Going Muons

The aim of this study is to prove that the data and the simulation agree well enough that we can use the WIMP simulated tracks to understand the performance of the trigger. In order to do so, first downward-going cosmic rays data and simulation are used to prove the agreement.

150 kHz of downward-going cosmic rays look just like the signal if one applies a parity operation on the detector. The triggering algorithm can then be run on downward-going cosmic-induced muons, inverting the timing requirement in the LLR. This property is an excellent tool for background and efficiency studies. As described below, to estimate the trigger efficiency, the offline version of the trigger and offline analysis cuts are applied on a sample of cosmic rays.

6.5.1 Trigger Pseudo-Efficiency

To calculate the exact trigger efficiency using the downward-going muons sample one would need to start with a number of raw events, run the trigger over them, and then look at the exact same events that would be recorded offline. Since in this case is not possible to exactly identify the same tracks online and offline, the one calculated here will be referred to as a trigger pseudo-efficiency. The trigger pseudo-efficiency is calculated as:

$$\text{Pseudo Efficiency} = \frac{\text{Events that fired trigger}}{\text{Good track offline}} \tag{6.7}$$

This quantity is considered a pseudo-efficiency because even if using the same data, the events that fired the trigger will not necessarily be the same as those selected offline.

For this study three different data-sets were used, one for each stage of the trigger.

A) Old Gain (100), old track linearity value (0.99)

B) New Gain (140), old track linearity value (0.99)

C) New Gain (140), new track linearity value (0.95)

To calculate the numerator in Eq. 6.5.1 for each data set, the following steps were taken:

1. Raw data from downward-going cosmic sample, DAQ files, were selected.
2. LLR cut inverted, such that downward-going will look like upward-going muons
3. The offline trigger version was run over those files
4. The events that pass the trigger cuts were saved and counted

For the denominator in Eq. 6.5.1

1. The same raw data from downward-going cosmic sample, *DAQ* files, were selected.

2. LLR cut inverted, such that downward-going will look like upward-going muons

3. Tracks were reconstructed using the offline reconstruction algorithm for upward-going tracks

4. The events that pass the good quality track selection were saved and counted

The results of this study are summarized in Table 6.5.

6.5.2 Comparing Cosmic Data and Simulation

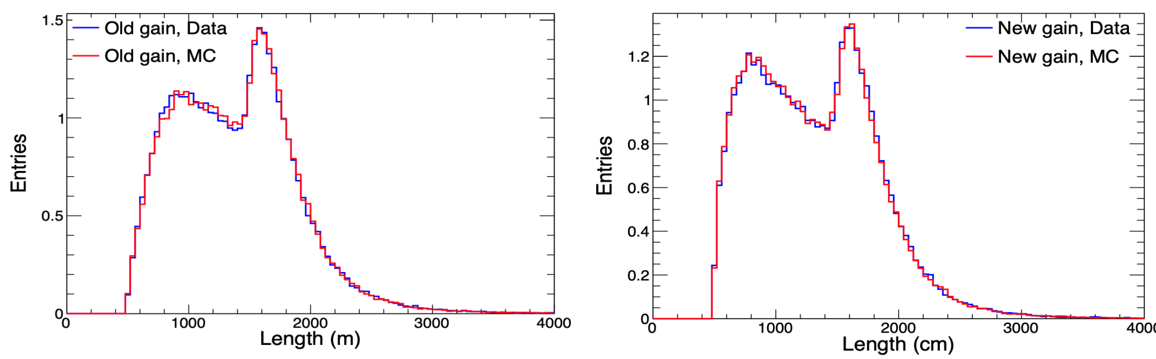

Figure 6.10: MC versus Data comparison. Length of the tracks distributions for the data and MC samples, with the two different gain. Those two distributions seem to match, as expected.

As for the data, also the simulations can be tested using the same process described in the Section 6.5.1. This study allows for identifying any discrepancy among data and simulations. While most of the variables examined seems to match, as can be seen in Fig. 6.10, a difference was found between the data and the simulation for the old gain data-set, as shown in Fig. 6.11. This shift is due to a slightly different value for the rise time used in the MC reconstruction, which can be seen in Fig. 6.12, taken from the study done in [55].

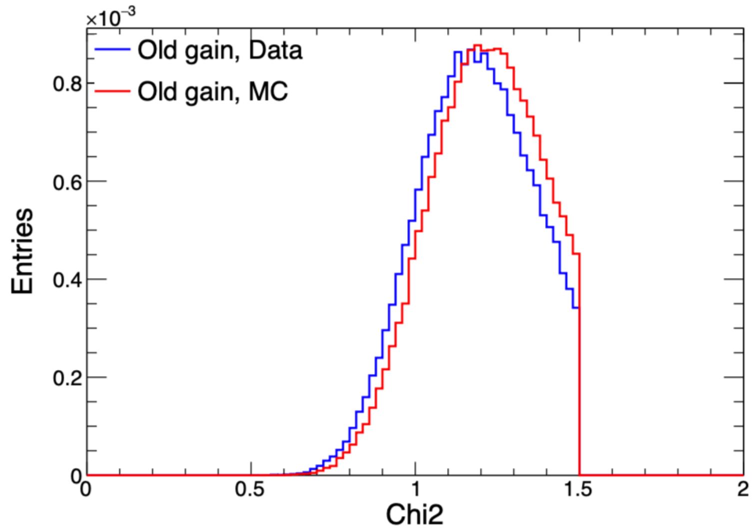

Figure 6.11: χ^2 distributions of data and MC downward-going cosmic samples. A shift of about 2% can be observed between the two distributions. This shift is due to a slightly different value for the rise time used in the MC reconstruction.

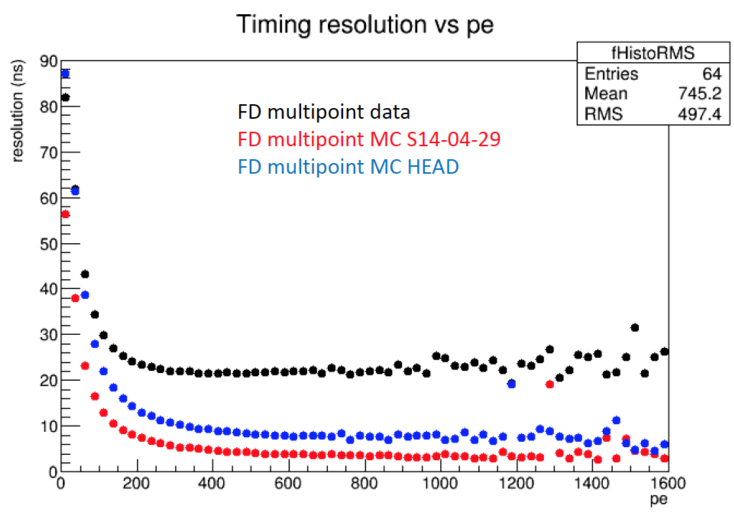

Figure 6.12: Single-hit timing resolution as observed in NOvA far detector data with four-point readout. See [55] for more details.

The results of the study are summarized in Table 6.5. This study shows that results with data and MC are compatible and that a MC study using upward-going simulated muons can be used to estimate the efficiency of the trigger.

Data Sample	Trigger Initial	Offline Initial	Trigger Final	Offline Final	"Pseudo Efficiency"
Gain (100), R2X and R2Y (0.99)	1337890	1335266	150580	422274	35%
Gain (140), R2X and R2Y (0.99)	1525351	1504157	187708	464589	40%
Gain (140), R2X and R2Y (0.95)	1508747	1501690	226475	507560	45%
MC Sample	**Trigger Initial**	**Offline Initial**	**Trigger Final**	**Offline Final**	**"Pseudo Efficiency"**
Gain (100), R2X and R2Y (0.99)	1087944	1040900	124635	355874	35%
Gain (140), R2X and R2Y (0.99)	478108	579314	75017	159610	47%
Gain (140), R2X and R2Y (0.95)	1197441	1193316	154225	328777	47%

Table 6.5: Pseudo efficiency calculated for cosmic data and MC, using the good offline track as the denominator and the events that fired the trigger at the numerator.

6.6 Measurements with Monte Carlo Samples

Given the consistency of the trigger efficiency results between data and MC, at the level of a few percent, one can safely use the MC to measure the trigger efficiency for the signal samples using upward-going muons.

To estimate the efficiency to attribute to the trigger when calculating the acceptance, a sample of WIMPs was used. More information about the simulation sample can be found in Chapter 9. A data set was created with simulated 10 GeV WIMPs using the $\tau^+ \tau^-$ annihilation channel. Only charge current (CC) ν_μ interactions were selected for the final sample.

To calculate the efficiency, the offline version of the trigger and offline analysis cuts were applied. Fig. 6.13 shows that the χ^2 distribution for WIMPS was comparable to the cosmic sample. Good agreement with the "new gain" cosmic sample can be observed.

Next, in order to understand the impact of our timing cuts, the trigger timing efficiency and the offline timing efficiency is calculated. The timing efficiency for the trigger is calculated as:

$$\text{Trigger Time Efficiency} = \frac{\text{Events that fired trigger}}{\text{Tight tracks in the trigger}}, \tag{6.8}$$

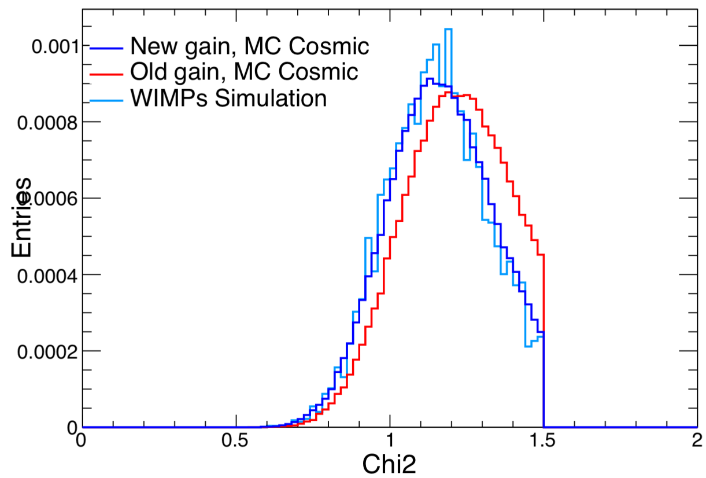

Figure 6.13: Comparison of the χ^2 distribution between WIMPs and the MC cosmic sample with old and new gain values. As described in the text, the MC cosmic old gain distribution differs slightly from that of the new.

while the timing efficiency offline is calculated as

$$\text{Offline Time Efficiency} = \frac{\text{Events that pass all offline cuts}}{\text{Tight offline tracks}}. \tag{6.9}$$

The denominator in this case is calculated as the number of tracks that passed all the good track selections at the trigger level, hence tight. By doing so, what one is really calculating is the efficiency for our timing cut.

Trigger Initial	**Trigger good track**	**Trigger Final**	**Time Efficiency**
124760	7722	5487	71%
Offline Initial	**Offline good track**	**Offline Final**	**Time Efficiency**
121820	7679	5373	70%

Table 6.6: Time efficiency calculated for the trigger and the offline signal, using good tracks as denominator and the events that pass all the trigger/offline cuts as numerator.

The trigger and offline time efficiencies are presented in Table 6.6. The results show that the *DDUpMu* trigger time efficiency is 71%.

6.6.1 Trigger Efficiency

To further estimate the price paid by having the trigger in place, a study using the WIMPs sample has been conducted, where the number of final events coming from the same file was counted with and without running them through the offline version of the trigger first. The result of this study is shown in Table 6.7. The analysis cuts introduce here will be deeply explained in Chapter 8.

An excellent way to estimate the trigger efficiency is to run the offline version of the trigger and the offline analysis over a sample of WIMPs and compare the results. In this way, the trigger's impact after applying all of the offline selection can be measured. The effect of applying the trigger in addition to the offline selection requirements is only about 5 % (see Table 6.7). Note that the impact of the trigger should be small. Much tighter cuts are applied offline to first reduce the background several orders of magnitude beyond the triggered level, and second, avoid the trigger turn-on making the sensitivity mostly dependent on the trigger efficiency.

	TRIGGER and ANALYSIS MODULE	**ANALYSIS MODULE ONLY**
Number of entries	4550	14039
Passed Length > 7 m	4106	6260
Passed Nhits > 70	4092	5986
Passed TrackHitsX > 20	4045	5884
Passed TrackHitsY > 20	4010	5821
Passed Length X > 2 m	3404	4456
Passed Length Y > 5 m	2308	2755
Passed Length Z > 1.2 m	2235	2600
Passed R2X > 0.99	2196	2521
Passed R2Y > 0.99	1840	2029
Passed Chi2 < 1.5	1829	1956
Passed Chi2X < 2	1827	1950
Passed Chi2Y < 2	1827	1950
Passed LLR > 7	1768	1865
Passed LLRX > 3	1728	1831
Passed LLRY > 3	1602	1694

Table 6.7: Number of events after each analysis cut, starting with the same WIMPs sample. The first one has also been run through the offline version of the trigger. Therefore the different number of initial events. The final number of events shows a 5% difference between the two methods.

The difference between those two numbers should indicate the effect that having a trigger has on the signal. This study showed that only 5% of the total events for the 10 GeV Dark Matter simulations were lost with the trigger in place.

6.7 Results and Conclusions

It was shown that the *DDUpMu* trigger successfully collects upward-going muon events, although with statistically limited samples of contained ν_μ events. An analysis to increase confidence in MC samples' use was first performed using downward-going muons events from data and MC simulation to build on these results. Those results showed a good agreement between data and MC. Lastly, a 10 GeV Dark Matter simulated sample was then used to calculate the trigger efficiency and the data lost due to the trigger.

Of the events that are used in the offline analysis, only about 5% are lost due to the trigger. These results will be taken into account when calculating the efficiency of the offline analysis.

Chapter 7

Event Processing, Calibration and Reconstruction

This chapter explains how raw data from a particle going through the detector becomes a reconstructed track that can be used for high-level analysis.

The first step is calibration. The calibration step is followed by the creation of several objects that contribute to the final reconstructed tracks used in the analysis. All these steps are handled by the data processing framework, which will be introduced first.

7.1 Event Processing

There are three main components to consider when processing data files: how to handle the data, who handles the data, and where to write the data files.

7.1.1 Sequential Access Via Metadata

The NOvA experiment produces a large number of data files. To deal with this, NOvA uses a data handling system called Sequential Access Via Metadata (SAM). SAM is made up of servers that work together to store and retrieve files and associate metadata. The metadata system allows users to handle files of interest without the need to know the specific name and location.

7.1.2 The Grid

Once the files are selected, the processing is handled by the Grid. The Grid is an extensive collection of worker nodes (CPU) controlled by a head node. The submission node maintains a queue of jobs that need to be run and distributes these jobs to worker nodes based on a user priority system.

7.1.3 Disks

The resulting files can be stored on different disks. Each disk has different properties. The *Scratch* disks have limited size, and files have a limited lifetime. The *Persistent* area is limited in size, but files are never removed automatically. For interactive analysis, *BlueArc* , which includes the *app* and *ana* area, is the best disk for quick performance. Finally, the last storage area is the *Tape*, used to archive long-term files.

7.2 Calibration

The data calibration in NOvA is done using downward-going cosmic rays because the characteristic of those events, such as being long straight tracks due to the high energy and low scattering, make them the most suitable for these kinds of studies.

For calibration purposes, tri-cells are used. Tri-cells are cell hits where the same cosmic ray also triggered both the adjacent cells in the plane, as can be seen in Fig. 7.1.

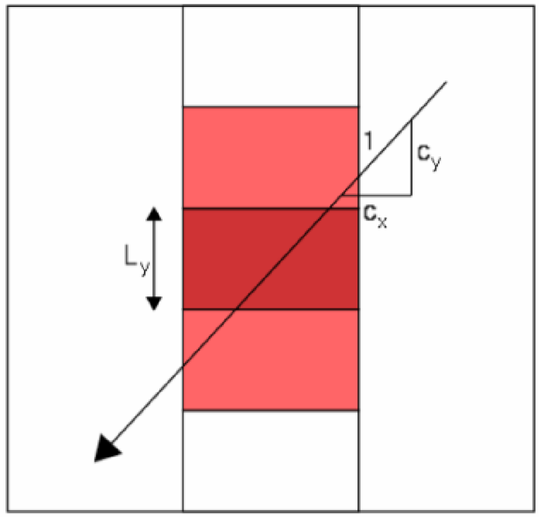

Figure 7.1: Tri-cells object used for calibration. The cell used need to have the most adjacent cells also triggered by the same cosmic rays event. Image Credit: [65].

7.2.1 Attenuation Correction

Depending on where the particle hits the detector, the amount of light that ultimately reaches the APD will differ. This is due to the fact that some of the light will be lost, and the amount of loss depends on the distance between the hit point and the APD. In the calibration process, this effect is taken into account and corrected. The correction is called the attenuation correction. The attenuation correction is applied on the pulse-height from the APD to correct the number of photoelectrons ($PECorr$). The correction factor is calculated starting from estimating W, the depth of the cell in cm. After that, the ADC/cm is recorded for each cell in the detector. A minimum of 500 entries per cell is required. The histogram so created is then fitted with an exponential function where the correction factor depends on the hit's depth. The correction factor is calculated as:

$$y = \begin{cases} 1 - \alpha_R(W - W_R)^4 & W > W_R \\ 1 - \alpha_L(W - W_L)^4 & W < -W_L \end{cases} \tag{7.1}$$

The different factors depending on the depth can be explained as follows. In the bulk of the cell, most of the light that hit the white PVC cell walls is reflected and captured by the scintillator, while for the hits at the beginning and end of the cell, the manifold that covers the top of the cell is made up of black plastic, which is much less reflective resulting in a more significant light loss.

7.2.2 Timing Resolution

The timing resolution applied in the calibration has been extensively explained in Chapter 6, which can be used for reference.

7.3 Event Reconstruction

Raw data coming from the detector needs to be transformed into physical variables to extract information that can be used for the analysis.

7.3.1 From Raw to Reconstructed

As seen in the previous Chapter 5, physical hits produced in the detector will be recorded if they are above a certain APD threshold. From these hits, called *CellHits*, several quantities are recorded: ADC charge for energy information, plane and cell positions for spatial information, and a timestamp for temporal information. The second step in the reconstruction process is calibration. In this step, a distinction is made between the cell activity due to signal *signal hit* and electric noise, *noise hit*.

The calibration correction step produces CalHits. After the calibration, these hits have a well-defined position and time in the detector.

The next step is to use this space-time information to cluster the hits together. To cluster hits into groups from the same physics event, the density-based Slicer4D clustering algorithm is used. This algorithm separates hits found in the same high-density space-time region from isolated hits, the latter being labeled as noise. The groups are called *Slices*, which can be seen in Fig. 7.2.

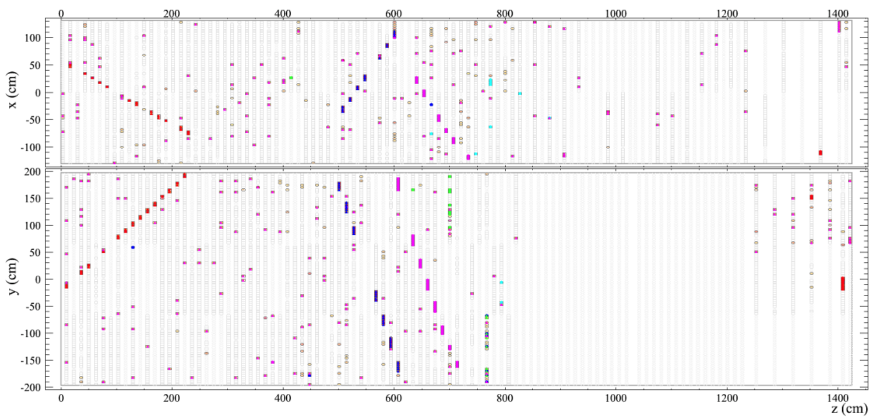

Figure 7.2: Example of cluster hit in the NOvA Detector. Image Credit:. [66].

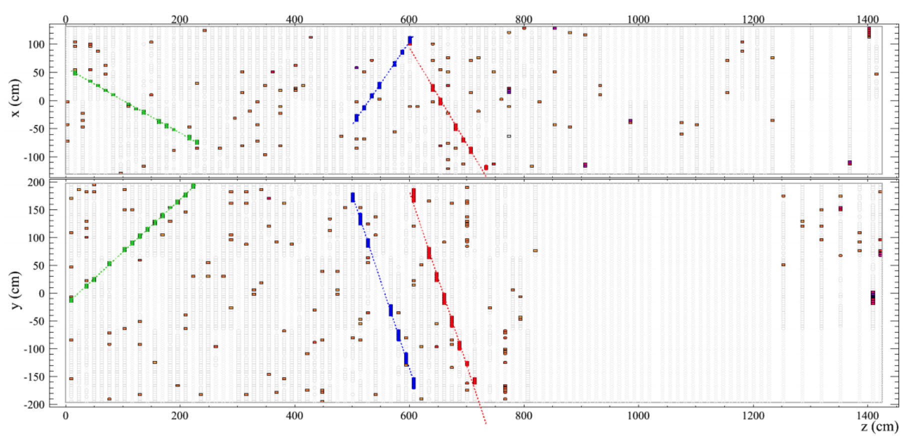

Figure 7.3: Example of fully reconstructed tracks. The same color of the hits corresponds to hits that have been associated with the same track. Image Credit: [66].

Different kinds of events, having different topologies, require different reconstruction chains. Usually, NOvA analyses using the tracker are based on a Kalman Filter and a multiple scattering model for v_μ events, while a cosmic tracker and a window tracker are used for the identification of cosmogenic events. The different tracker algorithms work by first reconstructing tracks for each view, as shown in Fig. 7.3, and then matching them together in Z to get a 3D reconstruction of the track.

In this analysis, only the muon tracks are taken into account, so only three track reconstruction algorithms are presented.

7.3.2 Kalman Tracker

The Kalman tracker is an adaption of the Kalman filter for tracking particles. The basic Kalman filter works by predicting the state in which the sistem will be at (t+1) by using information about the process and the measurement from time t. The evolution of process and measurement can be written as follows:

$$\begin{aligned} x_t &= Ax_{t-1} + W_{t-1} \\ z_t &= x_t + V_t \end{aligned} \tag{7.2}$$

where A is the state matrix, defined as:

$$A = \begin{pmatrix} 1 & \Delta z \\ 0 & 1 \end{pmatrix} \tag{7.3}$$

and x_t the state vector:

$$x_t = \begin{pmatrix} position \\ slope \end{pmatrix}. \tag{7.4}$$

The process noise W in Eq. 7.2 has variance Q, and the measurement noise V has variance R. The initial error covariance and measurement variance are used to calculate the Kalman gain. The Kalman gain allows for a reweighting of the prediction based on the measurement and process error, emphasizing the part with less error and therefore should be trusted more. The best estimate of the state based on the projection of the previous state and current measurement is then:

$$\hat{x_t} = A\hat{x}_{t-1} + K_t(z_t - \hat{x}_{t-1}) \tag{7.5}$$

The algorithm has been adapted to tracking and follows this general procedure. Initial track parameters are chosen and used to extrapolate the state in the next plane following the track's direction. The initial hits are also used to determine the track's initial slope and position and approximate the track's error covariance. The next steps depend on if there is a candidate hit in the next window. If there is, then calculate the estimated state, including the candidate hit in the track. If the inclusion does not change the track quality fit variable too much, then the hit is added to the track, and the extrapolation of the new state begins again with the new hits added. If that is not the case, the tracker will first check if the maximum number of consecutive planes without a hit has been reached and will end the track if that is the case or carry on to a new extrapolation of the state in the next plane. An example of a resulting track is shown in Fig. 7.4.

7.3.3 Cosmic tracker

The cosmic tracker was motivated by cosmic ray reconstruction. The algorithm works by finding the best-fit line to a collection of points in each 2-D view by minimizing the squared perpendicular distance from the points to the line, as shown in Fig. 7.5.

The cosmic slicer used in the tracker makes time slices that are at least 1000 ns time long and contain at least ten hits. The cells are first sorted by time, and then a

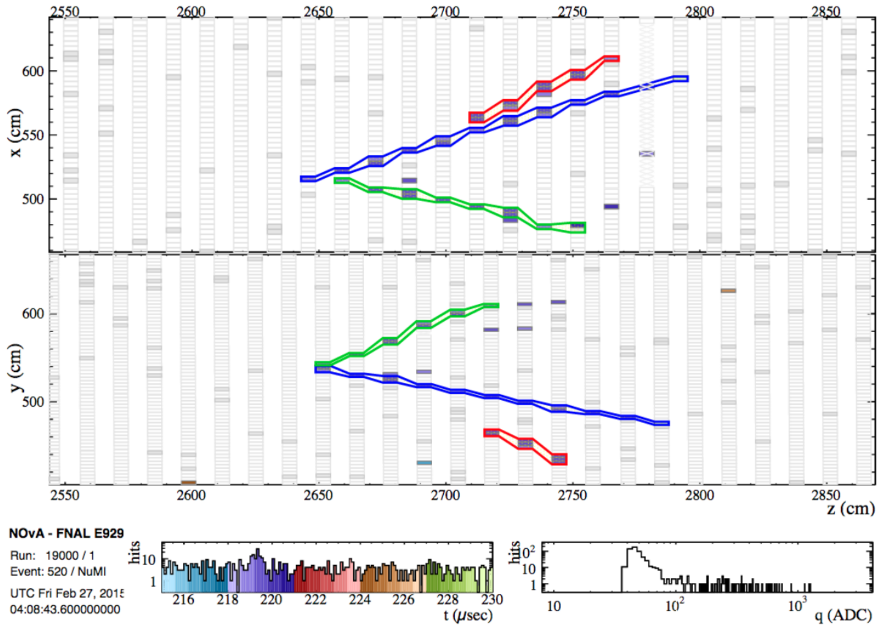

Figure 7.4: Example of simulated reconstructed tracks at the FD implementing the Kalman tracker algorithm. Each color represents an individual track that is part of a single event. Image Credit: [66].

window of length previously defined is slid on them. If not enough hits are present, then the hits are added to a noise cluster, and the process is repeated for the next hit onward. The process is repeated for all the hits. The next step in the algorithm is to loop over hits in a sliding window and fit using x and y positions in each view and a weight given by the number of hits.

The best fit line is the one that minimizes the squared perpendicular distance from the points to the line, and the hits that are consistent with the best fit line are added to a 2-D track. This method's strength is that it performs quickly, and it is therefore perfect for reconstructing events due to cosmic ray activity.

7.3.4 Window tracker

The cosmic tracker described in the previous subsection is handy when reconstructing high-energy cosmic rays but has some shortcomings. Because it uses a straight line to fit the hits, the underlying assumption is that the cosmic rays only

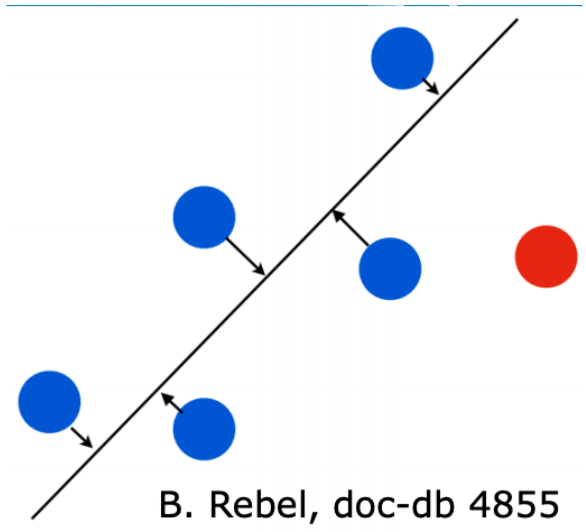

Figure 7.5: Example of hit fit in the cosmic tracker. Image Credit: [68].

travel on a straight line. This assumption is not always valid, especially for lower energy cosmic rays, which could undergo multiple Coulomb scattering in the detector and lose energy while traveling through the detector, deviating from a straight line. A new algorithm, called the window tracker, was implemented to overcome these shortcomings [68]. The window tracker assumes that muons follow a straight line trajectory only over a small portion of the track in the z-direction. The user sets the size of the window. After a window size is chosen, all the hits inside that window are fitted with a straight line. The best fit is added to the reconstructed track. The algorithm then slides over the next plane with hits, and all hits consistent with that line are added to a two-dimensional track. After this, a new straight-line fit is done and used for the next plane. As can be seen in Fig. 7.6, the smaller window size allows this algorithm to identify and track particles that do not follow a straight line for all their path, which can be considered a significant improvement to the cosmic tracker. For this reason, plus the computational efficiency and the smaller residual between the reconstructed hits along the track and the reconstructed trajectory points, this tracker was chosen to reconstruct the final data set used in the analysis.

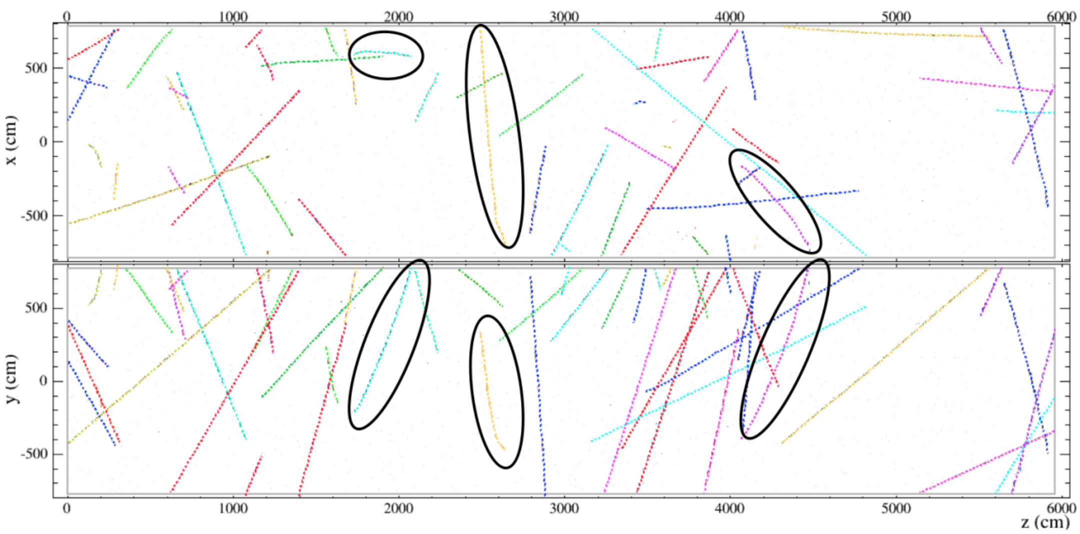

Figure 7.6: Example of tracks reconstructed using the window tracker. The tracker does a good job at fully reconstructing tracks that do no perfectly align with a straight line. Image Credit: [68].

Chapter 8

Upward-Going Muon Studies

This chapter has been mainly drawn from the internal note I wrote for the NOvA collaboration [69].

One advantage that NOvA has compared to past experiments that performed similar searches for dark matter annihilation is the relatively low energy threshold for muons. A 1 GeV muon travels approximately 5 meters in the NOvA detector. The challenge for the dark matter search is triggering efficiently on these low-energy muons. For shorter track lengths, the timing information will not be as powerful for rejecting downward-going backgrounds. Using stopping or fully-contained events and using the top and sides of the detector to veto downward-going events can provide an additional two orders of magnitude rejection.

There is a powerful data-based control region that can be used for estimating background in the dark matter search. One can measure the upward-going background during the day when the Sun is above the horizon, then perform the search during the night when the Sun is below the horizon. Using this method, a decomposition of the background need not be performed. Decomposing the background requires a full understanding of the atmospheric neutrino sample which would be a great thesis project for a NOvA student on its own. It would open the door to atmospheric neutrino physics and further optimization of this search. However to date, that analysis has not been completed and it is beyond the scope of this work. Note that relying exclusively on the data-driven background is a technique that has been used and published before (see, for example Ref. [70]).

This thesis presents and summarize those studies for the data-driven dark matter search using only tracks at least 7-m long. This chapter aims to show the event selection requirements and efficiencies for long tracks, the day/night comparisons for many observables using cosmic-ray muons to demonstrate that our control region is valid. Furthermore, it includes the details of the studies performed on data quality, offline background suppression and the Moon's shadow in cosmic ray muons to measure the NOvA angular resolution for pointing at celestial objects.

8.1 Feasibility: Timing and Pointing Resolution

For this analysis to be possible, two requirements need to be satisfied. First, that the timing resolution of the NOvA Far Detector is good enough to allow one to determine the directionality of a track by looking at the time of the hits to be able to discriminate between upward-going and downward-going tracks. Second, that the NOvA pointing resolution is good enough to allow for pointing at a celestial object, like the Sun. A demonstration of the feasibility of this analysis will be explained in this section.

8.1.1 Timing Resolution

A particle travelling at the speed of light will take approximately 50 ns to cross the NOvA detector. So, if the timing resolution is much better than this, it should be possible to tell the directionality of the track with a high level of success. Fig. 8.1 shows the single-hit timing resolution observed in the upward-going-muon triggered sample, as explained in details in Chapter 6. The expected timing resolution of approximately 20 ns at 250 PE value was obtained.

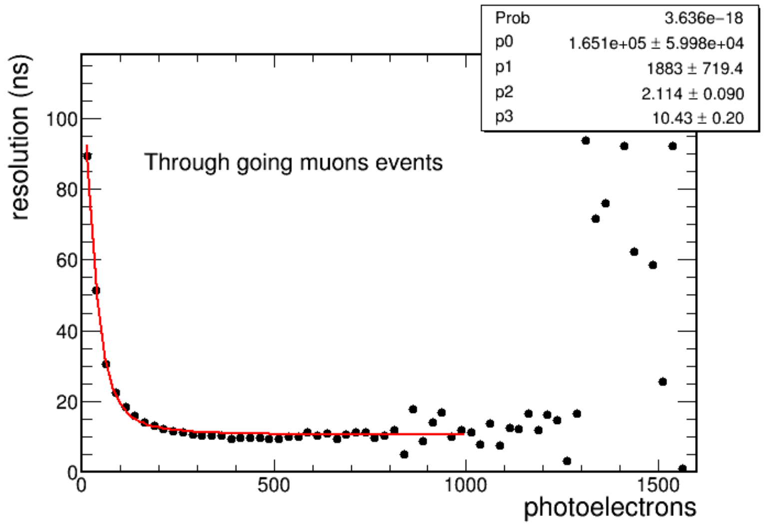

Figure 8.1: A fit to obtain the timing resolution in the upward through-going muon sample. This cross check ensure that the results obtained were consistent with the one in the triggered dataset as in the cosmic-ray sample.

8.1.2 Pointing Resolution

These results were obtained with the collaboration of A. Norman, L. Aliaga, A. Ataris and presented at ICHEP 2106 [62]. Atmospheric neutrinos generated on the other side of the Earth are also capable of producing upward-going muons in the detector. Based on timing, this is an irreducible background for the WIMP dark matter search. One way to discriminate atmospheric neutrino events from WIMP events is to reconstruct the directionality of the incident neutrinos and look for a signal pointing back to the sun.

One way to demonstrate the ability of NOvA to point to celestial objects is to observe the shadow of the Moon in the downward-going cosmic ray muon sample. Unfolding the angular size of the Moon should also make it possible to extract the angular resolution of the NOvA far detector for pointing at celestial objects. Note that without careful correction for distortion due to muons deflected from the direction of the cosmic ray primary, this estimate of the angular resolution should only be considered an upper limit (multiple scattering or the magnetic field of the Earth may cause deflection).

Similar observations have been made by other Collaborations such as MINOS [71], IceCube [72] and MACRO [73] using their deep underground detectors. The challenge for NOvA is to observe the Moon shadow in its Far Detector located on the Earth surface.

Taking advantage of its good track resolution of the high energy muons, in this first approach, unbiased cosmic pulser trigger files are used

Any track with at least 15 m length was allowed but only the one within 5° respect to the position of the Moon applying the standard selection cuts on the muons were analyzed. The tracks are reconstructed with the Cosmic reconstruction algorithm.

Fig. 8.2 shows the differential density of the cosmic rays seen by the NOvA Far Detector respect to the difference between the track direction and the position of the Moon ($\Delta\theta$). A preliminary shape of deficit yields due to the presence of the Moon is observed for $\Delta\theta < 1°$ and a flat distribution for $\Delta\theta > 1°$. Eq. 8.1 shows the relation between the solid angular distribution in the presence of an obstacle that can be modeled with a two dimensional Gaussian distribution as described in [71]. In the absence of the Moon (or any object that the obscures the cosmic rays), the distribution should be flat and given by λ. $R_m = 0.26°$ is the radius of the Moon and σ is the smearing caused by the detector smearing that is found by fitting to Eq. 8.1.

$$\frac{\Delta N}{\Delta\Omega} = \lambda[1 - \frac{R_m^2}{2\sigma^2}e^{-\Delta^2\theta/2\sigma^2}(1 + \frac{(\Delta^2\theta - 2\sigma^2)R_m^2}{8\sigma^4} + \frac{(\Delta^4\theta - 8\Delta^2\theta\sigma^2 + 8\sigma^4)R_m^4}{192\sigma^8})] \quad (8.1)$$

The result of the fitting is included in the Fig. 8.2 and gives a $\sigma = 1.23°$ with a $\chi^2 = 5.91/8$. So, this suggests that the NOvA pointing resolution is close to 1.5 degrees. This is much better than the average angle between the neutrino-induced muons and initial neutrino direction for the energies of the muons that we are interested in, so it will not limit the ability to perform this search at NOvA. More details are presented in [74].

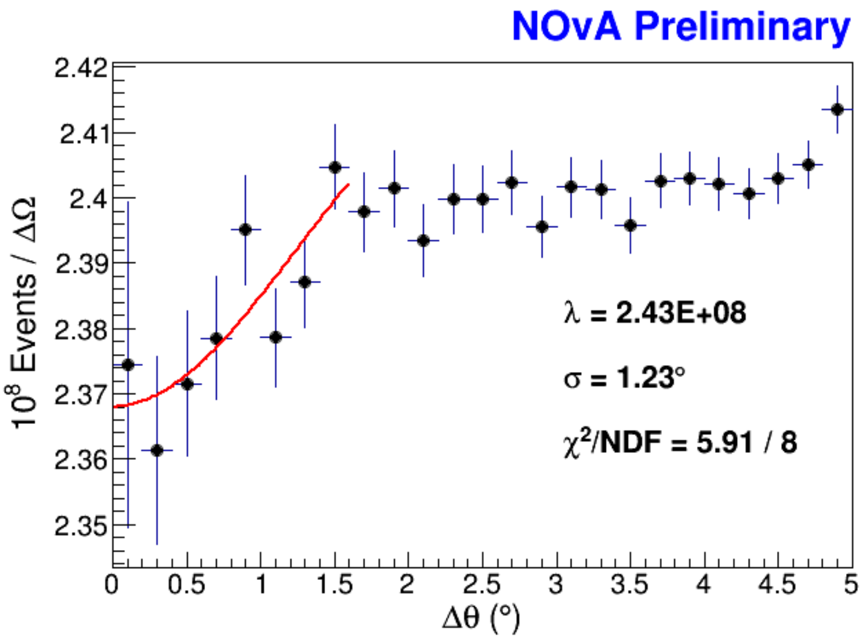

Figure 8.2: Differential density of the cosmic rays at the NOvA Far Detector respect to the Moon position. The figure also shows the result by fitting to Eq. 8.1.

8.2 Dataset

The upward-going muon trigger was first implemented and tested in August 2014, but did not run in a stable configuration until December 2014. The triggered sample examined in this note covers a period of approximately 3 years from December 2014 to late May 2018. The total live-time of this sample is $\sim$ 1073.5 days.

Over the period of this sample, the through-going trigger fired at a consistent rate of $\sim$1 Hz until September 2017 when a new version of the trigger was implemented and the rate increased to $\sim$4 Hz, see Chapter 6. Activity in the NOνA far detector is dominated by muons from cosmic ray interactions above and around the detector [59].

NOvA reconstruction software was run on the triggered sample to produce the desired track and hit objects and to perform the necessary timing calibrations.

8.2.1 Analysis Region Definitions: Background, Control and Signal Regions

The upward-going muon analysis utilizes three basic analysis regions for splitting the acquired data into different samples. Each of the samples is based on the position of the Sun. In all cases the position of the Sun is calculable in coordinates of right ascension and declination, which can be transformed into the elevation and azimuthal direction of the object relative to the NOvA detectors. Analysis regions are defined based on the elevation of the object relative to the detectors. Three general classifications are made in this manner and denoted as ("above horizon", "below horizon", "horizon region") or more colloquially as ("Day", "Night" and "Twilight") for the objects. In this manner an object is considered to be in its above/day region if its elevation is greater than a pre-determined fixed angular value which is defined as the above/horizon boundary. Similarly an object is considered to be in the below/night region if its elevation is less than a pre-determined fixed angular value which is defined as the below/horizon boundary. Objects are considered to be in the horizon region (twilight) region if their elevation is equal to or between the values established for the transition boundaries. With the typical convention that the "day/twilight" boundary is a positive elevation and the "twilight/night" boundary is a negative elevation, this leads to the diagram shown in Fig. 8.3.

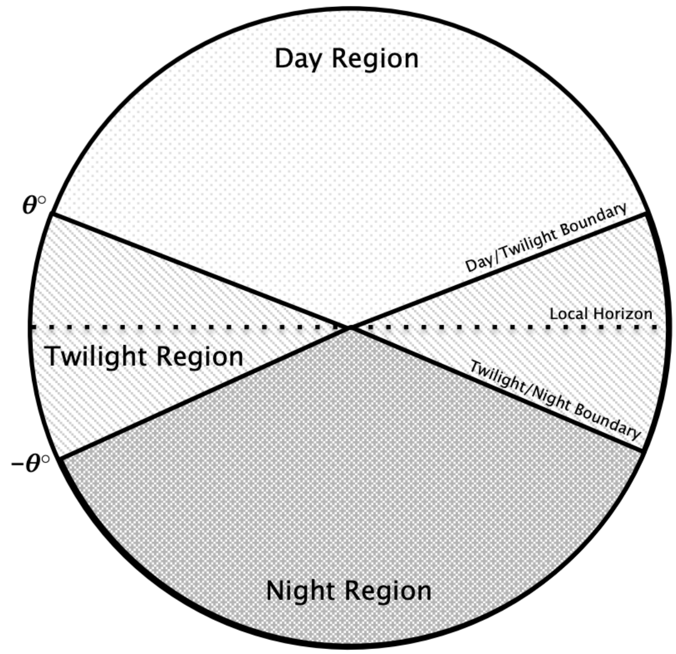

Figure 8.3: Celestial object analysis regions

So, using metadata parameters we can split out data into several signal and control regions. In particular, for this analysis, we define the regions as:

- **Signal Region (Night)**: We define the signal region to be when the Sun is at least 10 degrees below the horizon.

- **Primary Control Region (Day)**: We define a primary control region when the sun is at least 10 degrees above the horizon.

- **Secondary Control Region (Twilight)**: We define a second control region when the sun is within 10 degrees of the horizon.

The total data set, so divided, is made up of:

Region	Files Stage	Total
Night	in the definition	213237
Night	successfully processed	213220
Night	Total live-time	40290970 s
Twilight	in the definition	102114
Twilight	successfully processed	102107
Twilight	Total live-time	17844133 s
Day	in the definition	202108
Day	successfully processed	202106
Day	Total live-time	34609255 s

Table 8.1: For each of the three regions, the number of initial files (containing the raw data information), the number of the final processed files (containing the analysis reconstructed information), and the total live-time calculated from the files number is reported.

Upward-going muons signal region

The signal regions for the upward-going muon analyses are taken from the "night" region of the sun. In the initial data sets boundary points are defined at -10 degrees of elevation. The integrated exposure can vary significantly based on the seasonal procession of the sun at the high latitude of the NOvA detector (i.e. during the winter the sun spends less time up in the sky, so the length of the signal region during winter will be different from the summer one).

8.2.2 Data-Driven Background Estimation for the Signal

Is is important to notice that this analysis uses the day sample for the background estimation of the signal region, i.e., giving a totally data-driven prediction of the number of estimated background events that should be seen in the signal. This approach has been done before by an other experiment [70]. To do that, it is necessary to count the events in the day sample, then calculate the live-time for each region, and based on the number of events per live-time in the day region, predict the number of events to expect in the signal region.

8.2.3 Unblinding Criteria and Strategy

The analysis uses a blind strategy. Checks are performed in several control regions in order to validate using the 'day' control sample to predict backgrounds in the 'night' signal window.

To unblind the analysis, first the unbiased cosmic ray data sample will be used to establish that detector observables are stable between the day and night sample. Then several observables will be checked to ensure that their shapes are consistent in the day and night sample. Then the primary search variable – the angle between tracks and the position of the Sun will be studied by checking the ratio of this variable between the day and night sample in the cosmic ray control sample to ensure that it is flat. An important role will be played by the control region (day time) in which one can study the upward-going sample without any contribution from the solar dark matter source. In this sample the impact of the selection criteria and look for signs of misreconstructed background events in the upward-going sample.

Once selection is validated and day/night comparisons are completed in the cosmic sample there is one addition control check to perform: day v/s twilight for $\Delta\theta$ and other distributions using the upward-going sample. If everything looks good, lastly, the full signal region can be unblinded.

8.3 Data Validation Checks

8.3.1 Day versus Night Checks in the Cosmic Ray Sample

The cosmic ray "pulser" selects 550 μs windows at 10 Hz. This unbiased sample will include about 1/200th of the data and would have a negligible bias caused by any true upward-going event contribution. Appendix C shows several cross checks of variables in the day and night samples. Most agree to within 1 %. Note that the cleanup cut efficiency in both the day and the night sample have been checked and also found to agree better than 1 %.

The primary observable for this dark matter search is the angle between the track to the sun ($\Delta\theta_{Track,Sun}$). When checking a small sample of data (~1 month from November 2015) it was clear that this observable would not have the same shape in the day and night sample if the angle relative to the position of the Sun was used. In November, the Sun stays much lower in the sky during the day in the northern hemisphere than it does in the southern hemisphere. So, comparing $\Delta\theta$ for day tracks pointing at the Sun above the horizon with $\Delta\theta$ for night tracks pointing to the Sun below the horizon will have a very different path in the sky of the Sun in the two samples. That is, the azimuthal and zenith angle distributions are very different in day and night sample as shown in Fig. 8.5. Because the cosmic ray flux is strongly dependent on the zenith angle (see Fig. 8.4), any control region check using cosmic ray muons will have a different $\Delta\theta$ distribution unless the solar position is defined in a very careful way.

To solve this issue and to make sure that the primary observable would be sensitive to the dark matter signal, a 'phantom' position for the Sun in the data control region was implemented. Ignoring shadow effects, the cosmic ray flux is independent of the Sun's position for the background hypothesis. So, in the background model, it

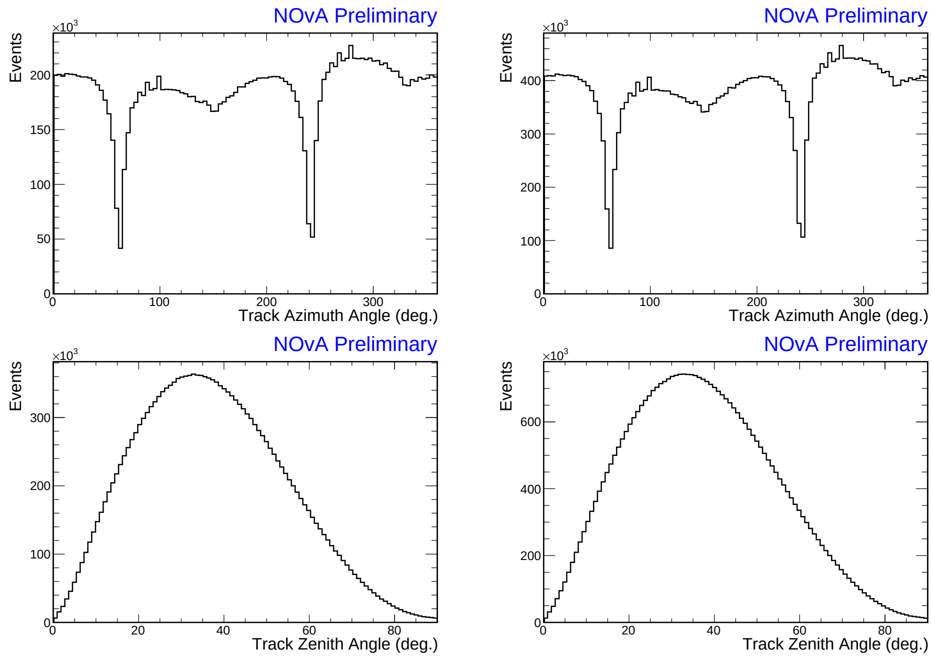

Figure 8.4: The azmuthal (top) and zenith (bottom) angle of the tracks in the day (left) and night (right) samples in the November 2015 data. The track angular positions don't depend on the the time of day. From

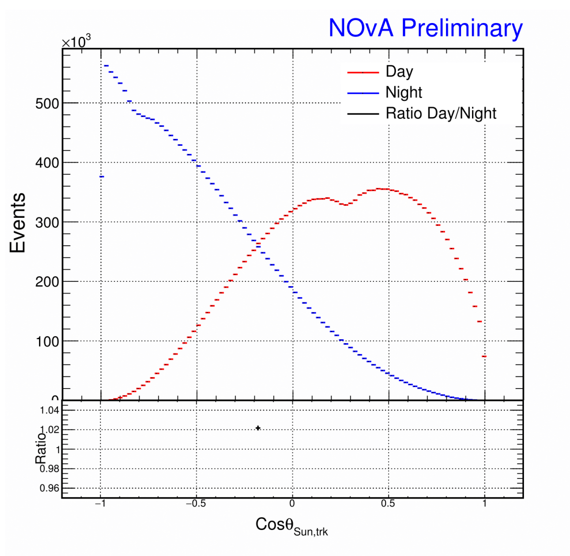

Figure 8.5: The azimuth and zenith angle of the Sun in the day (top) and in the night (middle). The bottom plot shows the $cos(\Delta\theta)$ distribution, where θ is the angular distance between the track and the solar position [62].

shouldn't matter where the Sun actually is in the sky for any given track, only that the the distribution of the 'phantom' Sun's position in the day sample matches that in the night sample. Basically, for the day sample the Sun position is drawn randomly from the distribution that it follows at night.

Using the 'phantom' position of the Sun in the day control region one can compare the $\Delta\theta$ distribution for the day and night samples in the cosmic ray unbiased sample in Fig. 8.6. A weak systematic trend that changes the ratio by about 2 % over the range of the distribution was observed.

The bias observed in the day v/s night $\Delta\theta$ distribution is caused by temperature/density differences between the Earth's atmosphere in the day and night samples. This difference means that muons attenuate a little bit differently in the day and night sample, and therefor the muon energy distribution reaching the detector is a little bit different in these two samples. A similar bias in the distribution of reconstructed muon energy was observed (see Fig. 8.7). Also the Cos(θ_y) distribution of Appendix C observes a similar bias while no significant bias is observed in the Cos(θ_x) and Cos(θ_z) distributions, leading to an effect not due to the detector. Cos(θ_x) and Cos(θ_z) would not be as sensitive to the a slight change in the energy of incoming cosmics while Cos(θ_y) is more directly related to the penetrating strength of the incoming particles. With this explanation our neutrino induced signal does not suffer the same day/night difference. Regardless of the source, a two-percent bias will be a very small effect compared to our statistical limitations and other systematic effects in the dark matter search. So, this effect will be included as a systematic uncertainty.

With the result of Fig. 8.6, we can be confident that the shape obtained an in the day control region should match the shape obtained in the night sample to 2 % or better in the absence of an upward-going signal correlated with the Sun's position.

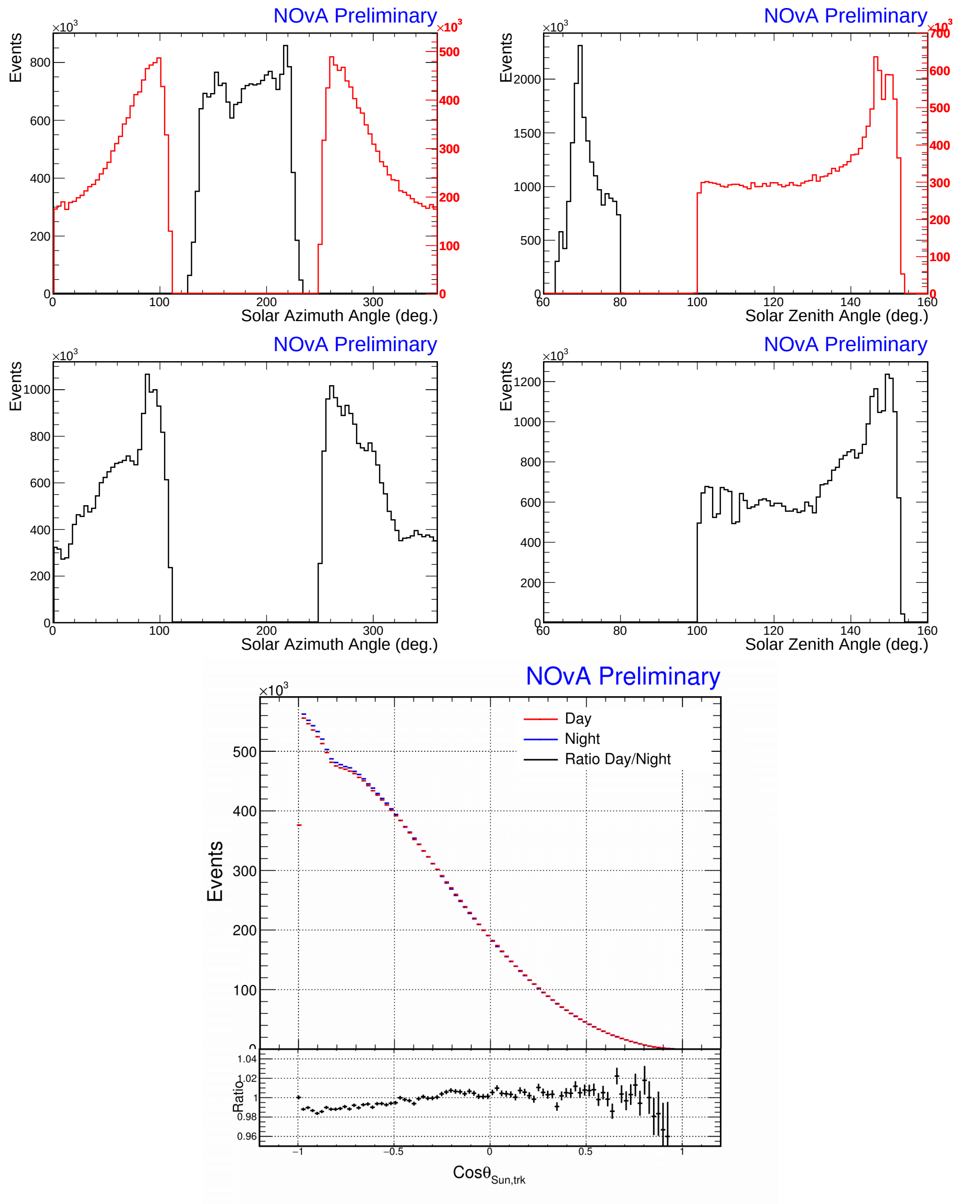

Figure 8.6: The top plots show the azimuth and zenith angle of the Sun during the day. The red curve is the Sun position drawn randomly from the distribution that it follows at night. The middle plots show the azimuth and zenith angle of the Sun during the night. The bottom plot shows the $cos(\Delta\theta)$ distribution, where θ is the angular distance between the track and the solar position. For the day sample the Sun position is drawn randomly from the distribution that it follows at night [62].

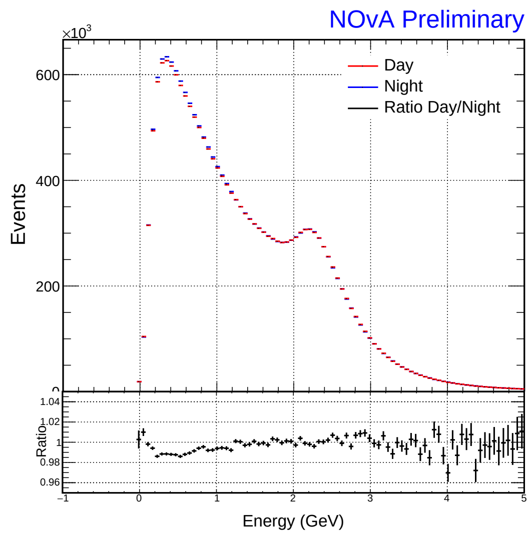

Figure 8.7: The energy distribution of muons in the cosmic ray sample.

8.4 Data Quality

A lot of work has been done to ensure a good quality of data. Many factors can influence the quality of a data set and if not taken into account lead to biased results. Unless these biases could be corrected, the data were eliminated for the total data set. The following section aims to explain how the data quality was defined and how the final data set was selected.

8.4.1 Data Quality Requirement

Following the NOvA requirement, a Subrun is determined to be good or bad based on criteria discussed in the good runs technical note [75]. The usual good Subrun information is propagated to the offline via the use of a SAM metadata parameter *DQ.isGoodRun*. This method has been proven to have some shortcoming and to not be up to date, especially during the shutdown time when there is no beam. In the Fig. 8.8, it can be seen the missing metadata information in blue:

A new method to access the good run information is available since September

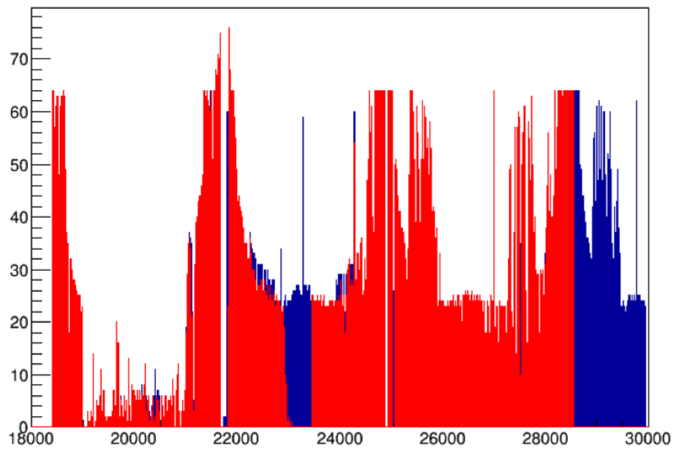

Figure 8.8: The run marked as DQ.IsGoodRun true in red, while the one missing that information are in blue

2017 [76]. The new method uses a SAM database table to store the relevant data quality information. The new dataset can be see in the Fig. 8.9.

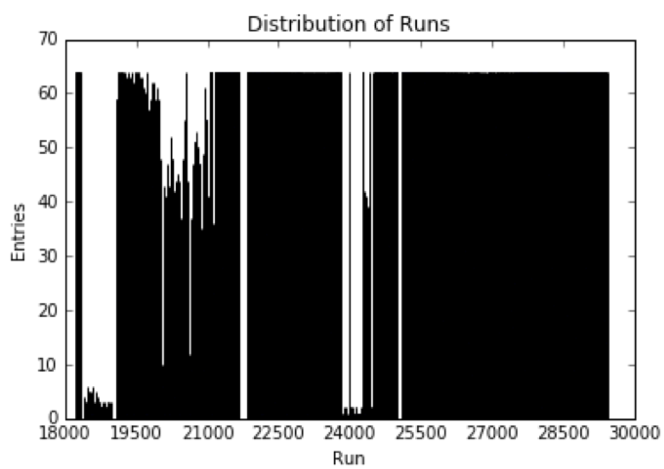

Figure 8.9: Run distribution of the new dataset. Requirement: novagr_good true and novagr_ngood_tot_diblock > 13 with novagr_tag "v5.8"

8.4.2 Data Quality Checks

Several checks on data quality were performed to ensure consistent performance in the data and to exclude data files with obvious anomalous properties. The total dataset was divided in three different periods, to take into account the change in the gain and in the trigger, since both changes have an effect on the variables examined for data quality. The three periods are:

- PERIOD I: From run 18399 to run 20752
- PERIOD II: From run 20753 to run 27000
- PERIOD III: Run greater that 27000

Mean track properties were compared among all of the subruns included in the analysis. Deviations from the normal of these parameters could be an indicator of malfunction of detector systems, data acquisition software, reconstruction algorithms or some combination of those factors. Anomalous subruns were excluded from further analysis in order to avoid any bias to our results. Figures 8.10 to 8.18 show the distributions studied for data quality checks. Run that lies outside the normal range, red line, were eliminated from the analysis. Overall, 1.7% of collected data was excluded from analysis after introducing data quality cuts.

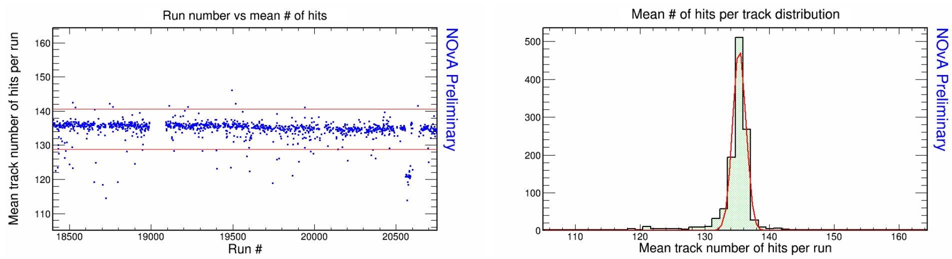

Figure 8.10: Old Gain. Histogram of distribution of average number of hits per track by subrun of NOvA Far Detector. Red line denotes a data quality cut on average number of hits.

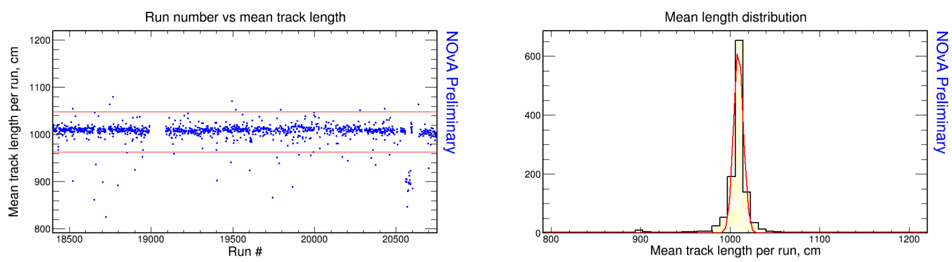

Figure 8.11: Old Gain. Histogram of distribution of average track length by subrun of NOvA Far Detector. Red line denotes a data quality cut on average track length.

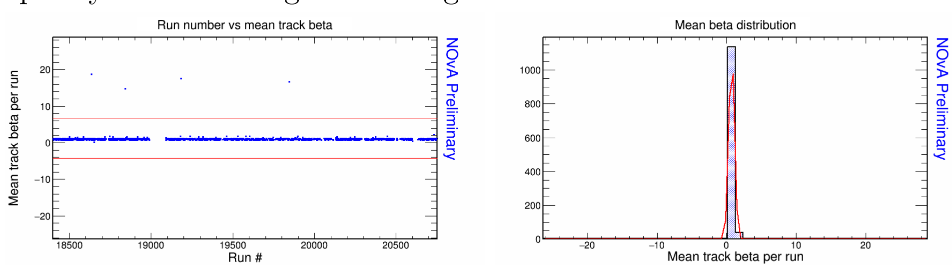

Figure 8.12: Old Gain. Histogram of distribution of average track β by subrun of NOvA Far Detector. Red line denotes a data quality cut on average track β.

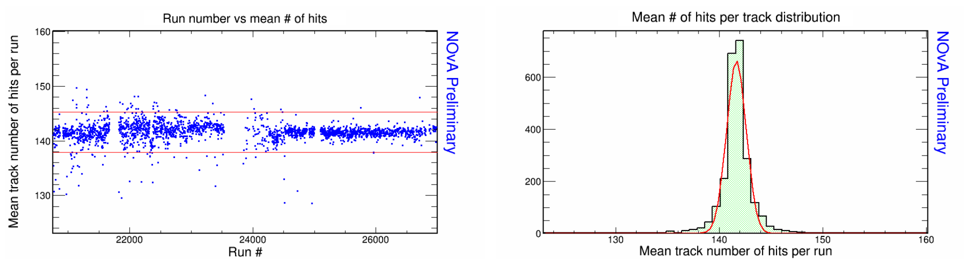

Figure 8.13: New gain, old trigger cuts. Histogram of distribution of average number of hits per track by subrun of NOvA Far Detector. Red line denotes a data quality cut on average number of hits.

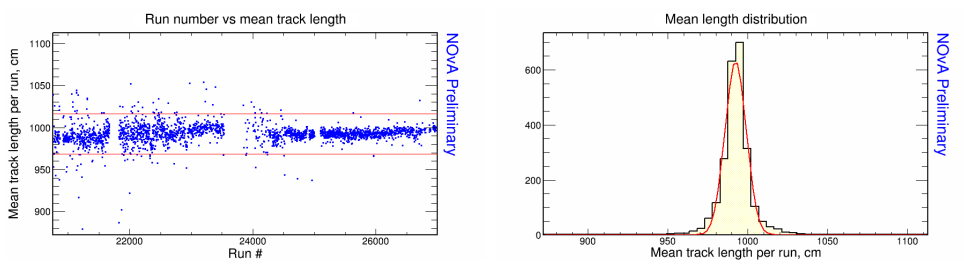

Figure 8.14: New gain, old trigger cuts. Histogram of distribution of average track length by subrun of NOvA Far Detector. Red line denotes a data quality cut on average track length.

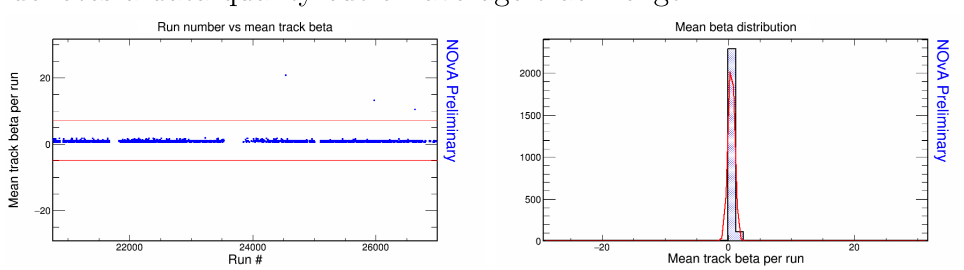

Figure 8.15: New gain, old trigger cuts. Histogram of distribution of average track β by subrun of NOvA Far Detector. Red line denotes a data quality cut on average track β.

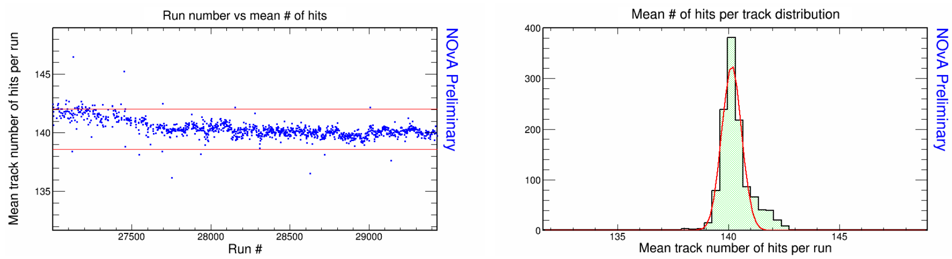

Figure 8.16: New gain, new trigger cuts. Histogram of distribution of average number of hits per track by subrun of NOvA Far Detector. Red line denotes a data quality cut on average number of hits.

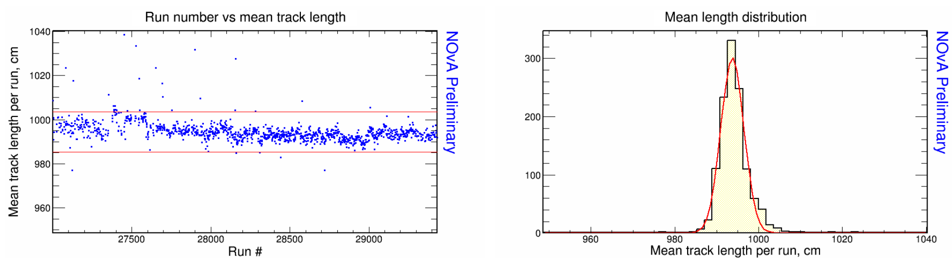

Figure 8.17: New gain, new trigger cuts. Histogram of distribution of average track length by subrun of NOvA Far Detector. Red line denotes a data quality cut on average track length.

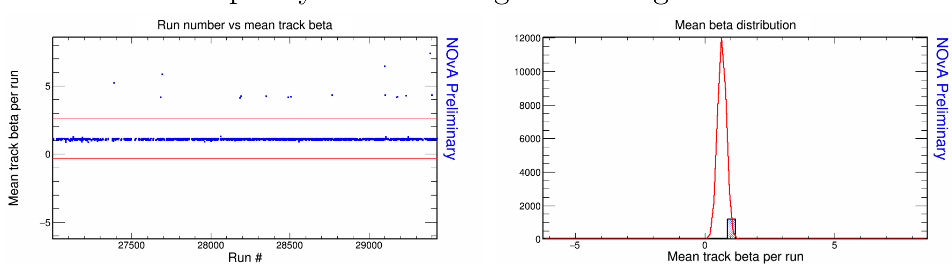

Figure 8.18: New gain, new trigger cuts. Histogram of distribution of average track β by subrun of NOvA Far Detector. Red line denotes a data quality cut on average track β.

8.5 Event Selection

The event selection falls into two general categories. The first category is designed to select long, well defined muon tracks which will be able to potentially yield a good log-likelihood for the upward/downward-going discrimination. These cuts are limited to mainly simple geometric and track topology quantities. The second category of selection criteria are designed to select the directionality of the tracks and separate them into an upward and downward-going sample. These are based on the timing information and log-likelihood metrics.

8.5.1 Track Quality Cuts

For this analysis, track reconstruction was done separately and validated separately for three different trackers. The tracks were selected using the kalman tracker, cosmic tracker and window tracker. The reason that three trackers were used were due to the strengths and assumptions that each tracker makes in seeding/forming its tracks, as explained in Chapter 7.

In the results that follow the distributions from the Window Tracker [77], which is best aligned with this analysis, is shown.

For all of these tracks identified with the Window Tracker, a set of track quality cuts designed to keep only well-reconstructed muons (golden muons) with lengths sufficient to calculate a reliable likelihood ratio were applied. These cuts were determined based on manual examination of the distributions. A further optimization of these cuts has been done against a signal and background figure of merit. The cuts are shown in Table 8.2.

The efficiency for these cuts is estimated from the minimum bias sample by assuming the standard Window tracker reconstruction efficiency and then computing the survival rates for each cut. In this process all of the muons from the minimum

Variable	Cut Value	Description
TrackLen	700.0 cm	3 dimensional reconstructed track length
TrackHitsXY	70	total number of hits associated with 3D track
TrackHitsX	70	number of hits associated with XZ projection of track
TrackHitsY	70	number of hits associated with YZ projection of track
dX	1.8 m	length of track along the x direction
dY	4.8 m	length of track along the y direction
dZ	1.2 m	length of track along the z direction
R2X	0.99	R value from linear fit to XZ projection
R2Y	0.99	R value from linear fit to YZ projection

Table 8.2: Track quality cuts applied to identified tracks from the window tracker algorithms. These cuts are designed to specifically select muon tracks with lengths and numbers of hits sufficient to compute reliable likelihood values for track direction.

bias sample are considered to be "signal" like in their track characteristics so that these efficiencies apply also to the upward-going tracks (i.e. the difference between upward and downward-going tracks are their timing distributions and dE/dx profiles, but not their physical extent or χ^2 distributions on the geometric fits). From these, it was determined the baseline track quality cuts, an overall 42% signal (track) reconstruction efficiency. Table 8.3 shows the effects of these cuts through the cosmic ray sample.

Cut	Initial # of events	Events after cut	Efficiency %
Track Length	37,902,972	16,805,471	– %
# of hits	16,805,471	16,185,372	96 %
# of hits/view	16,185,372	13,190,005	81 %
χ^2	13,190,005	12,378,344	93 %
χ^2/view	12,378,344	12,335,613	99 %
Track linearity/view	12,335,613	10,067,500	81 %
Length X, Y and Z	10,067,500	7,106,554	70%
Combined	16,805,471	7,106,554	42%

Table 8.3: Reconstructed track quality cut flow for cosmic-ray muon sample reconstructed with the window tracker. Data corresponds to the minimum bias cosmic data stream. We study efficiency relative to the number of events that pass the track length requirement.

Full distributions for each of these variables are shown in Appendix C for the cosmic muon study and in Appendix D.

8.5.2 Figure of Merit

A study of the figure of merit has been done to optimize the cut selection. The Figure of Merit is calculated as follows:

$$\text{FoM} = \frac{\text{Signal events after cut}}{\sqrt{\text{Background events after cut}}} \tag{8.2}$$

For each, all the other cuts (N minus one) at their lowest value were applied. The kinematic cuts results are shown in Table 8.4, while the timing cuts results, results are shown in Table 8.5. The variable distributions are shown in Appendix D. In choosing the lowest values for the study, the trigger cuts values are taken as the lower limit.

Variable	**I Cut**	**II Cut**	**III Cut**	**IV Cut**
Track Length	7 m	8 m	9 m	10 m
F.O.M.	9.5	9.15	9.0	8.8
Num. of hits	70	90	110	130
F.O.M.	9.5	9.3	9.0	8.5
Num. of hits in X	20	25	30	35
F.O.M.	9.5	9.0	8.4	8.0
Num. of hits in Y	20	25	30	35
F.O.M.	9.5	8.8	8.2	7.9
Length X	1.2 m	1.4 m	1.6 m	1.8 m
F.O.M.	9.5	9.55	9.6	9.6
Length Y	3.6 m	4 m	4.4 m	4.8 m
F.O.M.	9.5	9.7	9.8	9.9
Length Z	1.2 m	1.3 m	1.5 m	1.7 m
F.O.M.	9.5	9.5	9.4	9.4

Table 8.4: Figure of merit calculation, Eq. 8.5.2, for the kinematic variables

Variable	I Cut	II Cut	III Cut	IV Cut
χ^2	1.5	1.4	1.3	1.2
F.O.M.	9.5	7.9	6.3	4.3
$\chi^2\, X - view$	2	1.8	1.5	1.3
F.O.M.	9.5	9.4	8.8	8.2
$\chi^2\, Y - view$	2	1.8	1.5	1.3
F.O.M.	9.5	9.4	9.0	7.9
LLR	7	8	9	10
F.O.M.	9.5	9.0	8.6	8.5
LLRX	3	5	7	10
F.O.M.	9.5	8.3	7.5	7.0
LLRY	3	5	7	10
F.O.M.	9.5	7.8	7.0	6.4

Table 8.5: Figure of merit calculate from Eq. 8.5.2, for the timing variables

8.6 Directionality Determination

In addition to the basic quality cuts, several cuts are designed to select upward-going events, see Table 8.6.

Variable	Cut Value	Description
χ^2	1.5	Upward-going hypothesis fit
$\chi^2 X$	2	Upward-going hypothesis fit, X view
$\chi^2 Y$	2	Upward-going hypothesis fit, Y view
LLR	15	Log-Likelihood ratio
LLRX	10	Log-Likelihood ratio, X view
LLRY	10	Log-Likelihood ratio, Y view
ProbUp	0.0001	Probability of being upward-going

Table 8.6: Proposed sets of cut for the through-going upward-going muons analysis

8.6.1 Directionality Determination with Cosmic Rays Events

The efficiency for these cuts for upward-going muons can be estimated by inverting them and looking at their effect on downward-going cosmic-ray muons. In order to do that, clean up cuts are first applied on the sample and then each cut is applied separately. The estimated efficiencies for 10-m long muon tracks in Table 8.7.

Cut	Initial number of events	Events after cut	Efficiency %
Initial	3,045,992		
χ^2	3,035,985	3,020,806	99.5 %
$\chi^2\ X - view$	3,035,985	3,003,111	99 %
$\chi^2\ X - view$	3,035,985	3,003,155	99 %
ProbUp	3,035,985	2,806,669	92 %
LLR	3,035,985	3,003,097	99 %
LLRX	3,035,985	2,946,254	97 %
LLRY	3,035,985	2,771,769	91 %

Table 8.7: Efficiency of the cuts studied with the downward-going cosmic ray sample.

Fig. 8.20 shows how the LLR distribution changes as base cuts are applied. Actually, this is the inverted LLR:

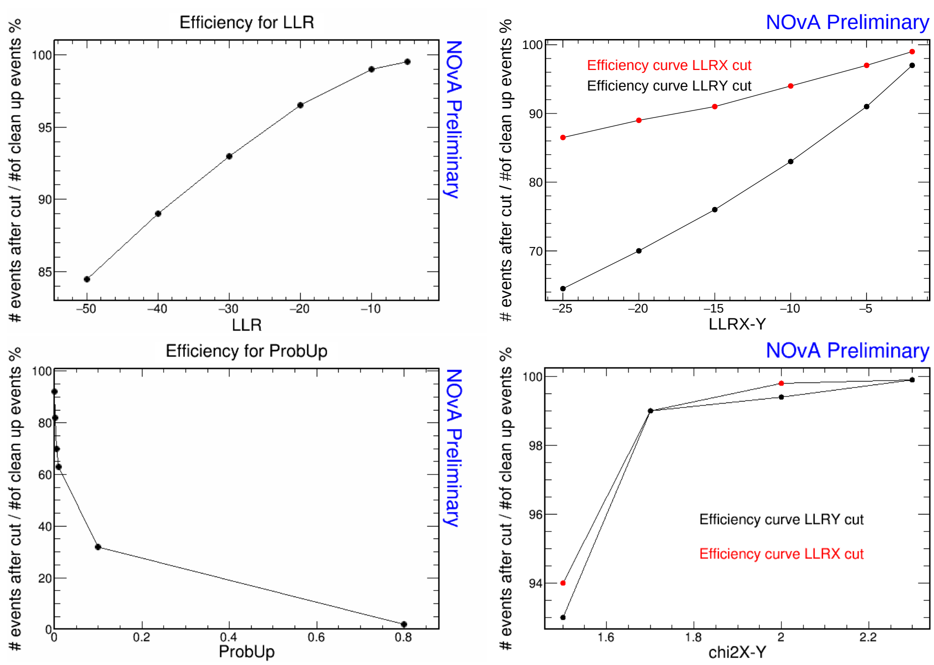

Figure 8.19: Efficiency scan for different cuts.Based on the results, we decided to apply a cut for $LLR > 10$,$LLRX - Y > 5$, $ProbUp > 0.0001$ and to loose the χ^2_X and χ^2_Y at 2

$$LLR_{invert} = Log(\frac{P_{\downarrow}}{P_{\uparrow}}) \tag{8.3}$$

Because it is the inverted LLR, downward-going tracks are represented by positive values on the Fig. 8.20. You can see that as the cleanup cuts are applied, especially track length, the LLR distribution becomes much more shifted to high values. For long tracks, > 10 m, the LLR can be used to select the correct direction of tracks with high confidence.

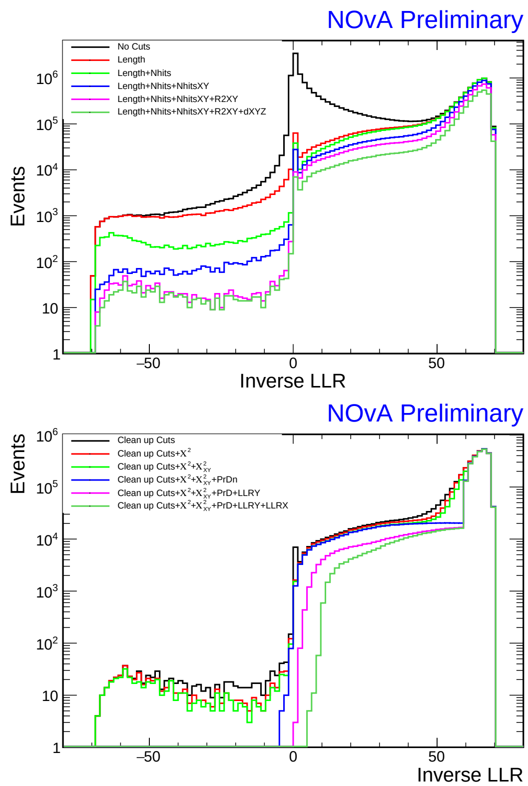

Figure 8.20: The figure shows how the LLR distribution varies as cleanup cuts are applied (top) and as timing cuts are applied (bottom). This is the inverted LLR distribution for the cosmic sample.

If the y-direction track length cut is relaxed, then tracks passing cleanup and timing cuts are predominantly horizontal or slightly upward-going, as shown in Fig. 8.21. The abundance of mostly-horizontal tracks in this subsample is explained by the position of the far detector on the surface. Slightly upward-going cosmic ray-induced muons may arise due to scattering or may penetrate the thin layer of the Earth's crust surrounding the NOvA detector hall. At steeper angles the Earth provides sufficient shielding from these upward-going cosmic ray muons, explaining the fall-off in the elevation angle distribution.

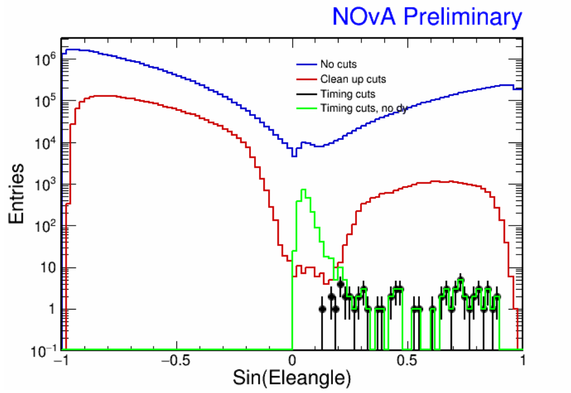

Figure 8.21: The distribution of sine of the elevation angle for each track in the timing-based candidate subsample (red) and all tracks including those excluded from the subsample (blue). Almost all candidates have an elevation angle near 0, indicating they are nearly parallel with the ground. A negative elevation angle indicates a downward-going track, while positive indicates an upward-going track. By cutting on the length of the track in the y-direction the near-horizontal cosmic-muon-induced background is eliminated.

Based on cosmic studies, inverting the LLR variable, as $LLR = log(\frac{Prob_{\downarrow}}{Prob_{\uparrow}})$, the efficiency of each timing cuts was calculated (see Fig. 8.19).

8.6.2 Elevation Cut

Below 10 degrees from the horizontal, the well-reconstructed cosmic component is virtually eliminated. By looking at the distribution of the upward-going muons day sample, it was clear that even after the timing cut, there were background events that were passing the selection.

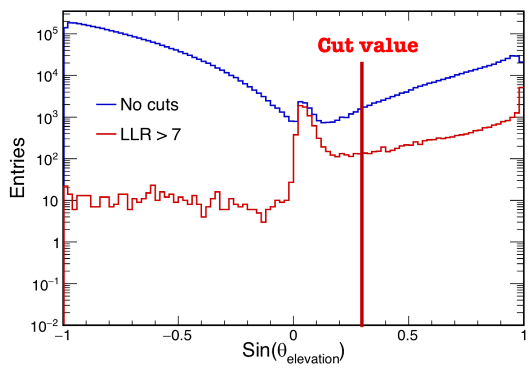

Figure 8.22: The elevation cut shown for the data, Ddupmu background sample.

Those events are mainly downward-going cosmic rays events that scatter on the rock surrounding the detector and go up. As it can be seen in the left plot in Fig. 8.22, one can reduce this background by adding a cut on the sine of the elevation angle at 0.3 . By looking at the Wimps distribution instead, in Fig. 8.23, can be notice that such a cut won't have a large effect on the signal events.

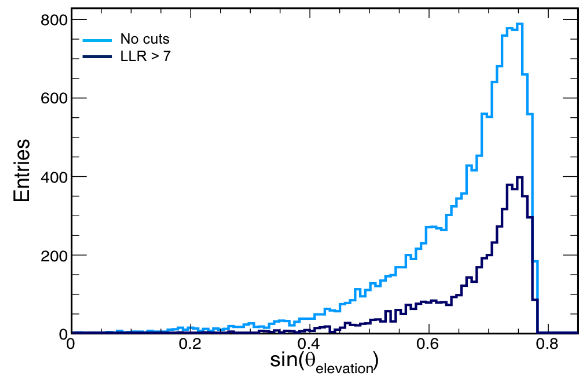

Figure 8.23: The elevation cut shown for the WIMPs 10 GeV tautau sample.

8.6.3 Proposed Set of Cuts

Based on all the study showed here and in Section 8.5, the following set of cuts were finally proposed, Table 8.8.

Variable Name	Variable	Final cut value
TrackLen	Length of the track	greater than 7 m
NHits	Number of hits per track	greater than 70
TrackHitsX	Number of hits in the X view	greater than 20
TrackHitsY	Number of hits in the Y view	greater than 20
dX	Length of the track in the X view	greater than 2 m
dY	Length of the track in the Y view	greater than 5 m
dZ	Length of the track in the Z view	greater than 1.2 m
R2X	Track linearity in the X view	greater than 0.99
R2Y	Track linearity in the X view	greater than 0.99
$\sin(\theta_{ele})$	Elevation angle of the track	greater than 0.3 rad
χ^2	Upward-going hypothesis fit	less than 1.5
$\chi^2 X$	Upward-going hypothesis fit, X view	less than 2
$\chi^2 Y$	Upward-going hypothesis fit, Y view	less than 2
LLR	Log-Likelihood ratio	greater than 15
LLRX	Log-Likelihood ratio, X view	greater than 10
LLRY	Log-Likelihood ratio, Y view	greater than 10
ProbUp	Probability of being upward-going	greater than 0.0001

Table 8.8: Proposed sets of cut for the through-going upward-going muons analysis

8.7 Background Studies

After applying all cuts, three main kind of events were found by eye scanning to compose the final background. The main physics background is given by the atmospheric neutrinos events, like in Fig. 8.24. This is an expected background, since the neutrino generated in the Earth's atmosphere happen isotropic through the 24 hours. At the NOvA Far Detector, one to three of those events are expected daily. Another source of background events is given by the downward-going cosmic ray muons that scatter up due to interactions, like in Fig. 8.25. Lastly, a huge part of the remaining background sample is made of events that due to a misreconstruction in which two unrelated but overlapping muon tracks create ambiguity in the reconstruction, as shown in Fig. 8.27.

8.7.1 Example of Background Events

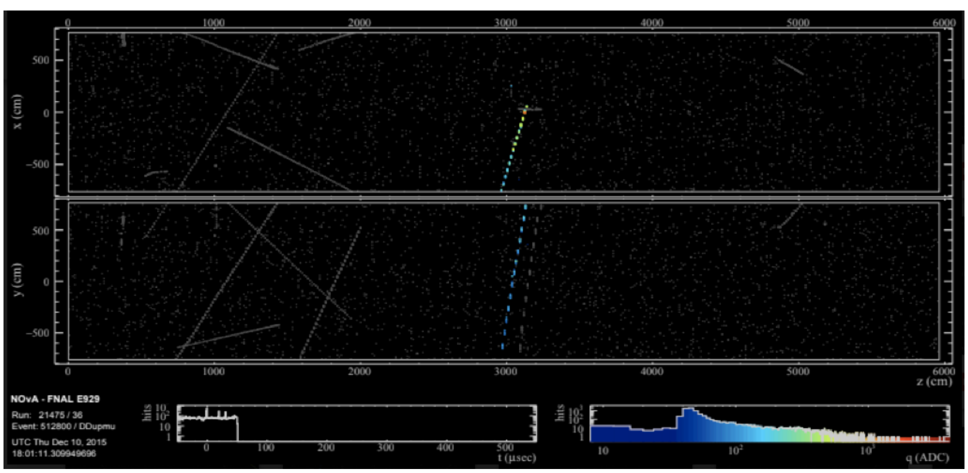

Figure 8.24: Example of an atmospheric neutrino event

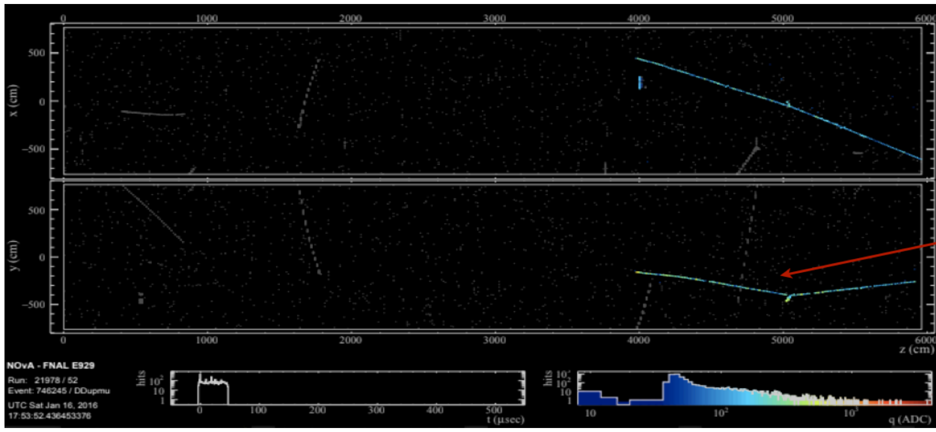

Figure 8.25: Cosmic ray muon from a side of the detector and scatter up

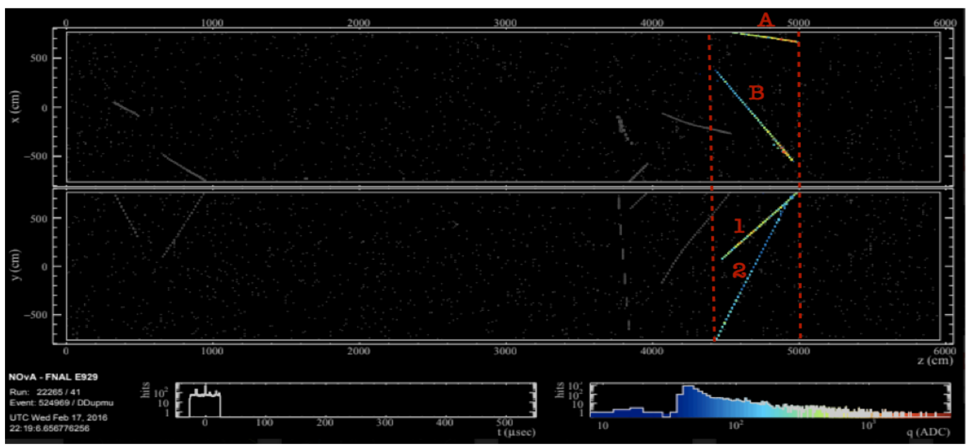

Figure 8.26: How would you pair it? A1-B2 or A2-B! ?

8.7.2 Misreconstructed Tracks

Possible solutions to eliminate this background have been considered (and tried, as shown in Appendix E). The first approach was to make sure that each slice contained only one track. The misreconstructed tracks that remain in the sample were the one mistakenly reconstructed as a single track by the algorithm. This is caused by reconstruction failures.

The solution for future analyses would be to implement a better reconstruction algorithm that would take care of those. We are still working on possible solutions to eliminate this kind of event. In this case, more than one track is associated with the same slice, and the misreconstruction seems to happen when those tracks have some overlapping.

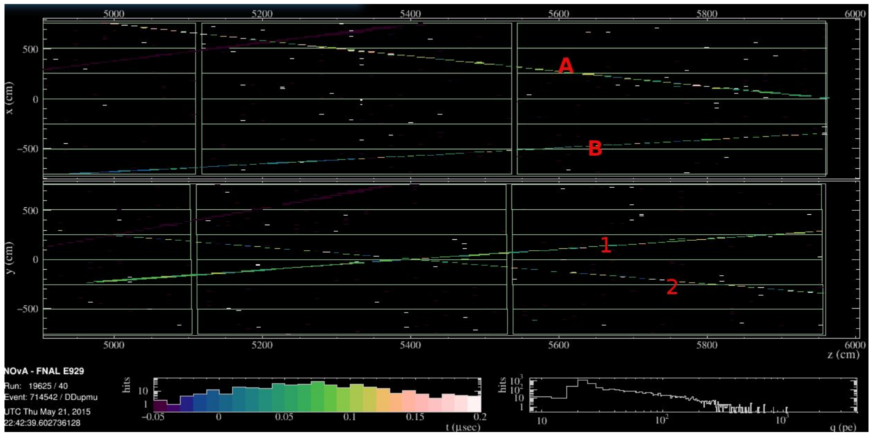

Figure 8.27: An example of an event that is prone to a possible misreconstruction. Note the two overlapping muon tracks (the two long colored lines in each plot) with similar extent in the z-dimension and near coincidence in time (hits are colored by time). The detector produces separate two-dimensional views of each event, and the 2D track objects from each view must be merged to produce a full 3D object. Cases such as this produce ambiguity in matching the 2D components between the views; is the correct matching (A1,B2) or (A2,B1)?

Chapter 9

Event Simulation

Anticipation is the heart of wisdom.

If you are going to cross a desert,

you anticipate that you will be

thirsty, and you take water.

Mark Helprin

This chapter gives an overview of the simulation done with the goal of better understanding the signal. The simulated signal has been used to study efficiency, acceptance, and cut optimization. Different tools have been used in this simulation. First of all, WIMPSIM [80], the most used WIMP Monte Carlo generator for neutrino telescope experiments. WIMPSIM was used to simulate the annihilation of DM particles in the Sun, SM particles' production, and their propagation outside the Sun till 1 AU. This process is represented in Fig. 9.1. At this point of the simulation, the flux drivers randomly place the neutrinos on a plane below the detector. The second step of the simulation was handled by GENIE [81], a framework for implementing neutrino event generators, and GEANT4 [82], a Monte Carlo toolkit to simulate the passage of particles through matter. GENIE simulates the neutrino flux interaction in the rock below the detector. Here GEANT4 takes care of the simulation of particles that leave hits in the detector. Lastly, the NOvA Transport and DAQ simulation provide a final output of simulated muon tracks that can be used for the analysis.

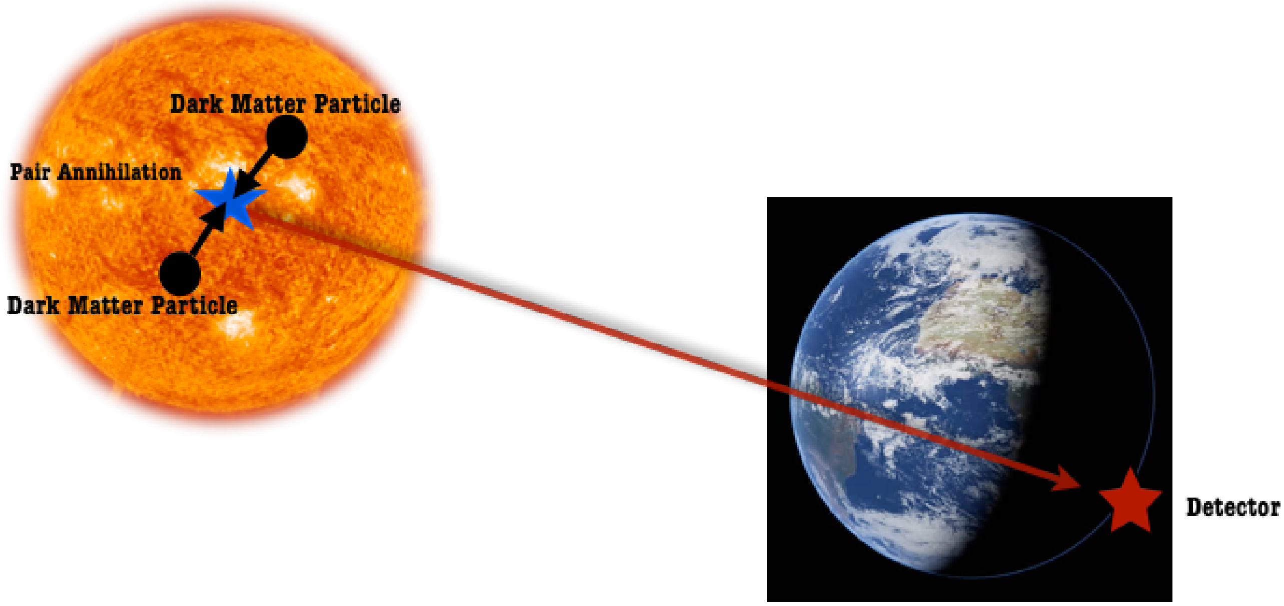

Figure 9.1: Cartoon representing the annihilation of DM particles in the Sun that produce SM Particles. Among the SM particles, there will be neutrinos that will travel until the Earth and interact in our detector.

9.1 WIMPs Simulation

As said before, the WIMPs annihilation in the Sun is handled by the WIMPSIM software [80]. WIMPSIM consists of two modules, *WimpAnn* and *WimpEvent*, here briefly explained.

9.1.1 WimpAnn

WimpAnn tackles DM particles' annihilation in the Sun, creating SM particles, and propagating the latest to 1 AU. Only neutrinos were selected as annihilation products in this analysis. This module requires different inputs like the annihilation channel, the energy of the center of mass of the DM particles to be simulated, the number of annihilation between DM particles, and the oscillation parameters.

The oscillation parameters used for these results are the ones reported in [83]. Only two annihilation channels were taken into account and studied here, a "soft" and a "hard" annihilation channel, $\tau^+\tau^-$ and $b\bar{b}$ respectively. For the energy of the center of mass, the focus was on the lower energy range since these energies correspond to the values at which the NOvA experiment could be more competitive with other experiments. After the events are generated, the code simulates the energy loss on the way out of the Sun.

9.1.2 WimpEvent

WimpEvent takes the neutrinos coming from WimpAnn and further propagates them in the detector. It includes the oscillation and the detector geometry and attaches a timestamp and weight to each event. Lastly, WimpEvent has been used to calculate the conversion factor. The conversion factor is used to transform the limit on the flux into a cross-section limit, as shown in Chapter 11.

9.1.3 Event Distributions of WIMPSIM Simulation

Different tests were done to demonstrate that the simulation was running correctly using the $\chi \to \nu_\mu - \bar{\nu_\mu}$ channel. The first cross-check compared the distribution obtained with the NOvA simulation with the one of the WimpSim website, shown in Fig. 9.2. The different distributions compared were found to match.

9.1.4 Energy of the WIMPSIM Simulation

The second cross-check is related to the maximum energy that the produced neutrino could inherit. Based on the model one wants to probe, WimpSim allows one to choose different parameters. The energy of the DM particle candidates, the annihilation channel, and the plane where the neutrino arrive are vital for the simulation. In

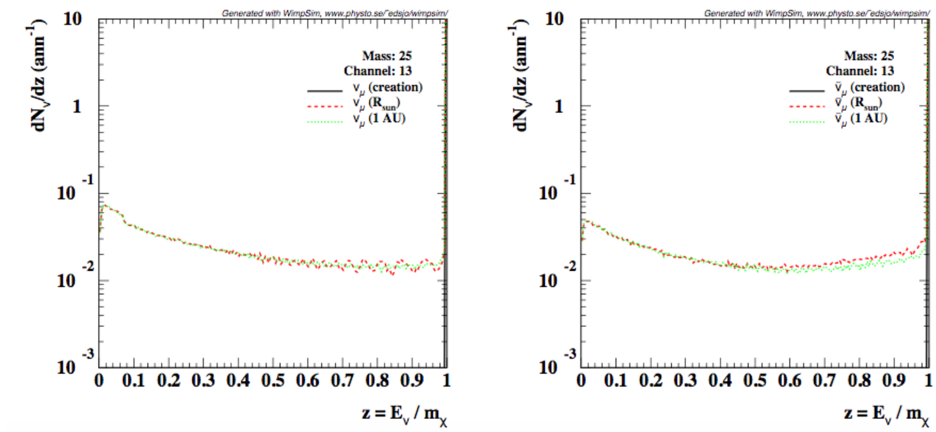

Figure 9.2: Antineutrino and Neutrino fluxes at 1 AU for the $\nu_\mu - \bar{\nu_\mu}$ for 25 GeV WIMP mass [94].

this analysis, a range of mass for the DM particles from 4 GeV to 50 GeV was probed, annihilating and subsequently producing the SM particles $\tau^+\tau^-$ and $b\bar{b}$. In the $\tau^+\tau^-$ annihilation channel, these particles can further decay, producing neutrinos, through the processes $\tau- > \mu + \nu + \bar{\nu}$ and $\mu- > e + \nu + \bar{\nu}$. The process is shown in Fig. 9.3. The maximum energy that these neutrinos could inherit is computed from the energy of the parent particles.

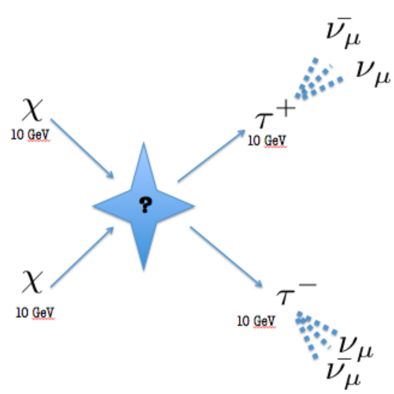

Figure 9.3: Cartoon of the simulated DM annihilation process with production of SM particles ($\tau^+\tau^-$) that will subsequently decay in neutrinos

In particular, in a three particle decay if two daughter particles are massless, the maximum momenta of all daughter particles coincide. In the rest frame of the mother particle, the maximum momenta it will be:

$$p_{max} = \frac{1}{2M}\sqrt{[M^2 - (m_1 + m_2 + m_3)^2][M^2 - (m_2 + m_3 - m_1)^2]}, \tag{9.1}$$

where in the tau decay M is the τ mass, m_1 is the muon mass, m_2 is the muon neutrino mass, m_3 is the tau neutrino mass, $M = 1.77$ GeV, $m_1 = 0.106$ GeV, and $m_2 = m_3 = 0$. The result is a maximum momentum value of $p_{\nu,max} = \pm 0.885$ GeV and $E_{\nu,max} = 0.885$ GeV for each particles in the rest frame of the tau.

One can also obtain the maximum momentum in the lab frame where the tau has an energy of $\tau = 10$ GeV (taking 10 GeV as an example). To calculate the relativistic momentum, one can use the relation:

$$E^2 = (p \times c)^2 + (m_0 \times c^2)^2 \tag{9.2}$$

where m_0 is the rest mass of the particle, from which one can compute

$$p = \sqrt{E^2 - m_0} \tag{9.3}$$

where $c = 1$, and obtain $p_\tau = 9.841$ GeV.

Using the relativistic momentum one can calculate the velocity of the particle in the lab frame:

$$\beta_\tau = \frac{p_\tau}{E_\tau} = 0.9841 \tag{9.4}$$

and from the relation $E = \gamma mc^2$,

$$\gamma_\tau = \frac{E_\tau}{m_\tau} = 5.627 \tag{9.5}$$

In the end, applying the Lorentz boost from the rest frame of the tau to the lab frame one can calculate the energy and the momentum (E^*, p^*) viewed from a frame moving parallel with velocity β_τ

$$\begin{pmatrix} E^* \\ p^*_\parallel \end{pmatrix} = \begin{pmatrix} \gamma_\tau & -\gamma_\tau\beta_\tau \\ -\gamma_\tau\beta_\tau & \gamma_\tau \end{pmatrix} \begin{pmatrix} E \\ p_\parallel \end{pmatrix} \tag{9.6}$$

that gives

$$\begin{cases} E^* = \gamma_\tau(E - \beta_\tau p_\parallel) \\ p^*_\parallel = \gamma_\tau(p_\parallel - \beta_\tau E) \end{cases} \tag{9.7}$$

giving two solutions. In the same direction as the tau boost ($p_\nu = +0.885$ GeV), $E^* = 0.079$ GeV and $p^*_\parallel = 0.079$ GeV, while in the opposite direction of the tau boost ($p_\nu = -0.885$ GeV), $E^* = 9.881$ GeV and $p^*_\parallel = -9.881$ GeV.As shown in Fig. 9.4, the final distribution of the neutrino energy is perfectly compatible with what has been calculated.

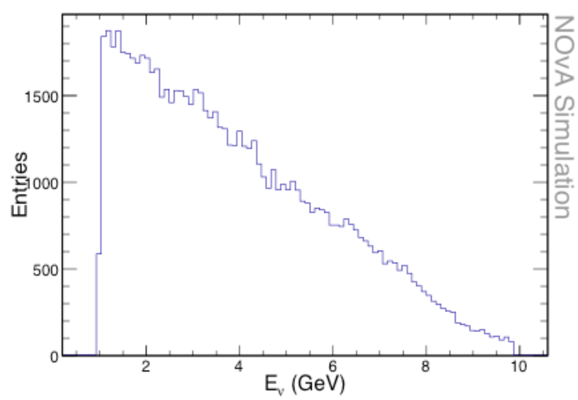

Figure 9.4: Energy distribution of the neutrinos produced by the decay of a 10 GeV τ particle.

9.1.5 Time of the WIMPSIM Simulation

Another essential feature in our simulation is time. It is crucial to simulate at least one round year of events since different effects are due to the distance between the Sun and the Earth that changes during the year (see Fig. 9.5) and the fact that the Earth's axis is tilted 23.5 degrees with respect to the Sun (see Fig. 9.6).

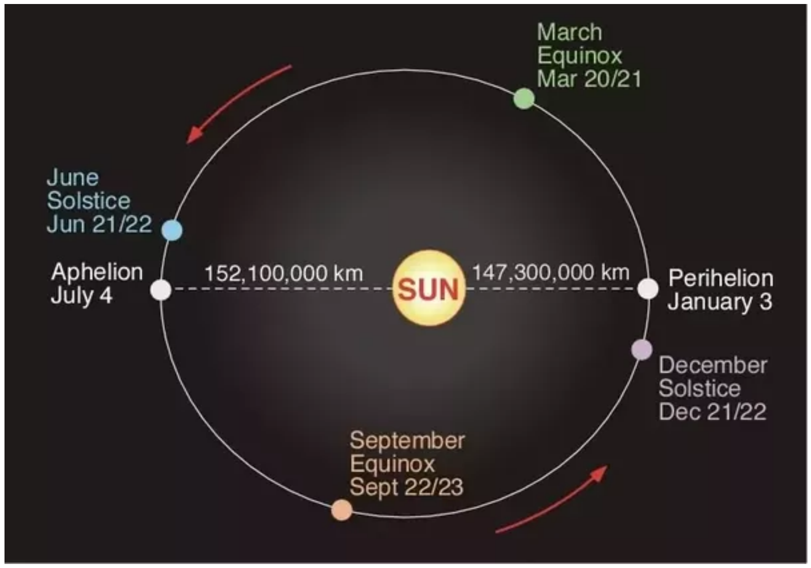

Figure 9.5: The distance between the Sun and the Earth changes during the year. This change will affect the number of WIMP events reaching the detector. Image Credit: [84].

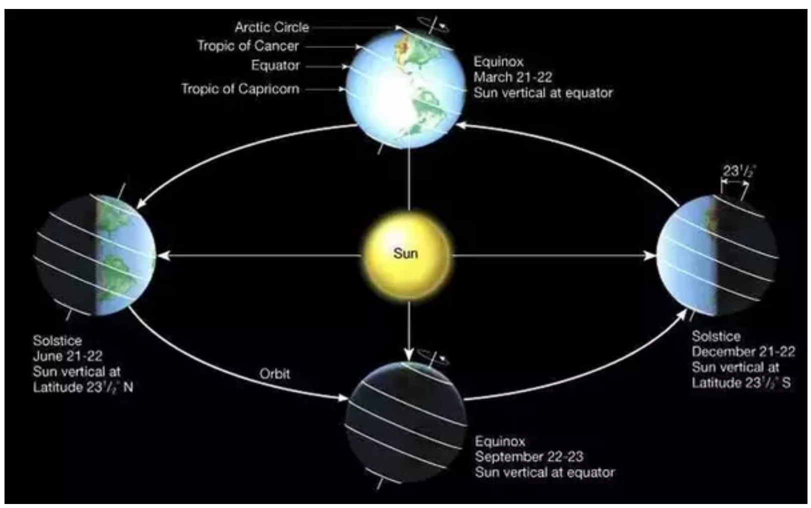

Figure 9.6: The Earth's tilted axis will result in a different number of upward-going muon events during different time of the year. Image Credit: [85].

WimpSim accounts for the changing distance between Sun and Earth by applying a weight to the neutrino flux. During the summer, the distance increases while it decreases during the winter. This effect can be seen in the number of events that varies after applying a weight of a factor of ten, see Fig. 9.7, as expected.

The Earth's tilted axis will also affect the number of downward and upward-going

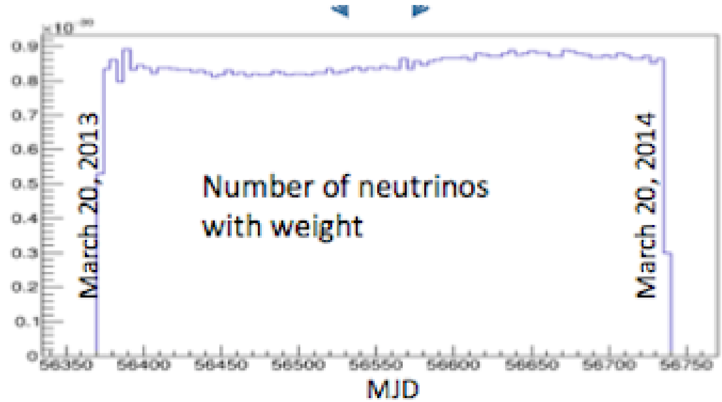

Figure 9.7: The simulated number of neutrinos in one year is just a flat distribution. To take into account the changing distance between the Aphelion and the Perihelion position, WIMPSIM calculates a weight to apply to the number of events. The result is a 10% effect in the distribution of the number of events, as expected

neutrino events that will reach the detector in one year. The different exposure to the Sun that the detector has during summer or winter will increase the number of upward-going muon events from the Sun during winter when the days are much shorter in the Northern Hemisphere and vice versa. The results of the simulation can be seen in Fig. 9.8.

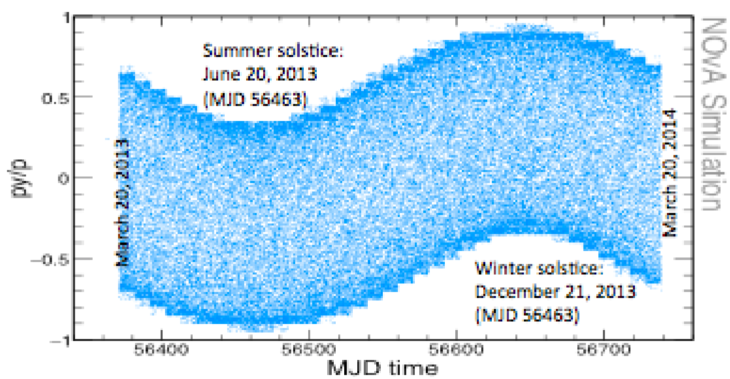

Figure 9.8: The tilted axis of the Earth affects the number of upward or downward neutrinos that reach the detector. In this plot, the variable $p_y/p = sin(-elevation)$ gives us information about the upward or downward nature of the event, where +1 corresponds to upward-going events -1 to downward. During the winter, when the days (in the Northern Hemisphere) are shorter, one will have more upward-going events, coming from the Sun, than during the summer.

9.1.6 WIMPSIM Plane and NOvA Coordinates

The last important parameter to choose in WimpSim is the plane's positioning where the neutrino will arrive and its size. It is also essential to optimize the neutrino energy with the y position to ensure that the daughter muon will have enough energy to reach the detector and leave a track inside. Taking into account that the energy loss is $\frac{dE}{dx} = 4\,\frac{MeV}{cm}$ in the rock and $\frac{dE}{dx} = 2\,\frac{MeV}{cm}$ in the liquid scintillator of the detector, the minimum plane position was chosen to be of approximately 23 m for the 10 GeV tau simulation. Instead, the x and z positions should be chosen to be wide enough to allow for all possible incidence angles. Since one does not select a horizontal track, there is also a maximum width allowed. Examples of the arrival plane are shown in Fig. 9.9 and Fig. 9.10.

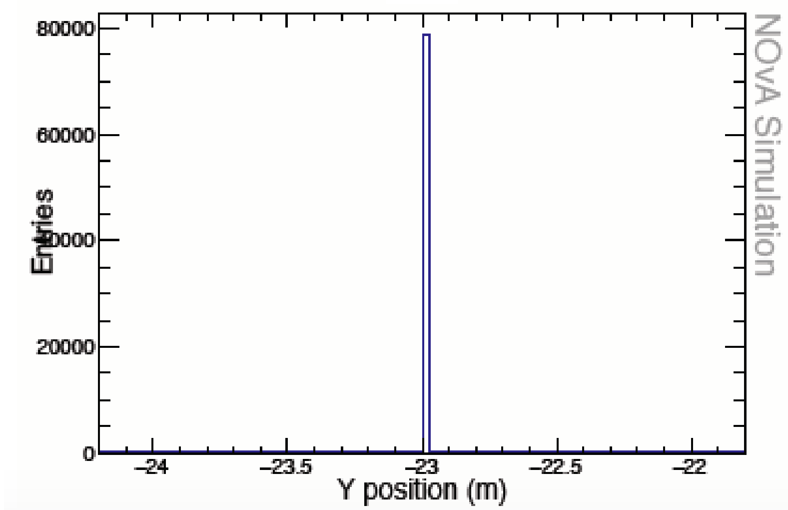

Figure 9.9: Arrival Y position of the plane. The Y position has to be chosen taking into account the energy of the simulated neutrinos, such that the majority of the particle will have enough energy to reach the detector considering the energy lost by the muons when traveling in a medium (either rock or liquid scintillator)

NOvA coordinates differ from the actual coordinates, so in order to have a consistency between the WimpSim simulation and the GENIE simulation, it is essential to correct the azimuthal angle that indicates the true North by 332 degrees to match

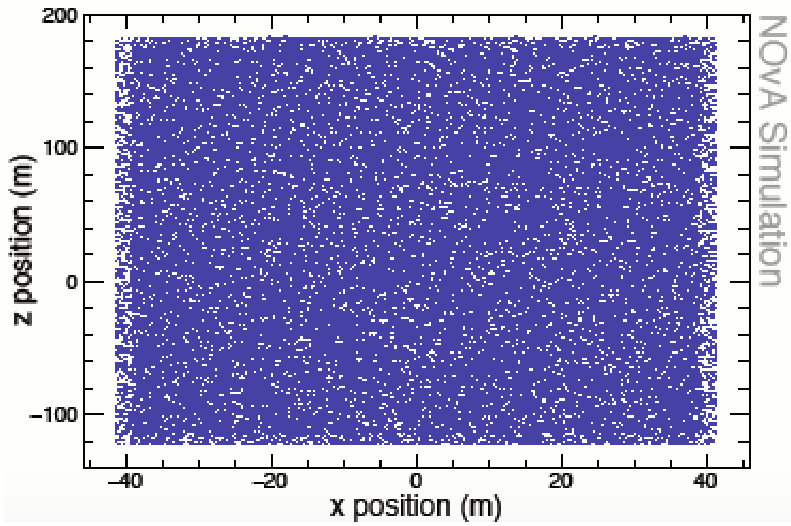

Figure 9.10: Arrival XZ plane of the neutrino events. This plane has to be big enough to include all the possible elevation angle of the muon in the simulation

the NOvA true North, as shown in Fig. 9.11.

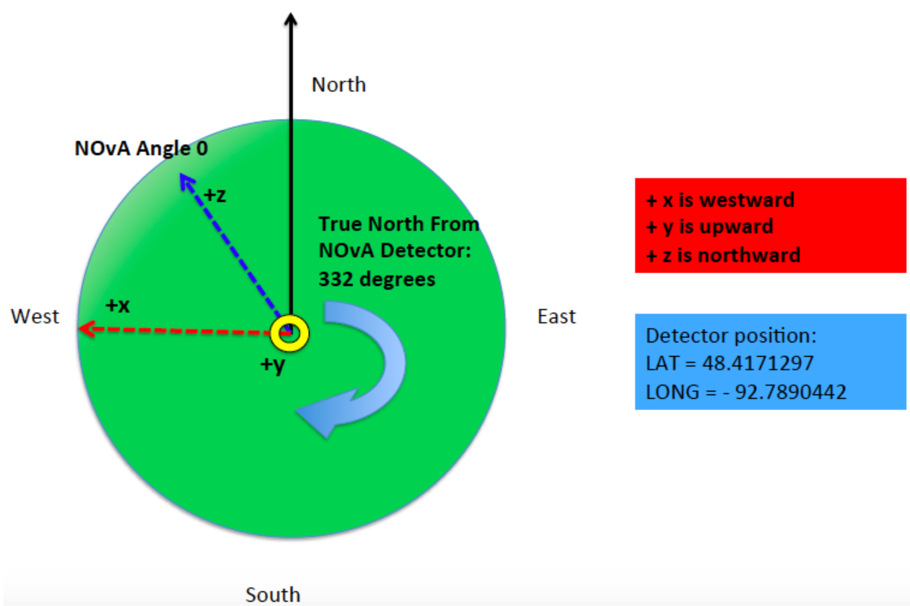

Figure 9.11: Nova coordinate for the Nova Far detector.

9.2 Detector's Simulation

Three steps have to be done to simulate a NOvA event: the event generation, the simulation of the physics process it undergoes, and the readout system's simulation.

9.2.1 GENIE for v Interaction

GENIE (Generates Events for Neutrino Interaction Experiment) is the event generator used to simulate neutrino interaction. The advantage of using GENIE is that it makes the interaction process much faster than GEANT4 alone because it has pre-calculated the neutrino cross-section data. The event generation drivers can be instructed to load the pre-computed data and estimate the cross-section by numerical interpolation rather than by performing numerous CPU-intensive differential cross-section integrations.

GENIE is made of three products, but the only one used was the Generator for this analysis. The Generator includes different tools (such as the flux driver, detector geometry, and the event reweight engine) and is used to simulate the complex experimental setup and support generator-related analysis. The fluxDriver used is called the *GSimpleNtpFlux*, and it is a kind of flux driver suitable for the simple ntuple-based flux that WimpSim provides.

As an input, it requires the particle flavor, four-momentum and position, the initial state (i.e., neutrino and nucleus information), the process that occurred, and the action (e.g., inter-nuclear scattering). Data files with neutrino flux created within the WimpSim package were provided. GENIE uses these files as a source of neutrinos.

After configuring GENIE with a neutrino source, it must propagate them through a geometry representing the detector to decide where the interactions occur and the target material. Generally, geometry represents the detector's environment, such as the detector's hall, and in our case of the rocks surrounding the detector.

GENIEHelper is the glue between GENIE and the ART software, the software used for analysis in NOvA. In the GENIEHelper geometry package, one can configure the desired detector position and where it wants the interaction to happen.

In the simulation a particular geometry, called *rockbox*, was used. The geometry, shown in Fig. 9.12, includes as much surrounding rock as needed. When generating events in the rock surrounding the detector, one is interested in events that have the potential to make it into the detector (like events that are energetic enough to reach the detector), so they can leave a signal that can be readout. The box has a minimum size and scales depending on the energy of the individual neutrino. To correctly calculate these event rates, the geometry is scanned to determine the material's maximum path lengths.

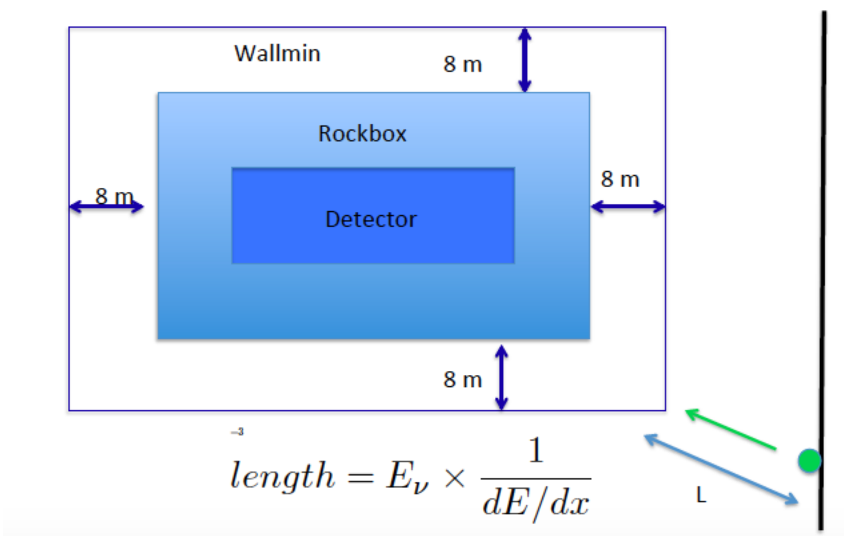

Figure 9.12: GENIE rockbox cartoon. GENIE extends the box size whence the neutrino is coming by. This extension is proportional to the energy of the incoming neutrino.

9.2.2 Understanding GENIE Events

At first, every kind of interaction is simulated. This includes Neutral Current (NC) and Charge Current (CC) interactions, where the NC are approximately 18 %

of the total simulated interactions. An example of NC interaction coming from a WimpSim neutrino can be seen in Fig. 9.13.

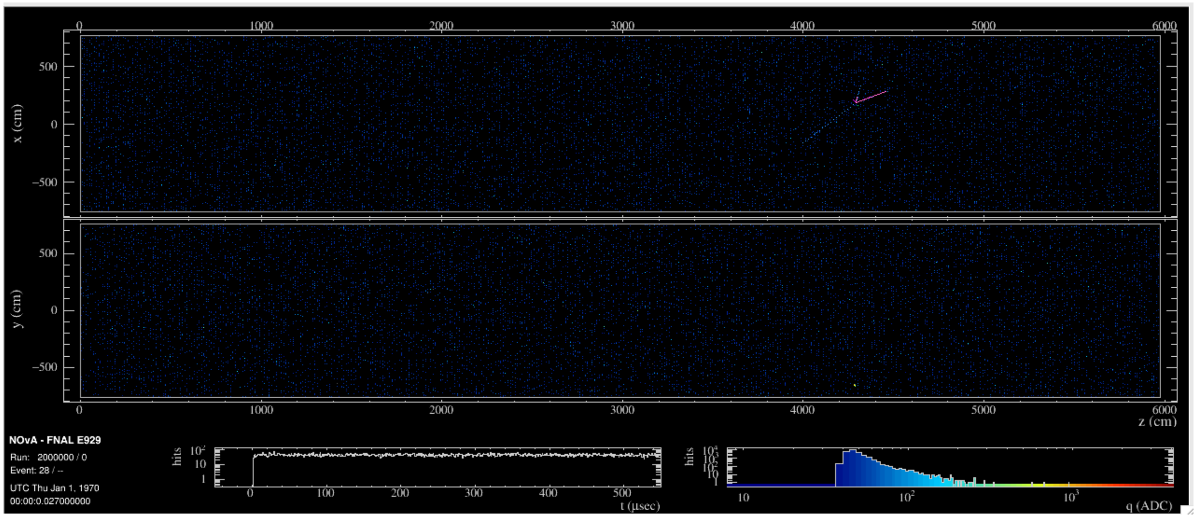

Figure 9.13: Simulated NC interaction in the detector.

When a cut on the track length is required, none of these interactions remain in our final sample. Therefore they were not included in the simulation.

Among the CC interactions, the neutrinos will undergo Quasi-Elastic (QE), Meson Exchange Current (MEC), Deep Inelastic Scattering (DIS), and Coherent interactions. The main contributions, for the energy values of interest, are given by DIS, then RES and QE processes as can be seen in Fig. 9.14.

If one compares the finding with the theoretical expectation [86], excellent agreement between the simulation and the neutrino energy theory was found in the range between a few to 10 GeV.

9.2.3 Producing FLSHits Using Geant4

Geant4 is used to propagate particles that come out of GENIE through geometry, also taking care of the physics processes such as energy loss (ionization), hadronic and electromagnetic interaction, multiple scattering, and decay. In particular, it takes care of the ionization in the active volumes that could generate a detectable signal. NOvA

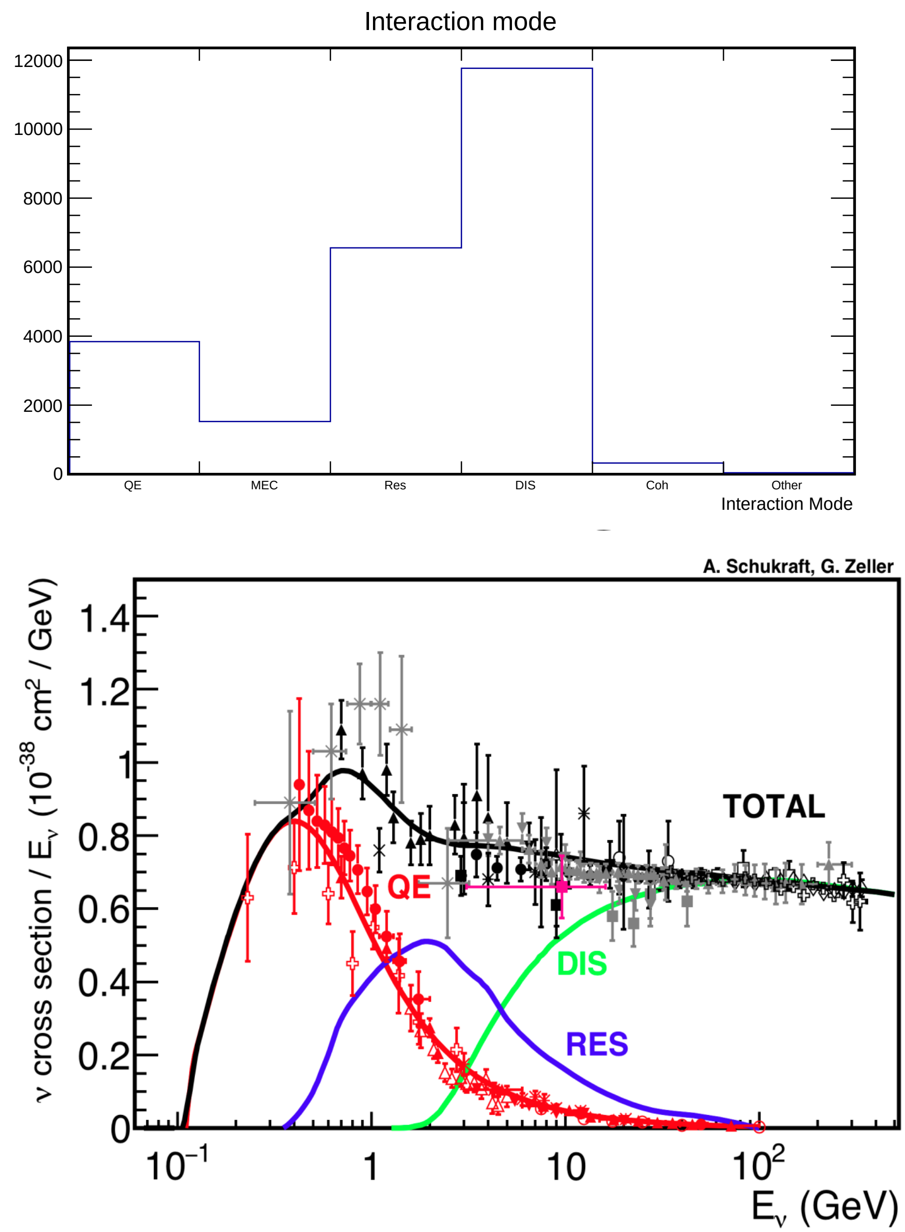

Figure 9.14: Interaction modes in the simulation and in the reference [86]. The simulation was done using 10 GeV. In the first plot, each bin represents a different interaction mode, and the y-axis the count of events for each of these interaction modes. The proportion of events agrees with what is expected from the theory for 10 GeV neutrinos, as can be seen in the second plot.

uses a data structure, FLSHit (Fiber Liquid Scintillator Hits), to record the signal information.

The default assumption regarding how the particles are propagated and interact in NOvA is the so-called *QGSP Bert*, where the Bertini cascade is used for primary protons, neutrons, pions, and kaons with energy less than 10 GeV. In addition to that, Users Actions can be added to the processing. Geant4 comes with "users hooks" that allow users to perform special tasks at the beginning and end of runs, events, tracks, steps. By using *UserActionManager*, each set of user tasks are separated into their class. The two Users Actions used in this simulations are: *FLSHitListAction* and *ParticleListAction*.

In the *FLSHitListAction*, for each particle position and time, the particle trajectory inside the detector is associated. The first check is that each particle has enough energy to leave a hit in the liquid scintillator cell, while for the low energy ones, the tracking is stopped. For each hit in the cell, the energy deposition considers Birks constant and the Cerenkov loss, and the momentum is also calculated.

ParticleListAction figure out the parentage of the particle with track ID, what process is making the track, and skips events that are not from CC interaction. The ancestors and descendants are found for each particle, while those that did not enter the detector are removed. The particles that pass the selection are written to a list. In this list, the track ID, the PDG code, the kind of process, the mother, the mass, and the polarization are stored.

To check that the interactions and the resulting particles were handled correctly by GEANT4, the daughter muon information was analyzed to discover possible anomalies, for example, if the daughter muon's energy had much higher energy than the parent's neutrino energy. Alternatively, if the parents' neutrino and the muons' angle were high in energy, the daughter will likely follow the parents' direction for high energy particles. Because one expects these events to be mainly upward-going muons, the muons' direction along the y axis can give hints.

9.3 Upward-Going Muons Analysis Simulation

The simulation's last step corresponds to running the reconstruction and the analysis tool on the data files generated by the GENIE and GEANT4. The angle between different reconstructed muon variables (like the direction), and the accurate MC information for the same events, was analyzed to check that the reconstruction was carried out correctly.

As can be seen in Fig. 9.15, the discrepancy between the two seems to be negligible. After the reconstruction, the analysis tools (from the UpMu analysis package) were applied to the signal events to get information on the track's directionality and the Sun's position. The first one is crucial in this analysis since it is used as the main discriminant against the downward-going muon events, so it will be necessary to compare signal and downward-going events. At the same time, the second one is important because the neutrino signal events will be coming precisely from the direction of the Sun but also as a cross-check to make sure that the timing in the simulation is well synchronized between all the simulation steps (WIMPSIM, GENIE, and GEANT4). Each neutrino event is associated with a simulated time over a user-chosen range and is used to extrapolate the Sun position. So selecting only upward-going events, one can confirm that the Sun position was expected below the horizon, under the detector. The last critical step involves the variable used to discriminate the WIMPs signal, which is the angle between the sun position and the incoming track. The muons will mainly follow the direction of the neutrinos that come in a straight line from the Sun position, expecting the signal to be peaked at the highest value of the cosine angle between the track and the Sun, $cos(\Delta\theta_{Sun,trk})$, while expecting the main physical background, the atmospheric neutrinos events, to have a flat distribution.

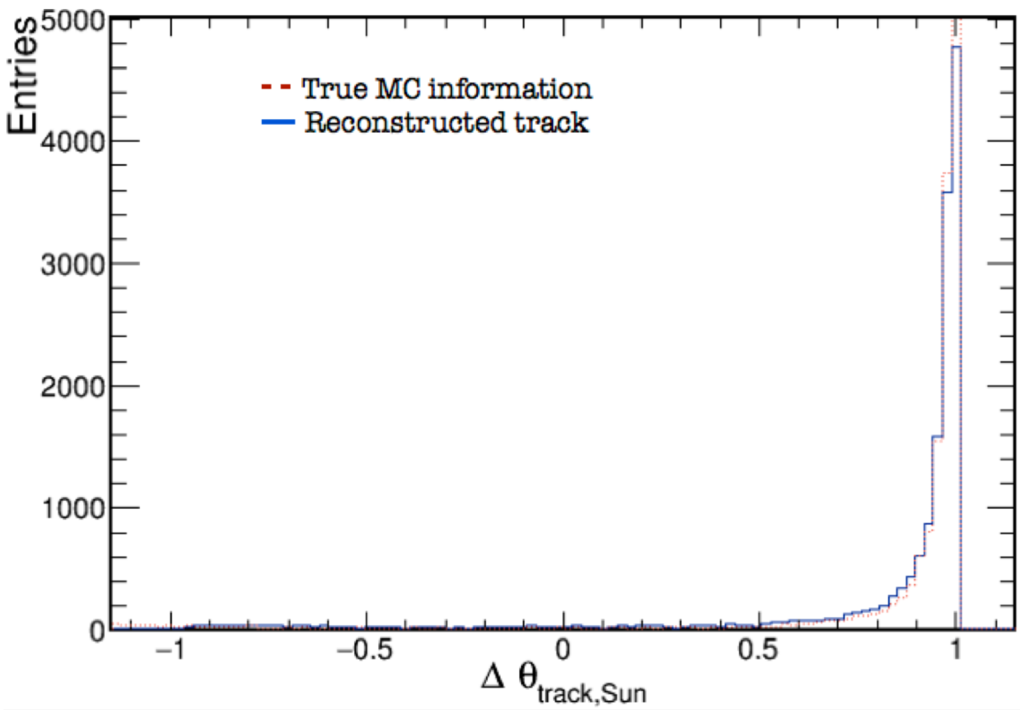

Angle between the Sun and the outgoing muon track.

Figure 9.15: Angle between the Sun and the outgoing muon track for the simulated upmu. This variable will be used as the final discriminant in the analysis. A good agreement between the MC information and the reconstruction it is important to trust the reconstruction process.

Chapter 10

Uncertainties in the Upward-Going Muon Analysis

Various sources of uncertainties need to be considered to set upper limits on cross-sections from the search for neutrinos coming from WIMP annihilation in the Sun. These can be divided into two major categories: uncertainty associated with the signal hypothesis and uncertainty associated with the estimated background. Following the same approach as the Super K and Baksan experiments [70, 92], the uncertainties associated with the signal hypothesis can be grouped into three categories: uncertainties associated with the annihilation model, uncertainty in the neutrino propagation, and uncertainty in the detection.

10.1 Uncertainties in Solar WIMP Signal

The three main signal systematic categories are summarized below and will be estimated in this chapter.

A) **Uncertainties on the annihilation rate in the Sun**: These uncertainties include astrophysical, particle, and nuclear uncertainties. They only affect the flux's normalization, so they need to be taken into account to convert from neutrino flux to a capture rate but are common to all the indirect WIMP searches.

Therefore, one can use the uncertainties already estimated by Super K. A study was performed to double-check that the results were compatible [88, 89].

B) **Uncertainties on the Neutrino Flux related to Neutrino Propagation From Sun to the detector**: These systematic uncertainties are estimated within DARKSUSY and WimpSim packages [90, 91].

C) **Uncertainties related to the flux measurement at the detector**: This last set of uncertainties needs to be explicitly studied for the NOvA detector.

For both WIMPs indirect search and direct detection experiments, the signal's strength depends crucially on either the spin-independent and spin-dependent WIMP-nucleon scattering cross-section. So, as the neutrino signal from the Sun searched for by neutrino telescopes depends strongly on these cross-sections, one can use these searches to put limits on the same scattering cross-sections. One needs to consider the Sun's capture, the subsequent annihilation, production of neutrinos, propagation, interaction, and oscillation of neutrinos, and finally scattering near the neutrino telescope to produce observable muons.

10.1.1 Uncertainties on the Annihilation Rate in the Sun

At equilibrium, the annihilation rate is solely determined by the capture rate ($\gamma_A = \frac{1}{2}\Gamma_C$), so one can use uncertainty on annihilation rate to group all uncertainty related to capturing and annihilation process.

The solar model and the form factor uncertainties are relevant for the spin-independent search only. In this first search, a limit will be put only on the spin-dependent cross-section for which NOvA is sensitive. See Section 11.11 for the results. The solar model uncertainty is small for the spin-dependent scattering, as this occurs on hydrogen, whose abundance in the Sun is well known.

Another systematic uncertainty is given by the gravitational effects from the planets, and in particular, Jupiter, reducing the capture rate, . If the WIMP's orbit reaches out to Jupiter, there is a large probability that Jupiter will affect the orbit and disturb it so that it no longer passes through the Sun and eventually throws the WIMP out of the solar system back into the Milky Way halo. This uncertainty is counterbalanced by the solar gravitational diffusion uncertainty, such that they cancel each other and are determined to be negligible.

The other two critical sources of uncertainty are the local dark matter density, particularly relevant since the capture rate depends linearly on the WIMPs' local DM halo and velocity distribution. Even if the local DM uncertainty is the heaviest and one of the most relevant when talking about DM, it affects all the experiments (including the direct direction experiment) in the same way, so it does not influence the relative interpretation of the results. Because of this, it is standard procedure not to include this uncertainty. Lastly, the uncertainty related to the velocity dispersion and circular velocity is smaller for smaller WIMP masses, like the masses used in this search.

These sources of uncertainty are summarized in Table 10.1.

10.1.2 Uncertainties on the Neutrino flux

The uncertainties on the neutrino flux are related to neutrino oscillation and absorption effects and neutrinos' regeneration in the Sun. These effects are fully implemented in DarkSUSY. The parameters are used to determine the flux of neutrinos in the simulation. Absorption is relevant for neutrinos above 100 GeV, well above the mass of interest for this search. The main effects of neutrino oscillations are the adequate mixing of muon and tau neutrinos during the propagation to the solar surface and the consequent mixing of electron neutrinos during the propagation from the surface of the Sun to the Earth.

Variable	Value (%)	Reference
Form factor	No spin-dependent	arXiv:0903.2986
Solar model	3% 10 GeV 3% 50 GeV	arXiv:0903.2986
Local DM density	Factor of 2 in the capture rate (same for all searches, doesn't affect the relative interpretation)	arXiv:1503.04858 arXiv:0903.2986
Dynamic of Solar System (Jupiter depletion) solar gravitational diffusion	Cancel each other Determined to be negligible	arXiv:1107.3182
Velocity distribution function and the orbital speed of the Sun and tail of DM halo	20% 20 GeV 40% 200 GeV	arXiv:1503.04858 arXiv:0903.2986

Table 10.1: Total uncertainties in the capture rate due to uncertainties of astrophysics, nuclear and particle physics for spin-dependent scattering

Several systematic errors are considered for oscillation parameters and matter effect inside the Sun and the Earth, as summarized in Table 10.2.

Variable	Value (%)	Reference
3 flavor oscillation parameters	8% τ^+ τ^- 5% bbar	arXiv:1301.1138v2
$\Delta\theta_{2,3}$	0.5%	Cross check
Neutrino interaction in the Sun	10 %	arXiv:1410.2008
Matter effect in the Earth	10 %	arXiv:1410.2008

Table 10.2: Uncertainties related to neutrino oscillation and matter effects.

Cross section uncertainties

For the cross-section systematic uncertainties, all the uncertainties that will only increase the total neutrino-nucleon cross-section are excluded because they will amplify the signal and lead to a more stringent upper limit. Thus the limits for low masses are conservative. These uncertainties are those from Baksan [70] and are summarized in Table 10.3.

Variable	Value (%)	Reference
Cross section	10 % 10 GeV χ 4% 1 TeV	arXiv:1301.1138v2

Table 10.3: Summary of cross section uncertainties.

10.1.3 Uncertainties of the Flux Measurement at the Detector

As mentioned earlier, these uncertainties need to be studied within the NOvA environment. In particular, the focus is on the ones that could affect the analysis's timing (and the tracks' direction). The uncertainties are summarized in Table 10.4 and are described in detail below. It is worth noting that these uncertainties are small compared to the theoretical uncertainties and have a small effect on the final result.

Variable	Value (%)	Reference
Timing resolution function	1%	Our own study
PE shift	2%	Our own study
Timing shift	7%	Our own study
Overlay	1%	Our own study
Smearing resolution	1%	Our own study
Trigger	1%	Our own study

Table 10.4: Summary of uncertainties related to the flux measurement at the detector.

Systematic Studies on Resolution function

The first uncertainty investigated is the one on the resolution function.

Since a different resolution function was used for data and MC,a check on the effect on the acceptance of using the wrong resolution function was performed. If the simulation were perfect, the resolution function in the data and MC would be the same. The resolution function's difference provides a measure of how far off the simulation is from the detector and should yield a conservative estimate of this imperfection's maximum impact. This result is significant because the timing resolution function determines the error associated with each hit on a track and so it becomes very relevant when one wants to fit all the hits on a track to determine whether the particle is upward or downward-going since the interest is only in upward-going tracks.

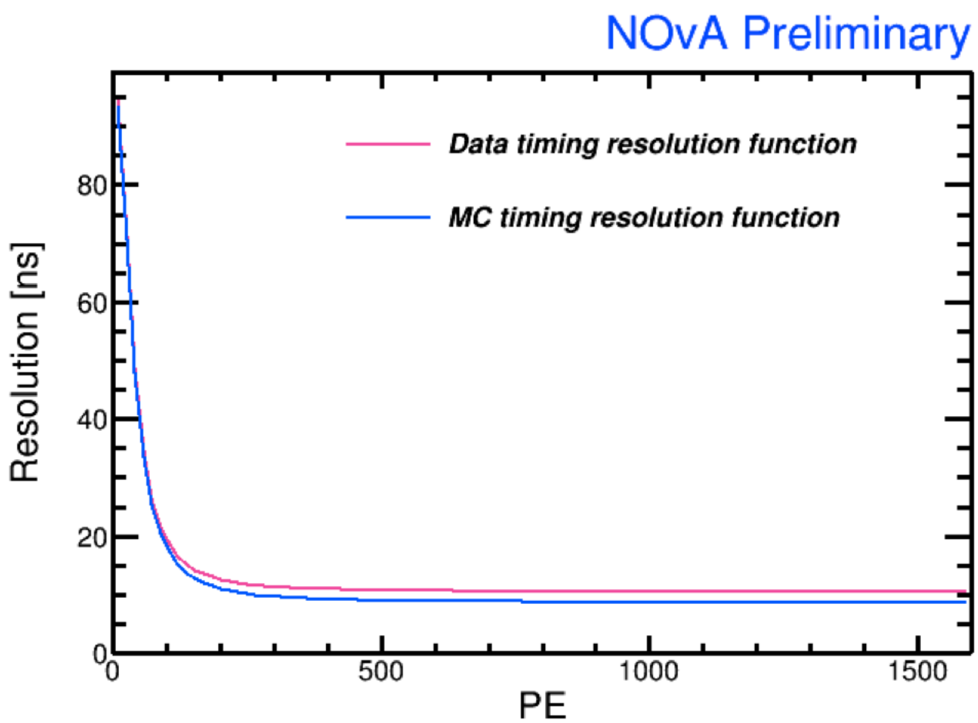

Figure 10.1: Resolution function for data and MC.

In order to estimate this uncertainty, the data resolution function was used on the signal MC and the acceptance change were measured. The data set used for this study is made up of WimpSim data files of $\tau^+\tau^-$ interactions, including CC only events for 10 GeV DM mass., The two slightly different resolution functions for data and MC are:

$$165143/(1882.9 + pow(PE, 2.11447)) + 10.4321 \tag{10.1}$$

$$163551/(1847.39 + pow(PE, 2.10082)) + 8.65312 \tag{10.2}$$

Using the first one instead of the second one on MC events gives us the results in Table 10.5. It can be seen the total shift in the acceptance is about 1%, as reported in Table 10.4.

Cut Flow	**# of entries**	**Wrong function**
	14039	14039
Passed Length > 7m	6260	6260
Passed Nhits > 70	5986	5986
Passed TrackHitsX > 20	5884	5884
Passed TrackHitsY > 20	5821	5821
Passed LengthX > 2m	4456	4456
Passed LengthY > 5m	2755	2755
Passed LengthZ > 1.2 m	2600	2600
Passed R2X > 0.99	2521	2521
Passed R2Y > 0.99	2029	2029
Passed Chi2 < 1.5	1956	2000
Passed Chi2X < 2	1950	1997
Passed Chi2Y < 2	1950	1997
Passed LLR > 7	1866	1875
Passed LLRX > 3	1832	1831
Passed LLRY > 3	1694	1683

Table 10.5: Effect of changing time resolution function.

Systematic Studies on Photo-Electrons

The second uncertainty investigated is related to the number of photo-electrons (PE) in a track. The study aimed to determine what happens if the calibration and scintillation light is shifted since the shift will result in a different PE for each hit. The oscillation and cross-section analysis does not explicitly express this uncertainty in terms of PE, but the closest value one can use is used for absolute hadronic energy scale (5% uncertainty), so that is the value used for the scaling. The largest value was chosen to be conservative.

This study is that the timing resolution function used in this analysis for each hit is calculated based on the PE value of that hit, so a value different from the nominal one will affect the acceptance. In order to estimate this uncertainty the PE value in the timing resolution function was shifted, adding and subtracting 5% of the nominal PE value. The data set used for this study is made up of WimpSim files, including only CC events and 10 GeV DM mass.

Shifting the PE values by $\pm 5\%$ gives the results shown in Table 10.6. It can be seen the total shift in the acceptance is about 2%, as reported in Table 10.4.

Cut Flow	**# of entries**	**PE 5% up**	**PE 5% down**
	14039	14039	14039
Passed Length > 7m	6260	6260	6260
Passed Nhits > 70	5986	5986	5986
Passed TrackHitsX > 20	5884	5884	5884
Passed TrackHitsY > 20	5821	5821	5821
Passed LengthX > 2m	4456	4456	4456
Passed LengthY > 5m	2755	2755	2755
Passed LengthZ > 1.2 m	2600	2600	2600
Passed R2X > 0.99	2521	2521	2521
Passed R2Y > 0.99	2029	2029	2029
Passed Chi2 < 1.5	2000	2001	1828
Passed Chi2X < 2	1997	1997	1822
Passed Chi2Y < 2	1997	1996	1821
Passed LLR > 7	1875	1876	1769
Passed LLRX > 3	1831	1824	1747
Passed LLRY > 3	1683	1661	1645

Table 10.6: Effect of shifting PE. The data set used for this study is made up of WimpSim files, including only CC events and 10 GeV DM mass.

Systematic Studies of the timing resolution function

In this case, what happens if there is a shift from the real value in the hits' time resolution simulation was studied. This check is essential for this analysis because the hits' time determines the tracks' direction, the main discriminant. A difference in the χ^2 distribution of the hit timing fit in the data, and the MC was observed.

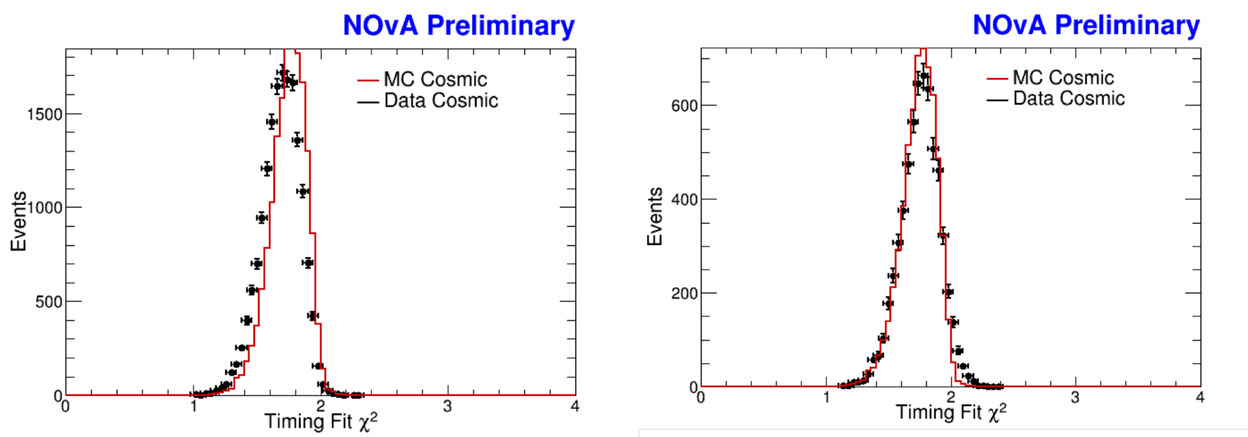

Figure 10.2: Cosmic ray sample Old gain, after upmu selection cuts. In the first plot, there is the original distribution; in the second plot, there is the new distribution, now matching, after the shift

The hit time was smeared such that the χ^2 distribution for Data and MC in cosmic rays agrees. A Gaussian function with mean zero and standard deviation equal to 7 ns was used to spread the hit time for MC in the UpMu analysis module. The signal was finally analyzed to see how it changes the acceptance when smearing the timing by this additional amount.

The data set used for this study is made up of Wimpsim files, including only CC events and a 10 GeV DM mass. The procedure gives the results shown in Table 10.7. It can be seen that using the wrong function causes a total shift in the acceptance of about 7%, as reported in Table 10.4.

Systematic Studies on the angle $\theta_{2,3}$

To double-check the validity of using the same results from the study that Super-K did, one of their studies was replicated, shifting the nominal value of $\theta_{2,3}$ in simulation by one sigma. $\theta_{2,3}$ was investigated since one knows from SuperK that this has a more significant effect on the flux normalization.

Cut Flow	# of entries	Wrong function
	14039	14039
Passed Length > 7m	6260	6260
Passed Nhits > 70	5986	5986
Passed TrackHitsX > 20	5884	5884
Passed TrackHitsY > 20	5821	5821
Passed LengthX > 2m	4456	4456
Passed LengthY > 5m	2755	2755
Passed LengthZ > 1.2 m	2600	2600
Passed R2X > 0.99	2521	2521
Passed R2Y > 0.99	2029	2029
Passed Chi2 < 1.5	1956	1803
Passed Chi2X < 2	1950	1794
Passed Chi2Y < 2	1950	1791
Passed LLR > 7	1866	1723
Passed LLRX > 3	1832	1690
Passed LLRY > 3	1694	1568

Table 10.7: Effect of time smearing. The data set used for this study is made up of Wimpsim files, including only CC events and a 10 GeV DM mass.

In order to do this, the simulation was remade from the beginning using a different value of $\theta_{2,3}$, where the nominal one is $\theta_{2,3} = 40.686$ and the 1 sigma shifted value is $\theta_{2,3} = 49$. The same analysis module was then used for reconstruction and applied to the data set created with the nominal value and the shifted value to measure acceptance change. The data set used for this study is made up of WimpSim files of $b\bar{b}$ interactions, including only CC events and a 10 GeV DM mass.

The results are shown in Table 10.8. There is a difference of approx 5% in the acceptance, in excellent agreement with the Super-K results.

Systematic Studies with Cosmic Overlays

In this case, what happens if one overlays cosmic rays on the detector's upward-going muon events were studied.

The detector is on the surface, and it has a high rate of cosmic rays. A sample of WIMPs was simulated and overlayed with a sample of real data cosmic rays to study

Cut Flow	**# of entries**	**Shifted $\Delta\theta_{2,3}$**
	33598	32538
Passed Length > 7m	14926	14383
Passed Nhits > 70	14208	13801
Passed TrackHitsX > 20	13950	13541
Passed TrackHitsY > 20	13816	13397
Passed LengthX > 2m	10526	10160
Passed LengthY > 5m	6497	6245
Passed LengthZ > 1.2 m	6085	5865
Passed R2X > 0.99	5887	5671
Passed R2Y > 0.99	4706	4539
Passed Chi2 < 1.5	4555	4378
Passed Chi2X < 2	4553	4375
Passed Chi2Y < 2	4552	4371
Passed LLR > 7	4354	4189
Passed LLRX > 3	4264	4100
Passed LLRY > 3	3966	3767

Table 10.8: Effect of shifting $\theta_{2,3}$. The data set used for this study is made up of WimpSim files of $b\bar{b}$ interactions, including only CC events and a 10 GeV DM mass.

this effect's size. Then the analysis cuts were applied, and a final check was done on the number of events selected. The results are shown in Table 10.9.

The table shows that while the effect is initially substantial, once one applies all selection criteria to the two samples, a similar number of events is left. The effect of the LLR cut is shown in Fig. 10.3. The total shift in the acceptance is about 1%, as given in Table 10.4. Further details on this study can be found in [69].

Systematic Studies on Smearing Resolution

Different effects can smear the angle between the Sun and the outgoing muon track. The neutrino comes exactly from the Sun's direction, while the muon track at the detection point will have an angle greater than zero. If there was no angle between the Sun's position and the track, one could quickly identify a muon coming straight from the Sun.

In this study, a comparison of the correct MC information for the neutrino coming

Cut Flow	Wimps	Wimps plus Overlay
	2483	81458
Passed Length > 7m	1158	48061
Passed Nhits > 70	1129	46947
Passed TrackHitsX > 20	1120	46773
Passed TrackHitsY > 20	1112	45311
Passed LengthX > 2m	1072	44078
Passed LengthY > 5m	877	38773
Passed LengthZ > 1.2 m	868	38437
Passed R2X > 0.99	866	38376
Passed R2Y > 0.99	835	36199
Passed Chi2 < 1.5	835	35973
Passed Chi2X < 2	833	35837
Passed Chi2Y < 2	833	35795
Passed LLR > 7	686	684
Passed LLRX > 3	619	622
Passed LLRY > 3	496	501

Table 10.9: Effect of adding the cosmic overlay background to the simulated WIMPs sample.

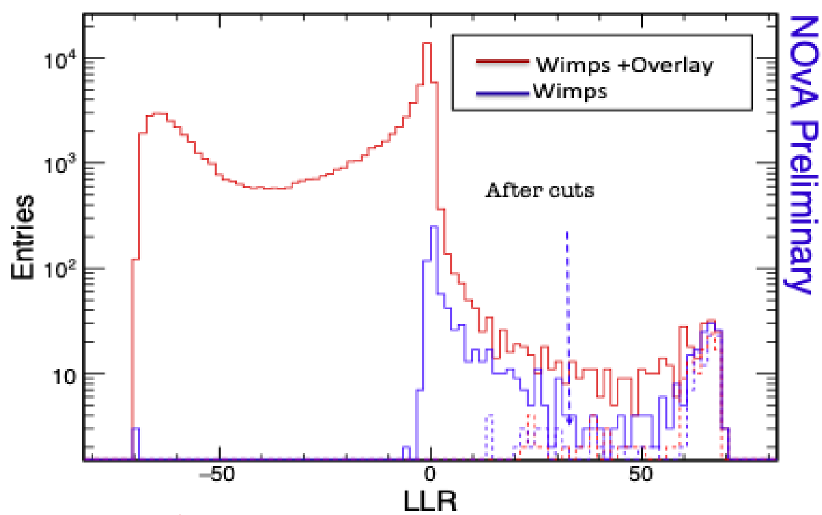

Figure 10.3: LLR distribution for Wimps and Wimps+overlay sample. The dotted lines represent the two distributions after cuts.

in a straight line from the Sun with the reconstructed information of the final muon track was made to see how much they differ. As shown in Fig. 10.4, there is a shift of ≈1% that is included as systematic in the signal sample. Further details on this study can be found in [69].

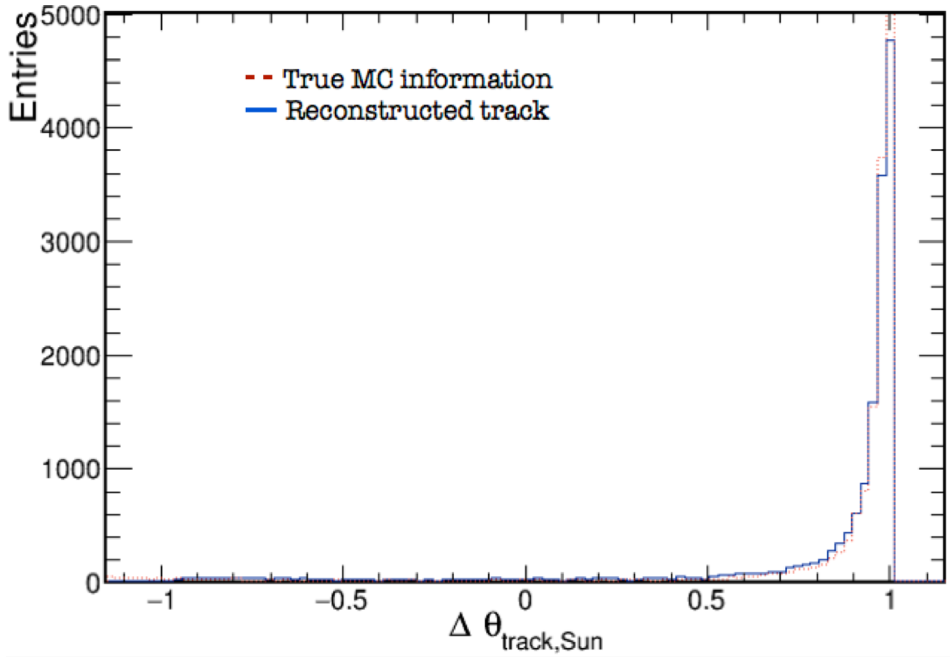

Figure 10.4: Angle between the track and the Sun position for True MC neutrino and reconstructed muon tracks.

10.1.4 Total Systematic for Signal

To summarize, the complete list of systematic uncertainties that are going to be included in the signal is presented in Table 10.10.

10.2 Systematic Errors on the Background

As a reminder, the day region will be used for background estimation. Once the live-time for three different regions is estimated, the number of events in the background sample/live-time is counted, and the number of background events one expects in the signal sample is measured. This results in an entirely data-driven background estimation. The advantage of using a data-driven background estimation is that the main uncertainty, in this case, will come from the statistical limitation of the background control region. The total number of background events expected in

Systematic	Value 10 GeV	Value 50 GeV
Solar model	3%	3%
Velocity distribution function and the orbital speed of the Sun and tail of DM halo	19%	23%
3 flavor oscillation parameters	8% $\tau^+\tau^-$ 5% $b\bar{b}$	$\tau^+\tau^-$ 5% $b\bar{b}$
Neutrino interaction in the Sun	10%	10%
Matter effect in the Earth	10%	10%
Cross section	10%	10%
Trigger	1%	1%
Timing resolution function	1%	1%
PE shift	2%	2%
Timing shift	7%	7%
Overlay	1%	1%
Smearing resolution	1%	1%
TOT	42%−40%	44%−42%

Table 10.10: Summary of all signal systematic uncertainties for the two simulated signal hypothesis $\tau^+\tau^-$ and $b\bar{b}$.

the signal region will have an uncertainty associated with it that follows the Poissonian statistics. Besides this statistical uncertainty, the only other effect that could change the number of expected events in the signal region, which happens at night, are due to possible difference with the day samples. For this reason, studies using cosmic rays collected during the day and the night have been done, see Chapter 8 for more information. The only difference observed between the day and night samples was a 2% effect in the distribution of the angle between the sun and the tracks.

This bias is caused by temperature/density differences between the Earths atmosphere in the day and night samples. The muons attenuate a little bit differently in the day and night sample, and therefor the muon energy distribution reaching the detector is a little bit different in these two sample. Regardless of the source, a two-percent bias represent a very small effect compared to our statistical limitations [69]. The uncertainties are summarized in Table 10.11.

Variable	Value (%)	Reference
Bin-to-Bin statistic	$\sqrt{Events}$	
Day-night Cosmic rays	2%	Nova docdb15862-v2

Table 10.11: Summary of uncertainties related to background.

Chapter 11

Results

I am not very clever but I am very stubborn and this is the proof.

Diani Patito

The first Dark Matter search result, using the full data set collected with the upward-going muon trigger in NOvA, is presented here. The upward-going muon trigger is used first to select high-quality muon tracks and estimate directionality using each track's hits' timing information. By doing so, the cosmic ray background flux is suppressed by more than a factor of 10^5 at the trigger level to a rate of approximately 1 Hz. Additional offline selection criteria optimize the search. Only upward-going muons that point to the Sun have been selected. For this reason, the search occurs at night when the Sun is on the other side of the Earth, and the day sample can be used for the data-driven background estimate. This strategy also allows the time when the Sun is near the horizon as a control region to check the background estimate. Ultimately, implementing a cut-based and maximum likelihood analysis provided a powerful tool for rejecting background and selecting a sample of neutrino-induced upward-going muons.

11.1 Final Data Set and Live-time

The total data set of the upward-going-muon analysis utilized in this thesis included approximately three years of data. The total live-time for the three primary analysis regions can be seen in Table 11.1. Each of the regions is based on the Sun's position. The night sample, with which the potential signal is associated, has the longest live-time, collecting few more months of day. The longer live-time is since fewer data taking interrupting activity happens at night, like maintenance activity or detector shut down.

Region	**Total live-time (s)**	**Total live-time (years)**
Day	34609255	≈ 1.1
Twilight	17844133	≈ 0.6
Night	40290970	≈ 1.3
Total	92744358	≈ 3

Table 11.1: Total live-time of upward-going muon data used in this analysis. In total approximately 3 years of data have been used.

11.1.1 Live-Time Normalization Factor

A normalization factor needs to be applied to compare the number of events in different regions. This correction takes into account the different live-times of the different regions. As previously described, each region has registered a different amount of data due to the region's size, possible malfunctions, or shutdowns of the detector for maintenance. The live-time was calculated for each region by adding each data file's total duration per region (in seconds). One can then normalize with the ratios shown in Table 11.2.

The number of background events observed in the day region multiplied by the live-time normalization factor will give the final number of expected background events

Region	Live-time correction	Live-time correction
Twilight	$\frac{\text{twilight live}-\text{time}}{\text{day live}-\text{time}}$	0.5
Night	$\frac{\text{night live}-\text{time}}{\text{day live}-\text{time}}$	1.2

Table 11.2: Live-time correction per region. The total live-time for each region can be find in Table 11.1

observed in the twilight and signal region:

$$\text{Expected number of events} = (\text{Background events}) \times (\text{live} - \text{time correction}) \quad (11.1)$$

11.2 Final Cut Flow

The final sample of events is selected based on specific properties of the data described above. A stringent set of cuts has been applied to the variables that identify and discriminate a muon from other particles and subsequently maximize the likelihood that the selected event contains an upward-going muon and not a downward-going muon. The final values chosen for each of the variables are shown in Table 11.3. Because the signal is not expected to contribute to the day region, the number of events detected in this region can be used to estimate the number of background events in the night (signal) region.

11.3 Final Number of Background Events

The cut flow described in Section 11.2 has been applied to the day (background) region. The results are shown in Table 11.4. These events represent an irreducible background, a set of upward-going muon events that leave the same trace and have precisely the same characteristics as the signal events coming from Dark Matter particles annihilating in the Sun's core.

Variable	Final cut value
Length of the track	greater than 7 m
Number of hits per track	greater than 70
Number of hits in the X view	greater than 20
Number of hits in the Y view	greater than 20
Length of the track in the X view	greater than 2 m
Length of the track in the Y view	greater than 5 m
Length of the track in the Z view	greater than 1.2 m
Track linearity in the X view	greater than 0.99
Track linearity in the X view	greater than 0.99
Elevation angle of the track	greater than 0.3 rad
Timing hypothesis fit	less than 1.5
Timing hypothesis fit, X view	less than 2
Timing hypothesis fit, Y view	less than 2
Log-Likelihood ratio	greater than 15
Log-Likelihood ratio, X view	greater than 10
Log-Likelihood ratio, Y view	greater than 10
Probability of being upward-going	greater than 0.0001

Table 11.3: Final cut values for the discriminant variables chosen in the analysis to eliminate background events from signal events

Variable	Final number of bkg events
After kinematic cuts	2409908
Timing hypothesis fit	1415363
Timing hypothesis fit, X view	1380426
Timing hypothesis fit, Y view	1375574
Log-Likelihood ratio	13057
Log-Likelihood ratio, X view	9267
Log-Likelihood ratio, Y view	125
Probability of being upward-going	75
Final number of background events	75

Table 11.4: Final number of background events.

11.3.1 Background Composition

The 75 background events found in Table 11.4 leave precisely the same trace and have precisely the same characteristics as signal events coming from Dark Matter particles annihilating in the core of the Sun. Because these upward-going events are collected during the day, when the Sun is high in the sky, they cannot originate in the Sun. Instead, they are a composition of atmospheric neutrinos, muon scattering on the rock outside the detector, and going up, and some misreconstructed events. The composition is shown in Table 11.5.

Background composition	**Percentage %**
Clean upward-going track	53
Double track due to algorithm mismatch	30
upward-going track due to interaction	17

Table 11.5: Final background events composition estimated by visual inspection.

For double tracks due to algorithm mismatch, a series of extra cuts were put in place to eliminate some of them, but an irreducible background is still left. As shown in Fig. 11.1, these tracks happened simultaneously in adjacent positions and were reconstructed as only one track. If the lower track happened a few nanoseconds earlier, it would be taken as the starting point, and it will subsequently be reconstructed as an upward-going track, see Appendix E.

11.4 Twilight Predictions and Observations

The twilight region provides a critical check of the data-driven background method used in the analysis. The events observed in the twilight region can be compared to the number of predicted events in the twilight region to test the approach's accuracy and add confidence in predicting the signal region's background events. The correction described in the Section 11.1.1 is

$$\mathrm{live-time\ correction} = \frac{17844133}{34609255} \approx 0.5 \tag{11.2}$$

and therefore

$$\text{Expected number of events} = 75 \times 0.5 \approx 38 \tag{11.3}$$

The number of events follows a Poisson distribution, and the statistical uncer-

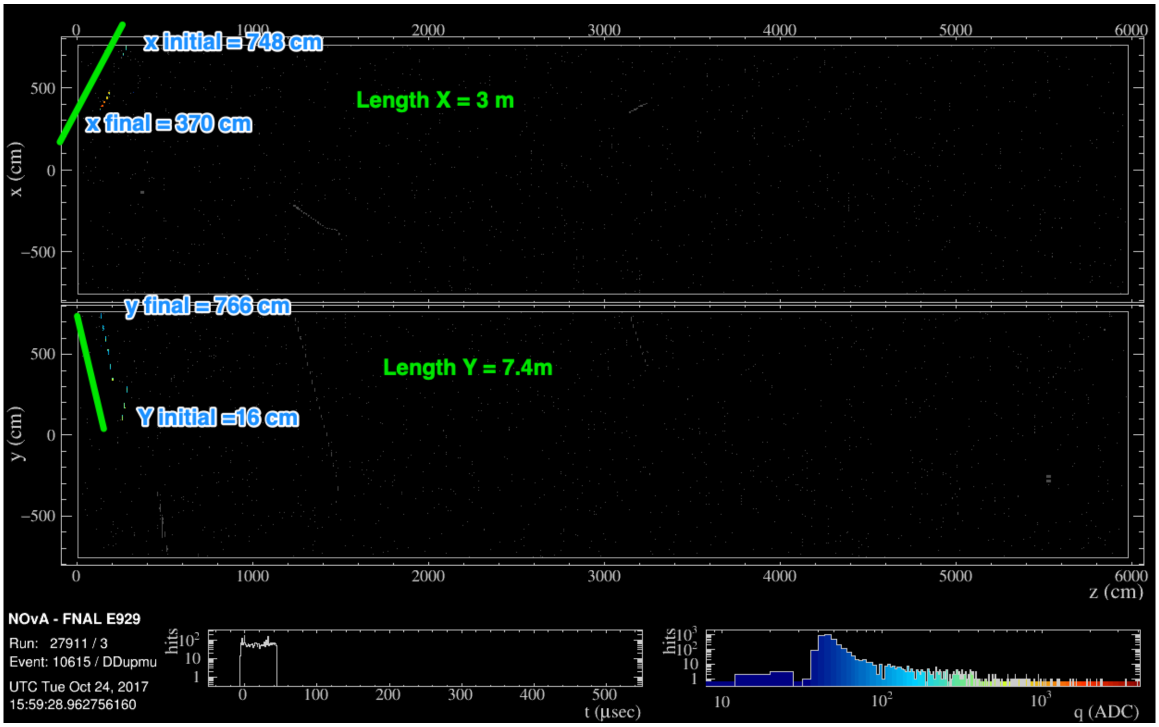

Figure 11.1: Example of how tracks that happen consecutively trick the algorithm. The green line shows the length of the one track that has been reconstructed by the algorithm. Looking at the cells in the event display two tracks can be seen, overlapping in the z-axis. Improved reconstruction techniques could reduce this background in the future.

tainty, or standard deviation of the Poisson distribution, is simply the mean's square root. If the prediction is correct and the number of events in the twilight region follows a Poisson distribution with a mean value of 38 events, there is a 68% probability that the number of observed events will lie within one standard deviation of the mean and be contained within the uncertainty of the number of predicted events.

Therefore,

$$\text{Statistical Uncertainty} = \sqrt{\text{Expected number of events}} = \sqrt{38} \approx 6, \tag{11.4}$$

and the expected number of background events to be observed in the twilight region and its statistical uncertainty is:

$$\text{Expected number of events} = 38 \pm \sqrt{38} = 38 \pm 6. \tag{11.5}$$

After applying the same cuts that were applied to the background (day) region to the twilight region, 40 events were observed. The number of observed events is well within the prediction of a number of expected events, validating the background model. The results of the twilight region are summarized in Table 11.6.

Region	**Number of expected events**	**Number of observed events**
Twilight	38 ±6	40

Table 11.6: Number of expected and observed event in the twilight region

11.5 Signal Region Prediction

Until this point, the analysis has been blinded, meaning that the signal region data have not been looked at or analyzed to avoid corrupting the final results. A first look at the signal region is done by looking at the distribution of the variables used to discriminate between upward and downward-going muons. Normalizing the number of the day region background events to the number of night region events takes care of the difference in the total number of events and exposes differences in the distributions' shape, which matters in this case. As shown in Fig. 11.2, after normalization, the distributions of one important variable, the χ^2 have the same shape.

As explained in Section 11.1.1 and done for the twilight region, a normalization factor is applied to the observed number of background events in the day region to obtain the expected number of background events in the night (signal) region. The number is approximated to the highest integer value because a non-integer number

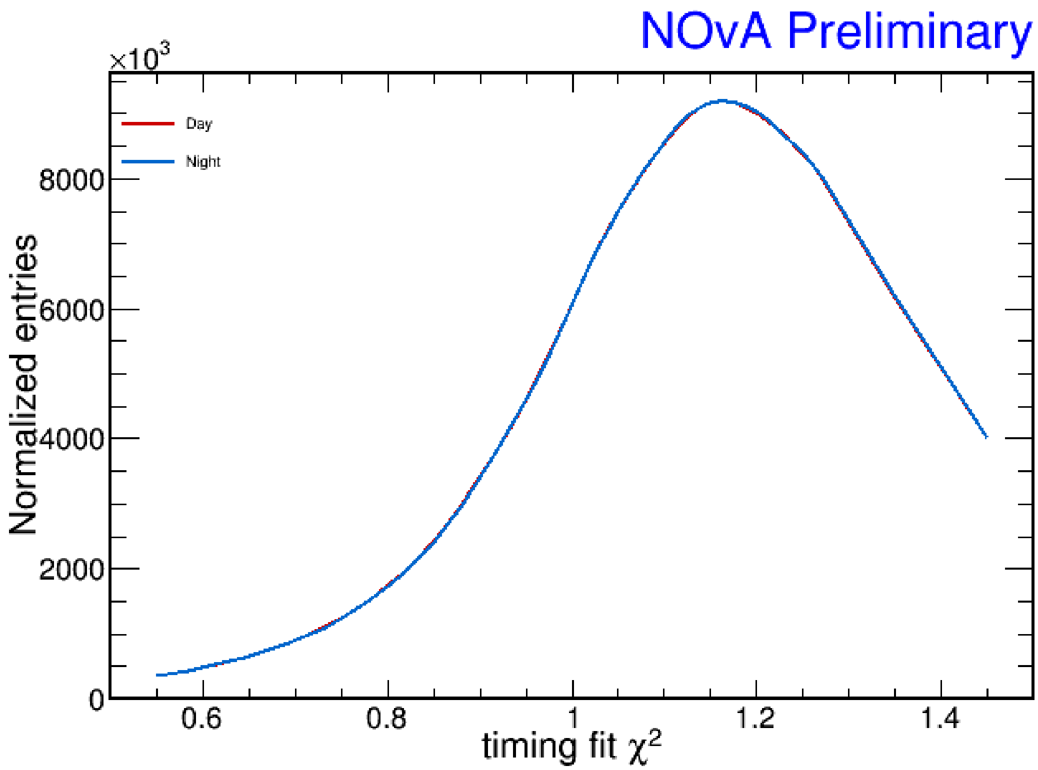

Figure 11.2: The χ^2 distribution of the day region events and the night region events before any cuts are applied. The number of entries of the background has been normalized to the number of entries of the signal. The two distribution match perfectly.

of events would not make physical sense.

$$\text{live} - \text{time correction} = \frac{40290970}{34609255} \approx 1.2 \tag{11.6}$$

such that

$$\text{Expected number of events} = 75 \times 1.2 \approx 90 \tag{11.7}$$

The statistical uncertainty on the final number of events in this case is then

$$\text{Standard deviation} = \sqrt{\text{Expected number of events}} = \sqrt{90} \approx 10 \tag{11.8}$$

The expected number of background events to be observed in the signal region is

$$\text{Expected number of background events} = 90 \pm 10 \tag{11.9}$$

Background composition	Percentage %	Predicted events
Clean upward-going track	53	48
Double track due to algorithm mismatch	30	27
upward-going track due to interaction	17	15

Table 11.7: Predicted background events composition in the signal region, estimated by visual inspection of the background events.

These events should be approximately made up of 53% clean upward-going tracks, 30% double tracks due to algorithm mismatch, and 17% upward-going tracks due to interaction, as listed in Table 11.7. An example of each kind of event as observed in the event display is shown in Fig. 11.3 - 11.5.

11.6 Signal Region Observation

The same procedure used in Section 11.3 has been used here to estimate the final number of events observed in the signal region. The relevant numbers of events are shown in Tables 11.8 and 11.9. The final number of events observed in the signal region is 107. The observed number of events is slightly higher than the expected number, but it is still within two standard deviations of the mean, which is not considered a statistically significant deviation.

11.6.1 Background Only Hypothesis

Comparing the predicted number of background events with the observed number of events shed light on the central question. This search is trying to answer if there is Dark Matter produced in the Sun's core and if it can be detected with the

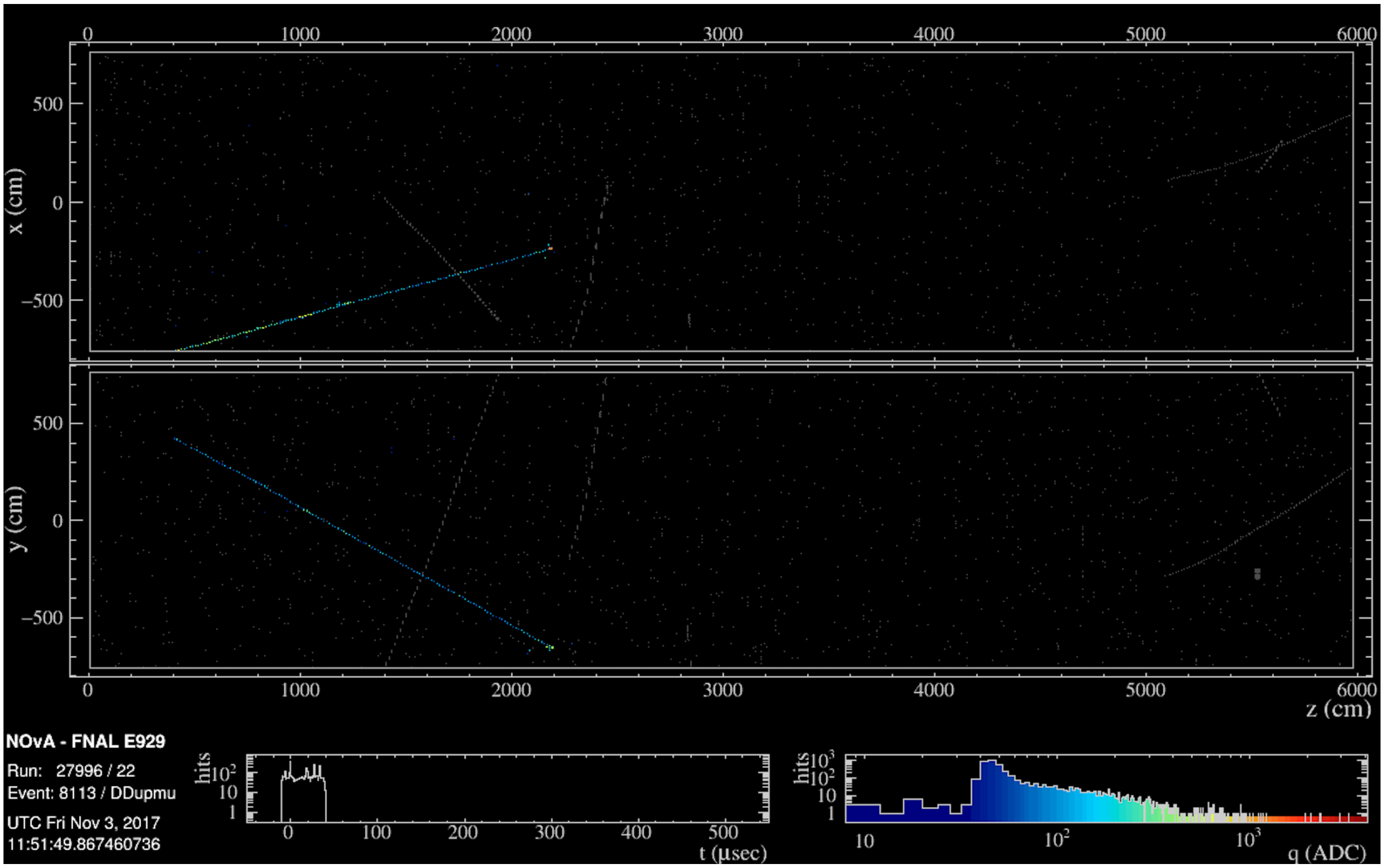

Figure 11.3: The event displays showing a clean upward-going track in the detector. The neutrino coming from the bottom interacts after few meters inside the detector and creates a muon that goes upward.

Variable	**Final number of bkg events**
After kinematic cuts	2582118
Timing hypothesis fit	1607888
Timing hypothesis fit, X view	1530298
Timing hypothesis fit, Y view	1512007
Log-Likelihood ratio	12994
Log-Likelihood ratio, X view	8834
Log-Likelihood ratio, Y view	154
Probability of being upward-going	107
Final number of background events	107

Table 11.8: Final number of events signal events.

NOvA detector. However, comparing the number of predicted and observed events alone gives limited insight because random fluctuations of the number of background events could be the main culprit for the differences observed. For this reason, a more

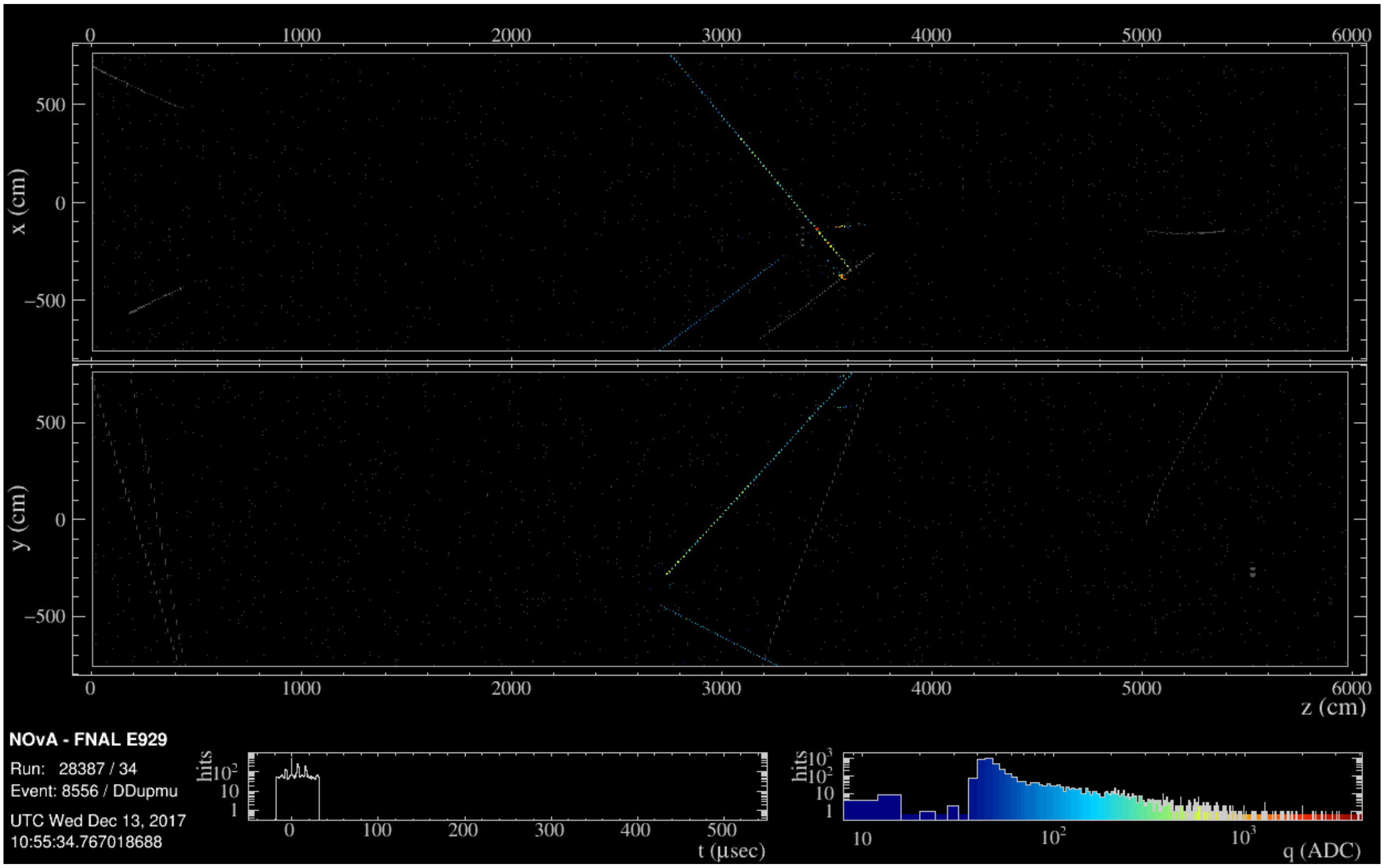

Figure 11.4: The event displays showing a double track due to algorithm mismatch, previously discussed.

Region	Number of expected events	Number of observed events
Night	90 ±10	107

Table 11.9: Number of expected background events in the signal region and number of observed events.

rigorous approach requires testing the significance of these results by comparing the observed data with a background-only hypothesis. The background-only hypothesis hypothesizes that the signal region's events are only background events, the same kind of events observed in the day region, due to the same physical origin. The procedure explained in detail in Appendix B has been used to test this hypothesis. The test uses pseudo-experiments, simulations of possible outcomes starting from the same initial hypothesis. One pseudo-experiment simulates an outcome (possible number of events) from a Poisson distribution with a mean equal to the predicted number of

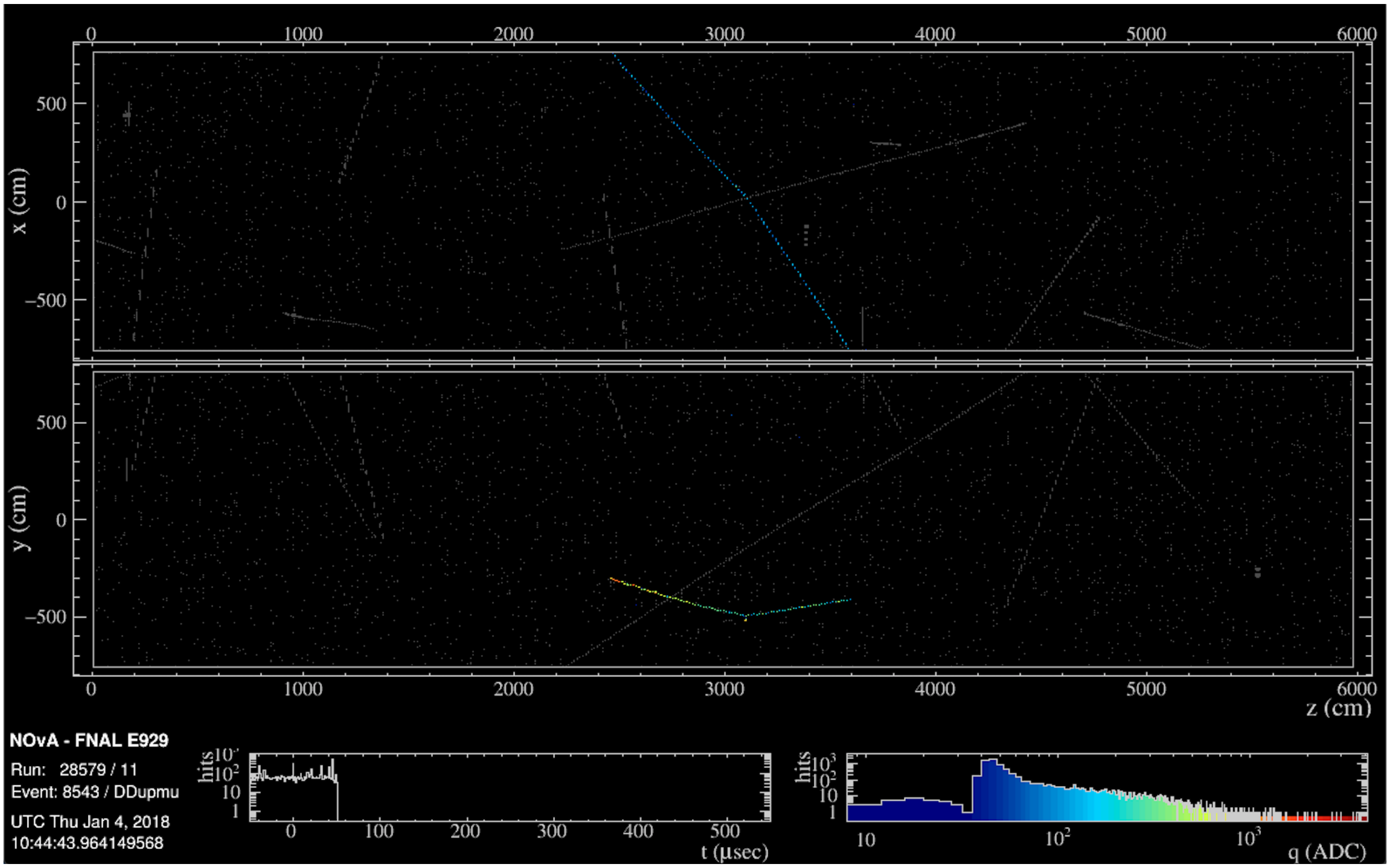

Figure 11.5: The event display showing an upward-going track due to interaction of the incoming muon, that scatters upward after

background events for the signal region. This step is repeated 1,000,000 times to create a distribution of possible outcomes. If this analysis were to be repeated 1,000,000 times in precisely the same way, these would be the different values that would be obtained as the number of expected background events. These values would only be different because of statistical fluctuation and systematic uncertainties – some would be more likely to happen than others, but all of them would be possible. Setting the significance level of this analysis at $\alpha = 0.1$, the confidence level chosen for the analysis is C.L. = 90%. Results of the test are shown in Fig. 11.6 and summarized in Table 11.10.

Even if the test results show that at 90% C.L. 102 number of events are expected, showing a deviation of 5 events from the observed number of events, this difference is

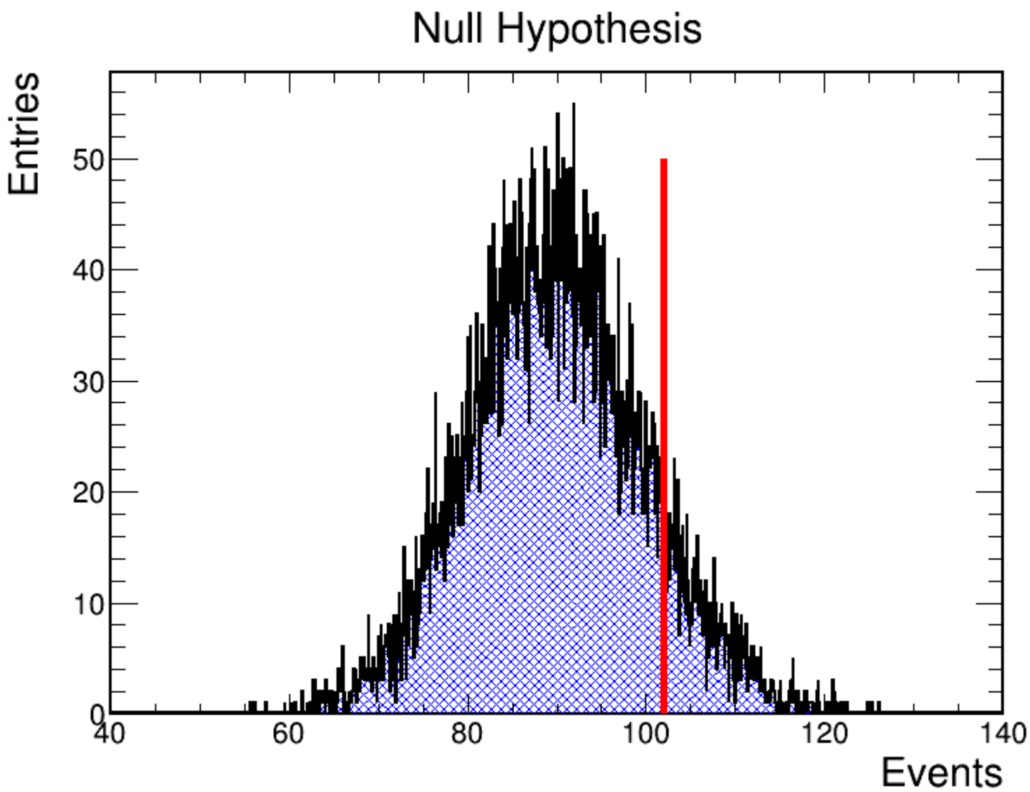

Figure 11.6: The null hypothesis distribution, with the red line showing the 90% C.L. 102 number of events.

Mean	Number of events at 90% C.L.	Number of observed events
90	102	107

Table 11.10: Statistical test results, show the number of events for a Poisson distribution with mean equal 90 at 90% C.L. to be 102.

not big enough to be practically significant. Values for the number of events greater than 102 would happen 1 in 20 times due to random fluctuation.

11.7 Final Discriminant

A final variable has been chosen as a discriminant between background and signal particles. The signal is expected to come from the Sun's core. The angle between the particles' direction and the Sun's position can be the strongest indicator of whether the particle originated in the Sun. A background particle can accidentally align with the Sun, and this can be estimated, as done before, using the background (day) region.

The angle between the Sun and the particle's direction can be estimated from the internal product of two variables:

$$\text{Sun position } \cdot \text{Track Position} = (x_{sun} * x_{track} + y_{sun} * y_{track} + z_{sun} * z_{track}), \quad (11.10)$$

which can be rewritten as

$$\text{Sun Position} \cdot \text{Track Position} = ||\text{Sun Position}|| \times ||\text{Track position}|| \times \cos\theta_{\text{Sun,track}}. \quad (11.11)$$

An example of the distribution of the angle between the sun and the track position for the simulated 20 GeV $b\bar{b}$ events, is shown in Figure 11.7.

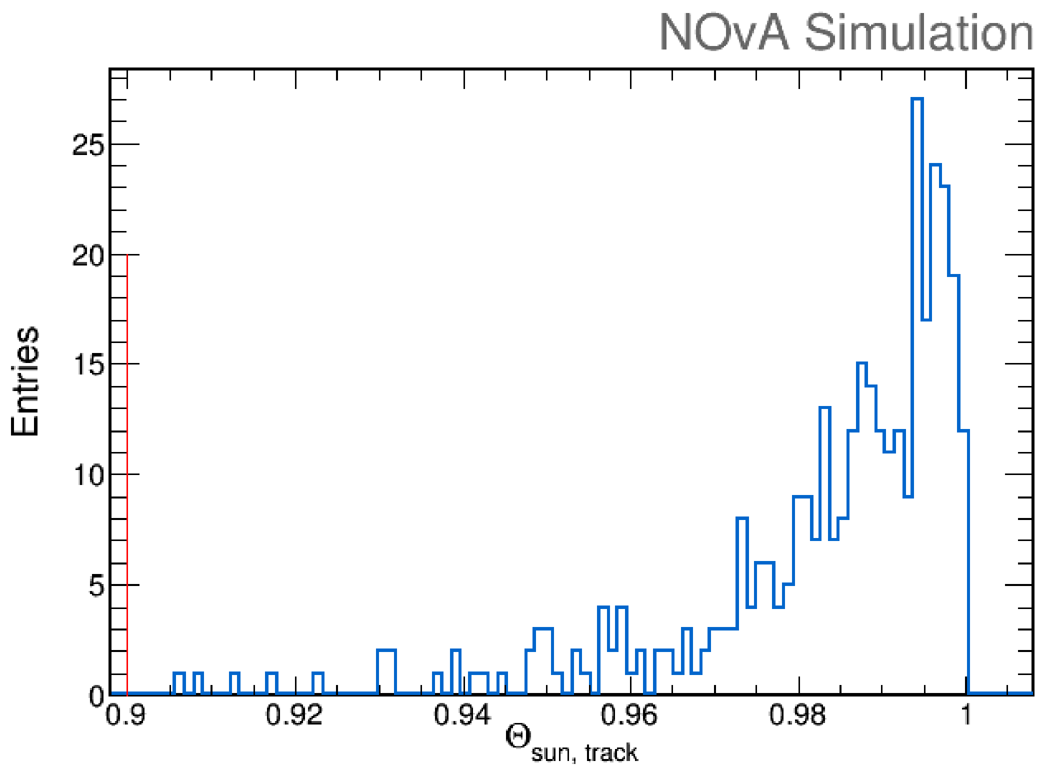

Figure 11.7: An example of the distribution of the angle between the sun and the track position for the simulated 20 GeV $b\bar{b}$ events. All of the simulated events are expected to peak at one, in line with the Sun position

More information about the final discriminant variable can be found in Appendix A.

11.8 Upward-Going Muons Flux Limit

Before applying the angular cut that discriminates between particles coming from the direction of the Sun and background particle coming isotropically, the final number of events for both the day (background) region and the night (signal) region has been studied as a function of $\cos\theta_{Sun,track}$. No significant deviation can be seen between the two distributions, as shown in Fig. 11.8.

Using the simulation of the signal for different energies and different annihilation channels of Dark Matter particles, the angular acceptance has been calculated for the variable $\cos\theta_{Sun,track}$. As shown in Fig. 11.9 a cut on $\cos\theta_{sun,track}$ at 0.90 contains more than 95% of the signal in first approximation. The accurate value depends on the hypothesis's mass, but for simplicity in the analysis, the same value (which is an upper limit) has been used for all of them.

The value chosen for the cut on this angle is $\cos\theta_{sun,track} > 0.9$.

The number of events observed after applying this cut to day and night region are shown in Fig. 11.10 and summarized in Table 11.11.

Region	**Num of observed event**	N_{obs} **for** $cos(\delta\theta_{track,sun}) > 0.9$
Day	75	6
Night expectation	90	7
Night	107	13

Table 11.11: Number of observed events after requiring that the angle between the Sun and the track position is greater than 0.9. The number of expected events based on the day region is 7 events.

The number of expected events for the signal region at a value of $\cos\theta_{Sun,track}$ greater than 0.9, based on the day region prediction, is seven events. The number of observed events in the signal region at a value of $\cos\theta_{Sun,track}$ greater than 0.9 is 13

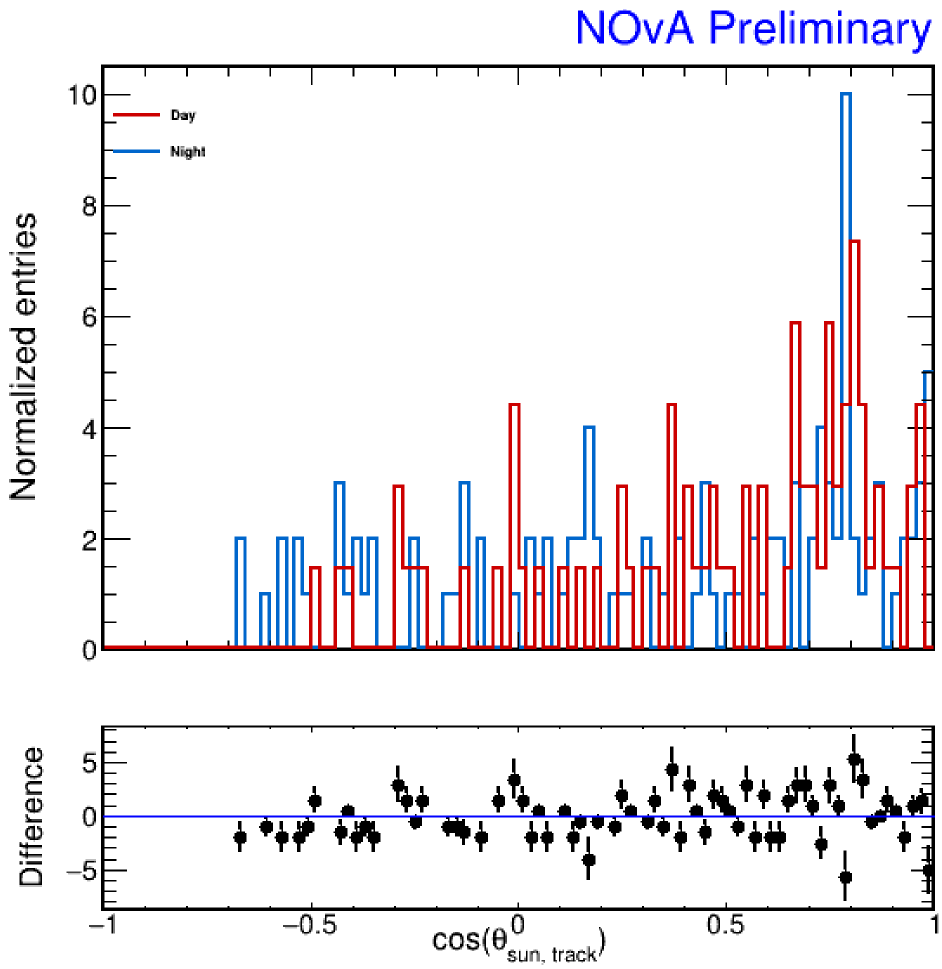

Figure 11.8: Day and night distributions of events as a function of the angle between the track and the Sun position.

events.

The same procedure applied in Section 11.6.1 has been applied here to estimate the statistical significance of the difference between the number of expected background events in the signal region and the number of observed events. A systematic uncertainty has been added here to take into account the 'phantom' position of the Sun in the day region, as studied in Chapter 10. This systematic uncertainty of 2% is added as a Gaussian with a mean of zero and has the effect of smearing the null hypothesis distribution to consider extra uncertainty. Results are summarized in Table 11.12 and shown in Fig. 11.11

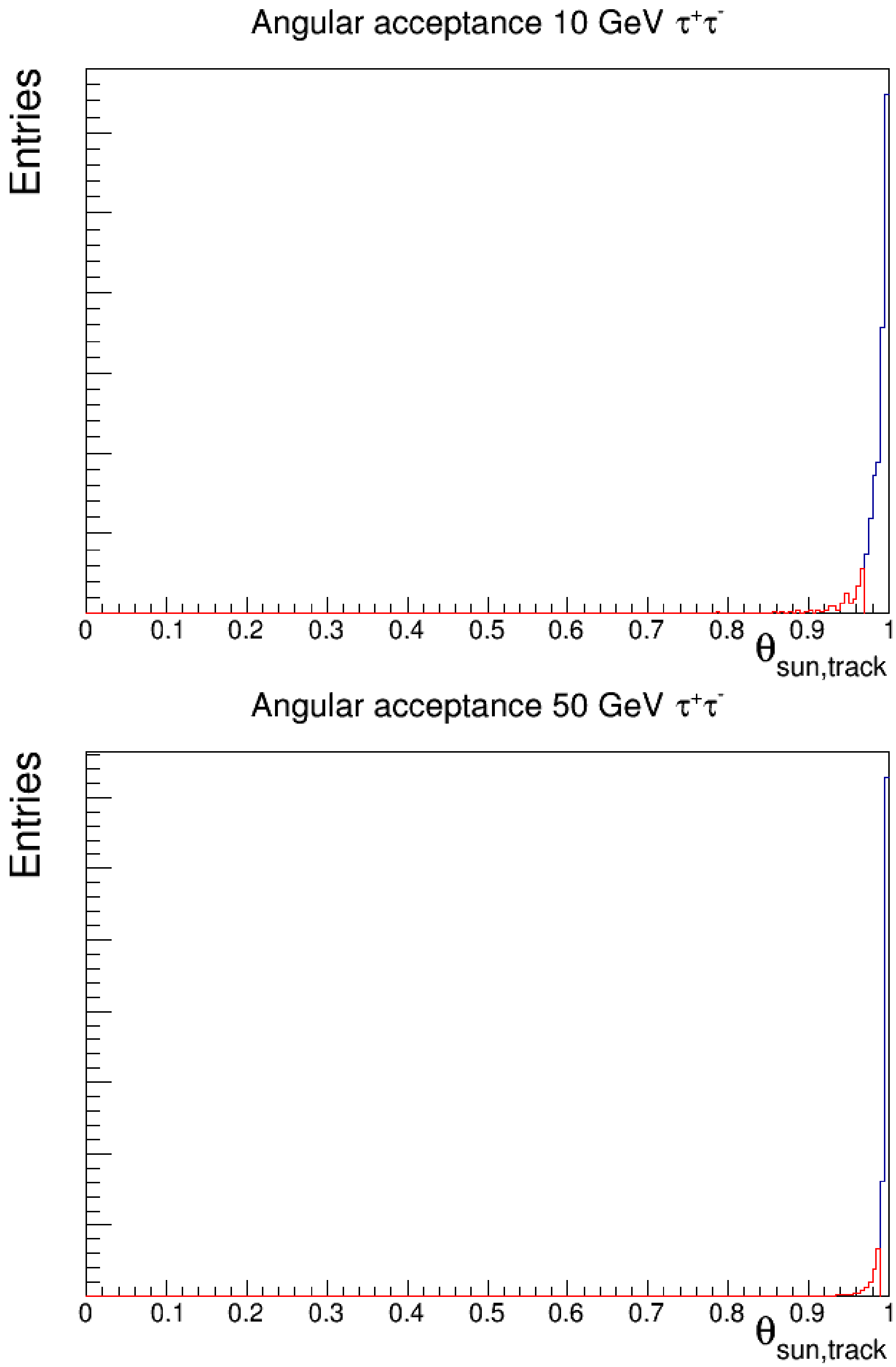

Figure 11.9: The angular acceptance has been calculated for the variable $\cos\theta_{sun,track}$ for two different signal simulations. A cut on the variable at value higher than 0.90 contains approximately 95% of the signal

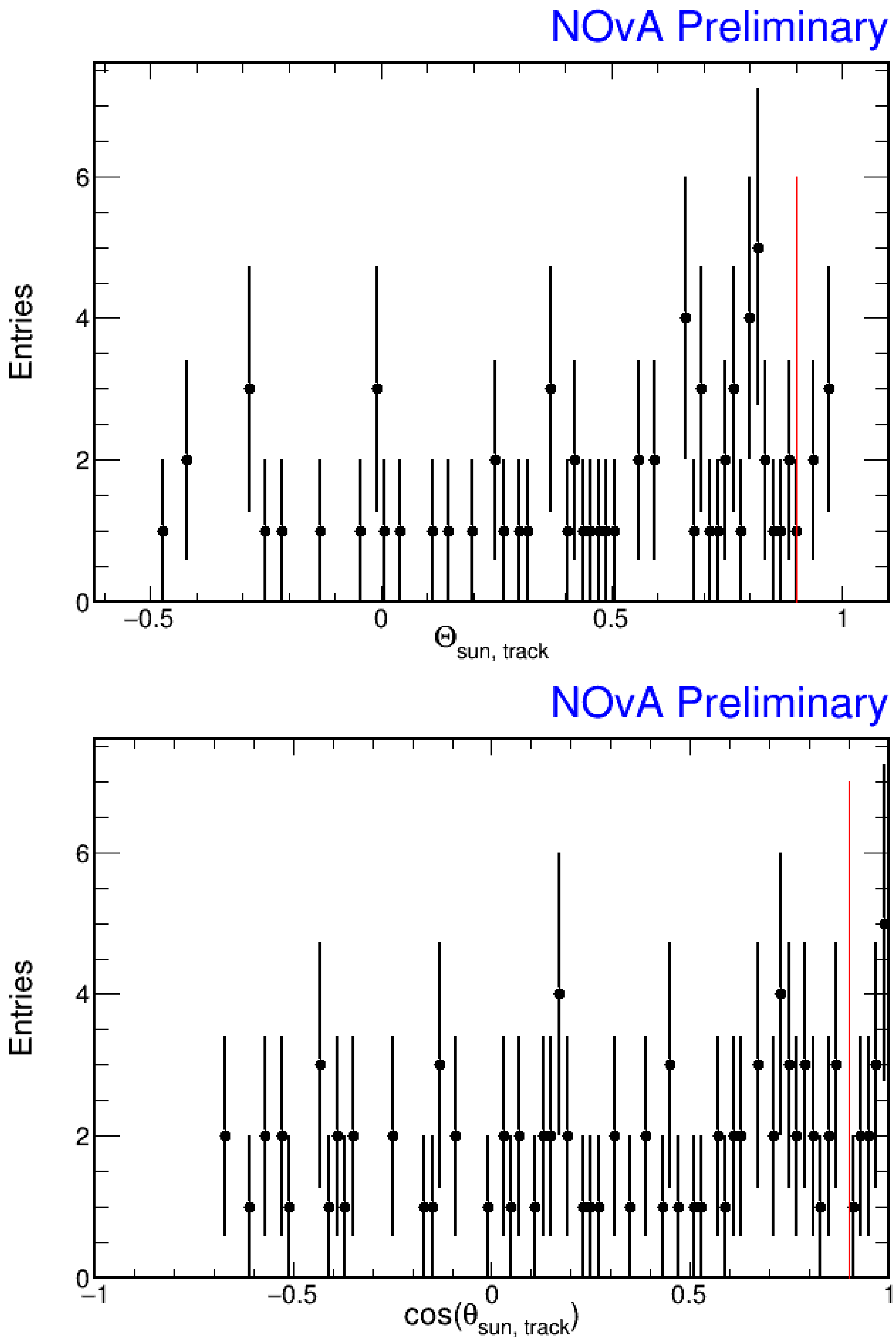

Figure 11.10: Number of observed events in the background region and signal region as a function of $\cos\theta_{sun,track}$, the final discriminant variable. The final cut applied on the discriminant variable $\cos\theta_{sun,track}$ is shown as a red line. The events above the red line are the final number of observed events taken into consideration for this analysis.

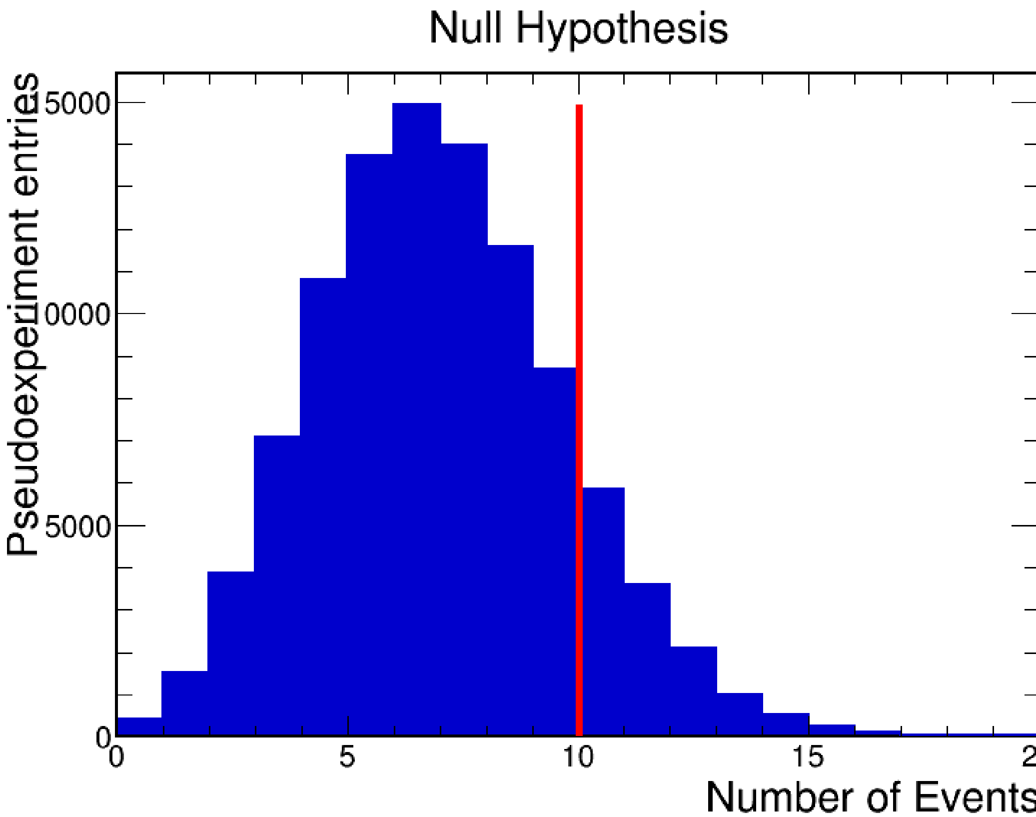

Figure 11.11: The null hypothesis distribution after a cut on $\cos\theta_{sun,track}$ has been applied, with the red line showing the 90% C.L. 10 number of events.

Mean	expected limit at 90% C.L.	Number of observed events
7	10	13

Table 11.12: In the background only hypothesis the mean is the number of expected events in the signal region. The expected limit at 90% C.L. is 10 and the observed number of events is 13.

As previously noted, even if the test results show that at 90% C.L., ten events are expected, showing a deviation of 2 events from the observed number of events, this difference is not big enough to be practically significant. The test's statistical significance showed that a deviation from the background-only hypothesis existed, but the magnitude of this deviation is not big enough to claim that the Dark Matter particle is the cause of it. Values for the number of events more significant than 11 would happen 1 in 20 times due to random fluctuation.

11.9 Upward-Going Muon Flux Results

Because no statistically significant excess was found in measured muons relative to the expected background, a conservative 90% C.L. upper limit on expected muon flux for the upward-going muons has been set. ${N_S}^{90}$ is the upper limit on the number of events given the number of observed events in the signal region, expressing how likely is it for the true value to fluctuate down to the observed number of muons. To estimate it, various background only pseudo-experiments has been thrown for different background hypothesis, with the ${N_S}^{90}$ value being the value that has only 10% of pseudo-experiments below the observed number of muons.

The results apply to muons with energy higher than 1.2 GeV, where the energy threshold has been estimated using

$$E_\mu = \text{mean path} \times (\frac{dE}{dx} \cdot \rho) \tag{11.12}$$

where the muon stopping power is $dE/dx = 2\text{MeV}/(g \cdot cm^{-2})$, given that a muon at relativistic energies is a MIP, for a mean path of 7 m, the minimum distance a muon needs to travel in the detector to pass the length cut and $\rho = 0.859 g/cm^3$.

To estimate the flux Φ_μ, the following formula is used:

$$\Phi_\mu(90\% C.L.) = \frac{{N_S}^{90}}{\epsilon \times A \times T}, \tag{11.13}$$

where the denominator, $\epsilon \times A \times T$, represents the exposure, where ϵ is the efficiency, A the NOvA detector effective area, and T the live-time. The live-time used here is the total live-time of the signal region calculated earlier. For the effective detector area, the detector's whole plane is taken, which is $1523 \times 5962\, cm^2$. The estimated efficiency takes into account multiple effects. The first one is the effect of having a trigger, that as previously shown in Chapter 6 is 5%. The second contribution is given by the muon reconstruction efficiency that is almost one hundred percent for cosmic rays in the NOvA detector, to which a 2% loss of efficiency due to the cut on the elevation angle needs to be subtracted. The most significant contribution to the overall efficiency is the cuts that we used offline to select the upward-going muon track, particularly the timing cuts, χ^2, and LLR. The overall efficiency is estimated to be 48%. The final exposure is $1.75 \times 10^{14}\, cm^2 \cdot s$.

${N_S}^{90}$ can be calculated for different angles. The bigger the angle, the higher the number of observed events, hence the higher ${N_S}^{90}$. The results of the limits are shown in Table 11.13 and an example of the test hypothesis calculation to obtain ${N_S}^{90}$ is shown in Fig 11.12.

$\theta_{Sun,Track}$ $(degree)$	$Observed\ events$	${N_S}^{90}$	Φ_μ $(cm^{-2}s^{-1})$
10	5	9	4.555×10^{-14}
15	6	10	5.12×10^{-14}
20	10	15	7.97×10^{-14}
25.8	13	18	9.68×10^{-14}
30	15	21	1.13×10^{-13}

Table 11.13: The upper limit, ${N_S}^{90}$, can be calculated for different angles. The bigger the angle, the higher the number of observed events, hence the higher ${N_S}^{90}$. The systematic uncertainty added to the background is 2%, see Chapter 10. The final exposure is $1.75 \times 10^14\, cm^2 \cdot s$.

This search's limits are shown with previous estimates by other experiments (Baksan, MACRO, and Super Kamiokande [70, 95–97]) in Fig. 11.13. The limits are plotted as a function of different cone half angles from the center of the Sun in degrees. The larger the cone, the smaller the initial WIMP particles' energy because they will more likely undergo through scattering resulting in a higher degree angle.

The resulting flux appears to be competitive with the other experiments. Compared to the NOvA detector and this analysis's live-time, most of the other experiments have been collecting data for more than ten years. Furthermore, SuperK obtained 100% efficiency for upward-going muons, compared to the NOvA efficiency,

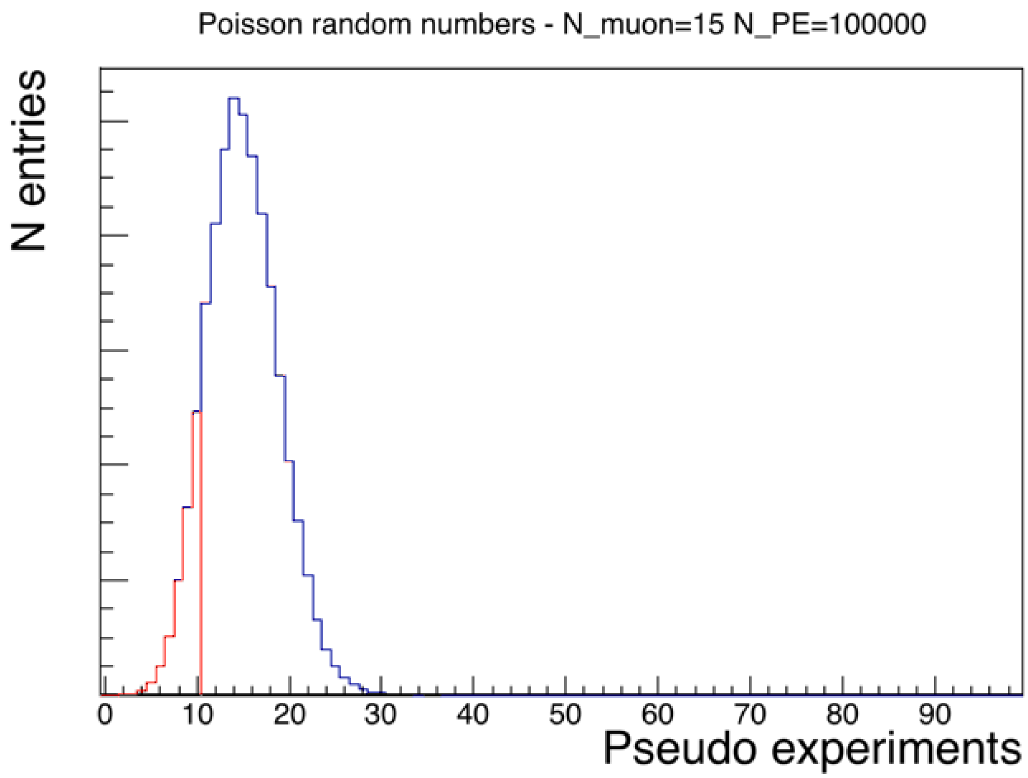

Figure 11.12: Example of the background only distribution. The distribution is created by 100,000 pseudo-experiments that use 15 muons for the mean value for the Poisson distributions. For the background-only hypothesis, the mean value is the number of expected events, smeared by the systematic uncertainties. The final number of signal events chosen as the 90% C.L. upper limit on the muon flux, ${N_S}^{90}$, is the one for which 10% of the pseudo-experiments are below the N_{obs} events.

which could be improved with a different signal selection criteria.

Lastly, the inclusion of contained events would allow the incorporation of lower energy tracks to make NOvA results more competitive.

These results could be extended to a broader class of models, which are not specific to the dark matter theory.

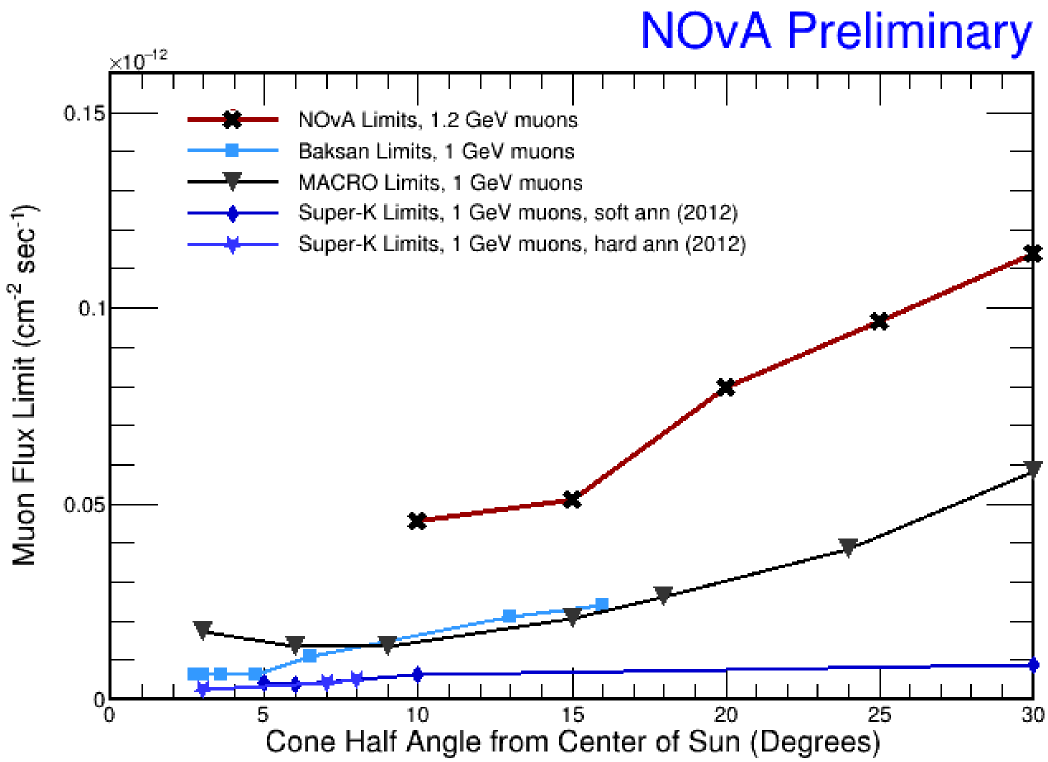

Figure 11.13: Comparison of NOvA excess neutrino-induced upward muon flux upper limits at 90% C.L. with limits from other experiments. The Y-axis shows the upward-going muon flux limits in $cm^2\,sec^{-1}$ while the X-axis shows half-cone angle size in degrees.

11.10 Upper Limits on WIMPs Calculation

Appendix B, describes in detail the calculation of the estimation of the upper limit using the C.L.s method. Here, the results are provided. The C.L.s method helps to estimate the upper limits on the number of signal events that could have been present in the observed data. The systematic uncertainties added to the signal are those summarized in Table 10.10. A 90% confidence level upper limit on the number of signal events, coming from the annihilation of WIMPs in the core of the Sun, can be obtained from Eq. B.6.1, assuming Poisson statistics for both expected background, signal, and observed events. The limits on the number of signal events differ slightly depending on WIMPs' mass and the annihilation channel due to the different uncertainties associated with each process. With N_{bkg} being the number of expected background events in the signal region estimated from the day region, N_{obs} being the number of observed events in the signal region, N_{signal}, the maximum number of signal events that could be present in the signal region and not been seen taken into account the statistical fluctuation of the number of events and effects of the systematic uncertainties. The upper limits for three WIMP mass values are given in Table 11.14.

N_{bkg}	N_{obs}	$m_\chi\,(GeV/c^2)$	$Channel$	$Systematic\,(\%)$	N_{Signal}
7	13	10	$\tau^+\tau^-$	42	17
7	13	10	$b\bar{b}$	40	16
7	13	20	$\tau^+\tau^-$	42	17
7	13	20	$b\bar{b}$	40	16
7	13	50	$\tau^+\tau^-$	44	17
7	13	50	$b\bar{b}$	42	17

Table 11.14: Upper limits at 90% C.L. on the number of signal events N_{Signal} that could be present in the signal region, given the number of expected background events from the background region, N_{bkg}, and the number of observed events in the signal region, N_{obs}. The limits are slightly different for different mass and annihilation channel hypothesis.

One example of the two hypothesis distributions, background only and background plus signal distribution, is shown in Fig. 11.14.

11.11 From Muon Flux to Scattering Cross Section

The underlying assumption that follows here is that WIMPs have only a single type of interaction with a nucleus (electroweak scale interactions).

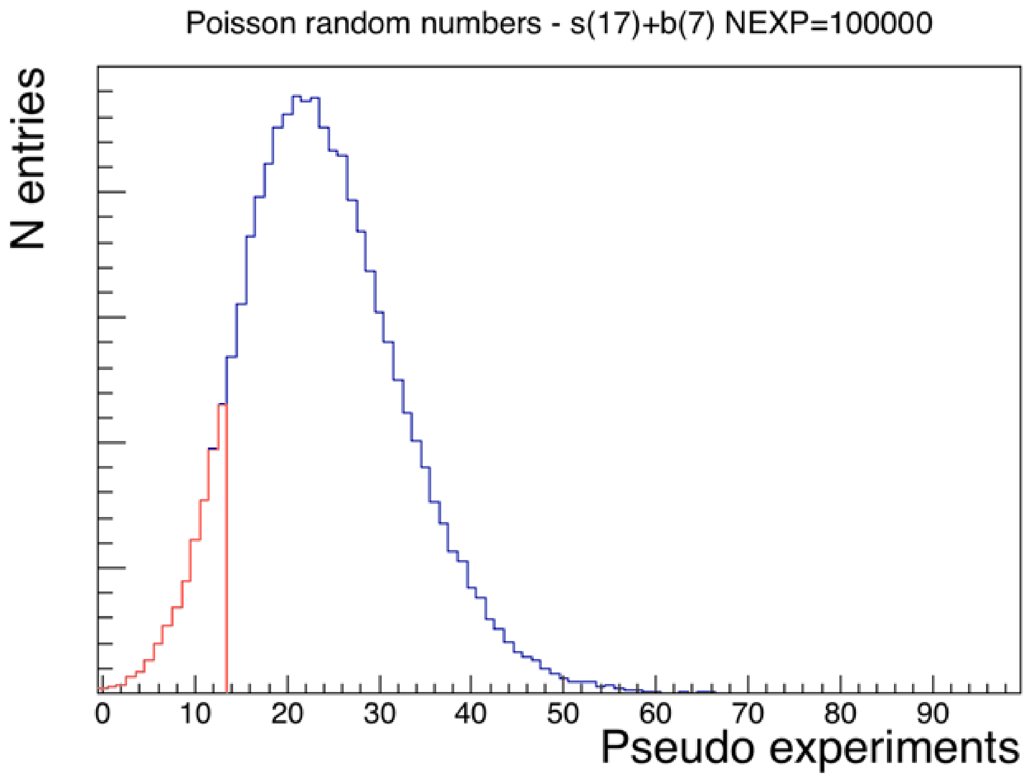

Figure 11.14: Example of the background plus signal distribution. As for the background only hypothesis, the distribution is created by 100,000 pseudo-experiments that use the background expectation N_{bkg}, 7 events, plus the signal expectation N_{signal}, 17 events, for the mean value of the Poisson distributions. The mean value of the distribution is smeared by the systematic uncertainties, which will be much higher in this case compare to the background only hypothesis. The final number of signal events chosen as the 90% C.L. upper limit on the WIMPS signal flux, N_{signal}, is the one for which 10% of the pseudo-experiments are below the N_{obs} events. This test gives an indication of the maximum signal value that could have been in the data. If the number of signal events were higher than that, there would have been a 90% chance that they would have shown an excess of events in the signal region.

11.11.1 Spin Dependent vs. Spin Independent Cross Section

One can distinguish between two types of interactions: spin-dependent (S.D.) and spin-independent (S.I.). In spin-independent interactions, WIMPs couple to the target nucleus's mass (scalar interaction). In the case of spin-dependent interactions, WIMPs couple to the spin of the target nucleus (axial vector interactions). Spin-dependent interactions are mainly the case for neutralino interactions with nuclei with an odd number of nucleons (spin is unpaired, "spin-spin interaction"). The SD scattering can be efficient when a nucleus has a large number of unpaired protons or neutrons, and because Hydrogen is the most abundant element in the Sun (73%), the S.D. elastic cross-section of dark matter particles on protons appears to be one of the most sensitive quantities in these searches (we can neglect the heavier elements in this case). Therefore, the limit derived on the S.D. scattering cross-section is highly competitive with those from direct detection experiments.

11.11.2 Calculating Scattering Cross Section

The muon flux at the detector (assuming that one annihilation channel dominates) and the S.D. cross-section is calculated from the WIMP annihilation rate in the Sun:

$$\Phi_\mu{}^{obs} = \Phi_\mu{}^f = \eta^f(m_\chi)\Gamma_A \tag{11.14}$$

$$\sigma^{SD} = \lambda^{SD}(m_\chi)\Gamma_A. \tag{11.15}$$

Relating the cross-section to the muon flux gives:

$$\sigma^{SD} = \frac{\lambda^{SD}(m_\chi)}{\eta^f(m_\chi)}\Phi_\mu{}^{obs} \equiv \kappa_f{}^{SD}(m_\chi)\Phi_\mu{}^{obs}. \tag{11.16}$$

The conversion factors used to convert a muon flux limit from a neutrino telescope to a limit on the S.I. or SD WIMP-proton scattering cross-section can be calculated using a web tool called DarkSUSY [93]. The web tool also contains more annihilation channels and converts from fluxes with different muon energy thresholds and angular cuts.

Note to calculate conversion factor using DarkSUSY

The tool is available as a main program in the latest DarkSUSY release. This version of the tool also uses the later and updated WimpSim runs, so it is the preferred tool [93].

Input parameters to the tool include WIMP mass (GeV), where the annihilation happens (Earth or Sun), annihilation channel, the density of target detector material (g/cm), and rock density. Next, information regarding the starting and ending flux must be provided. For this calculation, the starting flux is the upward-going muon flux at a plane in the detector, while the ending flux is the spin-dependent cross-section. The initial flux is integrated above $E_{min} = 1.2$ GeV and below $\theta_{max} = 25.8$ degrees. The conversion factors obtained with the tool are shown in Table 11.15. This conversion factor can be used to convert the muon flux to a SD cross section for WIMP on proton.

m_χ (GeV/c^2)	$Channel$	$Conversionfactor$
10	$\tau^+\,\tau^-$	2.97×10^{-7}
10	$b\,\bar{b}$	7.08×10^{-6}
20	$\tau^+\,\tau^-$	1.50×10^{-7}
20	$b\,\bar{b}$	3.28×10^{-6}
50	$\tau^+\,\tau^-$	9.995×10^{-8}
50	$b\,\bar{b}$	2.39×10^{-6}

Table 11.15: Conversion factor calculated from DarkSUSY, used to calculate the spin-dependent cross section for different mass and annihilation channel.

11.11.3 Spin-Dependent Cross Section Results

A limit on the S.D. cross-section of WIMP-proton annihilation in the Sun can be estimated by assuming the theory behind the upward-going muon flux. The annihilation channels taken into account are $b\bar{b}$ and $\tau^+\tau^-$. $b\bar{b}$ annihilation is an example of the "soft" spectrum, while $\tau^+\tau^-$ represents the "hard" spectrum. The results are summarized in Table 11.16.

m_χ (GeV/c^2)	$Channel$	$Systematic$ %	${N_{signal}}^{90}$	${\Phi_\chi}^{90}$ $(cm^{-2}s^{-1})$	$\sigma_{SD,p}$ (cm^2)
10	$\tau^+\,\tau^-$	42	17	9.68×10^{-14}	9.11×10^{-39}
10	$b\,\bar{b}$	40	16	9.11×10^{-14}	2.05×10^{-37}
20	$\tau^+\,\tau^-$	42	17	9.68×10^{-14}	4.62×10^{-39}
20	$b\,\bar{b}$	40	16	9.11×10^{-14}	9.45×10^{-38}
50	$\tau^+\,\tau^-$	44	17	9.68×10^{-14}	3.04×10^{-39}
50	$b\,\bar{b}$	42	17	9.68×10^{-14}	7.31×10^{-38}

Table 11.16: 90% C.L. upper limits on the WIMP-proton SD cross section for hard and soft annihilation channels over a range of WIMP masses.

In Fig. 11.15, the results obtained from this analysis are compared with indirect D.M. searches results from other experiments [95, 96].

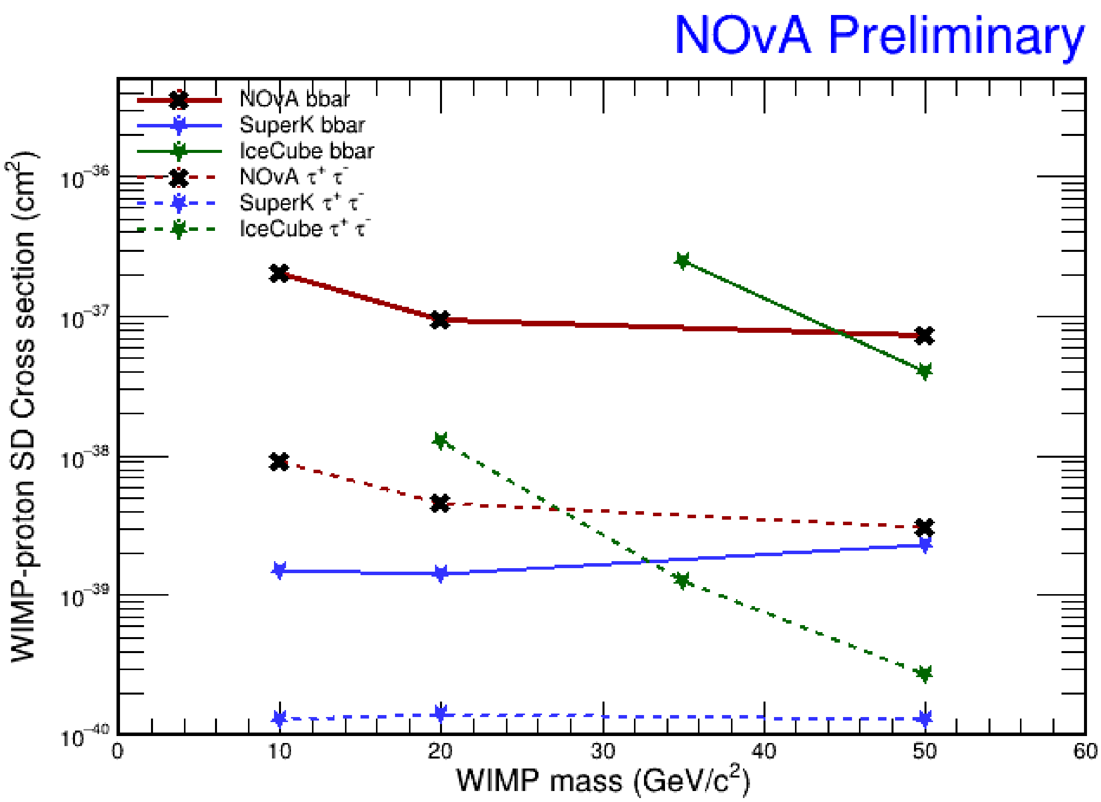

Figure 11.15: Comparison of NOvA excess neutrino-induced upward muon flux limits with limits from other experiments on the WIMP-proton SD cross section over a range of WIMP masses. The Y-axis shows the WIMP-proton cross section in cm^2 while the X-axis shows the WIMP mass in $\frac{Gev}{c^2}$.

Chapter 12

Conclusion

I love my story. Sure it's messy, but it's the story that got me here.

C.P.

Weakly Interactive Massive Particles (WIMPs) are a theoretical non-baryonic form of Dark Matter. The nature of Dark Matter is one of the most exciting open questions in modern physics.

Though its existence is proven by astrophysical evidence, its properties are not yet understood. If we assume that Dark Matter particles can produce Standard Model particles through their interactions, an indirect search can help shed light on this mystery.

I presented, here, the first Dark Matter search using three years of data collected with the upward-going muon trigger in NOvA.

The NOvA collaboration has built a 14 kton, fine-grained, low-Z, total absorption tracking calorimeter at an off-axis angle to the NuMI neutrino beam. Even though the detector is optimized to observe an electron neutrino appearance from a muon neutrino beam, it has a unique potential for more exotic searches given its enormous size, excellent granularity, energy resolution, and relatively low-energy neutrino thresholds.

Two fundamental pieces of this analysis are the upward-going muon trigger and a sufficient background suppression offline. The upward-going muon trigger's idea is to select high-quality muon tracks and then use the timing information of the tracks' hits to estimate directionality. In this way, the background flux is suppressed by more than a factor of 10^5 at trigger level to a rate of approximately 1-4 Hz.

To further optimize this search, we use only upward-going muons that point to the Sun. Our search occurs at night when the Sun is on the other side of the Earth. This strategy also allows us to use when the Sun is above the horizon as a control region to estimate the background. Ultimately, implementation of a cut based and maximum likelihood analysis provides a powerful tool for rejecting background and selecting a sample of neutrino-induced upward-going muons. The overall background rejection power achieved by the analysis is substantial and impressive. Starting with approximately 150,000 events per second,1 Hz - 4 Hz triggered, we cut it down to 40 events per year, a factor of 10^{11} of reduction.

A simulation was done in order to understand the WIMP signal behavior. The angle between the Sun position and the incoming track is used as the final discriminant in the analysis. The final number of events in the background region was used to estimate the number of events in the twilight region, which we used as a control region. The observation was in agreement, giving us confidence that the data-driven extrapolation method could also be used for the signal region.

Until this point, the analysis was blinded. The same procedure used for the twilight region was used to estimate the number of background events in the signal region. The observed number of events was within two standard deviations of the expected number of background events. This deviation is not big enough to be considered a statistically significant deviation.

Since no statistically significant excess was found, a 90% C.L. upper limit on the upward-going muon flux was set using the number of observed events in the signal region.

Lastly, by assuming a simple dark matter hypothesis for excess in the upward-going muon flux, a limit on the spin-dependent cross-section of WIMP-proton interaction in the Sun was estimated. The annihilation channels taken into account for the limits are $b\bar{b}$ and $\tau^+\tau^-$. The first one, $b\bar{b}$ annihilation, is an example of the "soft" spectrum, while $\tau^+\tau^-$ represents the "hard" spectrum.

The limits on the spin-dependent cross-section do not appear to be competitive with previous indirect Dark Matter searches. Different factors affect the spin-dependent WIMPs-proton cross-section limits: the total time the experiment has been collecting data, the angular acceptance, the muon efficiency, and the sensitivity to lower energy. Competing experiments, such as Super-K, which has the best limits for this analysis, have been collecting data for more than ten years, while in this analysis, we only used three years of data until 2018. NOvA will run for six more years, collecting a total of 12 years of data leading to a more competitive result. Besides, muon efficiency could be further improved using the latest convolutional neural network reconstruction techniques, leading to an improved reconstruction and higher efficiency [98]. Furthermore, NOvA results could be improved with different signal selection criteria, including muon events at lower energy using the contained trigger, which triggers upward-going muon events fully contained in the detector.

Lastly, although the spin-dependent cross-section limits do not appear to be competitive with previous indirect Dark Matter searches, the upward-going muon flux limits are promising. These results could be extended to a broader class of models that are not specific to the dark matter theory but produce upward-going muons. Leading limits could be reached with the aforementioned improvements.

Appendix A

Randomize Sun Position

A ‘shadow’ position for the Sun needs to be created in the background (day) region to predict the expected number of background events in the signal region that will pass the angular cut. This approach is studied in Chapter 8.

allows for one match between the two regions, day and night. The events should be ‘independent’ of the Sun’s position in the background-only hypothesis. So, in the background model, it should not matter where the Sun is in the sky for any given track, only that the distribution of the ‘phantom’ Sun’s position in the day sample matches that in the night sample.

For the day sample, the Sun position is drawn randomly from the distribution that it follows at night. The resulting distribution for the background events in the day region can be seen in Fig. A.1.

A.1 $\cos\theta_{Sun,track}$ possible range of values

All possible scenarios have been considered to estimate the possible range of values that this variable can take. These are shown in Fig. A.2. The day and night regions are defined from the Sun position before and after the twilight region.

The range of possible value can be estimated from the maximum and minimum value for an upward-going muon track minus the ten degrees of the twilight region, allowing values in the range (-0.98, 0.99) degrees, as shown in Table A.1.

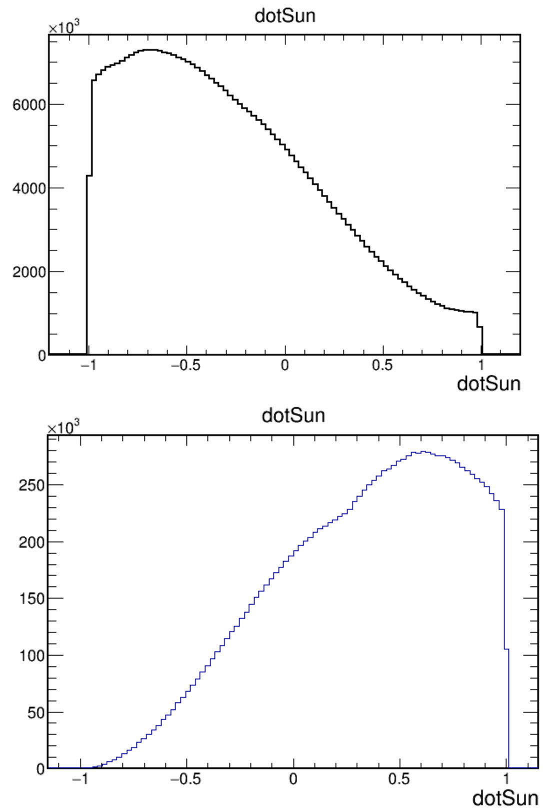

Figure A.1: The angle between the sun and the track position for the background region before and after correction to match the night region distribution. See Chapter 8 for the detailed study.

Range	$\cos\theta_{sun,track}$ **in degrees**	**Value**
Maximum value	cos(7)	0.99
Minimum value	cos(153)	-0.89

Table A.1: Range of possible values that the cosine angle between the Sun and track can take.

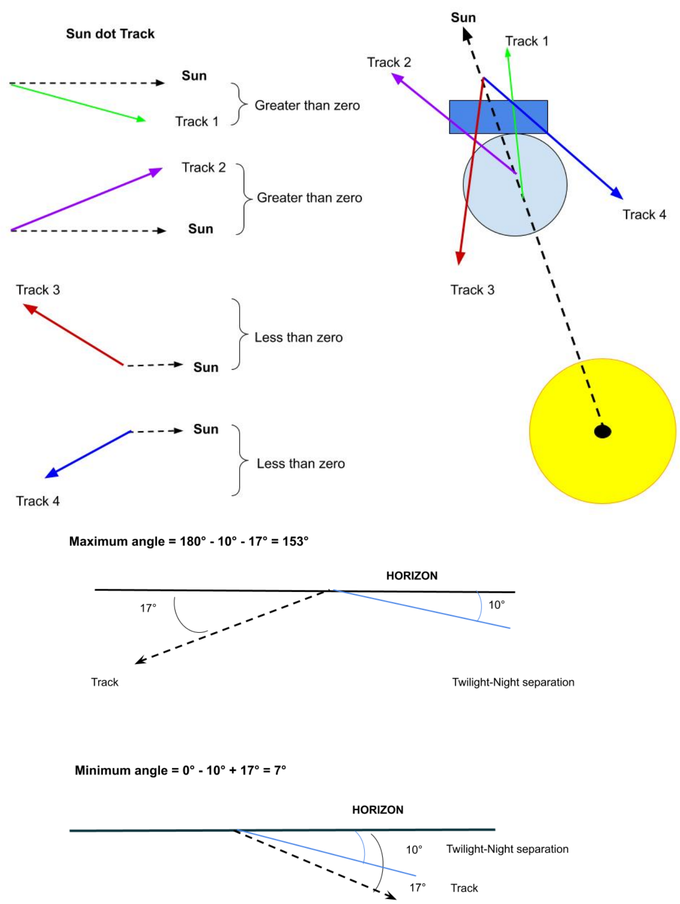

Figure A.2: Analysis of possible scenarios for the angle between the track and the Sun position to evaluate the values that this variable can have. The range of possible values for the cosine angle is also shown.

Appendix B

Exclusion in counting experiment

B.1 Motivation

One of the key components of the scientific method is to test theory predictions with experimental data. The observed data are compared to predictions of background and signal sources and their associated uncertainties. In a counting experiment, a comparison of the total data event counts to the total theory prediction is sufficient to test the theory. In this case, the events that satisfy certain criteria in a region where the signal is expected to be are counted. The selection criteria are designed in such a way as to maximize the number of signal events to be selected and reject background events, as explained in this chapter.

A counting experiment is characterized by the expected number of background events b, and the expected number of signal events s, while the outcome of the experiment is the actual number of observed events n_{obs}.

- If n_{obs} is significantly greater than b, the background hypothesis is rejected. This case is referred to as discovery.

- If n_{obs} is significantly less than $s + b$, the signal plus background hypothesis can be rejected. This case is referred as exclusion.

B.2 The Poisson distribution

To quantify the agreement between the observation and a hypothesis, the distribution of the number of events under this hypothesis must be known. The probability to observe k events is given by the Poisson distribution

$$P(k \mid \lambda) = \frac{\lambda^k e^{-\lambda}}{k!} \tag{B.1}$$

where λ is the expected (average) number of events and $\lambda = b$ under the background only hypothesis and $\lambda = s + b$ under the signal plus background hypothesis.

B.3 The Monte Carlo method

The probability distribution of the test statistic must be known in order to compute the p-values for exclusion. This may be done by generating many pseudo-experiments on a computer and counting how many times each value of the test statistic appears. To get the two p-values CL_b and CL_{s+b}, pseudo-experiments must be generated under both the background only hypothesis and the signal plus background hypothesis. Generating a background pseudo-experiment corresponds to generating one Poisson distributed random number with mean b, called Null Hypothesis. Generating a signal+background pseudo-experiment corresponds to generating one Poisson distributed random number with mean s + b, called Test Hypothesis.

B.4 Systematic uncertainties

The effect of systematic uncertainties may be included in the limit calculation. For each "nuisance parameter" a PDF must be chosen to model it. One typically uses a Gaussian with standard deviation corresponding to the uncertainty, which may need

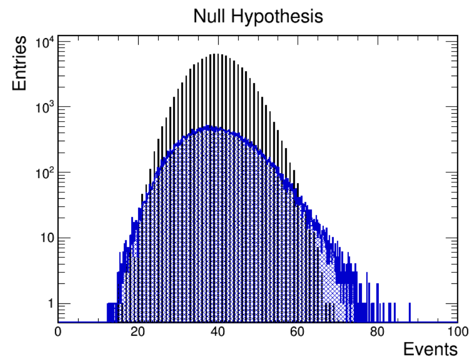

Figure B.1: Example of a background only distribution (black) and background distribution smeared by the systematic uncertainties distribution (blue).

to be cut off at unphysical values. For each pseudo-experiment, the value of each nuisance parameter is generated according to its PDF. This changes the distributions of the test statistic under the background only and signal plus background hypotheses.

B.5 Null Hypothesis

The Null Hypothesis can be used to quantify likelihood of an excess, assuming that no signal is present in the signal region.

Starting with the expected number of background events b, many pseudo-experiments can be generated to simulate the background only experiment, resulting in a different number of expected number of background events for each pseudo-experiment. Those values will be Poisson distributed around the median value b. Furthermore the distribution will be smeared by the systematic uncertainties distribution. The systematics uncertainties are assumed to be gaussian distributed, where the gaussian representing them will be centered in zero and with sigma equal to the systematic uncertainties value times the background expected value b.

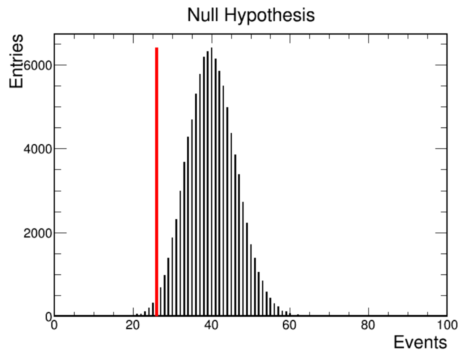

r0.4

Figure B.2: Example significance (red line) of a background only distribution

B.5.1 Significance

If we observe more events than the ones predicted by background alone, we can calculate the p-value, defined as the probability to observe the number of events observed in the experiment, n_{obs}, or more, given the background only hypothesis.
The p-value can be calculated as

$$p = P(n \geq n_{obs} \mid b) = \sum_{k=n_{obs}}^{\infty} P(k \mid b) \tag{B.2}$$

The smaller the p-value, the less compatible the observation is with the background only hypothesis.
The significance Z will be then defined by

$$p = \int_{-\infty}^{Z} \frac{e^{-x^2/2}}{\sqrt{2\pi}} \tag{B.3}$$

Discovery in particle physics is defined to be at least a 5 σ deviation from the background only hypothesis, which means for the p-value to be

$$p \leq 2.87 \cdot 10^{-7} \tag{B.4}$$

The probability to falsely discover something (falsely reject the background hypothesis when it is true) in the presence of background only, is then $2.87 \cdot 10^{-7}$.

B.5.2 Exclusion, CL_s method

Depending on the number of observed events we can calculate the corresponding p-value for the background only hypothesis, such that:

$$CL_b = P(n \leq n_{obs} \mid b) = \sum_{k=0}^{n_{obs}} P(k \mid b) \tag{B.5}$$

This value becomes important to calculate the "p-value" used to exclude a signal is defined as the ratio of two p-values

$$CL_s = \frac{CL_{s+b}}{CL_b} \tag{B.6}$$

In the case the number of observed events is zero, $n_{obs}= 0$, there will be:

$$CL_s = \frac{e^{-(s+b)}}{e^{-b}} = e^{-s} \tag{B.7}$$

so the signal will be equal to

$$s = -lnCL_s \tag{B.8}$$

It will then be possible to find the upper confidence limit s_{up} by inserting $CLs = 5\%$:

$$s_{up} = -ln(0.05) \approx 3 \tag{B.9}$$

What this means is that the exclusion is never stronger than 3 events in the CL_s method, regardless of the expected background.

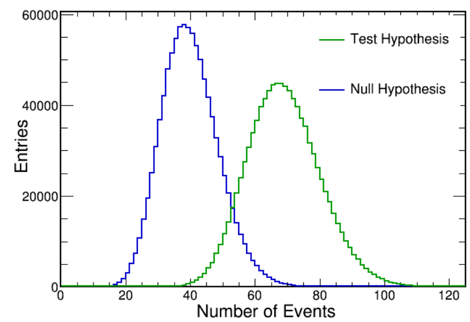

Figure B.3: Example of a background plus signal distribution (green) and background only distribution (blue), both smeared by the systematic uncertainties distribution

B.6 Test Hypothesis

If both, the signal and the background, are assumed to be present in the signal region, the hypothesis will be called test hypothesis.

In this hypothesis, starting with a expected number of events b and expected number of signal events s, many pseudo-experiments will be generated to simulate a signal plus background experiment, resulting in a different signal plus background events prediction for each pseudo-experiment. Also those values will be distributed following a Poissonian distribution centered around the median value (s + b). Again, this distribution will be smeared by the systematic uncertainties distribution. The systematics uncertainties for the signal are also assumed to be gaussian distributed, where the gaussian representing them will be centered in zero and with sigma equal to the systematic uncertainties value times the signal expected value s.
At the signal uncertainties distribution we need to add the background uncertainties distribution.

B.6.1 Exclusion, CL_{s+b} method

If we observe less events than the one predicted by signal plus background, we can calculate another p-value called CL_{s+b}, defined as the probability to observe the

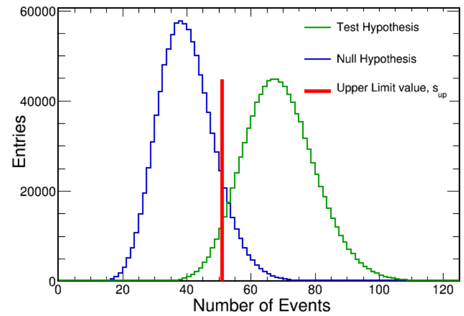

Figure B.4: Example an upper limit value s_{up} (red line) computed by the background plus signal distribution

number of events observed in the experiment, N_{obs}, or less, given the signal plus background hypothesis. The p-value CL_{s+b} is defined as

$$CL_{s+b} = P(n \leq n_{obs} \mid s+b) = \sum_{k=0}^{n_{obs}} P(k \mid s+b) \tag{B.10}$$

B.7 Upper limit on the signal

The signal plus background hypothesis is excluded at confidence level defined as

$$CL = 1 - CL_{s+b} \tag{B.11}$$

One typically defines a signal plus background hypothesis to be excluded when $CL_{s+b} \leq 5\%$, namely a 95% CL exclusion . The probability to falsely exclude an existing signal plus background, is then 5%. One can vary the expected signal s, and find the value s_{up} which gives exactly $CL_{s+b} = 5\%$. Since all $s \geq s_{up}$ are excluded at CL $\geq$ 95% ($CL_{s+b} \leq 5\%$), we say that s_{up} is an upper confidence limit on the expected signal. Any model which gives $s \geq s_{up}$ is excluded while any model which gives $s < s_{up}$ is not excluded.

The special case $n_{obs} = 0$ can be examined analytically,

$$CL_{s+b} = \frac{e^{-(s+b)}}{e^{-b}} \tag{B.12}$$

such that

$$s + b = -ln(CL_{s+b}) \tag{B.13}$$

So the upper confidence limit s_{up} can be found by inserting the value $CL_{s+b} = 5\%$:

$$s_{up} = -ln(0.05) - b \approx 3 - b \tag{B.14}$$

So in this case the limit depends on the expected background value b.

Appendix C

Distributions of Base Variables

Here we show the distribution of the base variables that are used for the cleanup cuts of the analysis. Note that we show distributions for the day and night samples as well as their ratio. The plots in this section are facilitate understanding the cut selection, and more importantly, they provide a proof for consistency of physics result and detector performance for the day and night sample in the control region.

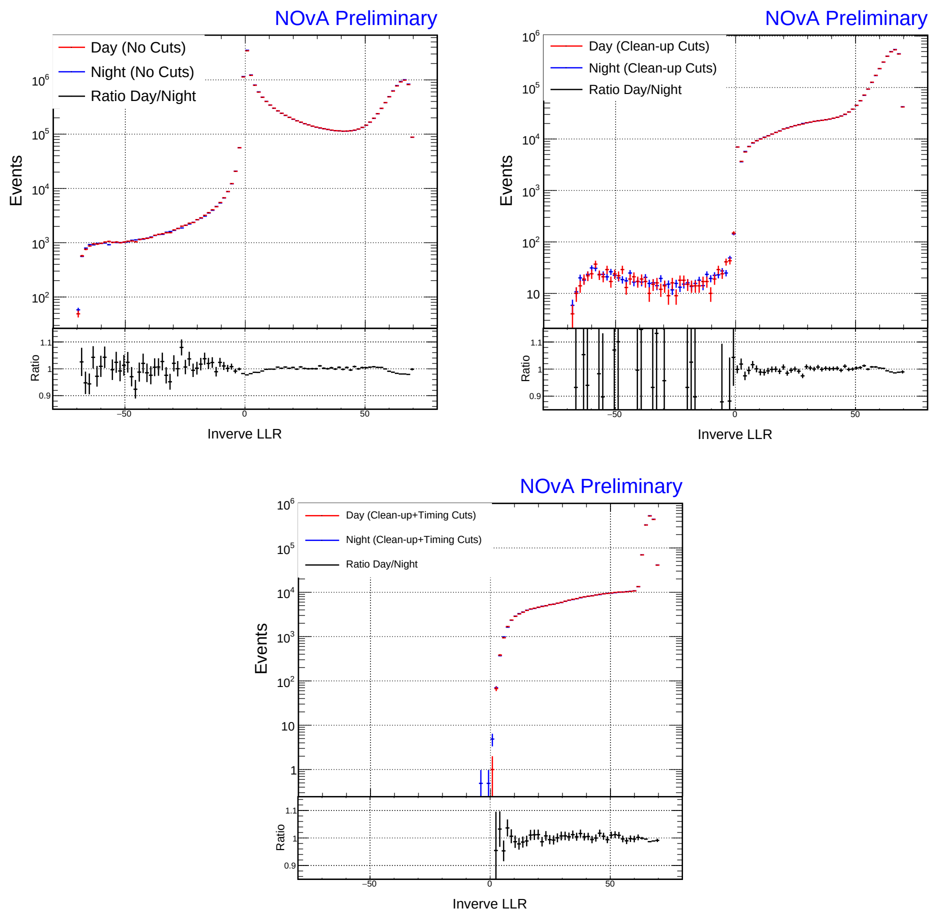

Figure C.1: The ratio between day and night for the inverse LLR with the for the cosmic sample with no cuts applied (top left), clean up cuts applied (top right) and full cuts applied (bottom).

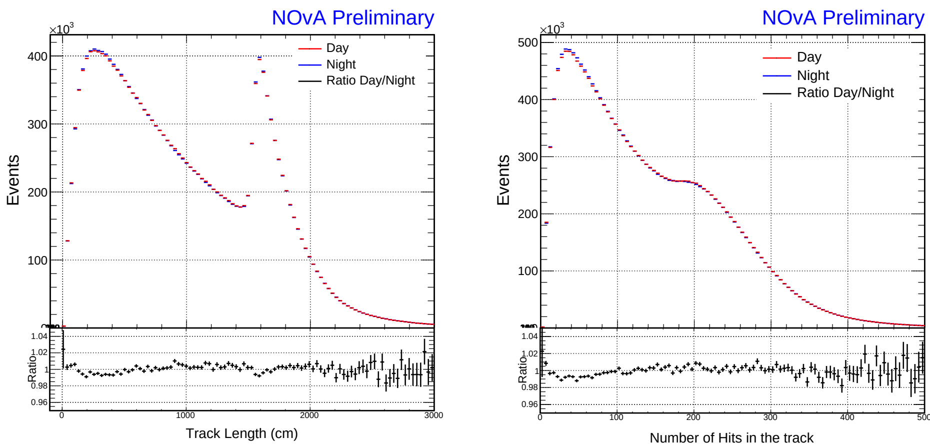

Figure C.2: The track length distribution (left) and the distribution of the number of hits on a track (right) in the cosmic-ray control region for the day and night sample. The distributions for day and night agree to better than 1 %.

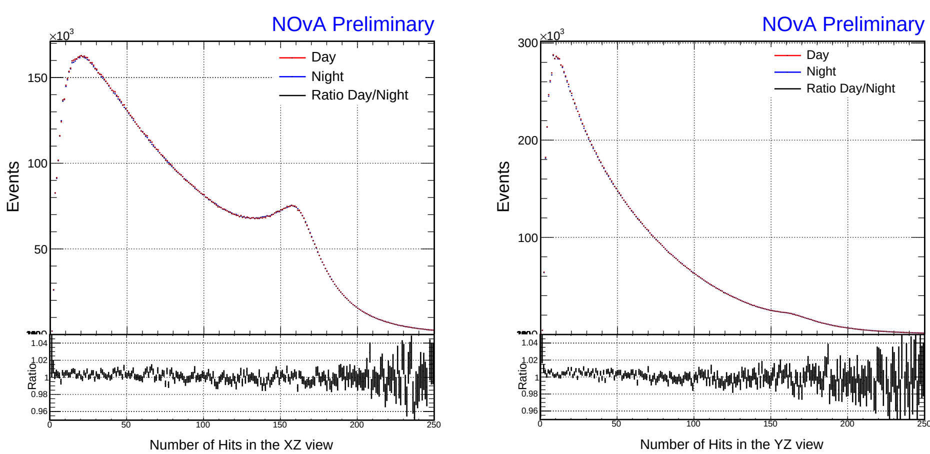

Figure C.3: The distribution of the number of hits on a track in the X-Z view (left) and the distribution of the number of hits on a track in the Y-Z view (right) in the cosmic-ray control region for the day and night sample. The distributions for day and night agree to better than 1 %.

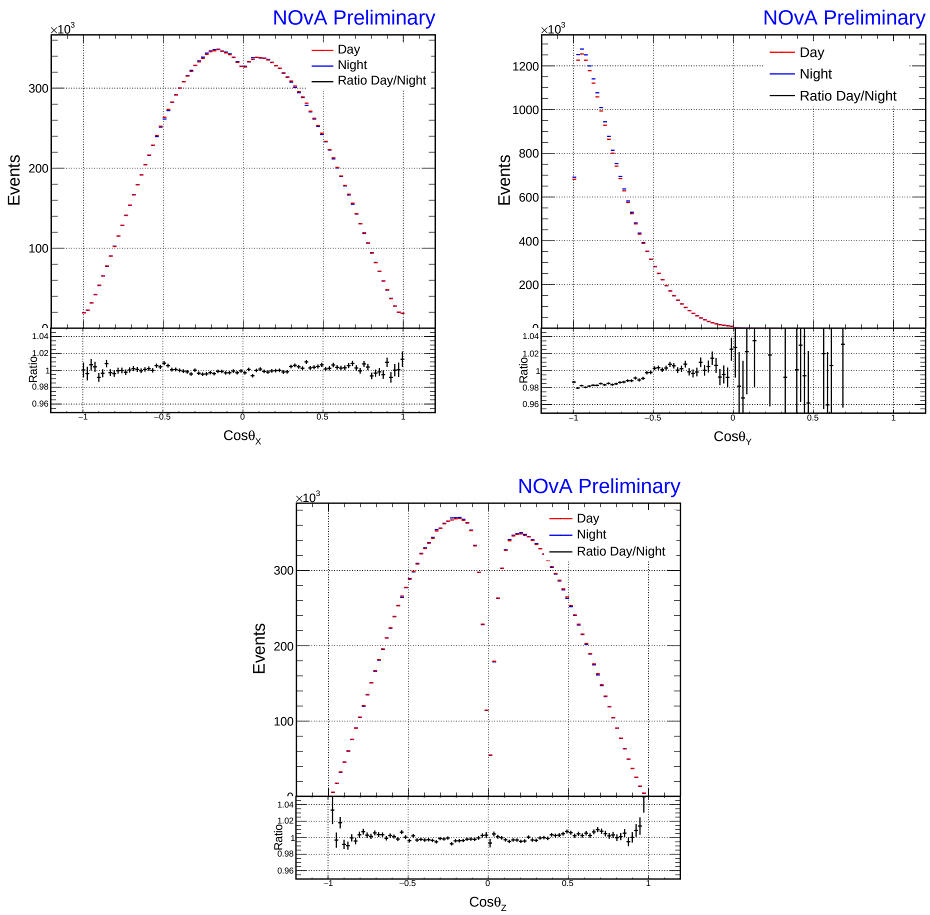

Figure C.4: The X (top left), Y (top right), and Z (bottom) directional cosines. The distributions for X and Z day and night agree to better than 1 %. For dirY, there is a systematic trend at the level of 2 %.

C.1 Distribution of Clean-up variables for the upward-going muon sample

This appendix shows distribution of the clean-up variables used to classify tracks as upward or downward-going. Figures C.5 and C.6 depict distributions of these separate variables with other variables fixed ($n-1$ plots).

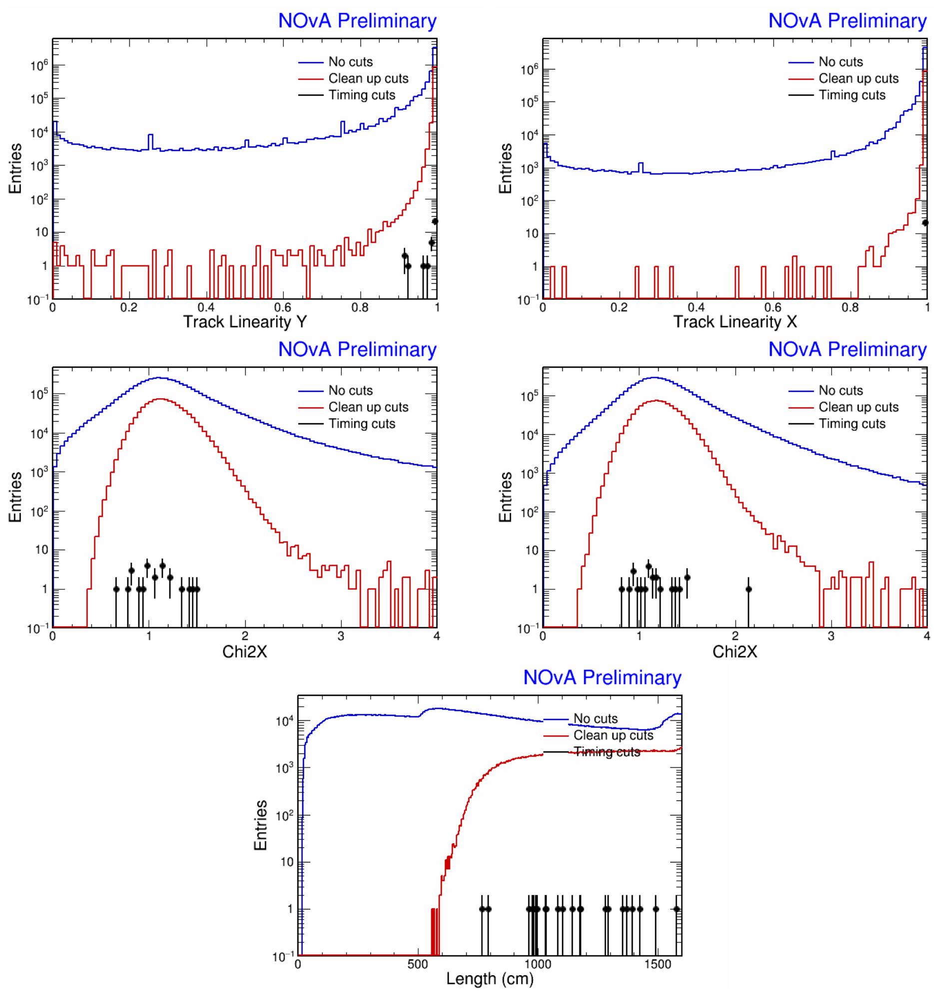

Figure C.5: Clean-up variables, plots are $n-1$ plots

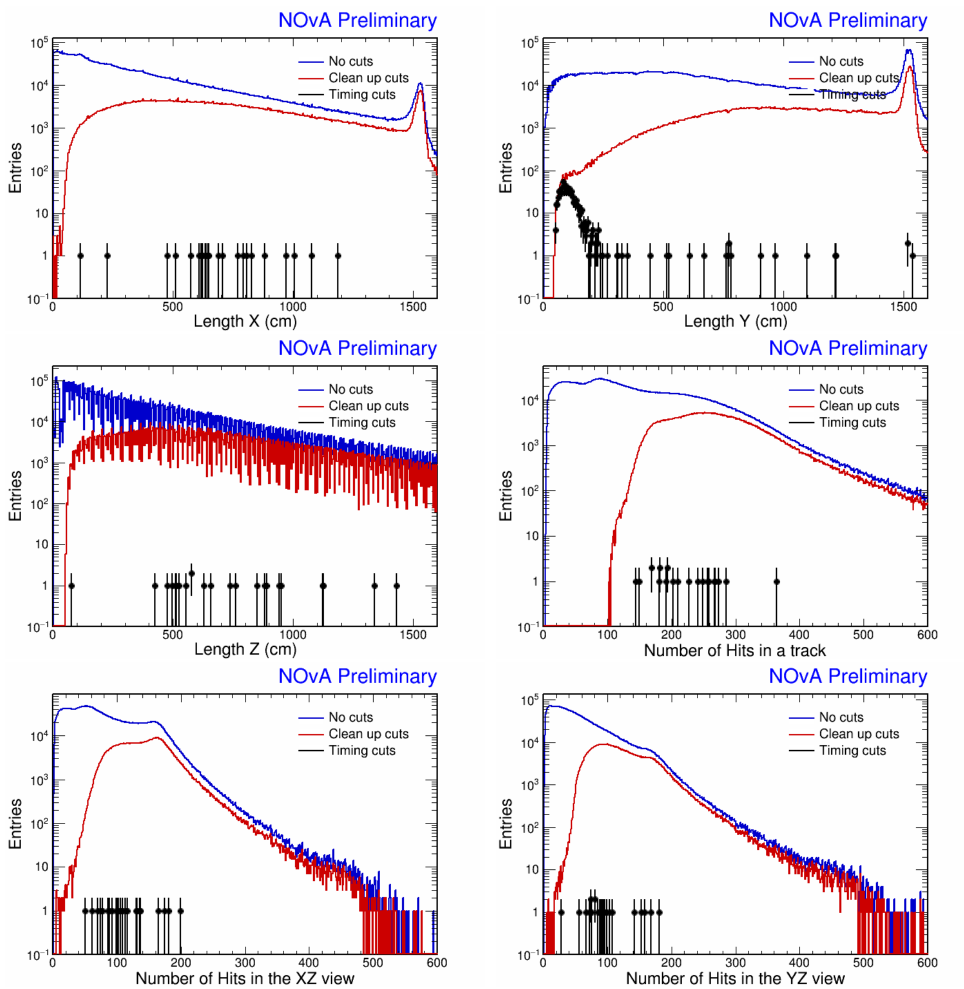

Figure C.6: Clean-up variables, plots are $n-1$ plots

Appendix D

N-1 Variable distribution of Upward-Going Muons

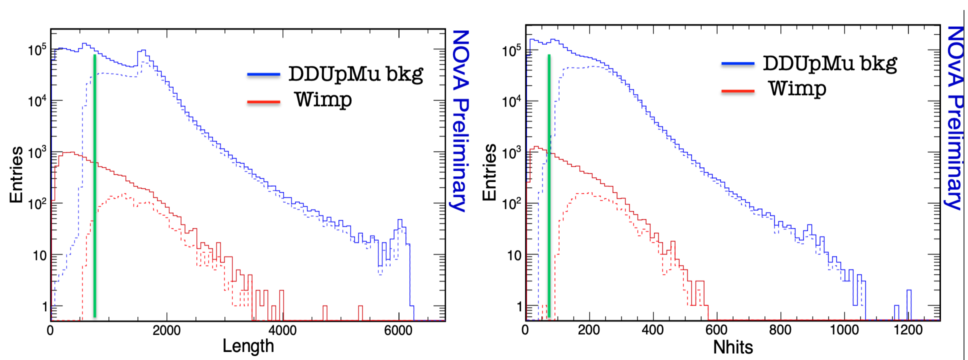

Figure D.1: $n-1$ plots with final cut values for Length and NHits

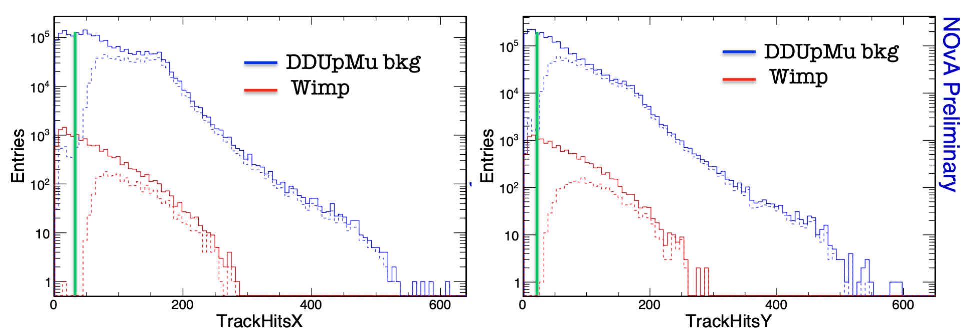

Figure D.2: $n-1$ plots with final cut values for the number of hits in a Track in X and Y

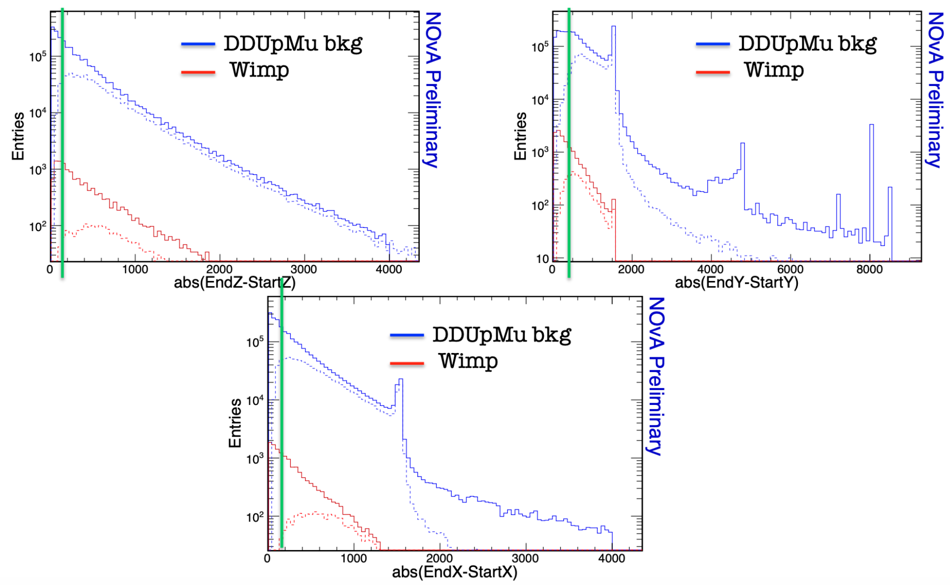

Figure D.3: $n-1$ plots with final cut values for X, Y and Z Length

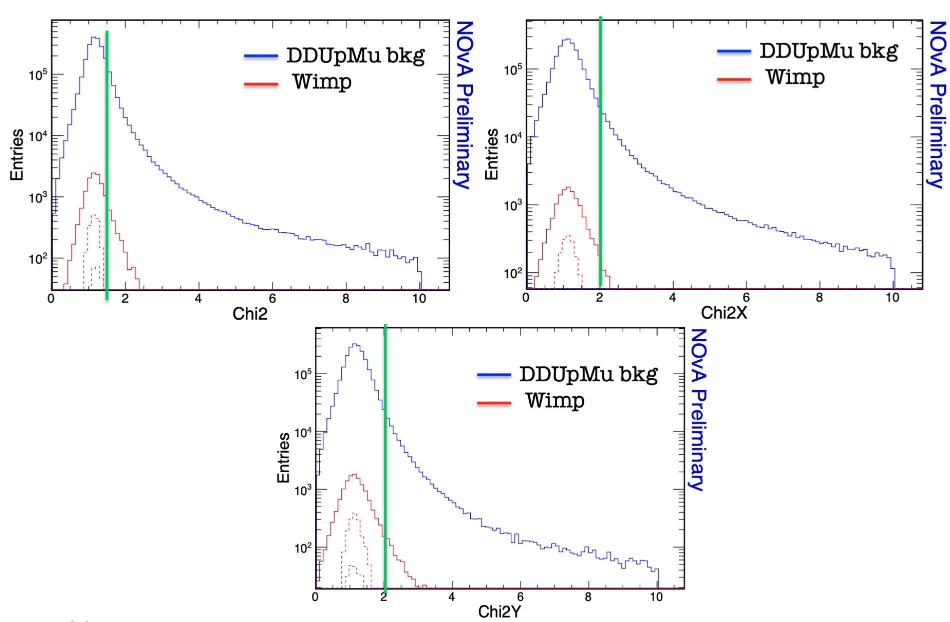

Figure D.4: $n-1$ plots with final cut values for Chi2 and Chi2 in X and Y views

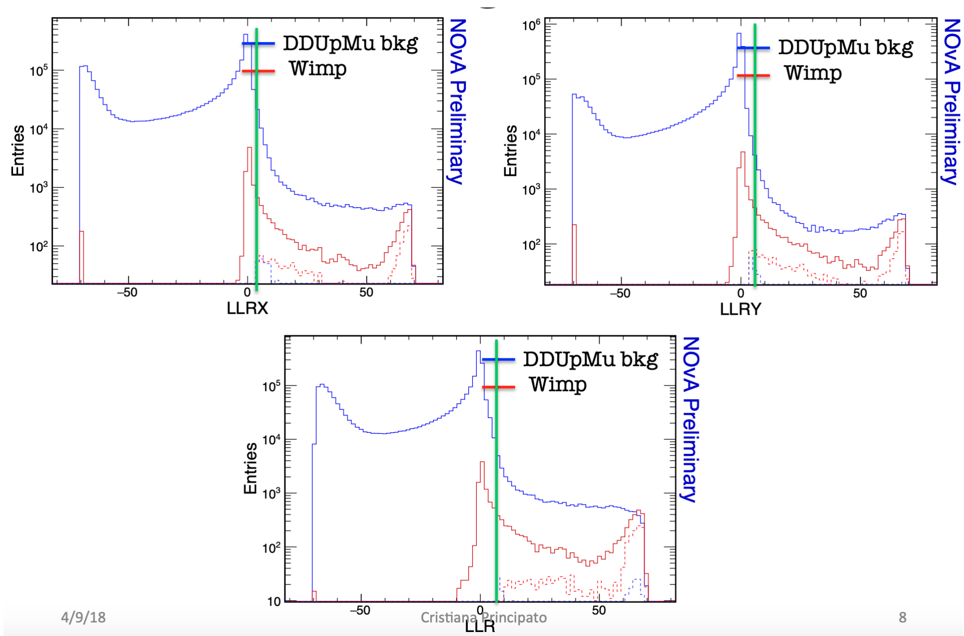

Figure D.5: $n-1$ plots with final cut values for LLR and LLR X and LLR Y

Appendix E

Further look at the mistmatch Events

The initial number of background events were dominated by mist-match in which two tracks were reconstructed as one upward-going tracks only, as it can be seen in Fig E.1.

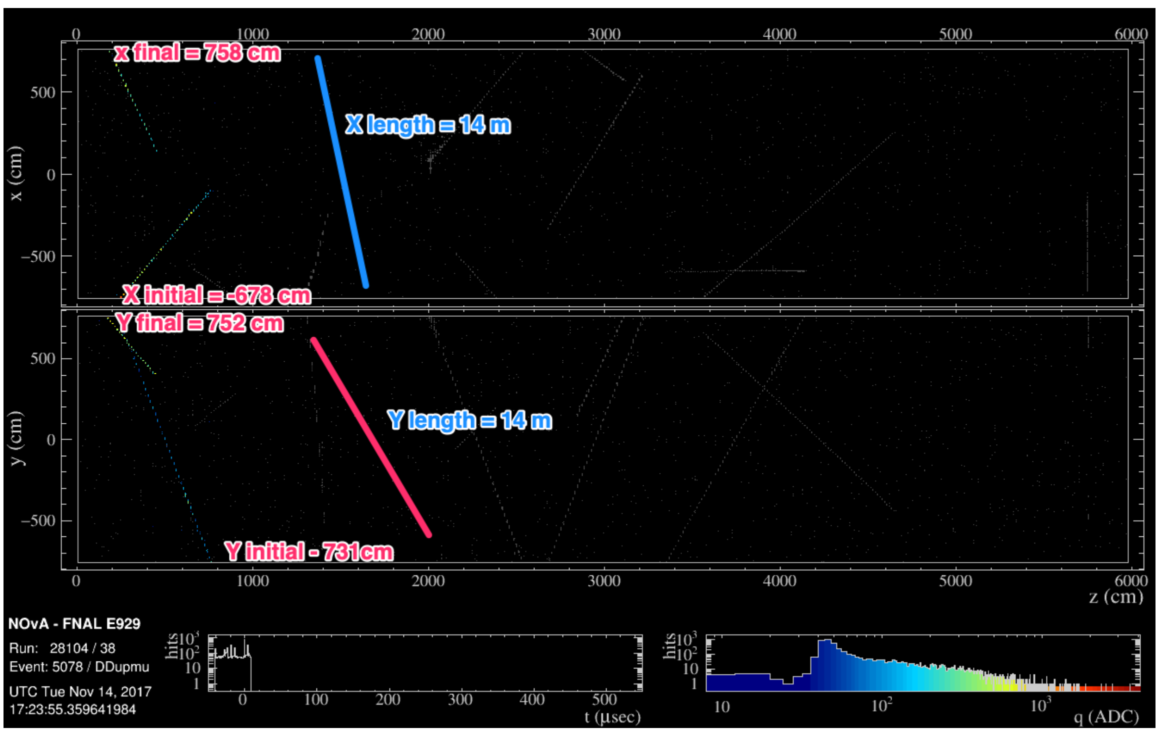

Figure E.1: Example of how tracks that happen consecutively trick the algorithm. The green line shows the length of the one track that has been reconstructed by the algorithm. Looking at the cells in the event display two tracks can be seen, overlapping in the z-axis. Improved reconstruction techniques could reduce this background in the future.

Initially this could happen because we were selecting slice that could contain more than one track. We then implemented new algorithm to remove the tracks that have more than one track in a slice if the other track happens at a distance shorter than

50 cm (start or end point) or if there is overlap between two tracks in a slice. This plus increase the LLRX and Y cut from 5 to 10, reduced our background from the initial number of 313,485,605 triggers to 98,056,207. The double tracks that remain

```
for(size_t k=0; k<v.size(); k++)
     {
       const T &t = v[k];
       if (v.size() > 1)
         {
           for(size_t i=k+1; i<v.size(); i++)
             {
               diffSS[i] = v[k]._startz - v[i]._startz;
               diffSE[i] = v[k]._startz - v[i]._ endz;
               diffES[i] = v[k]._ endz - v[i]._startz;
               diffEE[i] = v[k]._endz - v[i]._endz;
               if (fabs(diffSS.at(i)) < 50) matchSS++;
               if (fabs(diffSE.at(i)) < 50) matchSS++;
               if (fabs(diffES.at(i)) < 50) matchSS++;
               if (fabs(diffEE.at(i)) < 50) matchEE++;
             }
           if (matchSS> 1 || matchSE > 1 || matchES > 1 || matchEE > 1)
          }
```

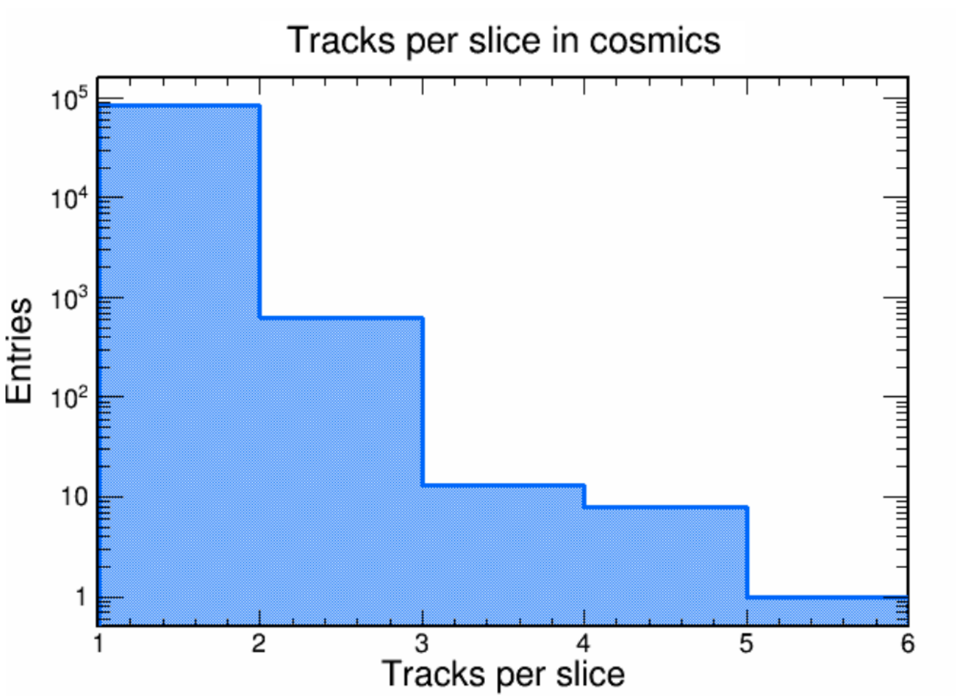

in our sample are not two tracks in a slide but are reconstructed as one only tracks. They are caused by reconstruction failures. This effect can be seen by looking at the cell hits and reco hits: First we checked that the algorithm calculating track linearity was working properly, doing different tests with cosmic rays muons (which follow a very straight trajectory at high energy). Further actions have been tried to eliminate there remaining events, like reducing outlier cuts (playing with different standard deviation values from 5 to 3 sigma). This cut had an impact on signal but did not

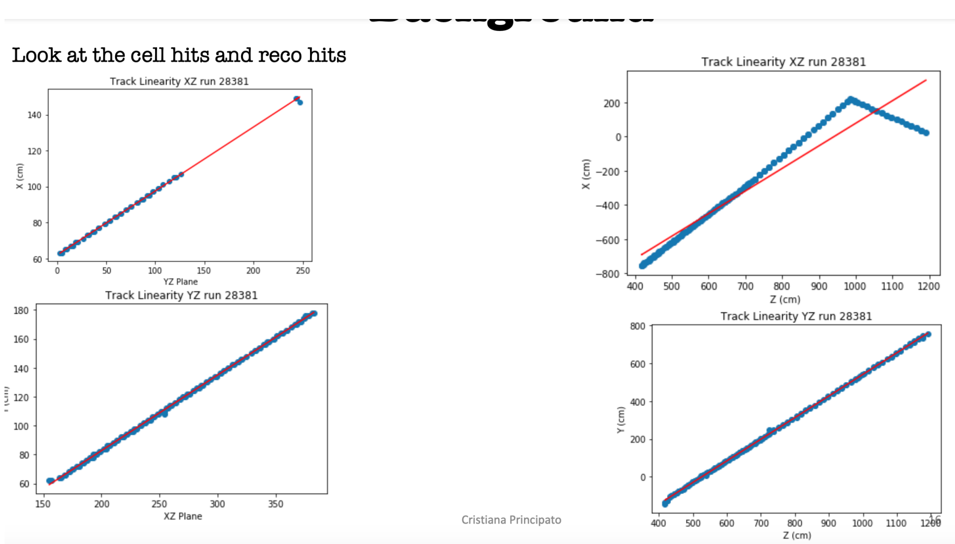

eliminate the double tracks in the background, so we decided to not use it. Not of the above solutions seemed to be effective, so since those events do not represent the main background, further steps were not taken.

Bibliography

[1] Hinshaw, G. F., et.al. *Nine-year Wilkinson Microwave Anisotropy Probe (WMAP) Observations: Cosmological Results*. arXiv:1212.5226 [astro-ph.CO], (2012).

[2] Zwicky, F. *Die Rotverschiebung von extragalaktischen Nebeln*. Helvetica Physica Acta, Volume 6, (1933).

[3] Edwin Hubble. *A relation between distance and radial velocity among extra-galactic nebulae*. PNAS March 15, (1929).

[4] S. Smith, *The Mass of the Virgo Cluster*, Astrophysical Journal, vol. 83, p.23, (1936).

[5] Rubin Vera C. *The Rotation of Spiral Galaxies*. SCIENCE, (1983).

[6] Frank Watson Dyson, Arthur Stanley Eddington and C. Davidson. *A determination of the deflection of light by the sun's gravitational field, from observations made at the total eclipse of May 29, 1919*. Philosophical Transactions of the Royal Society of London. Series A, Containing Papers of a Mathematical or Physical Character 220291333.

[7] A. S. Bolton, D. J. Schlegel, . Aubourg et. al. *Spectral Classification and Redshift Measurement for the SDSS-III Baryon Oscillation Spectroscopic Survey*. arXiv:1207.7326, Astronomical Journal 144, (2012).

[8] Ellis Richard S. *Gravitational lensing: a unique probe of dark matter and dark energy*. Philos. Trans. A Math. Phys. Eng. Science, (2010).

[9] Clowe Douglas, Marusa Bradac, Anthony H. Gonzalez, Maxim Markevitch, Scott W. Randall , Christine Jones, Dennis Zaritsky. *A direct empirical proof of the existence of dark matter*. arXiv:astro-ph/0608407, (2006).

[10] Planck Collaboration Ade, P.A.R. et al. *Planck 2015 results. XXIV. Cosmology from Sunyaev-Zeldovich cluster counts* arXiv:1502.01597 [astro-ph.CO] Astron.Astrophys. 594, (2016).

[11] Wayne Hu, Scott Dodelson. *Cosmic Microwave Background Anisotropies*. arXiv:astro-ph/0110414, (2012).

[12] Keith A. Olive. *Primordial Nucleosynthesis and Dark Matter*. arXiv:astro-ph/9707212, (1997).

[13] Subir Sarkar. *Primordial Nucleosynthesis and Dark Matter*. arXiv:astro-ph/9611232, (1996).

[14] Karsten Jedamzik and Maxim Pospelov. *Big Bang nucleosynthesis and particle dark matter*. New Journal of Physics, Volume 11, (2009).

[15] Peccei, R. D. *A Short Review of Axions*. PROC 19th INT. CONF. HIGH ENERGY PHYSICS, TOKYO, (1978).

[16] Leslie J Rosenberg. *Dark-matter QCD-axion searches*. Proc. National Academy of Science USA, (2015).

[17] K. Freese, B. Fields, D. Graff. *What are MACHOs? Limits on Stellar Objects as the Dark Matter of Our Halo*. arXiv:astro-ph//9901178, (1999).

[18] The MACHO Collaboration. *MACHO Project Limits on Black Hole Dark Matter in the 130 M Range*. The Astrophysical Journal, 550:L169-L172, (2001).

[19] Tisserand, P., et. al. *Limits on the Macho content of the Galactic Halo from the EROS-2 Survey of the Magellanic Clouds*. arXiv:astro-ph/0607207, Astronomy and Astrophysics, Volume 469, Issue 2, (2007).

[20] Udalski, A., Szymanski, et. al. *The Optical Gravitational Lensing Experiment. The Early Warning System: Real Time Microlensing*. Acta Astronomica, v.44, pp.227-234, (1994).

[21] Lee, Jae-Weon. *Brief History of Ultra-light Scalar Dark Matter Models*. EPJ Web of Conferences. 168. 10.1051/epjconf/201816806005, (2017).

[22] A. Boyarsky, M. Drewes, T. Lasserre, S. Mertens, O. Ruchayskiy, *Sterile Neutrino Dark Matter*, arXiv:1807.07938 [hep-ph], (2018).

[23] Nicols Bernal, Xiaoyong Chu, Suchita Kulkarni, Josef Pradler, Self-interacting dark matter without prejudice, Phys. Rev. D 101, (2020).

[24] F. Racine, K. Sigurdson, J. Zavala, T. Bringmann, M. Vogelsberger, and C. Pfrommer, ETHOS - An Effective Theory of Structure Formation: From dark particle physics to the matter distribution of the Universe, arXiv:1512.05344v4 [astro-ph.CO], (2017).

[25] Kamionkowski. *Week 3: Thermal History of the Universe*. Cosmology, Ay 127, (2008).

[26] Bertmat. *Supersymmetry: a bird eyes view*. https://people.sissa.it/ bertmat/lect1.pdf

[27] G. Jungman, M. Kamionkowski, K. Griest. *Supersymmetric Dark Matter*. arXiv:hep-ph/9506380, (1996).

[28] C. L. Cowan Jr., F. Reines, F. B. Harrison, H. W. Kruse, A. D. McGuire. *Detection of the Free Neutrino: a Confirmation*. Science, Vol. 124, Issue 3212, pp. 103-104, (1956).

[29] G. Danby, J-M. Gaillard, K. Goulianos, L. M. Lederman, N. Mistry, M. Schwartz, and J. Steinberger. *Observation of High-Energy Neutrino Reactions and the Existence of Two Kinds of Neutrinos*. Phys. Rev. Lett. 9, 36, (1962).

[30] DONUT Collaboration *Observation of Tau Neutrino Interactions*. Phys.Lett.B504:218-224, (2001).

[31] M. Goldhaber, L. Grodzins, and A. W. Sunyar. *Helicity of Neutrinos*. Phys. Rev. 109, 1015, (1958).

[32] John N. Bahcall *Solar neutrinos: Theory versus observation*. Space Sci Rev 24, (1979).

[33] B. Pontecorvo Report PD-205, Chalk River Laboratory, (1946).

[34] Takaaki Kajita, Super-Kamiokande and Kamiokande collaborations. *Atmospheric neutrino results from Super-Kamiokande and Kamiokande - Evidence for oscillations*. Nuclear Physics B - Proceedings Supplements, Volume 77, Issues 13, (1999).

[35] SNO Collaboration, A.B. McDonald *The Sudbury Neutrino Observatory project*. Nuclear Physics B - Proceedings Supplements, Volume 77, Issues 13, (1999).

[36] Lars Bergstrom, *Non-Baryonic Dark Matter: Observational Evidence and Detection Methods*. arXiv:hep-ph/0002126v1, (2000).

[37] J. Lewin and P. Smith, *Review of mathematics, numerical factors, and corrections for dark matter experiments based on elastic nuclear recoil*, Astropart. Phys. 6, (1996).

[38] Queiroz, Farinaldo S, *Dark Matter Overview: Collider, Direct and Indirect Detection Searches*, arXiv:1605.08788 [hep-ph], (2016).

[39] R. Primack, Ann. Rev. Nuc. Part. Phys. 38, (1990).

[40] R. Bernabei, P. Belli, A. Bussolotti, F. Cappella, V. Caracciolo, R. Cerulli, C.J. Dai, A. d'Angelo, A. Di Marco, H.L. He, A. Incicchitti, X.H. Ma, A. Mattei, V. Merlo, F. Montecchia, X.D. Sheng, Z.P. Ye. *First model independent results from DAMA/LIBRA-phase2*. Nucl. Phys. At. Energy 19, (2018).

[41] LUX Collaboration. *Results from a search for dark matter in the complete LUX exposure* Phys. Rev. Lett. 118, 021303, (2017).

[42] XENON 1T Collaboration. *Dark Matter Search Results from a One TonneYear Exposure of XENON 1T*. Phys. Rev. Lett. 121, 111302, (2018).

[43] JOHN ELLIS, ANDREW FERSTL, KEITH A. OLIVE. *THEORETICAL ASPECTS OF DARK MATTER DETECTION*. arXiv:hep-ph/0106148v1, (2001).

[44] A Baltz, et al. [GLAST Collaboration] *Pre-launch estimates for GLAST sensitivity to dark matter annihilation signals* J. Cosmol. Astropart. Phys. JCAP07, (2008).

[45] J. Buckley, D. F. Cowen, S. Profumo, A. Archer, M. Cahill-Rowley, R. Cotta, S. Digel and A. Drlica-Wagner *et al.*, *Working Group Report: WIMP Dark Matter Indirect Detection*, arXiv:1310.7040, (2013).

[46] Arghya Choudhury, Subhadeep Mondal *Revisiting the Exclusion Limits from Direct Chargino-Neutralino Production at the LHC*. Phys. Rev. D 94, 055024, (2016).

[47] CMS Collaboration, *Search for dark matter produced in association with a leptonically decaying Z boson in proton-proton collisions at s= 13 TeV*. Eur. Phys. J. C 81, (2021).

[48] ATLAS Collaboration, ATLAS sensitivity to dark matter produced in association with heavy quarks at the HL-LHC. ATL-PHYS-PUB-2018-036, (2018).

[49] B. Still, *On the path to precision*. Nature Phys 12, 292293 (2016).

[50] NOvA Collaboration (D.S. Ayres et al.), *The NOvA Technical Design Report*. doi:10.2172/935497, (2007).

[51] NOvA Collaboration (D.S. Ayres et al.). *Timing Calibration Technical Note*. NOvA Internal (Private) Document, DocDB-13579.

[52] A. Norman *et al.*, *Performance of the NOA Data Acquisition and Trigger Systems for the full 14 kT Far Detector*, J. Phys. Conf. Ser. **664**, 082041 (2015).

[53] S. Mufson, et al. *Liquid scintillator production for the NOvA experiment*. arXiv:1504.04035v2 [physics.ins-det] 30 Jun 2015

[54] A. Norman, R. Kwarciany, G. Deuerling, and N. Wilcer. *The NOvA Timing System: A System for Synchronizing a Long Baseline Neutrino Experiment*. J. Phys. Conf. Ser., vol. 396, (2012).

[55] Evan Niner. *Observation of electron neutrino appearance in the numi beam with the nova experiment*. PhD Thesis, Indiana University, (2015).

[56] A. Aurisano, [NOvA Collaboration], *The NOvA Detector Simulation*, NOvA Internal (Private) Document, DocDB-13577, (2015).

[57] A. Aurisano, [NOvA Collaboration], *ASIC fall time vs. pulse height*, NOvA Internal (Private) Document, DocDB-13779, (2015).

[58] C. Principato, [NOvA Collaboration], *Mc scans timing resolution.* NOvA Internal (Private) Document, DocDB-15047, (2016).

[59] R. Mina *et al.* [NOvA Collaboration], *Implementation of an Upward-Going Muon Trigger for Indirect Dark Matter Searches at the NOνA Far Detector*, J. Phys.Conf. Ser. **664**, 082034, (2015).

[60] R. Mina, E. Culbertson, M. J. Frank, R. C. Group, A. Norman and I. Oksuzian, *A First Look at Data from the NOνA Upward-Going Muon Trigger*, arXiv:1511.00155 [hep-ex], (2015).

[61] Hough, P.V.C. *Method and means for recognizing complex patterns*, U.S. Patent 3,069,654, (1962).

[62] A. Tsaris, P. Ding, C. Group, S. Kurbanov, Y. Oksuzian, C. Principato, L. Aliaga, R. Mina and A. Norman, *Proceedings, 38th International Conference on High Energy Physics (ICHEP 2016) : Chicago, IL, USA, August 3-10, 2016*, PoS ICHEP, **2016**, 201 (2016).

[63] Serdar Kurbanov, *Data Driven Trigger analysis for NOvA experiment*, MS thesis, University of Virginia, (2016).

[64] P. Adamson *et al.* [NOvA Collaboration], *Measurement of the Neutrino Mixing angle θ_{23} in NOvA*, Submitted to: Phys.Rev.Lett. [arXiv:1701.05891 [hep-ex]], (2017).

[65] Kanika Sachdev, *Muon Neutrino to Electron Neutrino Oscillation in NOvA*, PhD Thesis, University of Minnesota, (2015).

[66] N. Raddatz, [NOvA Collaboration], *KalmanTrack Technical Note*, NOvA Internal (Private) Document, DocDB-13545, (2015).

[67] Gavin Davis, [NOvA Collaboration], *A review of CosmicTrack algorithm* , NOvA Internal (Private) Document, DocDB-6890, (2012).

[68] B. Rebel, [NOvA Collaboration] *A Window Tracking Algorithm for Cosmic Ray Muons* NOvA Internal (Private) Document, DocDB-15977, (2016).

[69] C. Principato, [NOvA Collaboration] *Upward-going muon analysis, Technical note.* NOvA Internal (Private) Document, DocDB-26828, (2019).

[70] M. M. Boliev, S. V. Demidov, S. P. Mikheyev and O. V. Suvorova, *Search for muon signal from dark matter annihilations in the Sun with the Baksan Underground Scintillator Telescope for 24.12 years*, JCAP **1309**, 019, (2013).

[71] P. Adamson *et al.* [MINOS Collaboration], *Observation in the MINOS far detector of the shadowing of cosmic rays by the sun and moon*, Astropart.Phys.34:457-466, (2011).

[72] M.G. Aartsen *et al.* [IceCube Collaboration], *Observation of the cosmic-ray shadow of the Moon with IceCube*, Phys. Rev. D 89, (2004).

[73] M. Ambrosio *et al.* [MACRO Collaboration], *Observation of the shadowing of cosmic rays by the Moon using a deep underground detector*, Phys. Rev. D 59, (2003).

[74] L. Aliaga, P. Ding , C. Group, S. Kurbanov , R. Mina, A. Norman, Y. Oksuzian, C. Principato, A. Tsaris, [NOvA Collaboration], *Neutrinos from WIMP annihilations using a full three-flavor Monte Carlo*, NOvA Internal (Private) Document, DocDB-15860, (2016).

[75] Joao A B Coelho, [NOvA Collaboration], *Tech note: Good data selection*, NOvA Internal (Private) Document, DocDB-13546, (2017)

[76] Kanika Sachdev and Ryan Murphy, [NOvA Collaboration], *Data Quality Metadata in SAM- Technote*, NOvA Internal (Private) Document, DocDB-25581, (2017).

[77] B. Rebel, [NOvA Collaboration], *Window Tracking Update*, NOvA Internal (Private) Document, DocDB-11806, (2014).

[78] J. S. Hagelin, K. W. Ng and K. A. Olive, *A High-energy Neutrino Signature From Supersymmetric Relics*, Phys. Lett. B **180**, 375, (1986).

[79] M. Blennow, J. Edsjo and T. Ohlsson, *Neutrinos from WIMP annihilations using a full three-flavor Monte Carlo*, JCAP **0801**, 021, (2008).

[80] J. Edsjo, WimpSim Neutrino Monte Carlo, http://www.fysik.su.se/ edsjo/wimpsim/.

[81] Costas Andreopoulos, Christopher Barry, Steve Dytman, Hugh Gallagher, Tomasz Golan, Robert Hatcher, Gabriel Perdue, Julia Yarba, *The GENIE Neutrino Monte Carlo Generator: Physics and User Manual*, arXiv:1510.05494, (2015).

[82] S. Agostinelli, J. Allison, K. Amako, et. al, *Geant4a simulation toolkit*, Nuclear Instruments and Methods in Physics Research, Volume 506, Issue 3, (2003).

[83] M. Tanabashi et al. *Particle Data Group*, The Review of Particle Physics, (2017).

[84] Pidwirny, M. *Earth-Sun Geometry*, Fundamentals of Physical Geography, 2nd Edition, (2006).

[85] NEWBURY ASTRONOMICAL SOCIETY, MONTHLY MAGAZINE, (2018).

[86] J.A. Formaggio, G.P. Zeller, *From eV to EeV: Neutrino Cross Sections Across Energy Scales*, Rev. Mod. Phys. 84, 1307, (2012).

[87] Y. Oksuzian, C. Group, R. Mina, M. Frank, A. Norman, and E. Fries, [NOvA Collaboration] *Neutrinos from WIMP annihilations using a full three-flavor Monte Carlo*, NOvA Internal (Private) Document, DocDB-12116, (2014).

[88] C. Rott, T. Tanaka, Y. Itow, *Enhanced Sensitivity to Dark Matter Self-annihilations in the Sun using Neutrino Spectral Information*, arXiv:1107.3182v1 [astro-ph.HE], (2011).

[89] K. Choi, K. Abe, et al. [Super-Kamiokande Collaboration] *Search for neutrinos from annihilation of captured low-mass dark matter particles in the Sun by Super-Kamiokande*, arXiv:1503.04858v1[hep-ex], (2015).

[90] G. Wikstrm, J. Edsj, *Limits on the WIMP-nucleon scattering cross-section from neutrino telescopes*, Cosmology and Nongalactic Astrophysics, (2009).

[91] K. Abe, et al. [Super-Kamiokande Collaboration], *Limits on sterile neutrino mixing using atmospheric neutrinos in Super-Kamiokande*, Phys. Rev. D 91, (2015).

[92] K. Choi *et al.* [Super-Kamiokande Collaboration], *Search for neutrinos from annihilation of captured low-mass dark matter particles in the Sun by Super-Kamiokande*, Phys. Rev. Lett. **114**, no. 14, (2015).

[93] T. Bringmann, J. Edsjo, P. Gondolo, P. Ullio, L. Bergstrom, *DarkSUSY 6 : An Advanced Tool to Compute Dark Matter Properties Numerically*, JCAP 1807, (2018).

[94] WimpSim, *http://wimpsim.astroparticle.se/figures/wa-allplots-res-jan2013.pdf*

[95] T. Tanaka *et al.* [Super-Kamiokande Collaboration], *An Indirect Search for WIMPs in the Sun using 3109.6 days of upward-going muons in Super-Kamiokande*, Astrophys. J. **742**, 78, (2011).

[96] M. G. Aartsen *et al.* [IceCube Collaboration], *Search for dark matter annihilations in the Sun with the 79-string IceCube detector*, Phys. Rev. Lett. **110**, no. 13, (2013).

[97] M. Ambrosio et al, The MACRO Collaboration, *Limits on dark matter WIMPs using upward-going muons in the MACRO detector*, Phys.Rev.D60:082002, (1999).

[98] Pierre Baldi, Jianming Bian, Lars Hertel, Lingge Li Improved Energy Reconstruction in NOvA with Regression Convolutional Neural Networks, arXiv:1811.04557v3 [physics.ins-det], (2019).